UNIVERSITY OF KWAZULU-NATAL

Multi-wavelength study of radio sources in the universe

by

Khadija El Bouchefry

A dissertation submitted in fulfillment of the

academic requirements for the degree of

Doctor of Philosophy,

in the

School of Physics,

University of KwaZulu-Natal,

Durban

9 March 2009

Supervisors:

Prof. Jon Rash (School of Physics)

Dr. Kavilan Moodley (School of Mathematical Sciences)

Multi-wavelength study of radio sources in the universe

Examiners :

Prof. Chris Willott, Department of Physics, University of Ottawa, *External Examiner*

Dr. Matt Jarvis, Centre for Astrophysics, University of Hertfordshire, *External Examiner*

Dr. Amery Gareth, School of Mathematical Sciences, University of KwaZulu -Natal, *Internal Examiner*

Abstract

This thesis presents a detailed multi-wavelength study of radio sources. A major part of the thesis focuses on radio sources in the FIRST survey while the latter part of the thesis studies low redshift radio galaxies in X-ray selected galaxy clusters. In the first part of the thesis a cross correlation analysis of FIRST radio sources with optical data from the NDWFS and infrared data from the FLAMINGOS survey in the Boötes and Cetus fields was performed. Optical counterparts were found for 76% (688/900) of sources in one band or more i.e., *Bw, R, I* or *K*. Photometric redshifts for these sources have been computed using the *Hyperz* code. The redshifts obtained are fairly consistent with those expected from the $K-z$ relation for brighter radio sources. A total number of 57 counterparts have extremely red colour ($R-K>5$). Photometric redshifts derived using *Hyperz* imply that these Extremely Red Object (ERO) counterparts to FIRST radio sources are mostly located in the range $z\sim 0.7-2$, with the bulk of the population at $z\sim 1$. A total of 25 ERO counterparts to FIRST radio sources were identified in *R, J* and *K* bands. These objects were separated into passively-evolving and dusty star-forming galaxies using their *R, J* and *K* colours. The relatively blue $J-K$ colour of these galaxies suggest that most (72%, 18/25) are elliptical galaxies rather than dusty starburst galaxies.

Using data from the Chandra XBoötes survey, a total of 92 (10%) FIRST radio sources were identified above the X-ray flux limit, $f_X\,(0.5-7)$ keV $= 8\times10^{-15}$ erg s^{-1} cm^{-2}, and of these

79 optical counterparts are in common to the radio-X-ray matches. The majority (68%) of the radio-X-ray matched population were found to have $-1 < \log f_X/f_{opt} < +1$ indicative of AGNs. There is a significant population (23%) with high X-ray-to-optical flux ratio ($\log f_X/f_{opt} > 1$), suggesting high redshift and/or dust obscured AGN. In addition, there is also a population of sources that are X-ray faint optically bright sources with $\log f_X/f_{opt} < -1$. Spectroscopic identifications were found for 22 of the 79 sources. These optical spectra were dominated by broad line AGNs and also included narrow emission line galaxies. It was found that many classes of objects contribute to the X-ray/radio emission including quasars, BL Lacs, starburst galaxies, normal galaxies and galaxies with both AGN and starburst activity.

This thesis also investigated the clustering analysis of FIRST radio sources optically identified in the SDSS DR6 survey using the two point angular correlation function $\omega(\theta)$. The matched sources were found to have a larger amplitude of clustering compared to the full catalogue of radio sources consistent with similar studies in the literature. The angular correlation function was measured for different magnitude limited and flux limited subsamples. It was found that the angular correlation function scales with the depth of the optical survey as expected, whereas the amplitude of the angular correlation function increases as the radio flux increases.

The last part of this thesis is devoted to studying radio galaxies in galaxy clusters at high frequencies to explore their contamination to the Sunyaev-Zel'dovich effect signal in these clusters. A total of 139 galaxies at low redshift ($z < 0.25$) in X-ray selected clusters were observed at four frequencies, $4.9, 9, 22$, and 43 GHz using the NRAO Very Large Array. It was found that more than half of the observed sources have steep microwave spectra with steep spectral index, $\alpha < -0.5$, as generally expected. However, about 60% of the unresolved or barely resolved sources have flat or inverted spectra. Most of these sources show an upward turn in flux at $\nu > 22$ GHz, implying a higher flux than would be expected from an extrapolation of the lower frequency flux measurements. Our results quantify the need for careful source subtraction in increasingly sensitive measurements of the Sunyaev-Zel'dovich effect in clusters of galaxies.

Preface

The work described in this thesis was carried in the School of Physics, University of KwaZulu-Natal, Durban, from October 2004 to March 2009.

These studies represent original work by the author and have not otherwise been submitted in any form for any degree or diploma to any tertiary institution. Where use has been made of the work of others it is duly acknowledged in the text.

DECLARATION 1 - PUBLICATIONS

Details of contribution to publications that include research presented in this thesis:

▷ *Identifications of FIRST radio sources in the NOAO Deep-Wide Field Survey.*

K. El Bouchefry & C.M. Cress, 2007, Astron.Nachr, 328, 577.

For this work I performed the analysis, obtained the results and wrote up the paper under the supervision of Dr Cress.

▷ *The FIRST radio survey: Panchromatic properties of FIRST radio sources in the Boötes and Cetus fields.*

K. El Bouchefry, 2009, Astron.Nachr, 330, 107

I undertook the analysis and wrote up the results for this paper.

▷ *The FIRST radio survey: The K – z diagram of FIRST radio sources identified in Boötes and Cetus fields*

K. El Bouchefry, 2008, revised and resubmitted to Astron.Nachr

I undertook the analysis and wrote up the results for this paper.

▷ *X-ray Identifications of FIRST radio sources in the XBoötes field.*

K. El Bouchefry, 2008, revised and resubmitted to MNRAS.

I undertook the analysis and wrote up the results for this paper.

▷ *Clustering statistics of FIRST radio sources identified in SDSS DR6 survey.*

K. El Bouchefry et al., in preparation.

▷ *Spectral Energy Distribution of Radio Sources in Nearby Clusters of Galaxies: Implications for Sunyaev-Zel'dovich Effect Surveys.*

Lin, Y., Partridge, B., Pober, J. C., **El Bouchefry, K.**, Burke, S., Klein, J., Coish, J., Huffenberger, K., 2008, submitted to ApJ, astro-ph/0805.1750

My contribution to this work included the reduction and calibration of the data at Haverford College USA, where I spent six weeks in 2006, I obtained the fluxes of the radio galaxies in four spectral bands (C, X, Q, K).

Signed: **Khadija El Bouchefry** Date:

DECLARATION 2 - NON PLAGIARISM

I hereby declare that:

1. The research reported in this thesis, except where otherwise indicated, is my original research.
2. This thesis has not been submitted for any degree or examination at any other university.
3. This thesis does not contain other persons' data, pictures, graphs or other information, unless specifically acknowledged as being sourced from other persons.
4. This thesis does not contain other persons' writing, unless specifically acknowledged as being sourced from other researchers. Where other written sources have been quoted, then: a.Their words have been re-written but the general information attributed to them has been referenced b.Where their exact words have been used, then their writing has been placed in italics and inside quotation marks, and referenced.
5. This thesis does not contain text, graphics or tables copied and pasted from the Internet, unless specifically acknowledged, and the source being detailed in the thesis and in the References sections.

Signed: **Khadija El Bouchefry** Date:

♡♡♡

This thesis is dedicated to my Mother, my Father, my sister, for always giving me love, support and encouragement.

♡♡♡

Acknowledgements

This PhD has consumed the last four years of my life and there are many people I would like to thank who have helped me along the way.
I would like to thank my advisors Pr Jon Rash and Dr Kavilan Moodely for their guidance and support. Also, would like to thank Dr Kavilan Moodley for his meticulous proofreading of my PhD in the last months has rescued it from a quagmire of bad grammar and inaccuracy.

My mother truly deserves my most heartfelt thanks. She is the most amazing and beautiful woman I know, I have always felt that I have taken after her in more ways than one. My father deserves equal thanks. He too has always encouraged me along whichever path I chose and has always been my greatest role model. His pride in me has always made me happy. Special thanks to my sister, Kabira, always taught me that nothing is impossible and the importance of having a back-up plan. I owe everything to my family for standing by me at all times. The decision to come to South Africa to pursue my PhD was extremely difficult and I owe a lot to my parents for standing by me. If for once they had said no, I would never have come to be here.

I also would to thank so many researchers who helped via emails(Although I never meet them): Dr Anthony Gonzalez, Dr Matt Jarvis, Dr Chris Willott, Dr Roderick Overzier.

I also would like to thank Dr Matt Hilton (post-doc) for his proof reading my thesis. I would like to thank Dr Nicola Loaring for her help in the South African Astronomical Observatory (SAAO).

This research was financially supported by the National Research Foundation (NRF), South Africa Square Kilometere Array (SKA), Dr Kavilan Moodley and School of Physics.

It was a pleasure working with and learning from all the members of the Astrophysics and Cosmology Research Unit (ACRU) group and the members of the school of the Mathematical Sciences of the University of KwaZulu-Natal.

I wish to thank my friends and colleagues for their very pleasant company and lots of assistance along the way. Each in their own particular way, have enriched my life and made the experience as complete as can be.

My friends are greatly thanked for ‘being there’ for me and for the good times spent together.

Table of Contents

List of Figures

List of Tables

CHAPTER 1

Introduction

1.1 The evolution of the universe

Understanding the large scale distribution of galaxies in the universe is one of the primary objectives in modern cosmology. The extensive efforts devoted to this topic are repaid by the wealth of information that can be extracted from clustering measurements. And indeed, these measurements have been exploited since the 1970's to gain insight into the initial conditions of the Big Bang, to constrain the matter content of the universe and to cast new light onto the physical processes that have operated through cosmic time.

1.1.1 The isotropic universe

The philosophy that the universe appears to be the same in all directions combined with the Copernican principle - that we do not occupy a privileged position in the universe - implies that the universe should be the same everywhere, on the large scale. This is known as the cosmological principle which can be simply stated as:

On sufficiently large scales (i.e. averaged over regions that are several hundred mega-parsecs

across) the universe is homogeneous (i.e the same everywhere) and isotropic (i.e. the same in all directions).

1.1.2 The universe in equations

The nearly isotropic Cosmic Microwave Background (CMB) radiation provides the strongest support to the widely accepted model of a (statistically) homogenous and isotropic universe, with space-time described by Robertson-Walker metric. The derivation of the Robertson-Walker metric is given in any of the standard cosmology texts, for example Berry (1989), Longair (1984) or Peebles (1993).

The geometric properties of space-time in any Friedmann-Robertson Walker model (usually abbreviated to FRW model) can be deduced from the following expression for the space-time separation ds of two events that are moving away from one another, and which are located at a coordinate distance r from the origin. In terms of comoving coordinates (r, θ, ϕ) the metric is :

$$ds^2 = c^2\,dt^2 - R^2(t)\left(\frac{dr^2}{1-kr^2} + r^2\,d\theta^2 + r^2\,sin^2\theta\,d\phi^2\right), \tag{1.1}$$

where $R(t)$ is the scale factor which describes the expansion or contraction of space as function of time. The parameter k is the curvature of space-time and can take the values -1, 0, $+1$.

Equation (1.1) applies to all the FRW models, but in order to work out the details it is necessary to specify the value of k and to determine the precise form of $R(t)$ for a universe uniformly filled with pressure free matter of density ρ. The form of $R(t)$ can be determined by solving the Friedmann equation:

$$\left(\frac{\dot{R}}{R}\right)^2 = \frac{8\pi G\rho_M}{3} + \frac{\Lambda}{3} - \frac{k}{R^2}, \tag{1.2}$$

Here Λ is the cosmological constant and G is Newton's gravitational constant. This equation relates the value of R and the rate of change of R to the curvature parameter k, the cosmic density ρ and the cosmological constant Λ. Different values of k and Λ lead to quite different forms for $R(t)$, and these are illustrated schematically in Figure 1.1.

The expansion rate of the universe at a given time is described by the so called Hubble law,

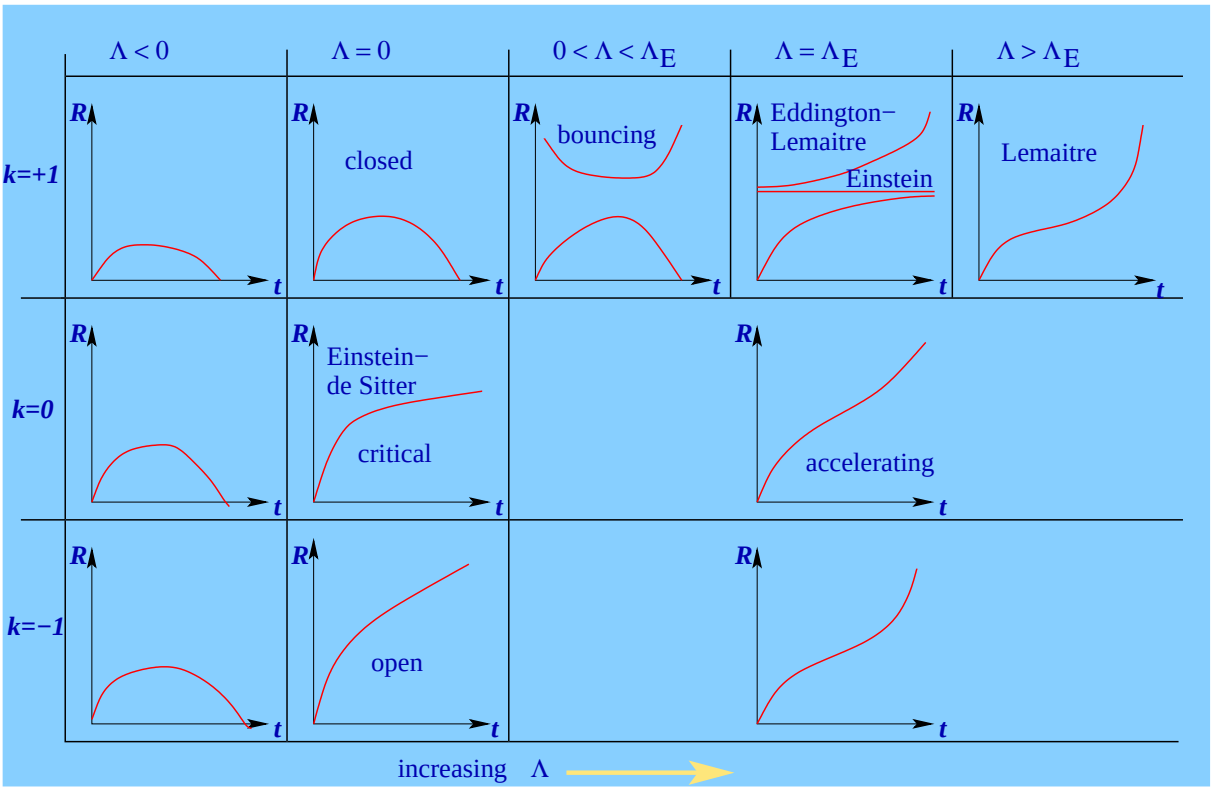

Figure 1.1: The cosmological scale-factor $R(t)$ as a function of time, for three possible curvatures: open ($k = -1$), critical ($k = 0$) and closed ($k = +1$) for different cosmological constant Λ. Here $\Lambda_E = \dfrac{k}{R_E^2}$, where R_E is radius of Einstein static universe.

which states that the relative recession velocity is proportional to distance,

$$\mathrm{v} = \frac{\dot{R}(t)}{R(t)}\, d, \tag{1.3}$$

where the parameter:

$$H(t) = \frac{\dot{R}(t)}{R(t)}, \tag{1.4}$$

is the *Hubble parameter* (which is spatially constant, by homogeneity, but in general is not constant with time). Equation 1.2 shows that there are three terms which determine the expansion of the universe: a matter term, a cosmological constant term and a curvature term. The relative contribution of the matter term Ω_M at the present epoch is given by :

$$\Omega_M = \frac{\rho_M}{\rho_c}, \tag{1.5}$$

where ρ_c is the critical density of the universe at redshift z defined as:

$$\rho_c = \frac{3\,H(z)^2}{8\,\pi^2\,G}, \tag{1.6}$$

A value of $\Omega_M < 1$ ($k = -1$) corresponds to an open universe that will expand for ever because there is not enough mass to halt the expansion, and $\Omega_M > 1$ ($k = +1$) to a closed universe that will collapse back into itself. The vacuum energy density parameter is related to the cosmological constant by:

$$\Omega_\Lambda = \frac{\Lambda}{3\,H_0^2}. \tag{1.7}$$

The contribution of the curvature of space term Ω_k can be found from the relation:

$$\Omega_M + \Omega_\Lambda + \Omega_k = 1. \tag{1.8}$$

These parameters completely determine the geometry of the universe if it is homogenous, isotropic and matter-dominated. For a complete description of Lambda-based cosmology see the review by Carroll et al. (1992) and references therein.

The expansion of the universe is measured via the cosmological redshift z; this redshift is caused by photons, which have been emitted in distant galaxies, having their wavelength stretched by the expansion of the universe from their emitted wavelength λ_{em} to a longer observed wavelength λ_{obs} and is defined by the equation:

$$z = \frac{\lambda_{obs} - \lambda_{em}}{\lambda_{em}}. \tag{1.9}$$

The measured cosmological redshift is directly related to the scale factor via:

$$1 + z = \frac{R\,(t_{obs})}{R\,(t_{em})}, \tag{1.10}$$

where $R\,(t_{obs})$ denotes the expansion factor at the present day.

In cosmology, distances are governed by the curved space-time of the Robertson Walker metric and are therefore dependent upon how one wants to measure “distance”. The key equations that will be used in this thesis for a flat (k=0) universe are outlined in the following

paragraph.

The comoving distance d_M is the distance between two objects which remains constant if they are moving with the Hubble flow, which can be interpreted as the distance between them which would be measured by rulers at the time they are observed, divided by the ratio of the scale factors between the times of emission and observation (i.e the $(1 + z)$ factor given in equation 1.2 (Hogg 1999)). For a flat universe d_M is given by:

$$d_M = \frac{c}{H_0} \int_0^z \frac{dz'}{\sqrt{(1+z')^2\,(1+\ \Omega_M\, z') - z'\,(2+z')\,\Omega_M}}, \tag{1.11}$$

where Ω_M and Ω_Λ are the density parameters defined by equation 1.6 above.

Another commonly used cosmological distance is the *luminosity distance* d_L, defined by the inverse square relationship between the bolometric flux S of an object and its bolometric luminosity L:

$$d_L = \sqrt{\frac{L}{4\,\pi\,S}}. \tag{1.12}$$

The luminosity distance, d_L is related to the comoving distance d_M by the relation:

$$d_L = (1+z)\,d_M, \tag{1.13}$$

and is used throughout this thesis to calculate luminosities and absolute magnitudes.

The angular diameter d_A is also frequently used in cosmology to calculate areas of space from solid angle Ω. It is defined as the ratio of an object's physical transverse size to its projected angular size on the sky. The angular diameter distance d_A is easily calculated from:

$$d_A = \frac{d_M}{1+z}. \tag{1.14}$$

1.2 The key parameters of the universe

Cosmology has entered a precision era since the release of microwave anisotropy data from the Wilkinson Microwave Anisotropy Probe (WMAP, Bennett et al. 2003). Many of the key cosmological parameters have been measured at the ten percent level or better. The formation and

evolution of structure in the Universe are governed by these parameters, and they are therefore of critical importance.

Galaxy and quasar clustering studies, the form of the CMB power spectrum and measurements of the Sunyaev-Zel'dovich (SZ) effect and X-rays gas properties in galaxy clusters provide very good tools for constraining the cosmological world model.

1.2.1 The Hubble constant

Modern cosmology probably began with the discovery that all distant galaxies have a component of velocity which is directed away from the Earth as revealed by the redshift seen in their spectra (Slipher 1917). Using galactic apparent magnitudes and Cepheid variable stars in nearby galaxies as 'standard candles', Edwin Hubble (1929) was able to estimate their distances and discovered that the universe is expanding in such a way that the recessional velocity of a galaxy v is proportional to its distance d from the earth:

$$\mathrm{v} = H_0\, d. \tag{1.15}$$

This equation applies to galaxies with redshift up to about $z = 0.2$; at larger distances equation (1.15) must be modified to take into account relativistic effects but it remains one of the most important discoveries in cosmology because it is directly related to the other cosmological parameters.

There has been much work since 1929 to test equation (1.15) and to determine H_0 : the velocity of a galaxy is measured from the redshift z of its spectrum, where $\mathrm{v} = c\,z$ for small v. The distance is measured from the inverse square law from galaxies'apparent magnitudes, and one must know the absolute magnitude of a galaxy in order to determine d. Herein lies the difficulty in measuring the Hubble constant, as galaxies have a considerable spread in absolute magnitude (intrinsic luminosity). Different approaches based on the global properties of a galaxies have been used to determine their luminosity and thus distance, leading to large errors in the value of H_0.

A different method has been developed to measuring d, using either Cepheid variable stars or Supernovae Type Ia. Leavitt & Pickering (1912) have shown that Cepheids follow a well-

Table 1.1: The Hubble constant in units of km s^{-1} Mpc^{-1}. Random (r) and systematic (s) errors are given at 1 σ confidence level. *) taking into account more recent calibrations of the LMC distance, this value increases to 74 (c.f Gibson and Brook 2001)

Method	H_0	Error (%)	References
Type Ia Supernovae	73	$\pm 2(r) \pm 7(s)$	Gibson & Brook (2001)
Combined HST methods	71	$\pm 2(r) \pm 6(s)$	Freedman et al. (2001)
Tully-Fisher clusters	71	$\pm 3(r) \pm 7(s)$	Sakai et al. (2000)
FP clusters	82	$\pm 6(r) \pm 9(s)$	Kelson et al. (2000)
SBF clusters	70	$\pm 5(r) \pm 6(s)$	Ferrarese et al. (2000)
Type II Supernovae	72	$\pm 9(r) \pm 7(s)$	Schmidt et al. (1994)
Cepheids, Metallicity-corrected	68*	$\pm 5(r\&s)$	Nevalainen & Roos (1998)
S-Z effect	66	$\pm 13(r) \pm 15(s)$	Mason et al. (2002)

defined relation between their luminosities and periods. Given the period of a Cepheid variable observed in a galaxy one can deduce its absolute magnitude and hence find its distance. Observations of Cepheids in the Virgo and Leo I clusters have yielded estimates for H_0 of 80 ± 17 km s^{-1} Mpc^{-1} (Freedman et al. 1994), 87 ± 7 km s^{-1} Mpc^{-1} (Pierce et al. 1994) and 69 ± 8 km s^{-1} Mpc^{-1} (Tanvir et al. 1995).

SN Ia have emerged as extremely powerful "standard candles" in a cosmological context because their luminosity, normalised by the shape of their light curve, does not vary between objects (see review by Leibundgut (2001)). Values of the Hubble constant from these studies have generally been lower than those measured by the Cepheid observers, for example, 57 ± 4 km s^{-1} Mpc^{-1} (Sandage et al. 1996), 63 ± 3 km s^{-1} Mpc^{-1} (Hamuy et al. 1996), 65 ± 6 km s^{-1} Mpc^{-1} (Riess et al. 1996), < 78 km s^{-1} Mpc^{-1} (Kim et al. 1997).

Until the late 1990's the exact value of the Hubble parameter was still uncertain although most agreed that the value was in the range $50 - 100$ km s^{-1} Mpc^{-1}. One of the most reliable results on the Hubble constant comes from the Hubble space telescope key project (Freedman et al. 2001). The group has estimated $H_\circ = 72 \pm 3$ km s^{-1} Mpc^{-1}, obtained by the combination of four methods (Type Ia Supernovae, Tully-Fisher, surface brightness fluctuations and Type II Supernovae). These results are in agreement with results derived from the WMAP CMB and large scale structure measurements. The Hubble constant as measured by different methods is summarised in Table 1.1.

1.2.2 Baryonic density, Ω_b

The tightest constraints on the value of the universal baryonic density parameter Ω_b come from standard Big Bang Nucleosynthesis (BBN) arguments and from the observed abundances of He, D, H and Li (cf. Sarkar (1999)), in particular from the low deuterium measured by Burles et al. (2001). Their estimate is:

$$\Omega_b h^2 = 0.020 \pm 0.001 \ \ (68\% CL) \tag{1.16}$$

where $h = H_o/100$. Note that BBN provides a probe of the universal abundance of baryons when the universe was only a few minutes old. The CMB anisotropy observations probe the baryon abundance when the universe was three to four hundred thousand years old, and SNe Ia supernovae and clusters of galaxies observations probe a more recent past, when the universe was several billion years old.

Recently, Dunkley et al. (2008) used the WMAP 5-year data alone to measure the six cosmological parameters i.e. the density of dark matter, the density of atoms, the expansion rate of the universe, the amplitude of density fluctuations, and their scale dependence, as well as the optical depth due to reionisation. Their quoted value for the baryonic density parameter is :

$$\Omega_b h^2 = 0.02273 \pm 0.00062 \ (68\% CL) \tag{1.17}$$

The five year WMAP measured parameters for ΛCDM are in good agreement with the three year WMAP results (Spergel et al. 2007, 2003), and the uncertainties are all reduced, significantly so for certain parameters. Table 1.2 shows the five year marginalised distribution for ΛDCM compared with the three years results.

1.2.3 Age of the universe

The ages of the constituents of the universe provide a lower limit to its age. Until recently, astronomers estimated that the big bang occurred between 12 and 14 billion years ago. Globular clusters can be used to constrain the age of the universe. By comparing the turnoff point of globular clusters from the main sequence with predictions from models of stellar evolution an

Table 1.2: ΛCDM model parameters and 68% confidence intervals from the five-year WMAP data alone. The three-year values are shown for comparison. For best estimates of parameters, the marginalised 'Mean' values should be used. The 'Max Like' values correspond to the single model giving the highest likelihood. This table is adapted from Table 2 of Dunkley et al. (2008).

Parameter	3 Year Mean	5 Year Mean	5 Year Max Like
$100\Omega_b h^{2}$ [a]	2.229 ± 0.073	2.273 ± 0.062	2.27
$\Omega_c h^{2}$ [b]	0.1054 ± 0.0078	0.1099 ± 0.0062	0.108
Ω_Λ [c]	0.759 ± 0.034	0.742 ± 0.030	0.751
n_s [d]	0.958 ± 0.016	$0.963^{+0.014}_{-0.015}$	0.961
τ [e]	0.089 ± 0.030	0.087 ± 0.017	0.089
$\Delta^2_{\mathcal{R}}$ [f]	$(2.35 \pm 0.13) \times 10^{-9}$	$(2.41 \pm 0.11) \times 10^{-9}$	2.41×10^{-9}
σ_8 [g]	0.761 ± 0.049	0.796 ± 0.036	0.787
Ω_m [i]	0.241 ± 0.034	0.258 ± 0.030	0.249
$\Omega_m h^{2}$ [l]	0.128 ± 0.008	0.1326 ± 0.0063	0.131
H_0 [o]	$73.2^{+3.1}_{-3.2}$	$71.9^{+2.6}_{-2.7}$	72.4
$z_{\rm reion}$ [x]	11.0 ± 2.6	11.0 ± 1.4	11.2
t_0 [s]	13.73 ± 0.16	13.69 ± 0.13	13.7

[a] Baryon density, $\Omega_b h^2$

[b] Cold dark matter density, $\Omega_c h^2$

[c] Dark energy density, with $w = -1$ unless stated

[d] Scalar spectral index at $k_0 = 0.002$/Mpc

[e] Reionization optical depth

[f] Amplitude of curvature perturbations at $k_0 = 0.002$/Mpc

[g] Linear theory amplitude of matter fluctuations on 8 h^{-1} Mpc scales

[i] Matter energy density $\Omega_b + \Omega_c + \Omega_\nu$

[l] Matter energy density

[o] Hubble expansion factor ($100h$ Mpc^{-1}km s^{-1})

[x] Redshift of instantaneous reionization

[s] Age of the universe (billions of years)

estimate of the globular cluster age, t_{GC}, can be made. Chaboyer et al. (1996) find that the age of the universe is greater than 12.07 Gyr with 95% confidence. They showed that the age is inversely proportional to the luminosity of the RR Lyrae stars which are used to determine the distance to globular clusters. Chaboyer (1996) gave a best estimate of 14.6 ± 1.7 Gyr for the age of the globular clusters. The Hipparcos astronomical satellite made improved parallax measurements and showed that the globular clusters are further away than previously thought. These new measurements have provided a revised age of $t_{GC} \sim 11 - 14$ Gyr (Chaboyer et al. 1998; Reid 1998).

By searching for faint white dwarfs, one can estimate the length of time the older white dwarfs have been cooling. Oswalt et al. (1996) have done this and find an estimated age of the disk of the Milky Way of $\sim 9.5^{+1.1}_{-0.8}$ Gyr. They estimate an age of the universe which is at least 2 Gyr older than the disk. Hansen et al. (2007) find an age of 11.47 ± 0.47 Gyr at 95% confidence using a detailed Monte-Carlo simulation of the white dwarf population in the metal-poor globular cluster NGC 6397.

Other studies of nearby halo stars yielded stellar ages consistent with both the globular cluster ages and the one estimated from the first year WMAP data (see Table1.3, Spergel et al. 2003). For example, studies of old halo stars gave an estimated age of 15.6 ± 4.6 (Cowan et al. 1999). Schatz et al. (2002) found an estimated age of 15.5 ± 3.2 Gyr similar to the previous one. The age of the universe based on the best fit to five year WMAP ΛCDM data only, is estimated to be $t_0 = 13.69$ (see Table 1.2, Dunkley et al. 2008). The WMAP result agrees well with estimates of ages based on globular clusters (Chaboyer & Krauss 2002) and white dwarfs (Hansen et al. 2004; Richer et al. 2004). In combination with other data like 2dFGRS and Lyα, WMAP gives an age of $t_0 = 13.4 \pm 0.3$ Gyr. The lower limits on the age of the universe from various astronomical measurements are summarised in Table 1.3.

Extrapolating back to the Big Bang

An alternative approach to estimating the age of the universe is to measure the "Hubble constant" and extrapolate back to the big bang. This extrapolation depends on the history of the expansion rate. For a flat universe composed mostly of matter, the age is $\sim 2/3H_0$. If the universe has very low density of matter, then its extrapolated age is larger ($\sim 1/H_0$).

Table 1.3: Cosmic age. This table is adapted from Spergel et al. (2003)

Method	Age
WMAP data (ΛCDM).....	13.4 ± 0.3
WMAPext + LSS.....	13.7 ± 0.2
Globular Cluster Ages.....	> 11 – 16 Gyr
White Dwarf.....	> 12.7 ± 0.7 Gyr
OGLEGC-17.....	> 10.4 – 12.8 Gyr
Radioactive dating.....	> 9.5 – 20 Gyr

1.2.4 Dark matter and dark energy

Type Ia supernovae and CMB anisotropies constitute one of the most reliable techniques for measuring Ω_M and Ω_Λ on truly cosmological scales. The key approach to determining the cosmological parameters from the supernovae observations is in the relation between the apparent magnitude, the absolute magnitude, and the luminosity distance (Riess et al. 1998, Perlmutter et al. 1999).

High-z Supernovae Search Team (HSST) and Supernovae Cosmology Project (SCP) have found Supernovae at different redshifts. HSST (Riess et al., 1998) has discovered 16 SNe Ia in a redshift range 0.16-0.62 and 34 nearby Supernovae to constrain H_0, Ω_m, Ω_Λ, the deceleration parameter q and the dynamical age of the universe ($t_\circ$), whereas the Supernovae Cosmology Project (Perlmutter et al. 1999) has discovered 42 supernovae in the redshift range 0.18-0.83 which were dimmer than would be expected in a critical density universe, implying either an open universe or $\Lambda > 0$. For a flat ($\Omega_M + \Omega_\Lambda = 1$) universe they found $\Omega_M = 0.28$ which corresponds to an age of the universe of $t_\circ = 14.9$ Gyr. This is consistent with current estimates derived from the ages of globular clusters. Riess et al. (2000), have also found consistent results ($\Omega_\Lambda = 0.7$, $\Omega_M = 0.3$). However, some uncertainties remain due to the possible evolution of type Ia SNe and any dimming by dust. Recently, Astier et al. (2006) have presented distance measurement to 71 high redshift type Ia Supernovae discovered during the first year of the 5-year Supernova Legacy Survey (SNLS). They have built a Hubble diagram extending to $z = 1$. For a flat ΛCDM model they found $\Omega_{\rm M} = 0.263 \pm 0.042(stat) \pm 0.032(sys)$, where *stat* stands for statistic errors and sys for systematic errors; and $\omega = -1.023 \pm 0.090(stat) \pm 0.054(sys)$ for a flat cosmology with constant equation of state w when combined with the constraint from the

recent Sloan Digital Sky Survey measurement of baryon acoustic oscillations.

Observationally, galaxy clusters are thought to be powerful independent cosmological probes, which complement the CMB and supernovae surveys. They provide a very good tool for measuring Ω_M, Ω_Λ and the power spectrum amplitude σ_8 (Bahlcall 1998; Viana 2004; Andemach et al., 2004) using the evolution of cluster number density with redshift.

1.3 Radio source population

By comparison with optical astronomy, radio astronomy can trace its history back over hundred years. After Maxwell had formulated his equations of electromagnetism based on the work of Faraday and others, experimentation in the transmission and reception of electromagnetic waves began. Since the first detection of radio emission from astronomical sources, it has proved to be a useful tool for understanding the properties of structures within our own galaxy and the nature of external galaxies. Extragalactic radio sources fall into two main categories, those whose radio emission is fuelled by processes related to star formation (star-forming galaxies) and those whose radio emission is fuelled by an active nucleus powered by a super massive black hole (Active Galactic Nuclei or AGNs). The radio properties of both these classes are discussed in this section.

1.3.1 A brief history of radio astronomy

The first detection of radio emission from space was made by Karl Jansky in the early 1930s (his name has been given to the unit of radio flux density, 1 Jansky = 10^{-26} W Hz^{-1} m^{-2}). Karl Jansky was working on the identification of sources on interference at radio wavelengths for Bell Telephone Laboratories in 1931 (at 15-30 MHz frequencies). Jansky was using a rotating wire frame antennae that allowed him to follow the source of any static, and he detected three separate groups of static: local thunderstorms, distant thunderstorms and a steady hiss-type static of unknown origin. Jansky pinpointed this third type of noise as coming from the constellation of Sagittarius. He had made the first detection of the centre of the Milky-Way at radio wavelengths. Jansky wrote three papers on his findings, but his work was largely ignored by the astronomical community. The field of radio astronomy was continued by another American

radio engineer, Grote Reber. He had heard of Jansky's discovery, and in 1937 built a 9.5 m parabolic radio dish in his own backyard. This was the first radio telescope used exclusively for astronomical research and is the prototype for modern reflecting radio telescopes. Reber, operated his dish for many years looking for astronomical sources of radio waves at several wavelengths. In 1944, he was able to publish the first radio frequency map of the sky.

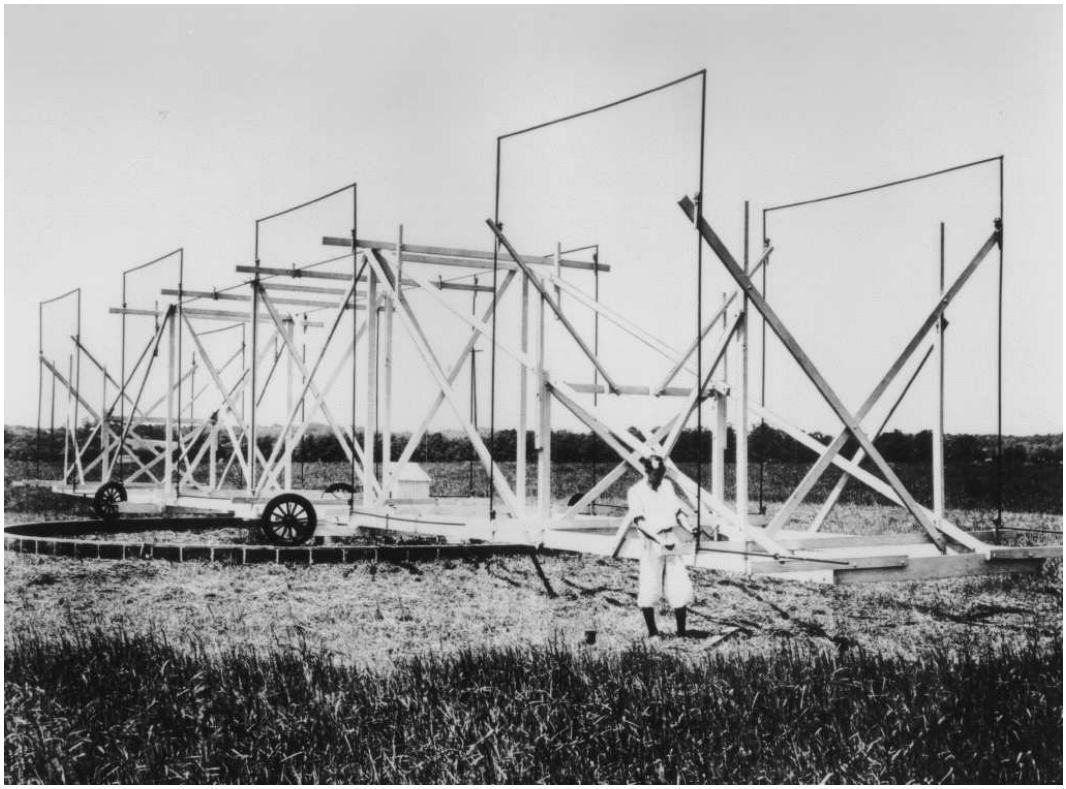

Figure 1.2: Karl Jansky and his rotating wire frame Antenna

The second World War had accelerated the development of radio with the need for better communications and accurate early warning radar. Most of the effort in science and technology were put into military development. Once the war was over, some of these technologies were inherited by science. The first discoveries were performed by engineers that had (mostly) turned into astronomers after World War II. The antenna technology improved enough to further understand the nature of extra-terrestrial radio emission. In 1946, J.S. Hey along with S.J. Parsons and J.W.Philips observed fluctuations in the intensity of cosmic radio waves from the constellation Cygnus. In 1949 Bolton, Stanley and Slee, working at Australia's CSIRO Radiophysics Laboratory identified the radio sources Centaurus A and Virgo A with the nearby

optical galaxies NGC 5128 and NGC 4486 (M87) (Bolton et al. 1949). This was the first optical identification of extragalactic radio sources and the subsequent identifications of other radio sources with distant galaxies established a new class of object known as “radio galaxies”. In the next ten years thousands of discrete radio sources were identified, including galaxies and Supernovae.

The earliest radio source surveys began soon after. During 1951 and 1952 Graham Smith at the Cavendish Laboratory, Cambridge University and Bernard Mills at Sydney University, in collaboration with Walter Baade and Rudolf Minkowski at Mt Wilson Observatory, attempted to improve the accuracy of the positions of radio sources to allow identification with faint optical objects. Their observations pushed radio astronomy to higher resolution to increase the positional accuracy with the aim of identifying the optical counterparts of bright radio sources. By the 1960s the accuracy achieved in radio source positions was such that radio sources were being identified with objects on optical plates that did not appear like galaxies at all but looked more like galactic stars. The optical spectra of these stellar objects had broad emission lines which were not identifiable with any atomic transitions seen before in galaxy or stellar spectra. In 1963 Maarten Schmidt realised while working on the spectrum of 3C 273, that its emission lines could be identified with the Balmer series of hydrogen at redshift of 0.16, larger than any previously obtained. Subsequently, spectra of other “stellar” radio sources were investigated and all were identified with moderately large redshift. These objects were known as “quasi-stellar radio sources” or quasars.

In the 1960s and 1970s a wealth of new types of radio source was discovered, both galactic and extragalactic. Radio telescopes were being built capable of much higher resolution and sensitivity. In the 1970s aperture synthesis interferometry had advanced far enough that a new telescope was built near Socorro, New Mexico called the Very Large Array (VLA). This telescope is composed of 27 movable antennas, each 25m in diameter, whose signals were combined by a state-of-the art correlator. These telescope dishes are configured in a “Y” shape over 40 km in diameter on over 136 km of railroad track such that the telescope can be steered into different configurations to allow a trade-off between sensitivity and resolution.

Here, discussion turns to the physical properties of two classes of extragalactic radio sources.

1.3.2 Active galactic nuclei

Active galaxies come in a variety of types including Seyfert galaxies, quasars, radio galaxies and blazars. These types were discovered separately and at first seemed quite different but they all have some form of spectral peculiarity. There is also evidence in each case that a very large amount of energy is being released in a region that is tiny compared with the size of the galaxy and so they are classified together. It is usually found that the tiny source region can be traced to the nucleus of the galaxy, so the origin of the excess radiation is attributed to the active galactic nucleus or AGN. An active galaxy may be regarded as a normal galaxy plus an AGN with its attendant effects. The engine that powers the AGN, the tiny nucleus of the active galaxy is a great mystery. It has to produce 10^{11} or more times the power of our own Sun, but it has to do this in a region little larger than the solar system. It has been proposed that the engine consists of an accreting super-massive black hole, around which gravitational energy is converted into electromagnetic radiation. AGNs emit strongly over the whole electromagnetic spectrum including the radio, X-ray, and γ-ray bands where most galaxies hardly radiate at all. They are broadly grouped into two distinct categories, 'radio-loud' and 'radio-quiet' based on their radio luminosity and spectral characteristics (Types 0, 1, 2). The division in radio-loud or radio-quiet corresponds to objects bright or faint in radio compared to their own optical emission (Kellermann et al. 1989). The radio emission mechanism from extragalactic sources is synchrotron emission from relativistic electrons spiralling around the magnetic fields within the host galaxy. The host galaxies of radio-loud and radio-quiet AGNs are essentially indistinguishable. Typical spectral energy distributions of radio loud and radio quiet AGNs are compared in Figure 1.3.

Type 1 AGN are those with bright continuum and broad emission lines while Type 2 AGN have weak continuum and only narrow emission lines. The most active and variable AGNs are sometimes classified as type 0 but usually referred to by their names (BLLacs, core dominated, etc). Differences in spectral properties are explained by a unification scheme in which the observed properties of an AGN are due to its orientation relative to the observer's line of sight

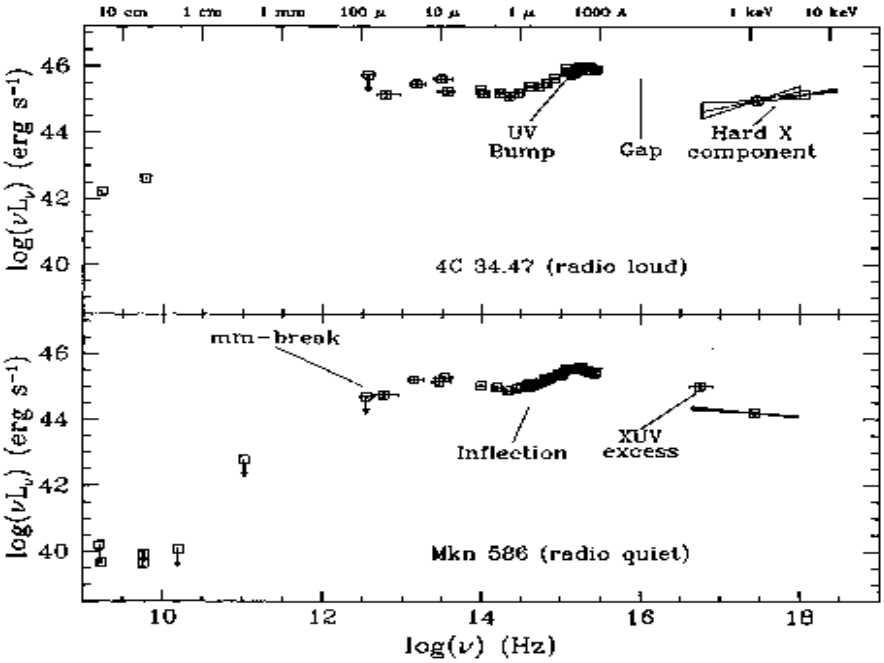

Figure 1.3: The upper figure shows the spectral energy distribution of a radio-loud quasar (4C34.47) and the lower figure shows the spectral energy distribution of a radio-quiet quasar (Mrk 586) with characteristics labelled. This figure was obtained from Elvis et al. (1994)

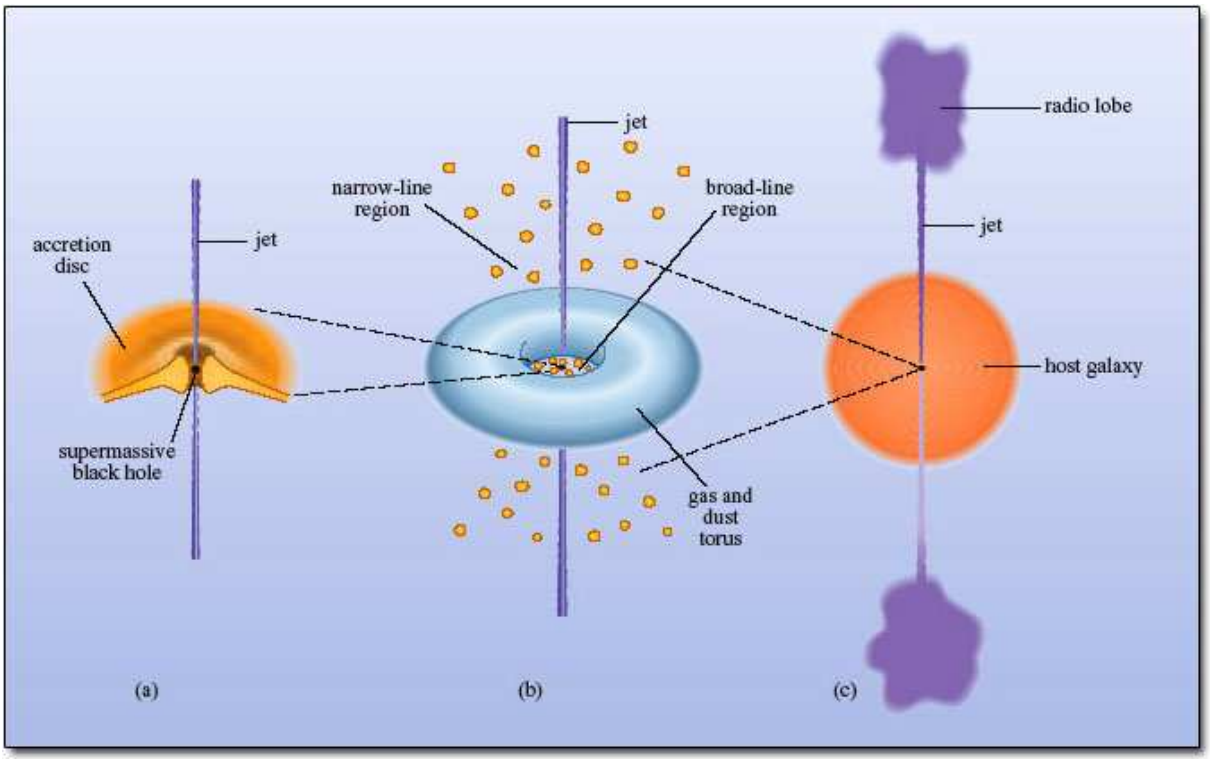

Figure 1.4: An illustration of AGN unification schemes. A luminous accretion disk is surrounding the central black hole. Broad emission lines are produced in clouds orbiting above the disk itself and narrow lines are produced in clouds much farther from the central source.

(Antonucci 1993). Such a scheme is shown in Figure 1.4. In this scheme matter is accreting onto a super-massive black hole from an accretion disc surrounded by a cloud of gas and dust in the shape of a torus and energy is transported via jets into the intergalactic medium. The broad line-region lies within 1pc of the central engine and the narrow line region lies further out, about 1kpc from the nucleus. For a thorough review of unification schemes see Antonucci (1993).

Radio-loud AGN are divided into two main classes according to their radio morphology (Fanaroff & Riley 1974). Examples of these two classes are shown in Figure 1.5:

- *Fanaroff-Riley type-I* (FRI): the lobes are brightened near the galaxy and grow dimmer as one looks farther away; the jet can be seen on both sides of the central galaxy and often exhibits a turbulent structure;

- *Fanaroff-Riley type- II* (FRII): the lobes are edge-brightened and have very bright, very

small hot spots near the outer surface of the lobes. The jet is usually very narrow and well aligned with the outer structure but its emission is relatively weak compared to the lobes and is virtually only on one side.

Interestingly FRI and FRII show a division in 1.4 GHz radio power: at low luminosity, $P_{1.4} < 10^{25}$ W Hz^{-1} sr^{-1}, the vast majority of radio sources have an FRI radio structure, while at high luminosity, $P_{1.4} \gtrsim 10^{25}$ W Hz^{-1} sr^{-1} the majority of radio galaxies have FRII radio structure (Ledlow & Owen 1995). These two types of radio-loud AGNs are often described by AGN unification models.

There are other classes of radio-loud objects in which, especially at higher frequencies i.e. several GHz, the region responsible for the bulk of the radio emission is unresolved even on arcsecond angular scales and the radio emission is essentially core-dominated. The populations of radio-loud quasars and BL Lac objects belong to this class of compact objects : radio loud quasars are assumed to be the same objects as FRII radio galaxies. BL Lac objects, which exhibit strong, rapid variability and featureless spectra, are FRI radio galaxies in which the jet is Doppler boosted along our line of sight (Urry & Padovani 1995).

Radio-loud AGNs are potential tracers of large-scale structure. Most radio sources at low redshift are found in groups of clusters of galaxies (Hill & Lilly 1991) and there is some evidence that distant radio-loud AGNs are associated with the densest environments (Brand et al. 2003). Analysis of samples of radio-loud AGNs at low redshift (Peacock & Nicholson 1991; Magliocchetti et al. 2004; Brand et al. 2005) has shown that these sources have clustering amplitudes in excess of the clustering amplitude of normal galaxies. This implies that radio-loud AGNs are biased tracers of the galaxy distribution, which means that they are preferentially located in regions of high galaxy density. Radio source catalogues contain almost exclusively AGNs above $z \sim 0.1$ and sample the universe to medium redshift $z \approx 0.8$ and are therefore powerful tools for investigating the clustering properties of galaxies at cosmological redshifts.

1.3.3 A ‘non-active’ class - the starburst galaxies

One of the major discoveries of IRAS was a class of galaxies undergoing massive bursts of star formation (see the review by Sanders & Mirabel 1996). The main energy output of these

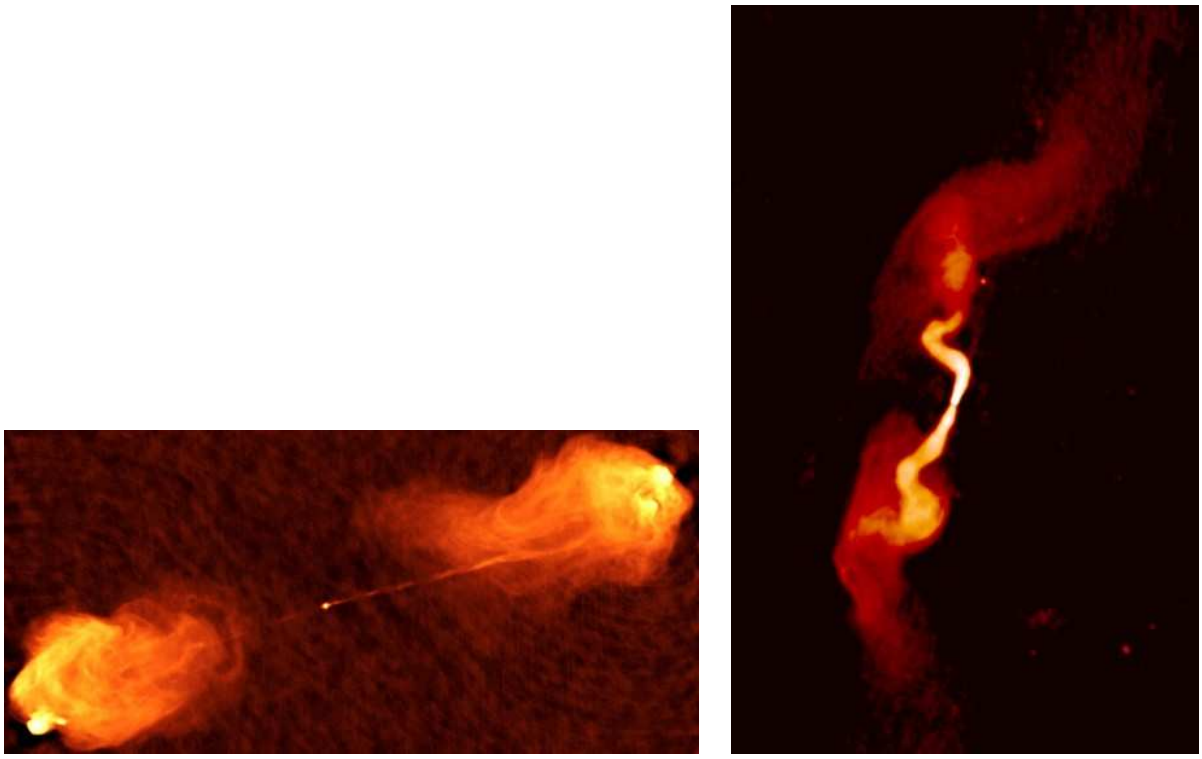

Figure 1.5: Left image: A radio image at 1" resolution of the FRII type radio galaxy Cygnus A. Two bright hot-spots are clearly visible at the extremities of the long thin jets that originate from the core of the host galaxy. Right Image: A radio image of the FRI type radio galaxy 3C31. This galaxy is distinct from the FRII type galaxy with well collimated jets emerging from a bright nucleus becoming increasingly turbulent further away. Both images were made with the Very Large Array and were obtained from http://www.nrao.edu/imagegallery, courtesy of NRAO/AUI.

galaxies is in the infrared (IR, $\lambda \sim 1 - 1000\,\mu$m) as the ultraviolet (UV) light from young stars is absorbed and re-radiated by dust. Morphologically speaking, they are typically irregular or spiral galaxies. Possible mechanisms for the gas inflow that results in star formation are the interactions or mergers between gas-rich galaxies (e.g. Hernquist 1989) or bars in spiral galaxies (Ho et al. 1997).

There is no exact quantitative definition of what constitutes a "starburst" galaxy. Broadly speaking, any galaxy that shows a Star Formation Rate (SFR) significantly higher than a normal galaxy can be classified as a starburst galaxy. The archetypal starburst is the local galaxy M82.

1.4 The star formation history

Answering the question of how galaxies have evolved since their formation in the early universe to the present epoch is one of the prime goals of modern cosmology. Some of the most important clues of the nature of this evolution come from observations of the variations with time of the global star formation rate in galaxies, the cosmic star formation history (SFH), which underlies galaxy evolution; the production of the elements; structure formation and the energy budget of the universe. An important development in observational cosmology has been the realisation that the SFH can be derived by a number of methods, helping to constrain galaxy evolution scenarios.

1.4.1 Spectral synthesis models of galaxies

Modelling the evolution of a galaxy spectrum as a function of stellar population and redshift, and comparing the models to the observed broadband colours of galaxies, enables important conclusions to be drawn about their ages and star formation history. The spectral evolution models most widely used are those of Bruzual & Charlot (2003), Bruzual & Charlot (1993), Leitherer et al. (1999), Guiderdoni & Rocca-Volmerange (1987), Arimoto & Yoshii (1987) and Worthey (1994). These use a grid of stellar evolution tracks to derive the effective temperatures and bolometric luminosities for various stellar masses as a function of time, which are converted to synthetic spectra using stellar atmosphere models. The individual templates are then summed together, weighted by an initial mass function to give luminosities, spectra and colours

of a single-age stellar population as a function of galaxy age. These can be added together to synthesise the predicted spectrum or colours of a galaxy with a selected star formation history. This allows the SFR to be estimated based on the integrated colour of the population. However, the degeneracy between metallicity, age, the initial mass function, and the reddening due to dust extinction, limits the accuracy of SFR estimation.

1.4.2 Ultraviolet and optical

Perhaps the most direct method of estimating SFRs is to make use of observations in the rest-frame near-UV (Lilly et al. 1996; Madau et al. 1996; Connolly et al. 1997; Madau et al. 1998; Treyer et al. 1998; Cowie et al. 1999). This part of the spectrum in those galaxies that do not contain active nuclei is dominated by emission from short-lived, massive stars, so the SFR scales linearly with luminosity. The optimal wavelength range is 1250-2500 A°, longer than the Lyα forest, but short enough so that the spectral contamination from older stellar populations is minimised.

Another method of estimating the SFR is to use rest-frame optical observations of nebular emission lines (Hogg et al. 1998; Tresse & Maddox 1998; Glazebrook et al. 1999; Hopkins et al. 2000; Teplitz et al. 2000; Pettini et al. 2001). The strength of the $H\alpha$ line is most commonly used, but other lines have been used as well.

The main limitation of both methods is the uncertainty in the extinction due to dust.

1.4.3 Infrared and submillimetre

A significant fraction of the bolometric luminosity of a galaxy is absorbed by interstellar dust and re-emitted in the thermal IR region. As the observed absorption cross-section of interstellar dust is strongly peaked in the UV region, where the emission from young stars dominates, it can be a sensitive tracer of the young stellar population and hence the SFR (Rowan-Robinson et al. 1997; Blain et al. 1999; Flores et al. 1999; Barger et al. 2000; Mann et al. 2002; Rowan-Robinson 2003).

1.4.4 Radio and X-ray

In large radio surveys it is important to disentangle the star-forming galaxy population from the AGN population because they arise from completely different physical processes. Unlike far infra-red (FIR) emission, which is a straightforward indicator of SFR, radio emission is a highly indirect indicator, relying on the complex and little understood physics of cosmic-ray generation and confinement (see the review by Condon 1992). A useful diagnostic for distinguishing between star-forming galaxies and AGNs has been the extremely tight FIR-radio correlation, whereby galaxies with a radio "excess" above that expected from the correlation are classed as AGNs and the remainder as star-forming. Compared to FIR and submillimeter studies, radio observations typically have better positional accuracy, allowing for more reliable identification with objects detected at other wavelengths. In recent years, radio samples constructed from large optical redshift surveys (Sadler et al. 2002; Magliocchetti et al. 2004; Best et al. 2005) have had the advantage of having optical spectra available for each source classification based on spectral line ratio. This provides an extremely robust method for distinguishing between star-forming galaxies and AGNs.

Star-forming galaxies are also found to be luminous in X-rays. This is due to a number of high mass X-ray binaries, young supernovae remnants and hot plasmas associated with star-forming regions (see the review by Fabbiano 1989). With the latest generation of X-ray satellites, such as Chandra and XMM, it is now becoming possible to study the X-ray-SFR correlation (Bauer et al. 2002a; Grimm et al. 2003; Ranalli et al. 2003). Early results show good agreement with FIR and radio estimates of the SFR.

1.5 Radio Surveys

The early history of radio surveys includes the 3C (Edge et al. 1959), 4C (Gower et al. 1967), 6C (Baldwin et al. 1985) and 7C (Visser et al. 1995) surveys all of which covered much of the northern sky at frequencies below 200 MHz. The lowest frequency Cambridge Survey, the 8C (Rees 1990) covered only the northern polar cap ($\delta > 70°$) at 38 MHz. In the south the Molongolo radio telescope operating at a frequency of 408 MHz surveyed the entire southern sky ($-85° < \delta < 19°$) to a limiting flux density of 700 mJy to produce the Molongolo reference

catalogue of radio sources (MRC; Large et al. 1981).

The next major advance in sensitivity for large area radio surveys came when the Green Bank telescope was used to produce the GB87 survey of the entire northern sky at 4.85 GHz (Condon 1989). The southern equivalent came soon after and was called the Parkes-MIT-NRAO survey (PMN; Griffith & Wright 1993) which was done with the Parkes radio telescope at a frequency of 4.85 GHz. These surveys remain the deepest and most uniform high frequency radio surveys ever completed. The limiting factor of all these early surveys was that they lacked the angular resolution required to make unambiguous optical identifications of most sources for further study. Obtaining large samples of radio sources with optical identifications was a lengthy process requiring repeat observations of individual sources at better angular resolution with interferometric telescopes.

It has only been in recent years that some of the most sensitive radio telescopes in the world, the VLA, the Westerbork Synthesis Radio Telescope (WSRT) and the Molongolo Observatory Synthesis Telescope (MOST) have been used to cover much of the northern and southern sky with milliJansky sensitivity and sufficient angular resolution to allow unambiguous identifications of large numbers of radio sources with objects from optical catalogues. The VLA has produced two surveys: the high resolution Faint Images of the Radio Sky at twenty-one centimetres (FIRST; Becker et al. 1995), and the lower resolution NRAO VLA Sky Survey (NVSS; Condon et al. 1998) both at 1.4 GHz (Rengelink 1998).

This thesis makes much use of the FIRST survey which covers ~ 9000 deg^2. At the same time as the NVSS and FIRST surveys the WRST was used to produce a complementary survey covering the northern sky at 325 MHz.

1.6 Radio Galaxies as probes of evolution

Only with the advent of the Hubble Space Telescope (HST) has it been possible to begin to study ordinary galaxies at redshifts $z \geq 1$. Before this, the only objects known in any large number at these redshifts were the radio galaxies (RGs) and quasars. The optical light of quasars is

dominated by the active nucleus and they were of little use for studying their host galaxies at high redshift. The radio galaxies, however, have a much smaller contribution to their optical-infrared light from the active nucleus than do quasars and it is the stellar populations of the galaxies which we can observe directly. In addition radio galaxy samples have well defined and understood selection criteria based on their radio emission and they often have strong emission lines making the determination of their redshift far easier than for normal galaxies at comparable distances. At low redshift ($z \leq 1$) the host galaxies of powerful radio sources are uniquely identified with massive elliptical galaxies. Although the mechanism that triggers the powerful radio emission in some galaxies rather than others is not fully understood, it is reasonable to suppose that the same mechanism would occur throughout the universe and that radio galaxies at high redshift are also associated with giant elliptical galaxies. For these reasons, radio galaxies have played a crucial role in our understanding of galaxy evolution, being the only massive galaxies visible at large look-back times. For an extensive review of the properties of high redshift radio galaxies see McCarthy (1993).

One of the motivations behind using radio galaxies as cosmological probes is the relative ease with which their redshift can be measured from emission lines. One of the earliest and most widely used tests to measure the curvature of the universe is the redshift-magnitude, or Hubble diagram. The idea underlying this is to find some "standard candle", for example the brightest galaxy in a cluster, that is assumed to have a constant absolute magnitude and to plot its apparent magnitude against redshift. Over large distances, such a diagram is sensitive to spatial curvature, and it was thought that this would be the most direct method for measuring Ω_0 (see Sandage 1988 for a review). However, galaxies evolve so it is no longer certain that such standard candles exist. Evolutionary models produce a variation in the diagram that is as large as the variation between $\Omega_0 = 0$ and $\Omega_0 = 2$, which thus masks the cosmological curvature. The Hubble diagram is now used primarily as a tool for exploring the formation epoch and evolution of galaxies.

1.7 Thesis summary

The goal of the first part of this thesis is to understand the faint radio population at the mJy level. Results will be presented from a study of radio sources in the Faint Imaging Radio Survey at Twenty centimetres (FIRST; Becker et al. 1995), which are identified in the NOAO Deep Wide Field Survey (NDWFS; Jannuzi & Dey 1999) and FLAMINGOS Extragalactic survey (FLAMEX; Elston et al. 2006). The NDWFS survey is a deep optical and near infrared (*Bw R I J H K*) survey that covers two 9.3 square degree fields; one is located in the north galactic cap (Boötes field) and the second one located in the south (Cetus field). FLAMEX is a deep near infrared imaging survey that covers 7.1 square degrees within the NDWFS survey regions. Results from the X-ray identification of FIRST radio sources in the XBoötes field will be presented, as well as the clustering measurement of the FIRST radio sources identified in the Sloan Digital Sky Survey (SDSS) sixth Data Release (DR6). The last part of this thesis focuses on the radio point sources contamination of Sunyaev-Zeldovich (SZE) effect in galaxy clusters. Powerful radio point sources reside in clusters and these constitute a non-negligible contamination to the SZ signal.

The structure of this thesis is as follows:

- **Chapter 2**

  This chapter describes the results of the multi-wavelength identification process of FIRST radio sources identified in the NDWFS survey and a first scientific analysis of these results. The process of optical identification and star-galaxy discrimination is presented. Optical identification of FIRST radio sources made use of two methods, simple positional coincidence and the likelihood ratio method. This latter method quantitatively evaluates the probability of each possible counterpart to a given source being the correct one. The identification procedure is followed by a description of the photometric redshift technique used in this thesis to derive photometric redshifts for FIRST radio sources identified in NDWFS. An application of the photometric redshift technique to the Hubble $K - z$ diagram for radio sources is then presented, extending to lower flux density levels of 1 mJy than studied previousely.

- **Chapter 3**

This chapter discusses the physical properties of the extragalactic populations identified in the NDWFS survey through an analysis of the colour-colour diagrams and redshift distribution of the sample. The results of a search to find the reddest companions around FIRST radio sources is also discussed. Using the optical infrared diagram of Pozzetti & Mannucci (2000) and the SED method, the Extremely Red Objects were classified into either evolved or dusty starburst galaxies.

- **Chapter 4**

  An analysis of the X-ray and radio correlation of FIRST radio sources in the XBoötes field is presented in this chapter. The technique of the cross correlation method between the radio and the X-ray catalogues is discussed. The radio-X-ray matches are classified according to their X-ray luminosity and hardness ratio.

- **Chapter 5**

  This chapter presents a brief study of the large-scale structure of FIRST radio sources optically identified in the SDSS DR6 catalogue. The clustering statistic is measured via the two point angular correlation function for the full sample and subsamples with different magnitude and flux cutoffs.

- **Chapter 6**

  This chapter presents a systematic study of the spectral energy distribution of cluster radio sources in four bands from 4.86 to 43.3 GHz, conducted with the NRAO Very Large Array in order to study the contamination due to radio point sources in Sunyaev-Zel'dovich effect surveys.

- **Chapter 7**

  This chapter presents a summary of the conclusions from each chapter and discusses the implications of this work. This chapter also suggests future work that builds on the identification of FIRST radio sources identified in the SDSS DR6.

CHAPTER 2

Identification of FIRST radio sources in NDWFS survey

2.1 Overview

The primary goal of this study is to investigate the physical properties and the environment of the faint radio population and to trace evolution in those properties. In order to do so, one needs to know the optical colours and the redshifts of the sources being investigated. This chapter presents the results of an optical and near infrared identification of 900 radio sources from the Faint Images of the Radio Sky at 20 cm (FIRST) with a flux-density limit of 1 mJy in the NOAO Deep Wide Field Survey (NDWFS) of Boötes and Cetus fields. A cross correlation of the FIRST survey with the FLAMINGOS Extragalactic Infrared Survey (FLAMEX) in both fields is presented. Deep multi-wavelength *Bw R I K* from NDWFS and (*J, K*) from FLAMEX have been exploited to identify FIRST radio sources over about 9.2 deg^2 in Boötes field and over about 2.4 deg^2 in Cetus field. Typical depths of the optical/infrared surveys are $Bw \sim 25.5$, $R \sim 25.8$, $I \sim 25.5$, $K \sim 19.4$ and $J \sim 21.1$ ($5\,\sigma$ detection limit in $2''$ aperture, Vega).

Photometric redshifts for the optical/infrared counterparts to the radio detections were computed from broad band photometry using the template fitting method, and have been used to investigate the $K - z$ relation for FIRST radio sources. The public code *Hyperz* was used to

derive photometric redshifts. This chapter also reviews the photometric redshift technique from a historical perspective, with a brief description of every method used so far.

Throughout this chapter it is assumed that $H_\circ$=70 km s^{-1} Mpc^{-1}, $\Omega_M = 0.3$, and $\Omega_\Lambda = 0.7$ unless stated otherwise.

2.2 Introduction

The 1.4 GHz deep radio imaging surveys such as NRAO VLA SKY Survey (NVSS; Condon et al. 1998), Faint Images of the Radio Sky at Twenty cm (FIRST; Becker et al. 1995), Westerbork Northern Sky Survey (WENSS; Rengelink 1998) and Sydney University Molongolo Sky Survey (SUMSS; Mauch et al. 2003) have great implications for both radio astronomy and cosmology. They represent an excellent opportunity to explore the cosmic evolution of the number density, nature and physical properties of the radio sources. These surveys compile large area samples of the faint radio galaxies down to mJy levels, and thus reach sufficiently high source densities required for studies of the large scale structure of the universe and its evolution up to high redshift $z \sim 4$ (Magliocchetti et al. 1998; Overzier et al. 2003; Blake et al. 2004a; Negrello et al. 2006). Analyses have shown that radio galaxies are more clustered than the optical ones, are ideal tracers of super-structures and are highly biased tracers of the mass residing in the most overdense regions of the universe (e.g. Peacock & Dodds 1994; Magliocchetti et al. 1999).

Indeed, at very faint flux densities at a frequency of 1.4 GHz, the radio source counts show a rapid increase in the number of faint radio sources. Several scenarios have been developed to interpret this "excess" in the number of faint radio sources, and it has often been interpreted as a rising new population of objects, which does not contribute significantly at higher flux density (Condon 1984). However, despite many studies, the exact composition of this faint radio population is not well established, and is rather controversial. For example, Windhorst et al. (1985) and Danese et al. (1987) suggested that the flattening of the source counts at lower flux density can be explained by an active star-forming galaxy population. Optical spectroscopy, obtained by Benn et al. (1993) for faint radio sources, with $S_{1.4\ \mathrm{GHz}} < 1$ mJy supported this suggestion, and the source counts at faint levels were successfully modelled with a population

of intermediate-redshift star forming galaxies Seymour et al. (2004). An alternative secanario suggests that the flattening of the source counts may be caused by 'radio-quiet' AGNs rather than star-forming galaxies (Jarvis & Rawlings 2004); spectroscopic observation by Simpson et al. (2006) supported this latter interpretation.

While radio surveys can address many fundamental questions in cosmology and galaxy formation in addition to providing a wealth of information on the class and emission mechanism of radio sources, optical observations are still required to identify radio sources unambiguously, to measure their redshift distribution, to determine the properties of their host galaxies and to classify their spectra (as AGN, starburst galaxy etc.). The largest previous sample of optical identifications for FIRST sources (Faint Images of the Radio Sky at Twenty centimetres; Becker et al. 1995) was based on the Cambridge Automated Plate-Measuring Machine (APM) survey (Maddox et al. 1990). An identification program described by McMahon et al. (2002) for $382,892$ sources in the north Galactic cap, using the APM scans of the Palomar Observatory Sky Survey (POSS) plates, was used as astrometric standard to improve the absolute astrometry of the POSS plates: matching the radio and the optical catalogues resulted in $70,000$ optical counterparts with E$<$ 20 and O$<$ 21.5 (where E and O bands are similar to R and B bands respectively). Magliocchetti & Maddox (2002) studied optical counterparts to FIRST sources in the 2-degree Field Galaxy Redshift Survey (2dFGRS, Colless et al. 2001). Magliocchetti & Maddox (2002) present a detailed analysis of the properties and angular clustering of approximately 4000 FIRST sources with bright optical counterparts in the APM survey. Ivezić et al. (2002) discuss the properties of approximately $30,000$ sources observed by the FIRST survey and the Sloan Digital Sky Survey (SDSS; York et al. 2000). The *ugriz* observations of the SDSS have limiting AB magnitudes of 22.0, 22.2, 22.2, 21.3 and 20.5 respectively with spectra obtained for objects with $r < 17.77$ as well as for luminous red galaxies described in Eisenstein et al. (2001).

While the studies discussed above have provided large amounts of information on the optically bright counterparts to 1.4 GHz sources, one requires deeper surveys to identify the bulk of the radio sources. Optical counterparts to sources in the Phoenix Deep survey (Hopkins et al.

2003) have been studied by Sullivan et al. (2004). They investigated photometric redshifts for sources in a region with varying sensitivity – thetheoretical rms noise ranges from 10 μJy to 0.36 mJy. They obtained *UBVRI* imaging over an area of 1 deg^2 but only had *K*-band observations for a $15' \times 15'$ region in which they could find a handful of sources with S> 1 mJy. Since IR observations provide important constraints for photometric redshift estimation at higher redshifts, little information is provided on the redshift distribution of the brighter sources. Similarly, in the work by Ciliegi et al. (2005) which investigated optical counterparts to 80 μJy sources, deep *K*-band data is only available over 165 arcmin^2 which allows potentially reliable photometric redshift estimation for a small number of sources and they did address this explicitly.

A complete subsample of the Leiden Berkeley Deep Survey (LBDS; Windhorst et al. 1984) has been studied with deep optical and IR observations. The LBDS Hercules subsample consists of 72 sources observed at 1.4 GHz with flux-density $S_{1.4\ \mathrm{GHz}} \geq 1$ mJy in a 1.2 deg^2 region of Hercules. They imaged sources in *G, R, I* and *K* bands, identifying 69 of the sources in at least two bands. They also obtained spectra of 47 of the sources (Waddington et al. 2000). Photometric redshifts were estimated for the rest of sample using the spectral synthesis code of Jimenez et al. (1998). The data was used to examine the evolution of the radio luminosity function and its high redshift cut-off (Waddington et al. 2001). This study has allowed the redshift distribution and nature of 1.4 GHz sources with $S_{1.4\ \mathrm{GHz}} > 1$ mJy to be studied fairly well but the area of sky is small and may not represent a fair sample. The Combined EIS-NVSS Survey of Radio Sources (CENSORS) survey (Best et al. 2003; Brookes et al. 2006) matched sources in the ESO Imaging Survey to 150 sources in the NRAO VLA Sky Survey (Condon et al. 1998) and is complete to 7.8 mJy. Complete spectroscopic data from this survey will provide further information on the nature and redshift distribution of faint radio sources.

An interesting application of the optical identifications of radio sources involves using the $K - z$ relation to probe the nature of radio galaxy hosts. Lilly & Longair (1984) showed that for 3CRR galaxies (sources with flux-densities greater than 10 Jy at 178 MHz) there is a tight correlation between the *K*-band magnitudes of host galaxies and the redshift of the galaxy. The simplest interpretation of these results is that radio galaxies formed at high-redshift and have

been evolving passively since then (see also Jarvis et al. 2001a). Best et al. (1998) argued that this interpretation could not be correct since there is evidence that radio galaxies at high redshift are found in richer environments than those at low redshift. Studies of fainter radio sources provide more information on the nature of radio-galaxy hosts, with results from the 6C catalogues indicating an offset in the $K-z$ relation to fainter magnitudes. Some studies (e.g. Eales et al. 1997) claimed the offset only applies to $z > 0.6$ galaxies but Willott et al. (2003) attribute the apparent lack of offset at low-z to the small number of sources in the sample. Their results, as well as those of McLure et al. (2004), are consistent with the idea that the $K-z$ relation for galaxies with brighter radio flux-densities ($S > 500$ Jy at 151MHz) can be understood using the correlation between stellar mass and black-hole mass (Magorrian et al. 1998) combined with a correlation between black hole mass and radio luminosity. Best et al. (1998) and De Breuck et al. (2002) also use this idea in explaining their results. While the reasoning involving black hole mass correlations works well for brighter sources, in McLure et al. (2004), it appears to break down for the fainter radio sources in the TexOx-1000 survey (Hill & Rawlings 2003) and further studies of the $K-z$ relation for fainter radio sources would help in understanding this. Observations of extragalactic radio sources also provide important tests for galaxy evolution theory, particularly in clusters of galaxies where AGN are believed to heat the intracluster medium (e.g. Croton et al. 2006).

This chapter discusses broadly the general properties and $K-z$ relation of optical counterparts of FIRST radio sources found in the Boötes field of the NOAO Deep-Wide Field Survey (NDWFS). The FIRST radio survey is used as it provides high positional accuracy, high resolution and faint sensitivity limit compared with other contemporary large area radio surveys (e.g. NVSS). The NDWFS survey is used as it has deep multiwavelength (*Bw R I* and *K*) coverage over a large area of ~ 9.2 deg^2, it has excellent data and is well suited to address a range of important astrophysical issues of the faint radio population. Many studies in various wave bands are being carried out in this region. Using FIRST matches to NDWFS sources, Wrobel et al. (2005) identified 55 candidates suitable for the study of parsec-scale properties of radio sources and McGreer et al. (2006) searched for high-redshift quasars, finding a $z = 6.1$ quasar. de Vries et al. (2002) and Wilman et al. (2003) studied the properties of radio sources in the

Boötes field detected in the Westerbork 1.4 GHz survey and pointed out that optical and IR identifications were important for further interpretation of their results. New photometric data at Spitzer wavelengths (Brodwin et al. 2006) and X-ray wavelengths (Brand et al. 2006), as well as a spectroscopic campaign called the AGN and Galaxy Evolution Survey (Brown et al. 2006) in the Boötes region, will provide further information on the radio sources in the field. The NDWFS data covers the range $216.1° < \mathrm{RA} \leq 219°$, $32° < \mathrm{Dec} \leq 36°$.

This chapter is organised as follows: Section 2.3 describes briefly the FIRST survey, the NDWFS surveys and the FLAMINGOS survey. Section 2.4 describes the cross correlation method and presents the results from the optical and infrared identifications. Section 2.5 deals with the photometric redshift estimation. The $K - z$ relation is investigated in section 2.6. In section 2.7, results are summarised.

2.3 The surveys

In this section, a brief description is provided of the optical/infrared and radio survey data catalogues used in this chapter (and the following chapters 3 and 4).

2.3.1 The FIRST survey

The Faint Imaging of the Radio Sky at Twenty centimetres (FIRST) (Becker et al. 1995) survey is a radio survey that has been carried out in recent years using the Very Large Array to produce a map of the 20 cm (1.4 GHz) sky with a beam size of $5.4''$ and an rms sensitivity of about 0.15 mJy/beam [1]. The 2002 version of the catalogue, which contains 811,117 sources from the north and south Galactic caps is used here. The catalogue covers a total of about 9033 square degrees of the sky (8422 square degrees in the north Galactic cap and 611 square degrees in the south Galactic cap). About 900 sources fall within the NDWFS Boötes field and about 242 sources fall within the NDWFS Cetus field.

[1] http://sundog.stsci.edu

2.3.2 The NDWFS survey

The NOAO Deep Wide Field Survey (NDWFS) is a deep optical and near infrared (*Bw R I J H K*) imaging survey that covers two 9.3 square degree fields designed to study the formation and the evolution of large scale structure (Jannuzi & Dey 1999; Brown et al. 2003). The depth probed by NDWFS survey is shown in Table 2.1. The optical filters used in this survey are from the Kitt Peak Harris set with the exception of the custom *Bw* (see Figure 2.1). This survey consists of two fields; the first one is located in Boötes field (near the north Galactic pole) centred on $\alpha = 14^h32^m05.571^s$, $\delta = +34^\circ\,16'\,47.49''$ (J2000) and the second one is located in a 2.3 by 4 square degree region in Cetus field. This latter is roughly 30 degrees from the south Galactic pole and is centred on: $\alpha = 2^h\,10^m\,00.00^s$, $\delta = -4^\circ\,30'\,00.00''$ (J2000).

The NDWFS third data release (DR3) obtained for the 27 subfields that comprise the Boötes fields is used here. I have used the merged *BwRIK* catalogue for the Boötes field which is available in ASCII tables from the NOAO website[2]. The NDWFS object catalogues were generated using the software package SExtractor 2.3.2 (Bertin & Arnouts 1996). This catalogue has been split by declination range into four strips ($32^\circ < \delta \leq 33^\circ$, $33^\circ < \delta \leq 34^\circ$, $34^\circ < \delta \leq 35^\circ$, $35^\circ < \delta \leq 36^\circ$) and four bands (*Bw R I K*) to give 16 files (each strip observed in four bands: *Bw, R, I* and *K*). The merged catalogue contains two flags which provide information about the catalogue data quality: 1) FLAG_DUPLICATE =1 indicates that the object is repeated elsewhere in the catalogue, 2) FLAG_SPLITMATCH=1 is used for object with uncertain matches (dubious matches or photometry).

2.3.3 The FLAMINGOS Extragalactic survey

The FLAMINGOS Extragalactic Survey (FLAMEX, Elston et al. 2006) is a wide area, deep near infrared imaging survey that covers 7.1 square degrees within the NDWFS survey regions; 4.7 square degrees in Boötes field and 2.4 square degrees in Cetus field in both J and K filters, with limiting magnitudes of $K = 19.3$ and $J = 21.4$ ($5\,\sigma$ detection limit in $2''$ aperture, Vega). The FLAMEX catalogue is publicly available [3].

[2] http://www.noao.edu/noao/noaodeep/

[3] http://flamingos.astro.ufl.edu/extragalactic/overview.html

Table 2.1: Survey Detection Limits from (Jannuzi & Dey 1999)

Observed band	5-σ Detection in 2″ diameter aperture		1-σ surface brightness limit per $\boxdot''$	
	AB mag	Vega-mag	AB mag	Vega-mag
Bw	26.6	26.6	29.0	29.0
R	26.0	25.8	28.4	28.2
I	26.0	25.5	28.4	27.9
J	21.0	20.2	23.4	22.6
H	21.0	19.6	23.4	22.0
K	21.4	19.5	23.8	21.9

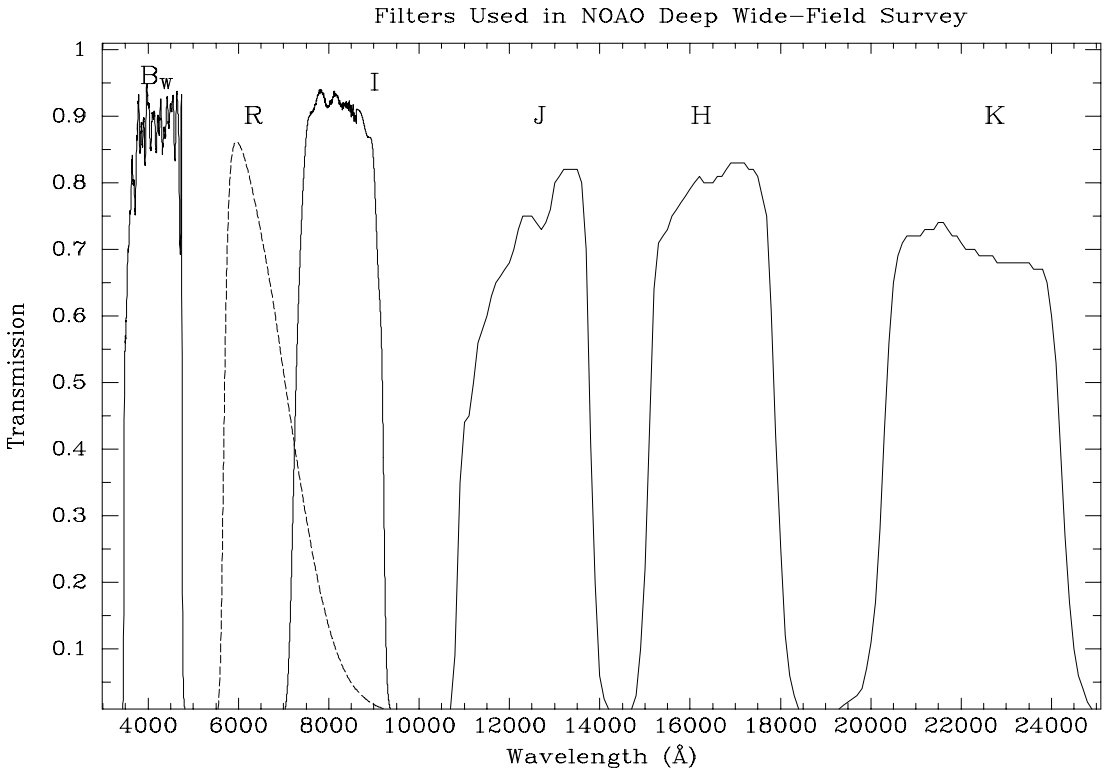

Figure 2.1: The optical/infrared filters used in the NDWFS survey. This figure is taken from the web page: http://www.noao.edu/noao/noaodeep

	1^{st} Strip	2^{nd} Strip	3^{rd} Strip	4^{th} Strip
	Boötes field (NDWFS survey)			
Bw	397531	650832	790446	670230
R	339584	606205	605044	565157
I	320125	568260	652376	526129
K	– – – ––	3793	51122	40810
	Boötes field (FLAMINGOS survey)			
J	– – – ––	95881	– – – ––	– – – ––
K	– – – ––	100610	– – – ––	– – – ––
	Cetus field (FLAMINGOS survey) $-5.56^\circ \leqslant \delta \leqslant -3.8^\circ$			
J		76738		
K		91066		

Table 2.2: The number of sources in both NDWFS and FLAMINGOS surveys observed in *Bw, R, I, J* and *K*. Each column gives the number of sources in a 1° strip, the first strip being $32^\circ < \delta \leq 33^\circ$, the second being $33^\circ < \delta \leq 34^\circ$ etc.

2.4 Matching Procedure

The following presents the cross-correlation method between the FIRST radio sources and:

1. Boötes field over the range $32^\circ \leq \delta < 36^\circ$ in the *Bw, R, I* and *K* bands using the NDWFS data, and in J and K bands (for the 2^{nd} strip; $33^\circ \leq \delta < 34^\circ$) using the FLAMEX data (there is no infrared data for the first strip $32^\circ \leq \delta < 33^\circ$).

2. Cetus field in *J, K* bands using FLAMEX data. There is no optical data publicly available from NDWFS for this field.

2.4.1 The positional matching of FIRST and NDWFS/FLAMEX catalogues

The literature describes several techniques that could be used to cross correlate radio and optical catalogues. These range from the simplest, distance based criterion, to more robust methods,

like the likelihood analysis. The accurate positions provided by the FIRST radio survey allow simple positional matching with high completeness and a low random contamination rate (Becker et al. 1995; Ivezić et al. 2002; McMahon et al. 2002; Best et al. 2005). Here I first positionally match all sources from both catalogues whose positions agree to better than 20″ and then take pairs with separation less than a chosen radius. The distribution of the distance between the NDWFS and FIRST positions is shown in Figure 2.2 (upper plot). One notes that the number of matches increases with the positional offset between the radio and optical sources which is consistent with expected random associations, as I will discuss shortly. Based on this histogram, I choose 2″ as the limiting distance for a match to be considered as an optical identification. I find 568/900 (63%) FIRST radio sources counterparts within 2″ (in Bw band).

Figure 2.3 shows the distribution of the residuals $\Delta\alpha = RA_{\rm radio} - RA_{\rm optical}$, $\Delta\delta = Dec_{\rm radio} - Dec_{\rm optical}$ between the positions of radio and optical pairs with separation less than 3 arcsec. The circle of radius 2 arcsec shows the $3\,\sigma$ error. Since the radio source and optical positions have a typical positional accuracy of about 0.5 arcsec and 0.3 arcsec respectively, the scatter is consistent with the measurement errors with perhaps small residual radio-optical offsets. Figure 2.3 clearly shows a small systematic offset between the optical and radio reference frames. This is not surprising given the separate astrometry carried out on the radio and optical data. It is common to shift the optical reference frame to match up to the radio using the median offset of matched objects. For the work carried out here, correcting this small offset have made negligible difference to the total matched sample (the total number of radio counterparts remained the same), so it is not necessary to do any corrections.

In order to estimate the number of spurious matches expected purely by chance, the radio positions were shifted by 1 and 3 arcminutes and the source matching performed again. Table 2.3 lists the results of this test, and shows the number of matches found within each search radius (1′, 3′). Figure 2.2 shows the distribution of the offset for random positions (lower curve) compared to the distribution of the offset between the FIRST and NDWFS sources (upper curve). The number of radio identifications within 2″ of the optical positions is seen to vastly exceed the random level, indicating that the majority of the radio identifications are true matches. Only 18 sources are found with offsets within the chosen matching radius of 2 arcsec, which corresponds

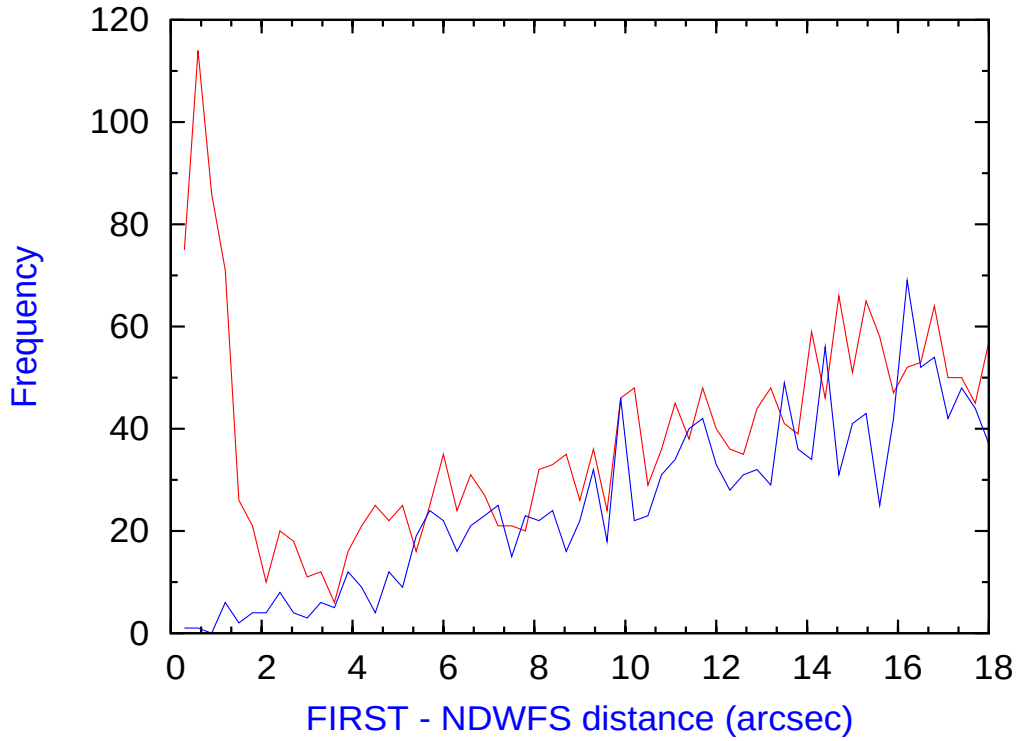

Figure 2.2: Distribution of the radio-optical positional offsets between each FIRST radio source and the nearest optical object (upper curve). This is compared to the expectation derived from random positions (lower curve).

to 3% of the true matches. Contamination at this level is not a problem in this analysis. These results are in good agreement with the results obtained by Magliocchetti & Maddox (2002) who found a 5% contamination rate for their studies of FIRST radio sources over 350 deg^2 in APM surveys (see also e.g. Georgakakis et al. 1999; Prandoni et al. 2001).

Table 2.3: Distribution of the number of matches as a function of radio - optical offset. The radio source positions were offset in declination by 1 arcmin, and 3 arcmin.

Distance (arcsec)	Real positions	Offset 1′ arcmin	Offset 3′ arcmin
0 – 1	299	2	3
1 – 2	103	11	15
2 – 3	50	13	28
3 – 5	120	52	72

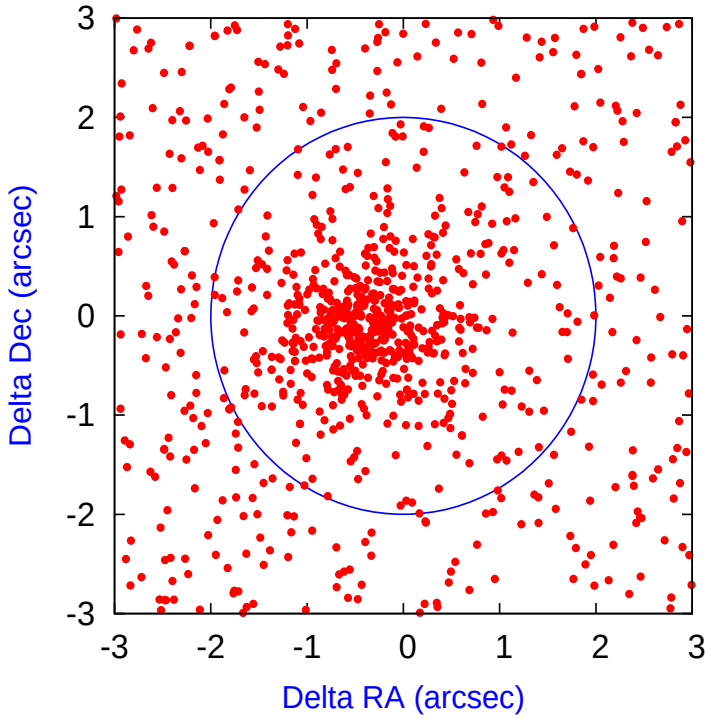

Figure 2.3: The difference between the radio and optical positions. The circle indicates the $3\,\sigma$ error.

2.4.2 The likelihood ratio technique

As a second way of quantifying the identification of the radio sources in the optical/infrared catalogues, one can consider only the subset of 'robust' radio identifications using the likelihood ratio technique. The likelihood ratio (*LR*) analysis has frequently been used to assess identification probabilities for radio and infrared sources (de Ruiter et al. 1977; Prestage & Peacock 1983; Wolstencroft et al. 1986; Sutherland & Saunders 1992; Mann et al. 1997; Rutledge et al. 2000; Ciliegi et al. 2003, 2005), especially in crowded fields and when the positional errors are large enough and may contain several matches within a few sigma of the radio position. It is described in detail by Sutherland & Saunders (1992), so only a brief review is presented here. The likelihood ratio *LR* is simply defined to be the ratio of the probability of finding the true counterpart at the observed position and with magnitude, m, (which is described by the Rayleigh distribution, $P_{\rm true}(r) = r\,\exp(-r^2/2)$) to the probability, $P_{\rm bg}(r) = 2\,\pi\,r\,N(m)\,\sigma^2$, that

the same source is a chance background object:

$$LR_{ij} = \frac{Q(m)\ \exp\left(-r_{ij}^2/2\right)}{2\,\pi\,N(<m)[(\sigma_{\alpha_i}^2+\sigma_{\alpha_j}^2)(\sigma_{\delta_i}^2+\sigma_{\delta_j}^2)]^{1/2}}, \tag{2.1}$$

where Q is the probability that true identification exists in the optical catalogue, $N(<m)$ is the surface density of background objects with magnitude m and the σ terms are standard deviations, which take into account the combined effect of the radio and the optical positional uncertainties. The value of σ was obtained by summing the positional uncertainties of the FIRST ($\sim$ 0.5 arcsec) and NDWFS ($\sim$ 0.3) arcsec surveys in quadrature. The adopted value for Q is 0.7. This choice is based on previous radio-optical identification studies undertaken down to similar optical depths (see e.g. Ciliegi et al. 2003, 2005; Sullivan et al. 2004). The optical surface density as a function of magnitude to be used in computing LR was determined from the total number of objects observed in the optical frames. The reliability of such an identification is given by (Sutherland & Saunders 1992):

$$Rel_j = \frac{LR_j}{\Sigma_i\, LR_i + (1-Q)}, \tag{2.2}$$

where the sum is over the set of all candidates for a particular source labelled by.

The LR value was computed for each radio source within the $3\,\sigma$ error circle. Different values of Q in the range $0.3-0.9$ were used in order to check the robustness of this identification technique and its dependence on the assumed parameters. No substantial difference was found in the final number of identifications and in the associated reliability. Figure 2.4 shows for different values of Q the likelihood ratio as a function of the radio-optical offset in the top panel, and the reliability as a function of the likelihood ratio in the bottom panel.

Once the likelihood ratio LR is determined, one has to find an optimum cutoff LR_c above which a source is taken to be a reliable and likely candidate. A candidate is selected to be the correct optical identification of a FIRST radio source when $LR \geq 0.2$. With this value, according to Eq. 2.2 and considering that the adopted value for $Q = 0.7$, 90% of the optical counterparts of FIRST radio sources with only one identification and $LR > LR_c$ have a reliability greater than 0.5. This maximises the combination of the sample reliability and completeness.

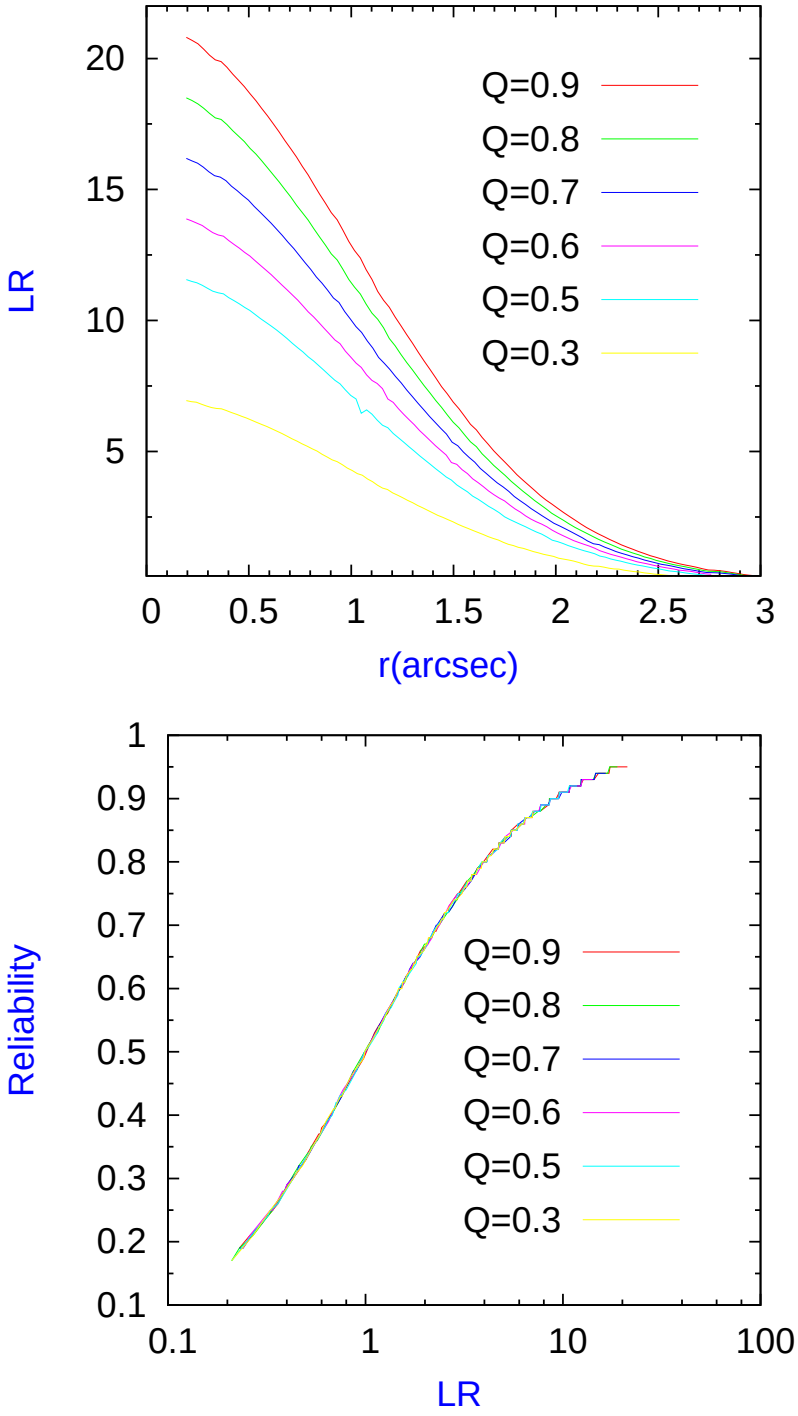

Figure 2.4: Upper panel: LR values vs radio-optical offset for FIRST radio sources identified in NDWFS survey for different values of Q. Lower panel: The reliability as a function of LR for all FIRST radio counterparts for different values of Q.

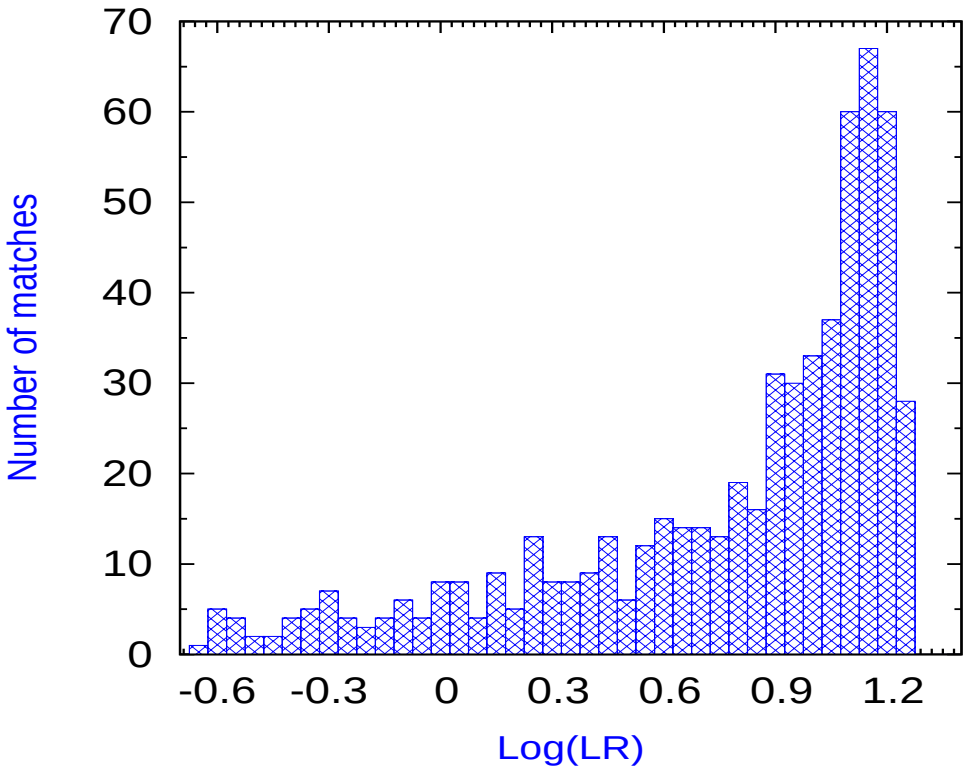

Figure 2.5: The distribution of LR values for all FIRST radio sources identified in NDWFS survey and lying within the 3σ error circle.

The distribution of $\log(LR)$ values for all FIRST radio sources candidates is shown in Figure 2.5.

2.4.3 Statistics of the radio matches

By using the two methods (likelihood ratio technique and the simple positional coincidence), it was found that the majority of FIRST radio sources have only one identification. Sources for which there are more than one candidate are flagged as repeated objects in the optical catalogue (flag_duplicate = 1) and represent $\sim$ 14 per cent. It was found that 92% of the FIRST radio sources identified based on simple positional coincidence alone are genuine. 568/900 radio sources are identified in *Bw* band based on positional coincidence while 519/900 are identified as genuine identifications using the likelihood ratio. This latter method gives a lower identification rate. In order to include all possible radio identifications, all sources that are not identified as genuine using the likelihood ratio (low reliability) were considered as plausible identifications because of their small distance (less than 2 arcsec from the radio position).

To summarise the counterparts matching (based on positional coincidence): A total number of 688/900 (76%) FIRST radio sources have candidate optical counterparts in one or more bands in Boötes field. There are 586/900 (65%) radio sources optically identified in *R* band, 577/900 (64%) are identified in *I* band, 338/700 (48%) are identified in *K* band, and 273 (39%) are identified in four bands (*Bw, R, I, K*). In Cetus field, there are 113/242 (47%) counterparts to FIRST radio sources in *J* band, 124/242 (51%) candidates in *K* band. The identification rate for the FIRST radio sources in Boötes and Cetus fields is shown in table 2.4.

Figure 2.6 shows the flux distribution for all 688 FIRST radio sources identified in the NDWFS survey (upper histogram) and for 273 sources identified in four bands (*Bw, R, I, K*; lower histogram). The FIRST radio sample consists of 92% radio sources fainter than 3 mJy, 3% radio sources brighter 50 mJy and 1% of radio sources brighter than 100 mJy. The optical/infrared identification rate of faint radio sources is estimated to be 56%, 67% for radio sources brighter than 50 mJy and 78% for radio sources brighter 100 mJy. The identification rate of faint ra-

Table 2.4: Optical and near infrared identification results (based on positional coincidence) for FIRST radio sources in Boötes and Cetus fields.

	Boötes Field				
	1^{st} strip $32^\circ \leq \delta < 33^\circ$	2^{nd} strip $33^\circ \leq \delta < 34^\circ$	3^{rd} strip $34^\circ \leq \delta < 35^\circ$	4^{th} strip $35^\circ \leq \delta < 36^\circ$	Whole field $32^\circ \leq \delta < 36^\circ$
			Sources identified in one band		
Bw	65%	60%	63%	97%	63%
R	77%	63%	64%	85%	65%
I	76%	59%	67%	86%	64%
J	-	46%	-	-	46%
K	-	51%	37%	46%	48%
			Sources identified in two bands		
BwR	56%	55%	58%	74%	57%
BwI	53%	52%	57%	72%	56%
RI	56%	56%	60%	78%	60%
IK	-	44%	35%	44%	39%
			Sources identified in three bands		
BwRI	51%	51%	54%	69%	54%
BwIK	-	40%	32%	39%	35%
RJK	-	41%	-	-	41%
			Sources identified in four bands		
BwRIK	-	39%	32%	38%	39%
RIJK	-	41%	-	-	41%
BwRJK	-	38%	-	-	38%
			Sources identified in five bands		
BwRIJK	-	38%	-	-	38%
			Cetus Field ($-5.56^\circ \leqslant \delta \leqslant -3.8^\circ$)		
J			47%		
K			51%		
JK			45%		

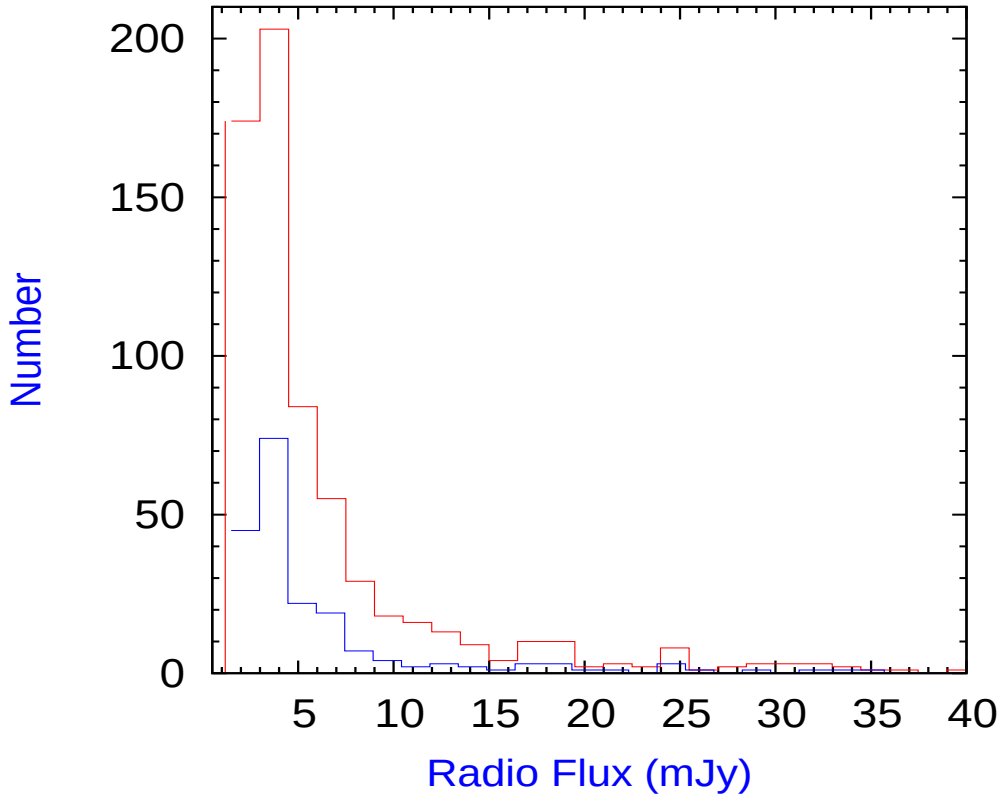

Figure 2.6: Histogram showing distribution in $S_{1.4}$(mJy) for all 688 FIRST radio sources identified in Boötes field (upper histogram) and sources identified in four bands (*Bw, R, I, K*; lower histogram).

dio sources is lower than the one for brighter sources. This lead to the conclusion that deeper surveys are required in order to identify more faint radio sources.

Figure 2.7 shows the projected distribution of FIRST radio sources identified in Boötes field in four bands (*Bw R I K*) over 7 square degrees ($33^\circ \leq \delta < 36^\circ$; blue circles) and sources that are identified in either one, two, three or four bands (red plus) over the whole sample ($32^\circ \leq \delta < 36^\circ$). As clearly seen from the figure there is no coverage in *K* band for the first strip. Figure 2.8 displays the projected distribution of FIRST radio sources identified in Cetus field. Circles correspond to 109 sources identified in two bands (*J* and *K*) and plus signs represent 113 sources identified in one band.

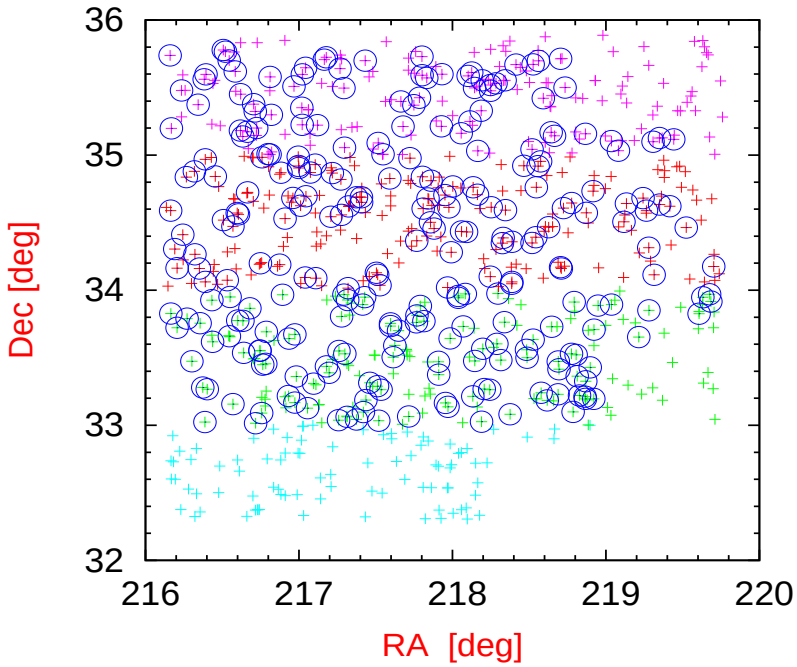

Figure 2.7: Projected distribution of FIRST radio sources with counterparts in Boötes field: circles represent sources with identifications in four bands (273 sources; $33^\circ \leq \delta < 36^\circ$) and plus signs correspond to sources identified in one or more bands (688 sources ; $32^\circ \leq \delta < 36^\circ$). The different colours of the '+' symbol stand for FIRST radio sources identified in each strip of the Boötes field.

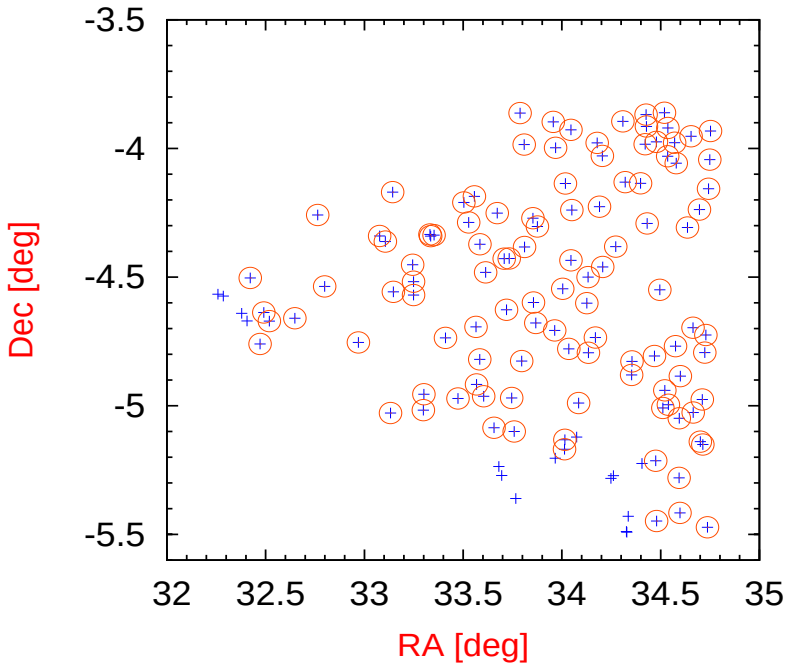

Figure 2.8: Projected distribution of FIRST radio sources with counterparts in Cetus field : circles represent sources with identifications in two bands (109 sources); and plus signs correspond to sources identified in one band (113 sources).

2.4.4 Multiple-component radio sources

Due to the high resolution provided by FIRST, many extended or large radio sources are resolved out and split into multiple components. The radio morphologies of such sources can be fairly complex (e.g. core-jet, core-lobe or double-lobed radio sources), and this makes it difficult to associate an appropriate optical counterparts with such radio sources (Ivezić et al. 2002; Best et al. 2005). These multicomponent sources would also affect the cosmological clustering signal if considered as single sources (Magliocchetti et al. 1998). An algorithm to address this issue was discussed by Magliocchetti et al. (1998), McMahon et al. (2002), Ivezić et al. (2002) and Best et al. (2005). I attempt first to identify groups of sources that are likely to be sub-components of a single source in the FIRST catalogue by using an algorithm similar to that adopted by Magliocchetti et al. (1998). I have employed a percolation technique where all sources within a given radius are replaced by a single source at an appropriate 'centroid'. Following Magliocchetti et al. (1998), I vary the link-length in the percolation procedure according to the flux of each source using the $\theta \propto S$ relation found by Oort (1987). Multicomponent sources are considered as a single object if their flux densities S_1 and S_2 differ by less than a factor of four and the projected separation of the two radio components is smaller than their link length $[(S_1 + S_2)/100\ \mathrm{mJy}]^{0.5} \times 100$ arcsec.

The applied matching criteria yielded a total of 97 FIRST groups in the 9.2 deg^2 region of sky covered by the NDWFS survey (Boötes field). Of these, I found 47 (8%) groups identified in Boötes field in *Bw* band, 45 (8%) groups identified in *R* band, 35 (6%) groups in *I* band and 12 (4%) groups in *K* band. 32/47 groups are identified as double radio sources, 13/47 are radio sources with triple components, 2/47 are radio sources that are resolved into four components and 1/47 radio source has complex morphology (resolved into more than 5 components). Figure 4.3 shows examples of identified multicomponent radio sources recognised by the selection algorithm. Each of these FIRST stamps is $2' \times 2'$, normalised to the maximum intensity. These images are extracted from the FIRST web site. To summarise, the FIRST - NDWFS/FLAMEX sources with complex morphology represent a small fraction $< 1\%$, and this does not significantly affect the results in this small sample.

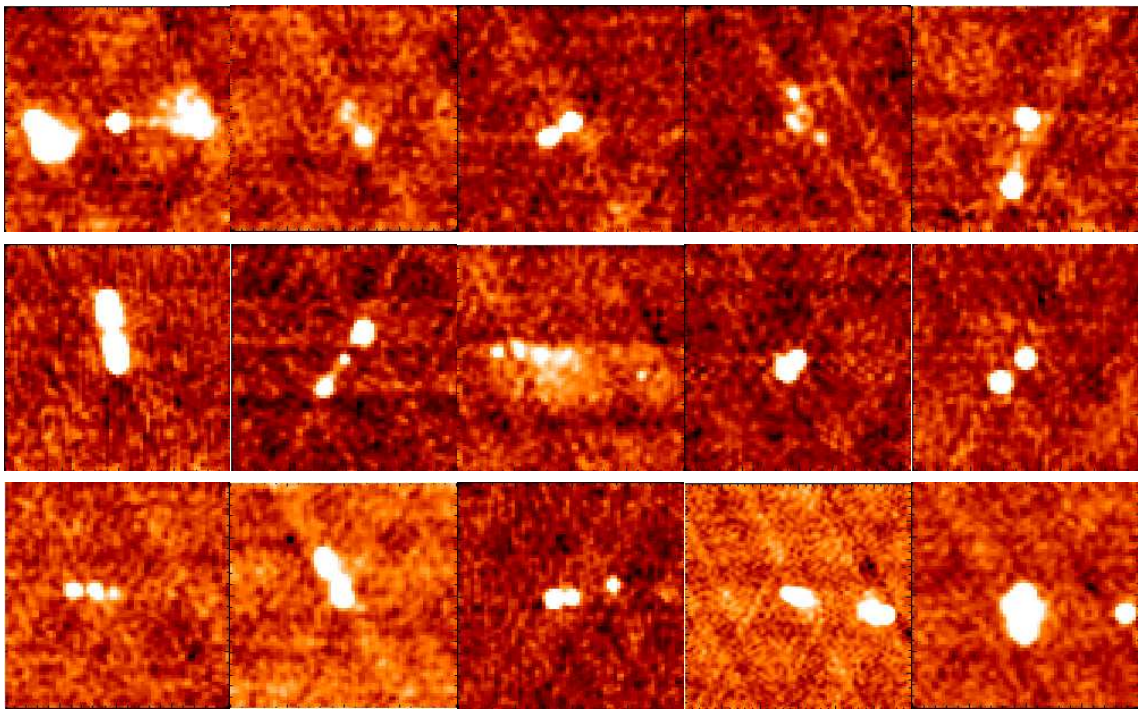

Figure 2.9: Examples of FIRST radio sources with multiple components identified by the selection algorithm (Magliocchetti et al. 1998). Each FIRST stamp is $2' * 2'$, normalised to the maximum intensity.

It is important to note that because many FIRST radio sources are resolved out and split into multicomponent sources, their total flux is underestimated due to the survey high resolution effect ($5''$). Best et al. (2005) have derived an hybrid method using both NVSS (Condon et al. 1998) and FIRST radio surveys in order to identify radio counterparts of galaxies ($14.5 < r < 17.8$) in the second data release (DR2) of the Sloan Digital Sky Survey with high completeness and reliability. FIRST and NVSS surveys have complementary properties; the first one provides high resolution needed to reliably identify the host galaxy and the second one (low resolution $45''$) accurately samples the total flux density of extended radio sources. I positionally cross correlate the FIRST candidates with the NVSS surveys. Figure 2.10 shows the total NVSS flux densities compared to FIRST flux densities for radio sources detected in both radio surveys and identified in Boötes/Cetus fields. One notes that, for sources fainter than $\sim$ 10 mJy, the FIRST flux densities tend to be lower than those measured by NVSS, and this is mainly due to the radio emission of extended sources being resolved out by the FIRST survey high resolution (Becker et al. 1995; White et al. 1997; Ivezić et al. 2002).

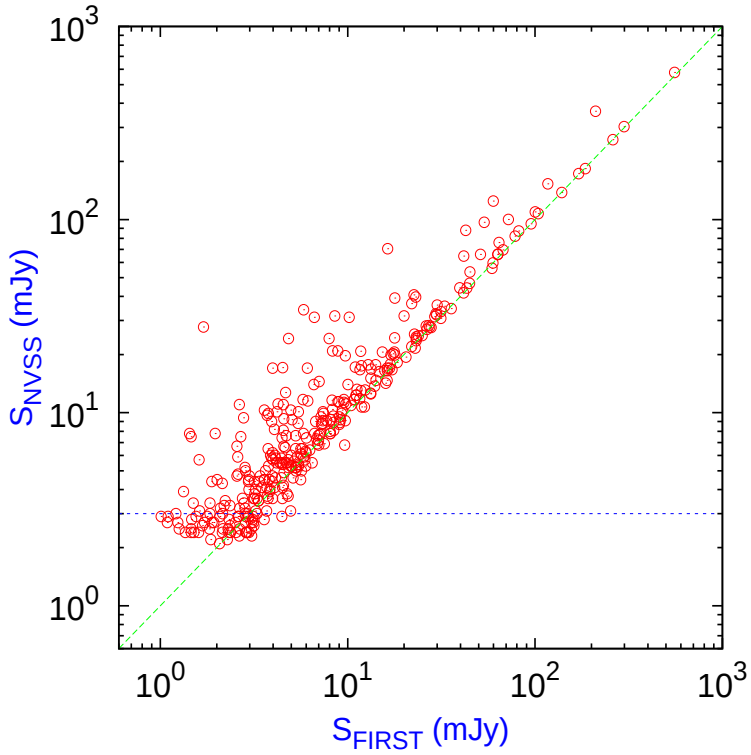

Figure 2.10: The NVSS flux density vs the FIRST flux density for all FIRST radio sources identified in Boötes/Cetus fields. The horizontal dashed line shows the NVSS flux density limit.

2.4.5 Morphological classification

For a simple morphological classification, I used the Source Extractor stellarity parameter S/G (Bertin & Arnouts 1996) from the NDWFS galaxy catalogue which has values between 0 (galaxy, more to the point, non-star) and 1 (for point-like sources well characterised by their point spread functions): an object is either a "star" (unresolved) or a "galaxy" (resolved). Figure 2.11, shows the stellarity parameter against the apparent *R*-band magnitude for all matched FIRST radio sources. There are 88 (15%) FIRST radio sources associated with point sources and 498 (85%) FIRST radio sources identified as a galaxy. Following (Brown et al. 2003), if I classify all sources that have stellarity greater than 0.7 in two or more bands brighter than $Bw = 23.8$, $R = 22.8$ and $I = 21.4$ as point-like, the number of FIRST radio sources identified as point-like drops to 45 (7%) point sources and to 181 (31%) radio sources identified as a galaxy. It is also important to note that the SExtractor classification is not perfect and will break down at the lower magnitude (for $R > 23$ in the NDWFS data Brown et al. 2003). It does not give another value for unreliable classification but assigns a random value between 0 and 1

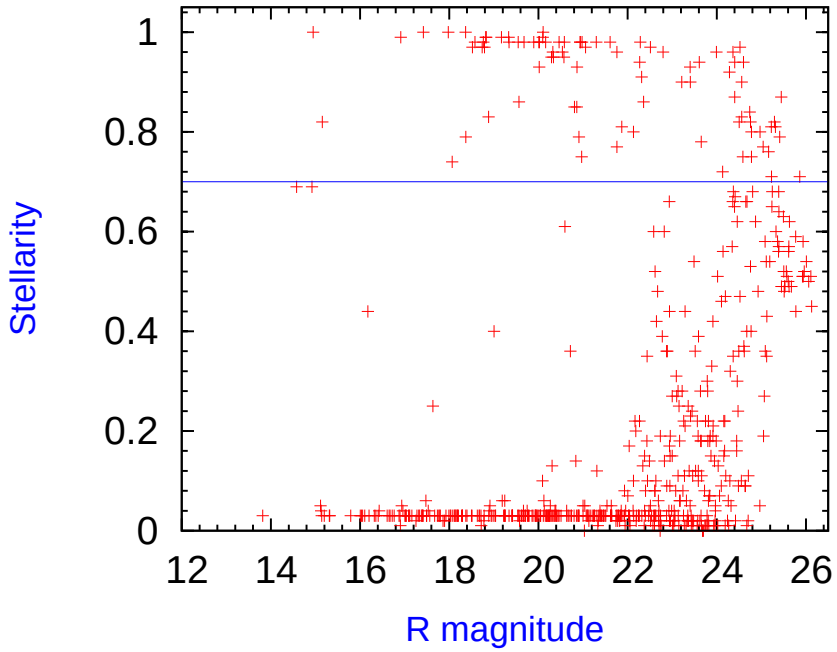

Figure 2.11: SExtractor stellarity parameter plotted against the apparent R-band magnitude for all FIRST radio sources identified in R band. The solid line shows the boundary that I have assumed in dividing the sample into point sources (stellarity > 0.7) and extended sources (stellarity < 0.7). The reliability clearly disappears at the faint end.

(see Figure 2.11). If I consider a subsample of FIRST radio counterparts with $R < 23$, I find 57 (8%) point sources and 311 (53%) extended, (resolved) objects.

2.5 Photometric redshift analysis

Photometric redshift estimation is a powerful statistical tool for studies of the evolutionary properties of galaxies, in particular of faint galaxies, for which spectroscopic data is hard or impossible to obtain. Photometric redshift techniques are based on the fact that magnitudes or colours of a galaxy allow a good estimation of its redshift. These techniques are very promising given the increasing precision of large photometric surveys for which obtaining spectroscopic redshifts is costly.

2.5.1 A brief history of photometric redshifts

Direct shift measurement

The technique of photometric redshifts can boast a relatively long history. Its first application dates back to the sixties. Baum was the first to propose (Baum 1957) and develop (Baum 1962) a technique for measuring redshifts photometrically. He used a photoelectric photometer and nine band-passes spanning the spectrum from 3730 Å to 9875 Å in order to observe the spectral energy distribution (SED) of 6 bright elliptical galaxies in the Virgo cluster and 3 elliptical galaxies in another cluster (Cl0925+2044, also known as Abell 0801). By plotting the average SED of the Virgo galaxies and the average SED of the Cl0925 galaxies on the same graph, he was able to measure the displacement between the two energy distributions and hence the redshift of the second cluster. His redshift value of $z = 0.19$ agreed closely with the known spectroscopic value of $z = 0.192$. Baum's technique was fairly accurate, but because of its dependence on the 4000 Å break spectral feature, it could only work on elliptical galaxies.

Colour-colour diagrams

Koo (1985) used a different approach. First, he used photographic plates instead of a photometer, making it possible to measure photometric redshifts for large number of galaxies simultaneously. Second, he used only 4 filters instead of nine, and the theoretical Bruzual A. (1983) no-evolution models for all galaxy types instead of using an empirical spectral energy distribution. The main difference, however, was the way the colours were used. Instead of converting the photometric colours into a kind of low resolution spectrum, he converted the Bruzual templates into colours, and plotted lines of constant redshift and varying spectral type, known as iso-lines, on a colour-colour diagram. He used his technique to calculate the photometric redshift of the galaxy by finding the iso-line closest to the point that represented the galaxy.

Linear regression

Perhaps the simplest and certainly the most empirical photometric redshift technique yet is that of Connolly et al. (1995). This method requires a "training set" of a large number of galaxies with multicolour photometry and a derived spectroscopic function of the magnitudes (M_i) of

the galaxies. If N is the number of the filters :

$$z = a_0 + \sum_{i=1}^{N} a_i M_i \tag{2.3}$$

or

$$z = a_0 + \sum_{i=1}^{N} a_i M_i + \sum_{i,j=1}^{N} a_{ij} M_i M_j \tag{2.4}$$

The constants, a_i and a_{ij}, are found by linear regression. This technique is extremely simple and it is completely empirical: one does not have to assume that the galaxies in question have the same spectral energy distribution as local galaxies. But a substantial collection of spectroscopic redshifts must have been measured before the technique can be used and extension to fainter magnitudes or even higher redshifts is not possible.

ANNz

ANNz is an Artificial Neural Network (ANN) software package commonly used for photometric redshift estimation (Collister & Lahav 2004). It is one of the most competitive tools currently available for galaxy photometric redshifts. ANNz used a particular species of ANN known formally as a multilayer perceptron (MLP) which consists of a number of layers of nodes. The first layer contains the inputs which are the magnitudes, m_i, of a galaxy in a number of filters (for ease of notation these can be arranged in a vector $\mathbf{m} \equiv (m_1, m_2, ..., m_n)$). The final layer contains the outputs (e.g photometric redshifts, spectral type). Intervening layers are described as hidden and there is complete freedom over the number and size of hidden layers used. The nodes in a given layer are connected to all the nodes in adjacent layers, a commonly used form is to have an N_{in}:N_1: N_2:.....N_{out} where N_{in} is the number of input nodes, N_1 is the number of the nodes in the first hidden layer, and so on. A schematic ANN of this type is shown in Figure 2.12.

For a set of galaxies for which both photometry, m, and a spectroscopic redshift, z_{spec}, are available, the network is trained by minimising the cost function:

$$E = \sum_k (z_{\rm phot}(w, m_k) - z_{\rm spec})^2, \tag{2.5}$$

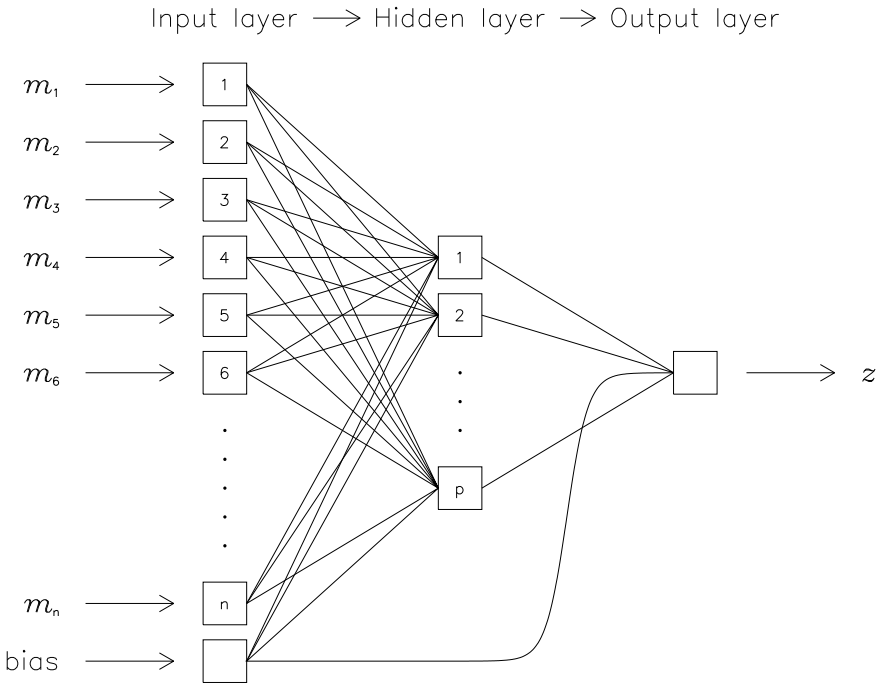

Figure 2.12: Schematic diagram of a multi-layer perceptron, as implemented by ANNz, with n inputs, a single hidden layer of N neurons and a single output neuron. Multiple hidden layers are possible, each with its own number of neurons. Figure from Collister & Lahav (2004).

with respect to the weights, w, where $z_{\rm phot}$ (w, m_k) is the network output for the given input and weight vectors, and the sum is over the galaxies in the training set.

Template fitting

The template fitting technique developed by Loh & Spillar (1986) more closely resembles that of Baum (1962) than that of Koo (1985). There are basically two different approaches to estimate the photometric redshift for a galaxy from its broad band photometry: The empirical training set method (and this has been described in the previous section) and the fitting of the observed spectral energy distributions (SEDs). The template fitting technique can be divided into three steps:

1. The photometric data for each galaxy (through various filters) are converted into spectral energy distributions (SEDs). The magnitude in each bandpass is converted into a flux (power per unit band width per unit aperture area) at the central effective wavelength of the bandpass.

2. A set of template spectra for different Hubble types is compiled from various sources. These spectra are then redshifted, corrected for intergalactic and internal extinction, and reduced to the passband averaged flux at the central wavelengths of the passbands in order to compare the template spectra with the SEDs of the observed galaxy magnitudes.

3. The spectral energy distribution derived from the observed magnitudes of each object is compared to each template spectrum, and the redshift is determined by minimising a χ^2 statistic.

The two methods are comparable in their performance at $z \leq 1$. The training set method is not always feasible at high redshifts because (1) there are degeneracies in the colours of galaxies at very different redshifts and (2) this method cannot extrapolate to redshifts beyond the highest redshifts in the training set. Photometric redshift codes using the SED fitting method were developed for the Hubble deep field (HDF) by Sawicki et al. (1997), Lanzetta et al. (1996), Fernández-Soto et al. (2001) with an accuracy of typically $\triangle z \sim 0.06\ (1 + z)$. The SED fitting method works best when there is a strong feature in the SED, such as the 4000 Å break, or the 912 Å Lyman break. In other words, this method fits the shape of the SED, which in turn provides an estimate of the redshift $z_{\rm phot}$ via a χ^2 minimisation.

2.5.2 The template fitting method as used in this thesis

A number of codes have been developed based on template fitting photometric redshifts estimation, including BPZ (Benítez 2000; Benitez 1998), IMPZ (Babbedge et al. 2004), Le Phare[4], and *Hyperz* (Bolzonella et al. 2000). In this thesis, I used the publicly available code *Hyperz*[5] (Bolzonella et al. 2000), which fits GISSEL 98 (Galaxy Isochrone Synthesis Spectral Evolution Library) synthetic spectra (Bruzual & Charlot 1993) galaxy templates to photometric data points. The spectra were corrected for intergalactic extinction from the Lyman forest (Madau 1995) and for internal extinction from dust in galaxies. For the internal extinction, I used the Calzetti extinction curve (Calzetti et al. 2000) which is suitable for starburst regions. Eight syn-

[4]http://www.oamp.fr/people/arnouts/LE_PHARE.html
[5]The code is publicly available at: http://webast.ast.obs-mip.fr/hyperz/

thetic spectral types were used representing starburst galaxies (Stb), Elliptical (E), Lenticular (S0), Spirals (Sa, Sb, Sc and sd) and Irregular (Im) galaxies. The time evolution of the Star Formation Rate for all galaxy types is represented by an exponential model, i.e. SFR $\propto \exp(-t/\tau)$, where τ is the SFR time scale. Each galaxy type has a value of τ assigned. The early type galaxies can be matched by a delta burst ($\tau \rightarrow 0$) or by an exponentially decaying SFR with a time scale between 1 and 2 Gyr (E, S0). The spiral galaxies (Sa, Sb, Sc and Sd) are represented by an exponentially decaying SFR with time scales ranging from 3 to 30 Gyr. The irregular galaxies (Im) are represented by a constant SFR ($\tau \rightarrow \infty$). The SEDs for different spectral types are shown in Figure 2.13. All the models have solar metallicity and Miller & Scalo (1979) initial mass function. While there are a large number of filters predefined in *Hyperz*, the *Bw* filter is not included, I added the profile transmission of the filter from the NDWFS website [6]. The spectra were then convolved with the filter response curves (Figure 2.1) to obtain the expected fluxes $F_{\mathrm{temp},i}$. The χ^2 calculation considered all redshifts, spectral type, and extinction values. The minimisation of the χ^2 statistic found the most likely redshift and the corresponding 'best' template:

$$\chi^2(z,\ \mathrm{template}) = \sum_{i=1}^{N_{\mathrm{filters}}} \left[\frac{F_{\mathrm{obs},i} - b \times F_{\mathrm{temp},i}(z)}{\sigma_i} \right]. \tag{2.6}$$

Here $F_{\mathrm{obs},i}$, $F_{\mathrm{temp},i}$ and σ_i are the observed and template fluxes and the uncertainty in the filter i, respectively, and b is just a scaling factor. For each source *Hyperz* computes the best fit redshift z_{phot} as well as the z_{phot} error bars corresponding to the 68%, 90%, 99% confidence intervals where $\Delta\chi^2 = 1.00, 2.71, 6.63$ respectively. In this study, a source is considered to have a reliable photometric redshift if $\chi^2 < 2.7$ (90% confidence limit).

Photometric redshifts were determined for all FIRST radio sources identified either in five bands (*Bw, R, I, J, K*) or four bands (*Bw, R, I, K*) obtained by the joint use of the two surveys NDWFS and FLAMEX for the second strip ($33^\circ \leq \delta < 34^\circ$), and for the whole sample ($32^\circ \leq \delta < 36^\circ$) including sources that are identified in two or three bands. The possible photometric redshift was allowed to range from 0.0 to 6.0 with a redshift step of $\triangle z = 0.05$ and the maximum absolute magnitude set to -24. Setting a maximum redshift allowed for the possibility of identifying the highest redshift counterparts to faint radio sources. The host galaxy

[6] http://www.noao.edu/noao/noaodeep

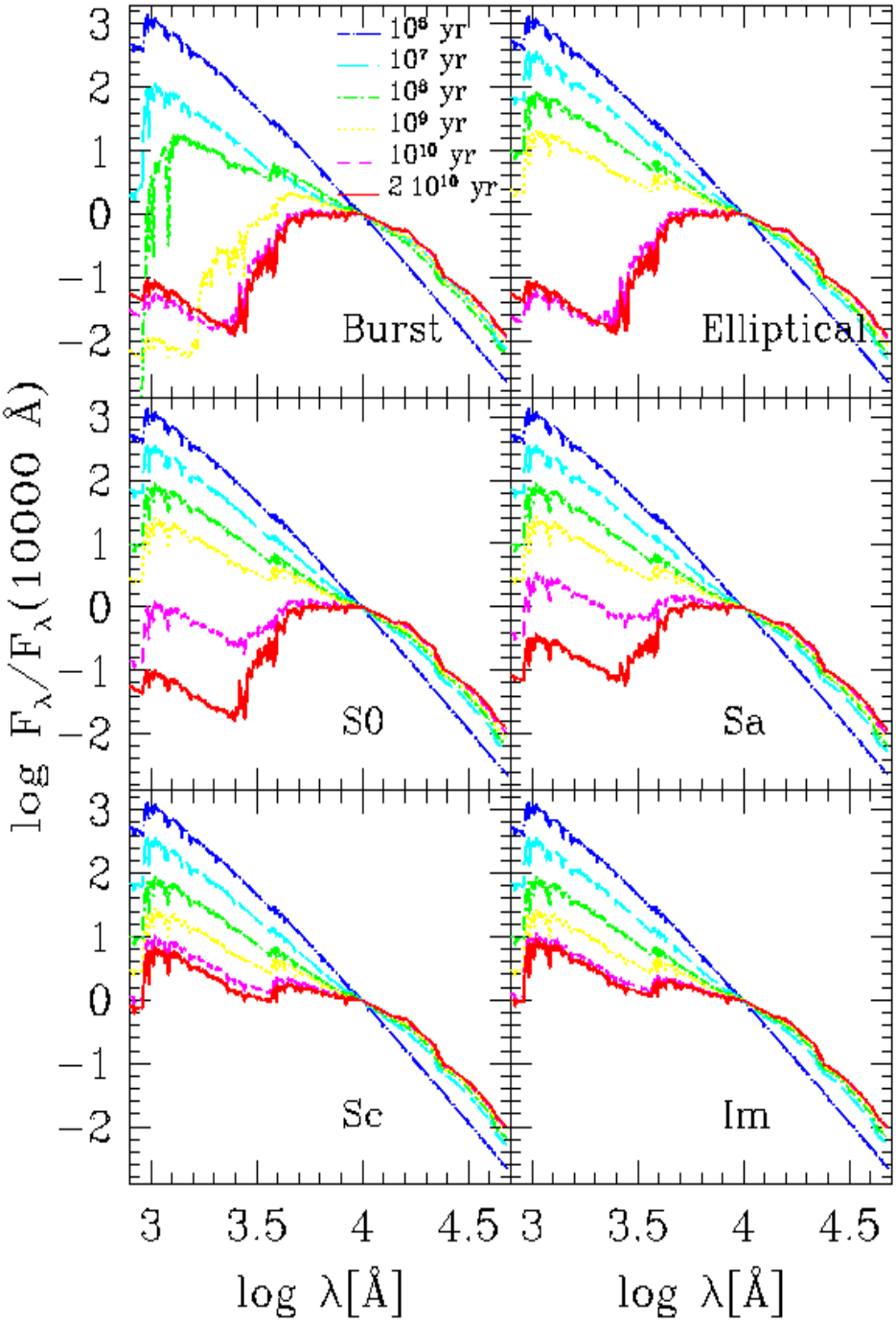

Figure 2.13: Synthetic SEDs of different spectral types and different ages created from the spectral evolutionary models of Bruzual & Charlot (1993) and used by *Hyperz* (Bolzonella et al. 2000). The different spectral types correspond to different star-formation histories (τ = $0, 1, 2, 3, 15, \infty\, Gyr$ for Burst, Elliptical, S0, Sa, Sc, Sd and Im, respectively. Taken from the *Hyperz* manual(Bolzonella et al. 2000))

extinction was ranged in a $A_v = 0 - 1.2$ mag interval with a step of $\triangle A_v = 0.2$ mag.

2.5.3 Redshift distribution and galaxy type

In 256/688 (36%) cases it was not possible to assign a reliable $z_{\rm phot}$ and spectral type to the optical radio sources counterparts since $\chi^2 > 2.7$. A total number of 67 (9%) of these sources are identified in four bands, and 189 (27%) are identified either in two bands or three bands. The probability distribution calculated for each of the above sources has either significant secondary peaks or is relatively flat. Figure 2.14 shows examples of unreliable solutions derived from the use of *Hyperz*. In the following discussion will focus on sources with reliable photometric redshifts.

Among the 688/900 FIRST radio sources identified in NDWFS survey, I have assembled the best estimates of photometric redshifts for 432 (63%) FIRST radio counterparts. These are reasonably well-fit by SED, $\chi^2 < 2.7$ (90% confidence limit). Figure 2.15 displays examples of the probability distribution as a function of redshift for FIRST radio sources with reliable photometric redshifts. As clearly seen from the figure, the probability distribution has only a single peak.

Figure 2.16 shows the photometric redshift distribution for all radio sources identified in NDWFS, for which a reliable redshift estimate was obtained. The left panel shows the photometric redshift distribution (red histogram for Boötes field; blue histogram for Cetus field) for all sources identified in four bands (*Bw, R, I, K*; Boötes field) including the one introduced in El Bouchefry & Cress (2007). The distribution shows a significant peak at $z = 0.80$ with a tail extending up to $z \sim 2.80$. The mean photometric redshift is $z = 0.74$. The right panel in Figure 2.16 shows the photometric redshift distribution for all FIRST radio sources ($32^\circ \leq \delta < 36^\circ$) identified either in two bands, three bands or four bands. About 68% of the sources are estimated to be at $z < 1.5$, with a mean of $z = 0.88$ and a high redshift tail extending up to $z \sim 6$.

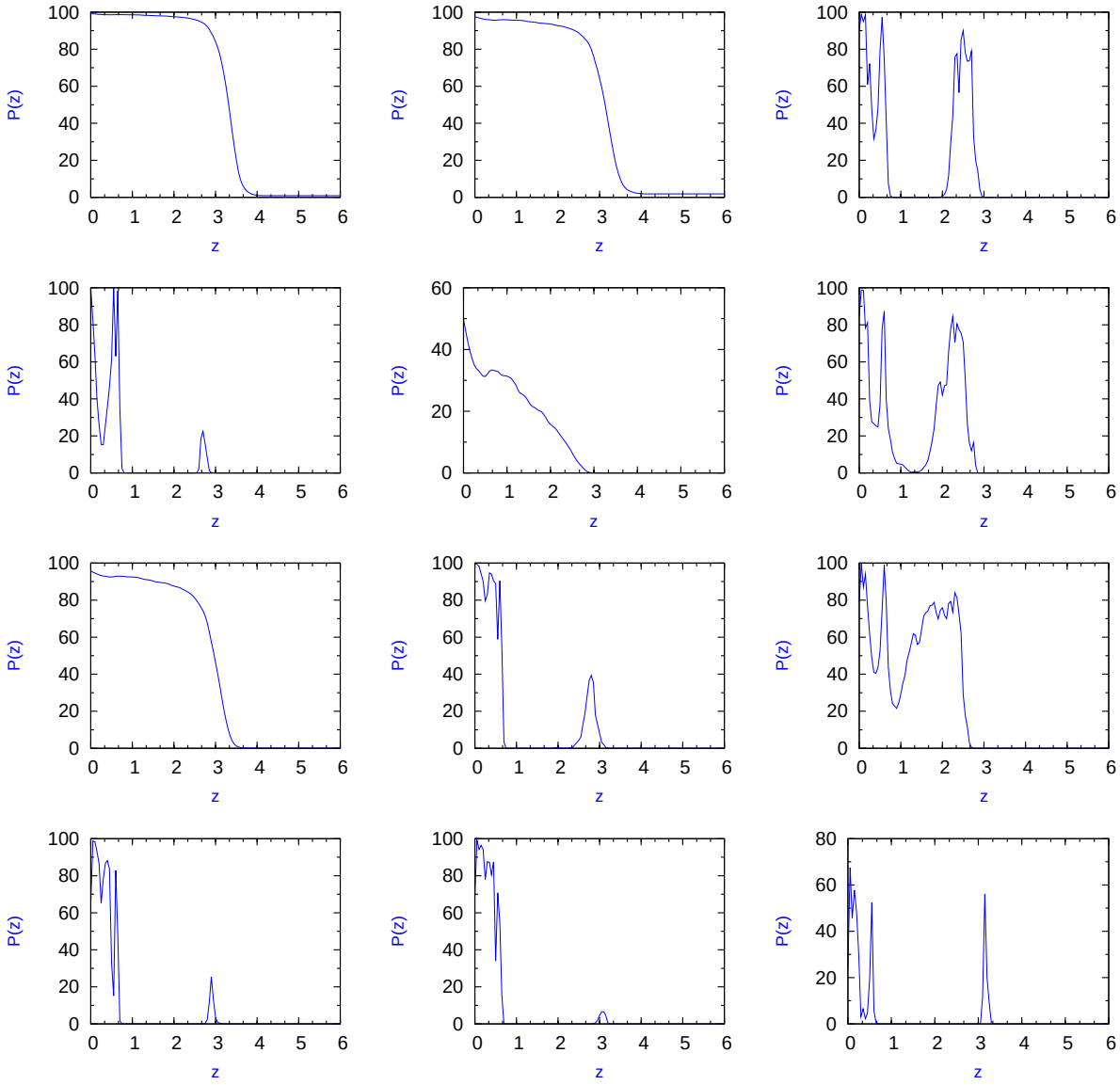

Figure 2.14: Examples of probability distributions as a function of photometric redshift as derived by *Hyperz* for FIRST radio source counterparts with unreliable photometric redshift. This examples illustrate that the assignment of a single number for the photometric redshift can be misleading. These sources which have poor photometric redshift determination are not considered in the $K - z$ relation (see section 2.6).

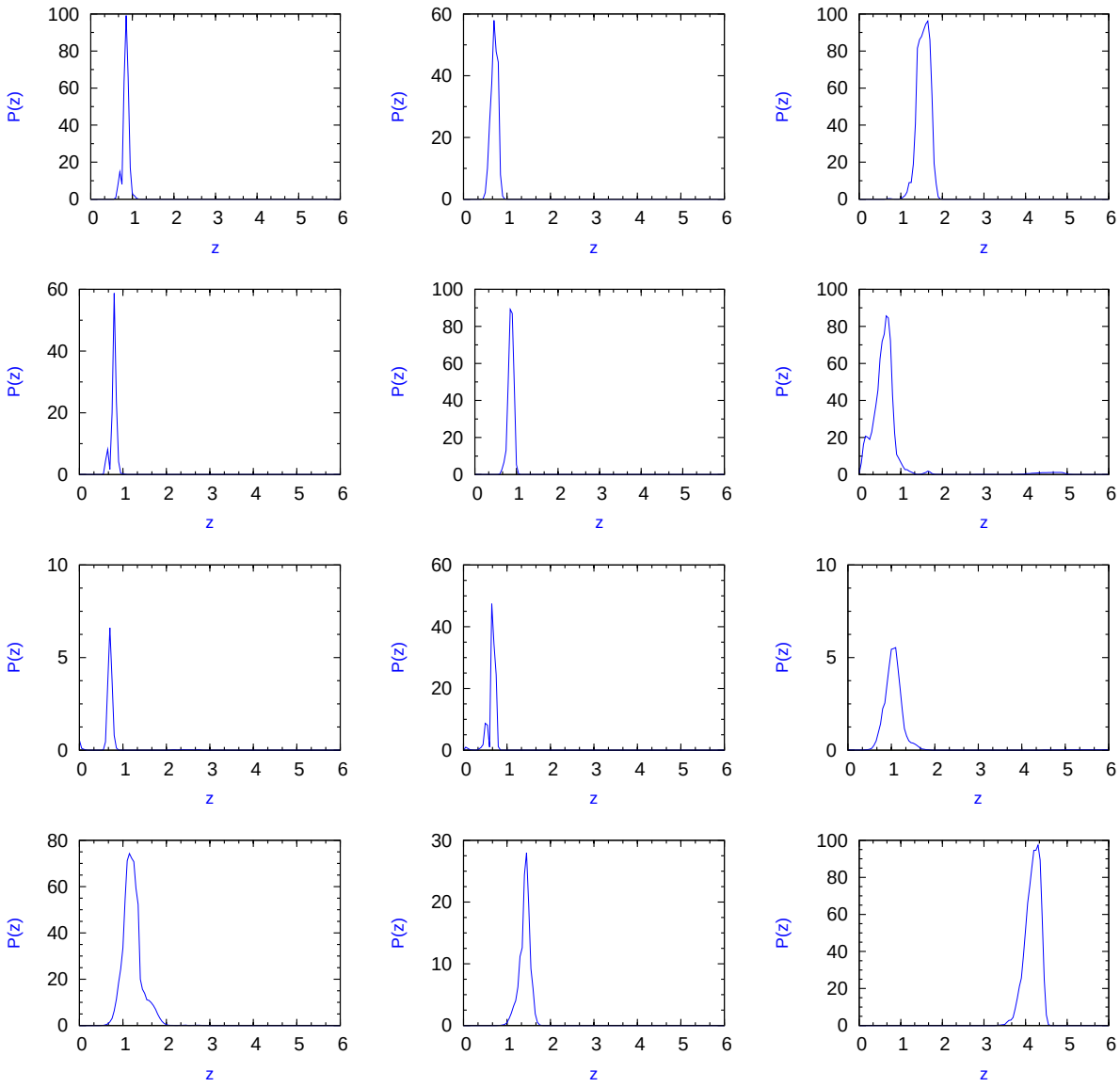

Figure 2.15: Examples of probability distributions as a function of photometric redshift as derived by *Hyperz* for FIRST radio source counterparts with reliable photometric redshift.

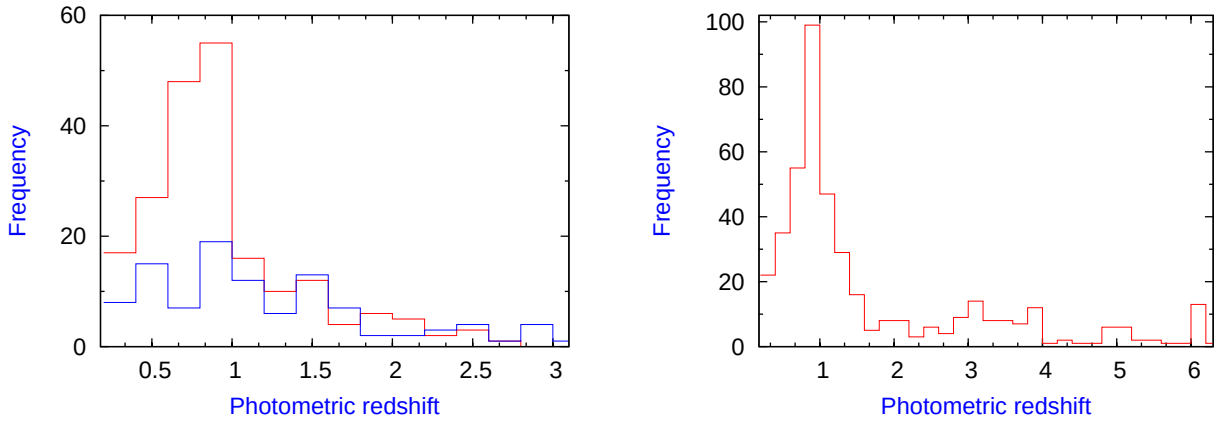

Figure 2.16: The left panel shows the photometric redshift distribution as calculated by *Hyperz* for all 273 FIRST radio sources identified in Boötes field (four bands *Bw, R, I* and *K*; red histogram) and for 109 FIRST radio sources identified in Cetus field (*J* and *K* bands; blue histogram). The right panel shows the photometric redshift distribution for all FIRST radio sources identified either in two bands or more in Boötes field.

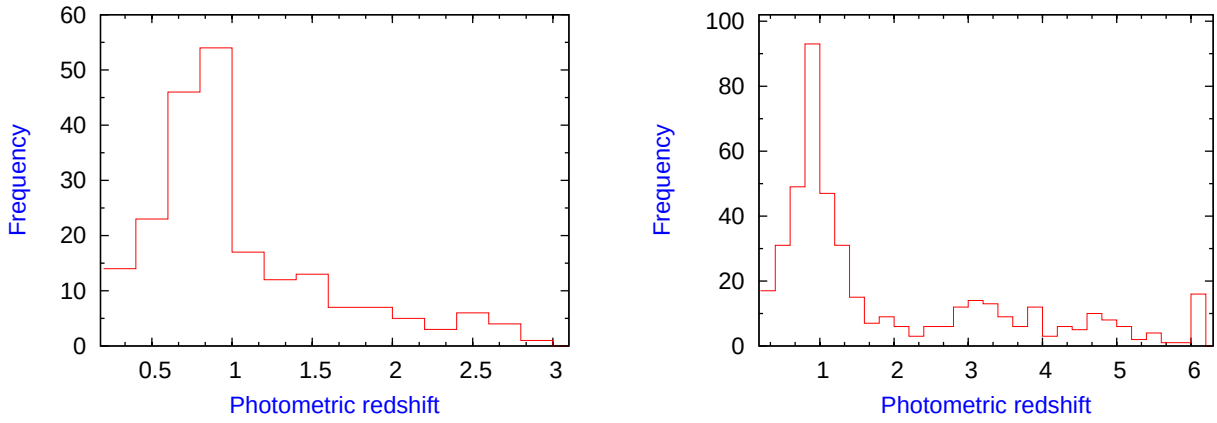

Figure 2.17: The photometric redshift distribution when the QSO templates are included. The left panel shows the photometric redshift distribution for all 273 FIRST radio sources identified in Boötes field (four bands *Bw, R, I* and *K*; red histogram). The right panel shows the photometric redshift distribution for all FIRST radio sources identified either in two bands or more in Boötes field.

When using the synthetic templates for the fit, I found that the favoured galaxy type was the burst template. This template were selected in 61% cases. The rest of the cases were distributed between Elliptical (18%), Spirals (21%) and Irregular (4%) templates. When the 'burst' option was removed, the elliptical template was selected as the best option for 230/386 (60%) sources. It is important to note that passively evolving single bursts (defined as burst in *Hyperz* BC templates) can be considered early or late, depending on their age. As in Bolzonella et al. (2000) the 'burst' spectra can be interpreted as elliptical galaxies with star formation on timescales shorter than 1 Gyr (age $<$ 0.1 Gyr). When sources were identified as bursts, their ages range from 0.001 to 12.5 Gyr with a mean of 1.3 Gyr. When the burst option was removed and sources were identified as elliptical, ages range from 0.001 to 12.5 Gyr with a mean age of 4.7 Gyr.

The photometric redshift estimates described so far neglect the AGN or QSO population, since no spectral templates representing these systems have been added to the BC SED set used. I therefore added to the standard template spectra provided by *Hyperz* a set of four quasar templates compiled from the LE PHARE web-site[7] and limited the absolute magnitude to -27. 449 out of 688 FIRST radio counterparts are estimated to have reliable photometric redshifts and spectral types. 33 sources (7%) were best fitted by the quasar spectrum and 13 of these (3%) were the highly reddened quasar template. 248 sources (55%) were identified as 'bursts', 73 sources (16%) were identified as elliptical and 20 (4%) as S0's, leaving 75 sources (17%) identified as late-type galaxies. When the 'burst' option was removed, 418/688 FIRST radio sources had a reasonable redshift and spectral type. In this case the reddest QSO template was selected as the best fit for 59/418 sources (14%) and the elliptical template was selected for 176 sources (42%).

In Figure 2.17 I show the photometric redshift distribution when the quasar templates were included. The left panel shows the photometric redshift distribution for all FIRST radio sources identified in Boötes field in four bands with a mean photometric redshift of 0.846 and a tail extending up to $z \sim 3$. The right panel displays the photometric redshift distribution for the whole sample $32^\circ \leq \delta < 36^\circ$ (including sources identified either in two, three or four bands) with a

[7] http://www.oamp.fr/people/arnouts/LE_PHARE.html

mean photometric redshift of $z = 1.76$ and a tail extending up to $z \sim 6$. One notes, from the right panel of Figure 2.17, that the addition of QSO templates results in an increase of sources in the range $3 < z < 5$.

The excess at $z = 6$ in the right panels in both Figures 2.16 and 2.17, is mainly due to objects identified in two bands and is clearly spurious (even if $\chi^2 < 2.7$). For such objects the photometric redshift determination based on one colour clearly fails, and this is due to the degeneracy in the dependence of a single colour on redshift and spectral type. However, in special cases where the morphological types of galaxies are specified, a single colour can provide an extremely accurate estimate of the redshift (e.g. McGreer et al. 2006).

A subset of identifications which were unresolved (SExtractor stellarity parameter > 0.7) has been considered. When the QSO spectra are included, 5% are identified as such and 32% were best fitted with the burst template (QSOs generally have power law spectra thus they can look very flat in broad band filters and could easily be fit with a starburst-type template). For a subset of identifications which were resolved (SExtractor stellarity parameter < 0.7), 4% are identified as QSOs. One should note that it is difficult to obtain reliable spectral classification from broad band photometry alone (Bolzonella et al. 2000) due to the poor spectral resolution. The *Hyperz* code can reliably identify early type galaxies (Bolzonella et al. 2000), whereas only a rough estimate of the SED type could be obtained for late-type galaxies in terms of a "blue" or "red" continuum (see Bolzonella et al. 2000, for more details).

2.5.4 Radio flux distribution by spectral class

Figure 2.18 shows histograms of 1.4 GHz flux density for five bins in best-fitting SED type, based on photometric redshift results. It is clear that the bulk of the early type SEDs, tend to lie at the lower flux densities. Their radio fluxes lie in the range $1 < S_{1.4}$ (mJy) ≤ 5, and optically they appear as relatively faint (about 76% of the sources have $Bw > 19$). A detailed analysis of the optical properties of the radio - detected population will be explored in the following chapter.

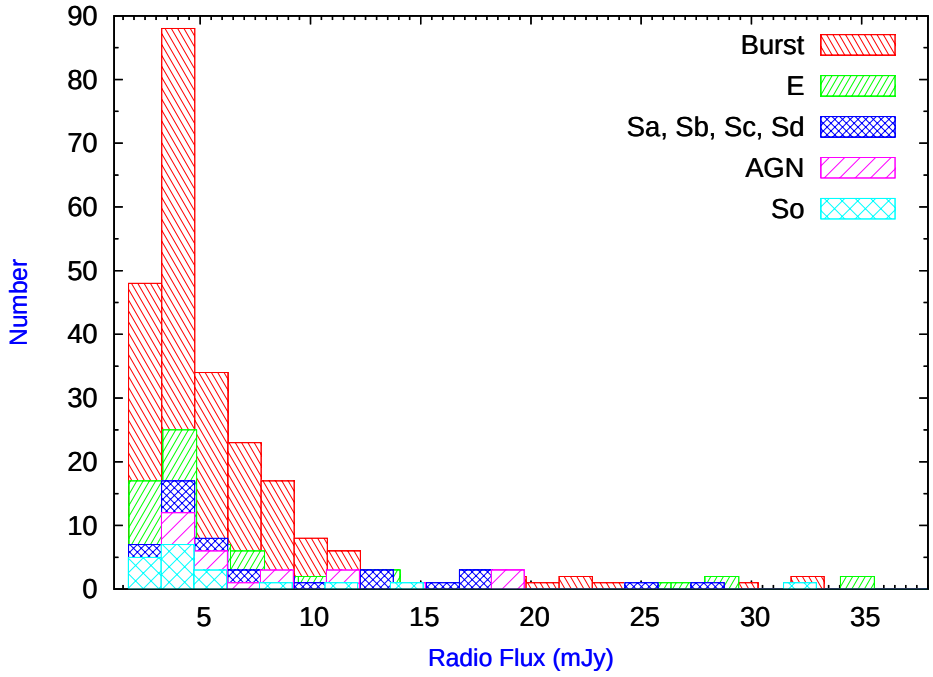

Figure 2.18: Histogram showing distribution in radio flux $S_{1.4}$ (mJy) by best-fitting photometric redshift SED type. The five bins are: Burst galaxies at the top of then E , (Sa, Sb, Sc, Sd) and AGN, with S0 type galaxies at the bottom.

2.6 The Hubble diagram

The infrared K-magnitude against redshift relation has been widely used as a tool for investigating the evolution with cosmic epoch of stellar populations of luminous galaxies, since k corrections, dust extinction corrections, and the effect of any secondary star formation are all relatively unimportant at near infrared wavelengths. The infrared K-magnitude has played an important role in the search for and the study of high redshift galaxies (e.g Lilly & Longair 1984; Eales et al. 1997). For example, the first radio galaxy discovered at $z > 3$ was selected on the basis of a faint $K \sim 18.5$ magnitude (Lilly 1988). The empirical fit to the combined 3CRR and 1-Jansky Hubble diagram quoted by Lilly & Longair (1984) is as follow:

$$\log_{10} z = -5.368 + 0.384\,K - 0.00385\,K^2 \tag{2.7}$$

Willott et al. (2003) have investigated the $K-z$ relation for 205 radio galaxies with high spectroscopic completeness ($z \sim 0.05-4.4$) obtained from a combined data set selected at different flux limits: 3CRR (Laing et al. 1983), 6CE (Eales et al. 1997; Rawlings et al. 2001), $6C^{\star}$ (Jarvis

et al. 2001b,a) and the 7CRS (Lacy et al. 2000; Willott et al. 2003) showing that 3CRR and 7CRS radio galaxies are offset by ~ 0.55 mag in K-magnitude over all redshift while the 6C differ from the 3CRR ones by ~ 0.3 mag. These results have been interpreted as a correlation of both properties with black hole mass (Willott et al. 2003; McLure & Jarvis 2004). However the correlation between the radio luminosity and the infrared luminosity is still uncertain. The best fit for the combined sample (3CRR, 6CE, 7CRS) quoted by (Willott et al. 2003) is:

$$K(z) = 17.37 + 4.53 \log_{10} z - 0.31 (\log_{10} z)^2 \tag{2.8}$$

2.6.1 The $K - z$ diagram for FIRST radio sources

In order to investigate the $K - z$ relation for the FIRST radio sources identified in both fields (Boötes and Cetus), I used the best photometric redshift estimates with $\chi^2 < 2.7$ (90% confidence) for all FIRST radio sources identified in *Bw, R, I, K* (Boötes field) and *I, J* (Cetus field). Radio sources that were identified as unresolved sources on the basis of their stellarity measure being $S/G > 0.7$ (Bertin & Arnouts 1996) are excluded from the $K - z$ analysis due to the fact that the $K - z$ relation is applicable only to radio galaxies for which the K band emission is dominated by an old elliptical galaxy.

The $K - z$ relation for the FIRST radio source counterparts in the second strip ($33^\circ \leq \delta < 34^\circ$) augmented with those introduced in El Bouchefry & Cress (2007) for the Boötes field ($34^\circ \leq \delta < 36^\circ$), represented by stars and crosses respectively, is shown in Figure 2.19. The green line is the best fit second order polynomial relationship between the K band magnitude and $\log_{10} z$ for all the data:

$$K(z) = 17.52 + 4.34 \log_{10} z + 0.86 (\log_{10} z)^2, \tag{2.9}$$

the red line is the best fit of the combined sample of 3CRR, 6C and 7CRS (Willott et al. 2003), and the blue line shows the best fit for the 7CRS sample alone. Brookes et al. (2006) claim that they found a similar fit of the 7CRS data alone to the fit they obtained for the CENSORS survey. Since the FIRST radio sources are much fainter than 7CRS sources, which have flux densities $S_{151\ \mathrm{MHz}} > 500$ mJy, and are selected at a much higher frequency, one might not expect

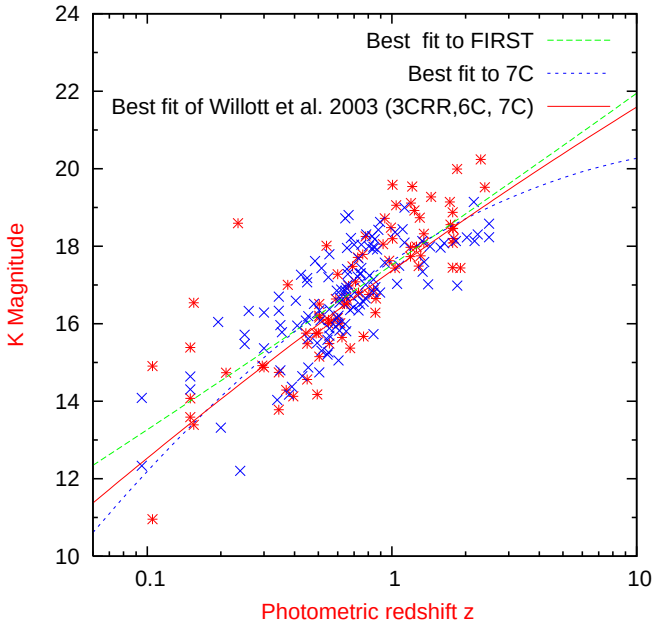

Figure 2.19: *K* band magnitude against redshift for all FIRST radio sources identified in Boötes in four bands (*Bw, R, I, K*). Crosses present sources identified in the range $34° \leq \delta < 36°$ (introduced in El Bouchefry & Cress (2007)) and stars indicates the new counterparts of FIRST radio sources in the second strip ($33° \leq \delta < 34°$). The solid line shows the best fitting relationship between *K* magnitude and $\log_{10}(z)$ for the data.

the established $K - z$ relation to hold. The fit for the FIRST radio sources is shifted slightly to fainter magnitudes which could support the finding that brighter radio sources are associated with galaxies that are brighter in *K* band, even for faint radio sources. But a more complete and deeper sample is required to investigate this further. I considered FIRST radio sources with flux-densities greater than 10 mJy but did not find a better fit to the relation given in (Willott et al. 2003).

The mean *K* magnitude of the FIRST-Boötes sample is 16.75. The dispersion about the mean $K - z$ relation is given by $\sigma_K = 1.53$. Similar correlation is found in other bands (*Bw, R* and *I*; see Figure 2.20) but with a larger scatter. One notes that the scatter in *K* band is smaller at high redshift ($\sigma_K = 0.76$ at $z > 1$), than at lower redshift, consistent with the idea that fainter radio surveys include fainter galaxies that are different from the typical galaxies associated with bright radio sources. Once again, a more complete sample and more reliable redshift estimates from spectroscopic measurements, are required to investigate this further.

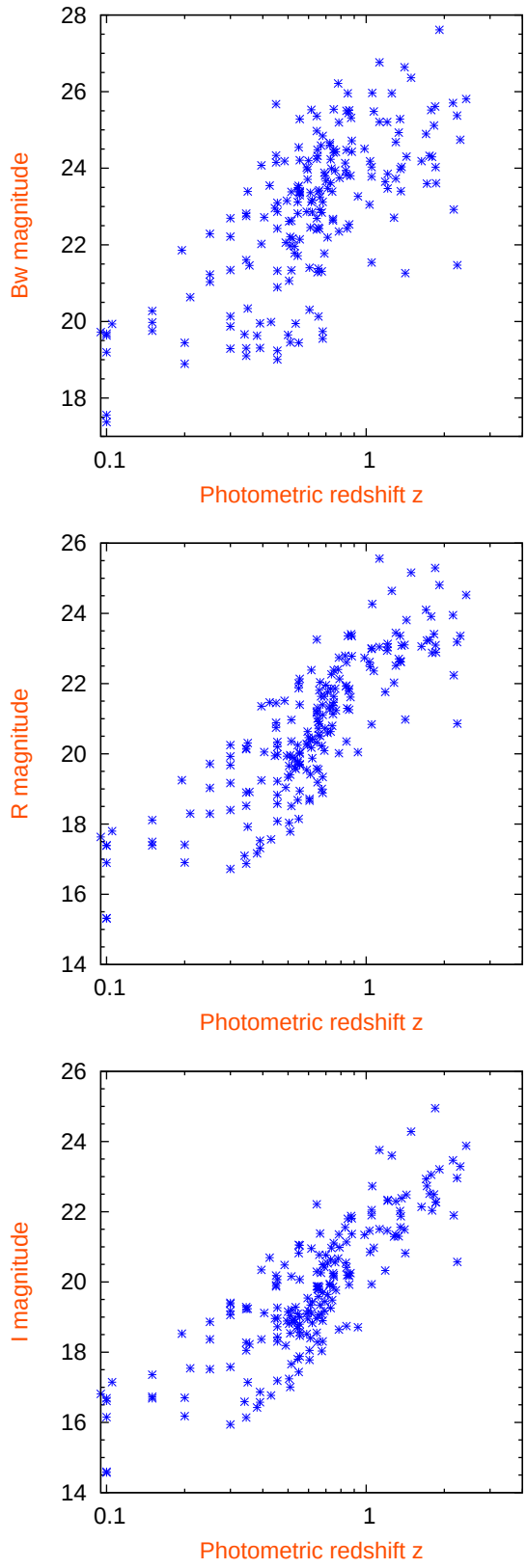

Figure 2.20: *Bw, R,* and *I* magnitudes (from top to bottom) against redshift for all FIRST radio sources identified in Boötes field in four bands (*Bw, R, I, K*).

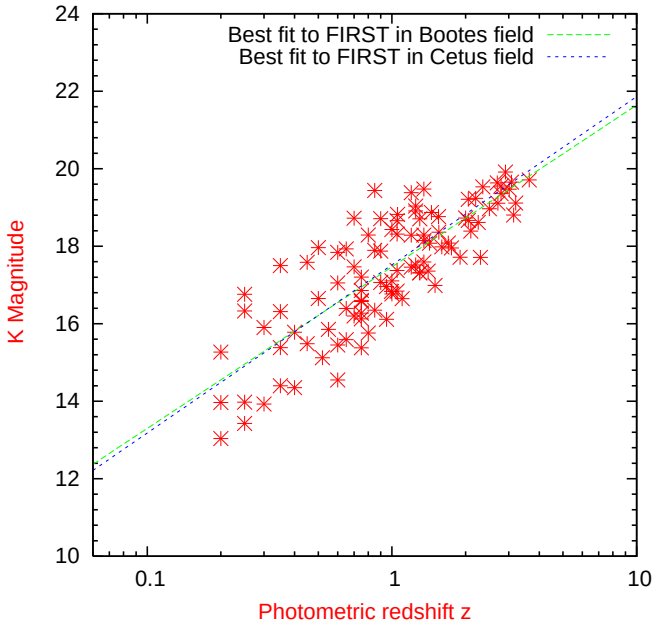

Figure 2.21: The K band magnitude against redshift for all FIRST radio sources identified in Cetus field ($-5.6^\circ \leq \delta < -3.8^\circ$). The green line shows the $K-z$ relation as derived for FIRST radio sources identified in Boötes field and the blue line is the best fitting relation based upon the FIRST radio sources identified in Cetus field. The two fits are very similar.

Figure 2.21 displays the K band magnitude of FIRST radio sources against photometric redshift obtained for sources identified in Cetus field. The blue line in the plot shows the best fit $K-z$ relation for FIRST radio sources in Cetus field which is similar to the one presented for FIRST radio sources identified in Boötes field (green line).

In Figures 2.22 and 2.23, the three curves show the K band magnitude for non-evolving and passive evolution $L_\star$ galaxies as a function of redshift. The passive evolution models (blue and green plots) assume that the stars in the galaxies formed at $z = 5$ and $z = 10$ respectively. The three lower curves illustrate passive stellar evolution tracks of a $3\,L_\star$ galaxy for an instantaneous burst of star formation (0.1 Gyr) and one in which the burst of star-formation lasts 1 Gyr at $z = 5$, as well as a no evolution curve as derived by Jarvis et al. (2001a). For comparison in Figure 2.24 I have plotted the near infrared Hubble diagram of K magnitude versus redshift for the NDWFS-FIRST sample combined with data of four samples compiled from the literature: 3CRR, 6CE, 6C*, and EIS-NVSS. The brightest sample is 3CRR observed at 178 MHz with a flux density limit of $S_{178} \geq 10.9$ Jy, the intermediate samples are the 6CE and 6C* observed

at 151 MHz with flux density limits of $2.0 \leq S_{151} \leq 3.93$ Jy and $0.96 \leq S_{151} \leq 2.00$ Jy respectively. The 7CRS was observed at 151 MHz with a flux density limit of $S_{151} \geq 0.5$ Jy. The EIS-NVSS sample (Brookes et al. 2006) was observed at 1.4 GHz with a flux density limit of 7 mJy. The 3CRR, 7CRS, 6CE and 6C* data have been gathered from the web site provided by Willott et al. (2003)[8]. The K-band magnitudes and the corresponding redshifts for the EIS-NVSS sample have been obtained from the work of Brookes et al. (2006). The model curves in Figure 2.24 show non-evolving and passive evolution $3\,L_\star$ galaxies. All magnitudes are on the same metric system (63.9 kpc) except the FIRST radio sources counterparts. It is important to note that aperture corrections are generally small and less than 0.05 mag at $z \geq 0.6$ (Eales et al. 1997); see also Fig 3 in Cruz et al. (2007) for an $8''$ aperture (corrections are less than $\pm\,0.05$ mag). As clearly seen from the figures, the majority of the FIRST radio sources lie fainter than the no-evolution curve (for $3\,L_\star$ galaxies) due to the fact that the FIRST survey is deeper than the low-frequency complete samples that were used to make the $K-z$ diagrams in Jarvis et al. (2001a) and in Willott et al. (2003): The trend also highlights the fact that the galaxy luminosity is likely correlated with the radio power (Willott et al. 2003; McLure et al. 2004).

it is important to not that the Boötes and Cetus $K-z$ samples are not complete; i.e they do not contain every radio galaxy down to a radio flux limit. Here we only dealt with radio galaxies identified in four bands (in order to get accurate photometric redshift), moreover with the additional criteria, one excludes sources with a not very good fit, and this makes the sample incomplete. Other effects of incompleteness come from the NDWFS survey itself. The K band catalog is not as deep as the optical catalog (there is no K band data for the first strip ; $32^\circ \leq \delta \leq 33^\circ$, other strips are partially covered in K band). The Boötes and Cetus K band magnitude histograms drop of at $K \sim 19.5$. This is evident in the plotted $K-z$ relation. The lack of $K \geq 20$ galaxies could cause several effects: (i) the slope of the $K-z$ relation for FIRST is a little bit flatter than for 3C/6C/7CRS. (ii) the scatter in FIRST is quotted as 1.53 for whole sample and 0.76 at $z > 1$. This difference can be explained if most of the missing galaxies are at $K \geq 20$ and $z > 1$. (iii) if there are a significant number of K band faint radio galaxies missing, then the observed FIRST $K-z$ relation having a very small offset from 3CRR, 6C, 7CRS of 0.15 mag at $z = 1$ could be misleading and in reality there could be a larger difference in magnitudes

[8] http://www.astro.physics.ox.ac.uk/ cjw/kz/kz.html

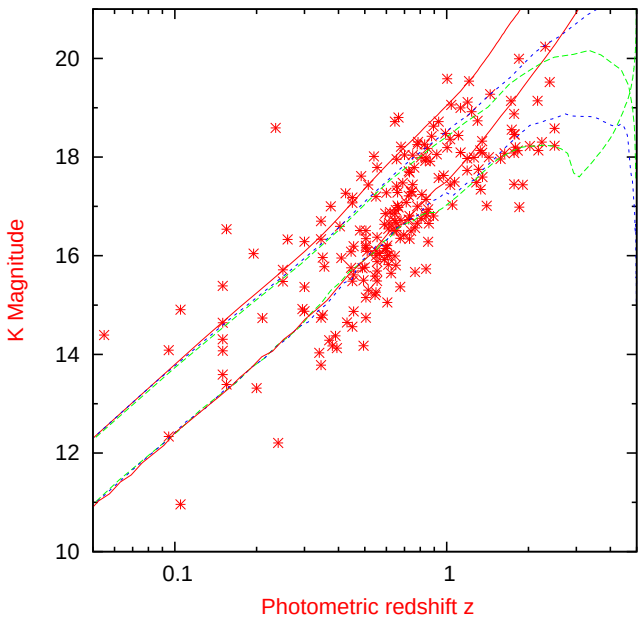

Figure 2.22: The $K-z$ Hubble diagram for all FIRST radio sources identified in Boötes field as defined in Fig 2.19. The three upper curves show : non evolving galaxies with luminosity $1\,L_\star$ (red curve), the blue and green curves correspond to a passive evolution for galaxies with $1\,L_\star$ assuming all stars in the galaxies formed at $z=5$ and $z=10$ respectively. The three lower curves are : a non-evolution curve for galaxies with $3\,L_\star$ (red colour), instantaneous starburst for galaxies with $3\,L_\star$ beginning at $z=5$ (blue colour) and a starburst for galaxies with $3\,L_\star$(green colour) lasting $1\,Gyr$ and starting at $z=5$ (Jarvis et al. 2001a).

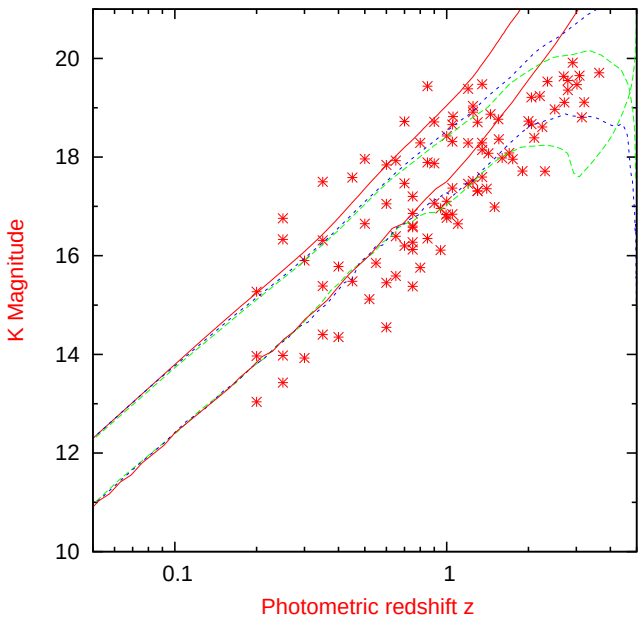

Figure 2.23: The $K-z$ Hubble diagram for all FIRST radio sources identified in Cetus field as defined in Fig 2.21. The three upper curves show : non-evolving galaxies with luminosity $1\,L_\star$ (red curve), the blue and green curves correspond to a passive evolution for galaxies with $1\,L_\star$ assuming all stars in the galaxies formed at $z=5$ and $z=10$ respectively. The three lower curves are: a non evolution curve for galaxies with $3\,L_\star$ (red colour), instantaneous starburst for galaxies with $3\,L_\star$ beginning at $z=5$ (blue colour) and a starburst for galaxies with $3\,L_\star$(green colour) lasting $1\,Gyr$ and starting at $z=5$ (Jarvis et al. 2001a).

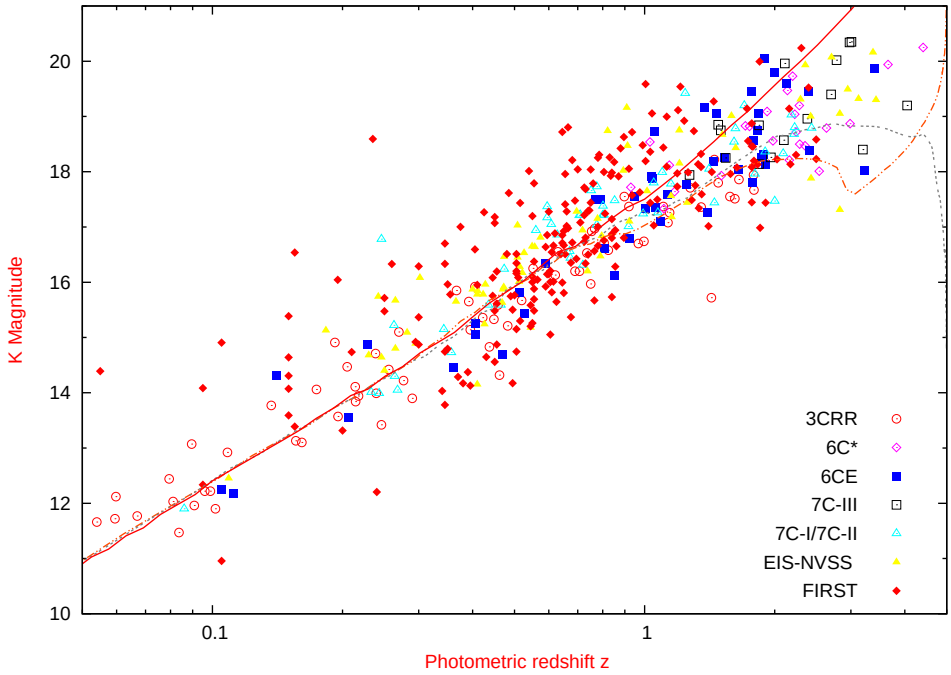

Figure 2.24: The $K - z$ Hubble diagram for radio galaxies for the 3CRR, 6CE, 6C*, 7CI/7CII, 7CIII, EIS-NVSS and NDWFS-FIRST-FLAMEX samples. Over-plotted are : a non evolution curve (red colour), instantaneous starburst (black colour) beginning at $z = 5$ (orange colour) and a starburst lasting 1 *Gyr* and starting at $z = 5$ (Jarvis et al. 2001a).

between the samples. In addition, the uncertainties in the photometric redshift estimates are large and different aperture size for photometry could affect the results. So it is interesting that the K band magnitudes with the photometric redshifts agree with Willott et al. (2003), But a more complete sample and deeper optical/infrared survey are required to investigate this further.

2.7 Summary

In this chapter I have identified FIRST radio sources in both Boötes and Cetus fields. The optical Bw R I K imaging covers an area of 9.2 deg^2 to $Bw = 26.5$, $R = 25.8$, $I = 25.5$ and $K = 19.5$ in Boötes field; and 4.7 deg^2 in Cetus field to $J = 21.4$ and $K = 19.9$. With this optical/infrared imaging, robust counterparts for FIRST radio sources have been identified based on the positional coincidence and the likelihood ratio technique (688/900 and 109/242 in Boötes and Cetus fields respectively).

Photometric redshifts have been derived for all sources optically identified in Boötes and

Cetus fields using the public code *Hyperz*. The redshift distribution of FIRST radio sources counterparts peaks at $z \sim 0.737$ with 68% of the population estimated to be at $z < 1.5$.

The photometric redshift derived for FIRST radio sources identified in Boötes and Cetus fields (based on the multi-wavelength *Bw R I J K* bands) has been used to investigate the near infrared Hubble diagram of the faint radio population at high frequency (1.4 GHz) and to a limiting flux-density of 1 mJy level. I showed that there is a remarkably tight correlation in the Hubble $K-z$ diagram of FIRST radio source counterparts in Boötes and Cetus fields. The $K-z$ relation that I obtained is similar to that obtained for brighter sources investigated by Willott et al. (2003) and Brookes et al. (2006). The $K-z$ relation for FIRST radio sources is well fitted by a second order polynomial between K magnitude and $\log_{10}\ z$ (in Boötes/Cetus fields):

$$K(z) = 17.52 + 4.34\ \log_{10}\ z + 0.86\,(\log_{10}\ z)^2. \tag{2.10}$$

A composite $K-z$ diagram of FIRST radio sources and low-frequency selected radio samples (3CRR, 6CE, 7CRS and the EIS-NVSS) with progressively fainter flux-density limits is presented. The majority of the FIRST radio population tends to lie at fainter magnitudes possibly indicating that the galaxy luminosity is correlated with radio power (Willott et al. 2003; McLure & Jarvis 2004).

The next chapter will shed light on the properties of FIRST radio sources and their host galaxies.

CHAPTER 3

Panchromatic properties of FIRST radio sources identified in Boötes and Cetus fields

3.1 Overview

This chapter investigates the general properties of FIRST radio sources identified in the NDWFS survey in both Boötes and Cetus fields. The multi-wavelength optical/infrared information of FIRST radio sources counterparts over ~ 9.2 deg^2 in Boötes field and over ~ 2.4 deg^2 in Cetus field is used. The optical/ infrared colour of the radio galaxies and quasars is investigated. The sources span a broad range of colour, with a significant number being very red ($R - K \geq 5$). The reddest populations of galaxies are of great interest for the study of galaxy formation and evolution, because they show one of the most extreme aspects in the history of galaxy formation and structure formation. A total number of 57 FIRST radio sources have been found to be associated with the so called Extremely Red Objects (EROs; $R - K \geq 5$), showing very red optical-to-near infrared (NIR) colours, either because of old populations or dust reddening. Two methods are applied here in order to separate between the two ERO populations.

3.2 Introduction

The radio sources in deep radio surveys at 1.4 GHz (20 cm) consist of two main populations; active galactic nuclei and star forming galaxies (Condon 1984; Windhorst et al. 1985). It has long been known that powerful radio sources are associated with AGN or giant ellipticals (e.g. Windhorst 1990). At mJy level and fainter, deep radio surveys at 1.4 GHz (Condon 1984; Windhorst et al. 1985; Condon 1992) have shown that the faint radio population is a mixture of different classes of objects namely: radio loud, and radio quiet AGN, starburst galaxies, and spirals. To date the nature and the level of contribution of each population is still not well established, and very little is known about the cosmological evolution of different kinds of objects despite so many studies (Hopkins et al. 1998; Richards 2000; Hammer et al. 1995; Georgakakis et al. 1999; Gruppioni et al. 1999a; Prandoni et al. 2001; Afonso et al. 2005; Bondi et al. 2003; Ciliegi et al. 2003; Hopkins et al. 2003; Seymour et al. 2004; Huynh et al. 2005; Prandoni et al. 2006; Fomalont et al. 2006; Simpson et al. 2006; Ivison et al. 2007; Bondi et al. 2007). This is mainly due to the incompleteness of optical identification and the optical depth of the spectroscopic follow up. Large, statistically complete, homogeneously selected samples, with very deep optical imaging and spectroscopic follow up are required for reasonably large and deep radio samples, in order to investigate the nature and evolution of the faint radio population.

Studies of extragalactic radio sources are among the most interesting and challenging areas of modern cosmology and astrophysics and are at the beginning of a new era. These studies have been invigorated due to the recent advent of photometric and spectroscopic large area surveys, such as NVSS (Condon et al. 1998), FIRST (Becker et al. 1995), SDSS (York et al. 2000), and 2dFGRS (Colless et al. 2001). These surveys have provided additional photometric and optical/infrared spectroscopic observations (Sadler et al. 1999; Best et al. 2005). For example, Ivezić et al. (2002), Best et al. (2005) and Obrić et al. (2006) cross correlated FIRST and SDSS, and analysed the optical and radio properties of quasars and galaxies in detail. Best (2004), studied the environmental dependence of radio luminous AGN and star forming galaxies, and their luminosity function has been investigated in other studies (Sadler et al. 1999; Jackson & Londish 2000; Chan et al. 2004; Best et al. 2005). Recent searches have been undertaken

to search for clustering of galaxies (Hall et al. 2001) and extremely red objects (EROs) around high redshift quasars and radio galaxies (Cimatti et al. 2000; Wold et al. 2003; Zheng et al. 2006, and references therein). EROs are of special interest in the study of galaxy evolution, in that their colours and other properties suggest that they are the high-redshift ($z = 1 - 2$) counterparts and progenitors of local elliptical and S0 galaxies, and are amongst the oldest galaxies present at these redshifts.

This chapter will discuss the general properties of FIRST radio sources identified in NDWFS in both Boötes and Cetus fields. The general properties of the radio/optical sample are investigated including the magnitude distributions, radio-to-optical flux ratio and colours. In particular the EROs counterparts to FIRST radio sources are classified as dusty starburts or old ellipticals.

3.3 Magnitude distribution

In the absence of spectroscopic data, the magnitude and colour distributions of the optical counterparts can be used to derive some information on the nature of faint radio sources. The apparent magnitude distribution is of cosmological interest because it it closely related to the radio source redshift distribution. Broadly speaking, the fainter a source is the more distant it is expected to be. Figure 3.1 compares magnitude distributions of sources identified in all four bands (*Bw, R, I* and *K*) in the NDWFS survey. The unshaded histogram shows the magnitude distribution of all NDWFS sources in the region in the given band, the hatched histogram displays the magnitude distribution of the FIRST radio sources identified in the given band and the filled histogram shows the magnitude distribution of the FIRST radio sources identified in all four bands *(Bw, R, I, K)*. The first observation that is apparent from this figure is the greater depth of the optical observations. The limiting magnitudes of the NDWFS data correspond to $Bw = 25.5$, $R = 25.8$, $I = 25.5$ and $K = 19.4$.

It is clear from Figure 3.1 that the magnitude distributions of the optical counterparts of the FIRST radio sources are significantly flatter than those of the global optical catalogue. Comparing the first and second histograms, one notes that the number of FIRST galaxies per magnitude interval does not continue to increase down to the magnitude limit, but rather turns over at

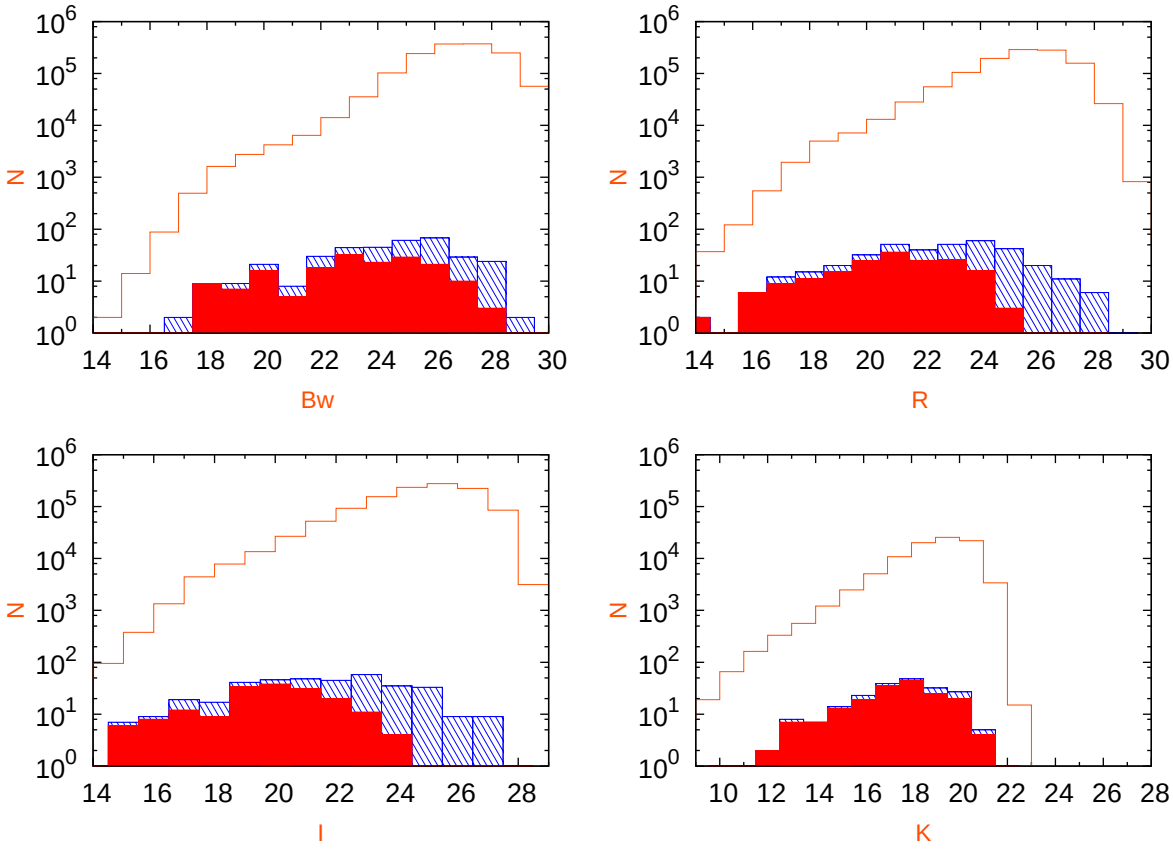

Figure 3.1: Magnitude distribution in the *Bw*, *R*, *I* and *K* band for histograms showing, from top to bottom: all sources in the NDWFS, the optical counterparts of the FIRST radio sources identified in the one band, the optical counterparts of the FIRST sources which have identifications in all four bands.

Bw ∼ 25, *R* ∼ 24, *I* ∼ 23 and *K* ∼ 18, consistent with the fact that a large fraction of the radio sources are optically identified. The turnover is ∼ 0.5 magnitudes brighter than the magnitude limit for *Bw*, about ∼ 1.5 magnitudes brighter for *R* and ∼ 2.5 mag brighter for *I* and *K*, possibly highlighting an evolution of some form in the radio source population–if the radio sources formed an homogenous class of objects present throughout the history of the universe, the numbers would continue to increase towards the magnitude limit. This turnover in the magnitude distribution of faint radio sources was initially hinted in the Leiden-Berkeley Deep Survey (LBDS) radio sample (Windhorst et al. 1984) and confirmed in the LBDS Hercules subsample (Waddington et al. 2000) and in the identification of radio sources in the Hubble Deep Field region (Richards et al. 1999). Similar results have also been obtained by Ciliegi et al. (2006) in the identification of μJy radio sources in the VVDS (VIMOS VLT Deep Survey)-VLA (Very Large Array) deep field.

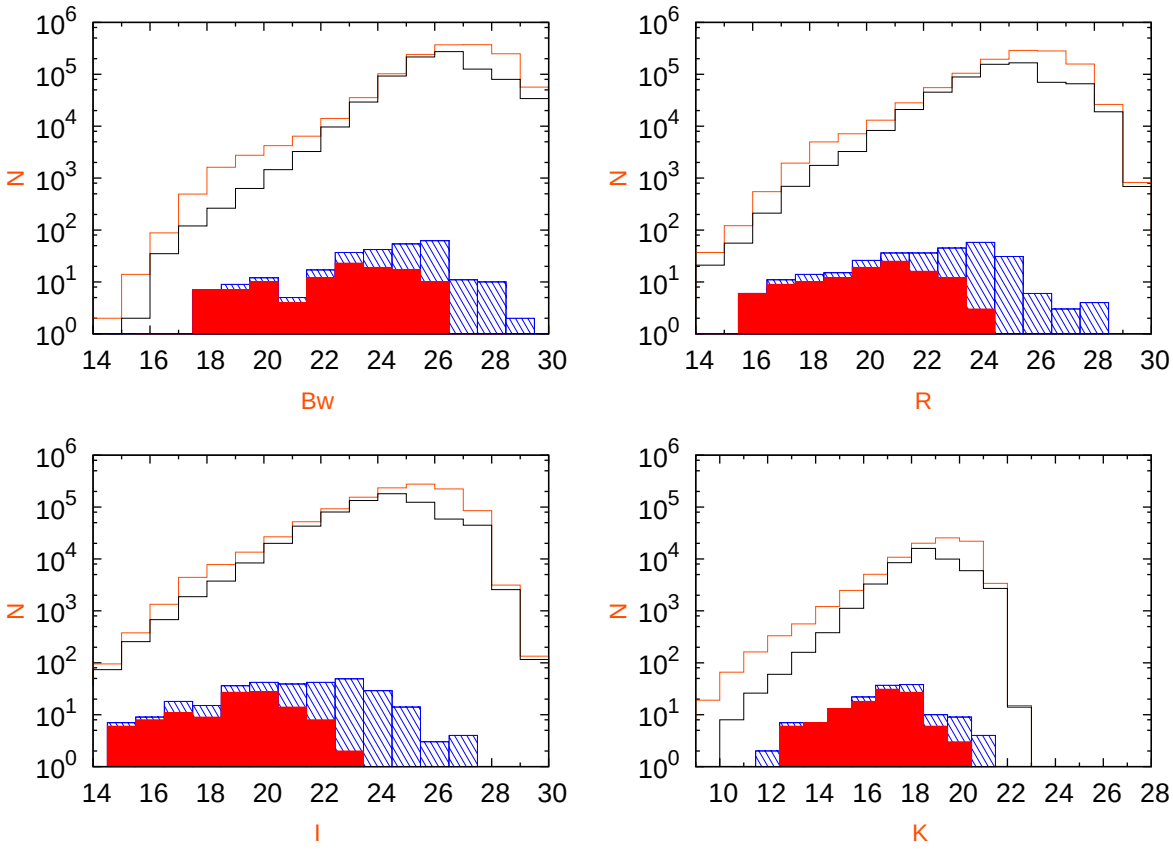

Figure 3.2: Magnitude distributions in the *Bw, R, I* and *K* bands for histograms showing, from top to bottom, all sources in the NDWFS, sources in the NDWFS which are extended (have stellarity index < 0.7), the extended optical counterparts of the FIRST radio sources identified in the one band, the extended optical counterparts of the FIRST sources which have identifications in all four bands.

In Figure 3.2, the magnitude distribution of FIRST radio sources which are resolved in the NDWFS (have a SExtractor stellarity parameter of less than 0.7) is investigated. From top to bottom, the histograms show the distributions for (i) all NDWFS sources in the region in the given band, (ii) for all the NDWFS sources in the region with galaxy identifications in the given band, (iii) the FIRST sources identified in the given band and (iv) the FIRST sources identified in all four bands (*Bw, R, I, K*). Comparing the top two histograms, one sees that fainter sources are less likely to be characterised as galaxies, presumably because it is difficult to resolve more distant and intrinsically fainter sources, otherwise the trends are similar to those seen in Figure 3.1.

It is interesting to note that in Waddington et al. (2001) 54 out of 72 sources (75%) have *K*-band matches with $K < 19.4$ while only 41% of sources are identified here. This supports the claim that studying areas larger than $\sim$1 deg^2 is required to get a fair sample of mJy sources and is perhaps to be expected when one considers that radio sources are clustered. One should also note that, the low identification rate of FIRST radio sources in NDWFS survey could be mainly due to the incompleteness of the NDWFS survey. The *K* band catalog is not as deep as the optical catalog (there is no *K* band data for the first strip and the other strips are partially covered).

3.4 Magnitude - flux distribution in Boötes field

In chapter 2, optical/infrared counterparts have been identified for 688 of 900 FIRST radio sources either in one band or more, 338 are identified in *K* band, and 273 FIRST radio sources have identifications in four bands (*Bw, R, I, K*). The FIRST radio source counterparts were divided into galaxies and stellar-like objects by means of the SExtractor Class-Star parameter S/G (Bertin & Arnouts 1996). This parameter is provided by the NDWFS catalogue and ranges from 0.0 to 1.0 being the most point like. Of the 273 IDs in four bands (*Bw, R, I, K*), 243 sources were identified as galaxies and 30 sources identified as stellar-like objects. Combining the analysis of the radio and photometric properties can provide a first indication of the nature of the faint radio population. Figures 3.3, 3.4, 3.5 and 3.6 show the 20 cm radio flux versus *Bw, R, I* and *K* magnitudes respectively for all FIRST radio sources with an optical/infrared

identification. Superimposed are the lines corresponding to constant values for the observed radio-to-optical ratio, r, defined by Condon (1980) as follows:

$$r = S \times 10^{0.4\,(m-12.5)}, \tag{3.1}$$

where S is the 1.4 GHz flux in mJy and m is the apparent magnitude of the optical/infrared counterparts in a given band.

The filled circle in both Figures 3.5 and 3.6 represents a radio-loud quasar (J142738.5+3312) discovered by McGreer et al. (2006) as a counterpart to FIRST radio sources by combining NDWFS and FLAMEX data. A radio-loud source is considered to have $r > 10$ (Urry & Padovani 1995). Magliocchetti & Maddox (2002) showed that for star-forming galaxies, $r < 100$. Therefore, the *Bw* magnitude flux diagram (Figure 3.3) shows that there are a few star-forming galaxies in the FIRST-NDWFS/FLAMEX sample down to 1 mJy. Previous studies reported that the star-forming galaxies dominate the sub-mJy population. For example, Gruppioni et al. (1999b), in the study of the Marano field, Georgakakis et al. (2005) in the Phoenix survey and Magliocchetti & Maddox (2002) in the FIRST-APM sample. This is not necessarily true, this is controversial issue and radio quiet AGN may form a significant fraction (see i.e. Simpson et al. 2006; Wilman et al. 2008).

It is interesting to note that the radio population of radio galaxies is shifting towards brighter red magnitudes, highlighting the fact that faint radio galaxies are typically early-type objects with red colours (see section 3.5). The same effect is not seen for the stellar-like identifications, possibly suggesting that the stellar-like population is not changing as rapidly as the radio galaxy population. Figure 3.7 displays the $Bw - R$ colour as a function of radio flux $S_{1.4}$ for the two populations: resolved sources (empty squares) and stellar-like objects (filled diamonds). The $Bw - R$ colour is an interesting diagnostic of a possible emission mechanism for the faint radio population. A relatively blue colour could be an indication of star-forming galaxies, whilst a relatively red colour is consistent with both old passively evolving distant elliptical galaxies and dust-reddened starbust galaxies. It is clearly seen from the figure that the majority of FIRST radio source counterparts consist of galaxies with very red colours, up to $Bw - R \sim 4.6$. One also notes that radio galaxies appear mostly with $Bw - R > 1$, and stellar-like objects (mainly

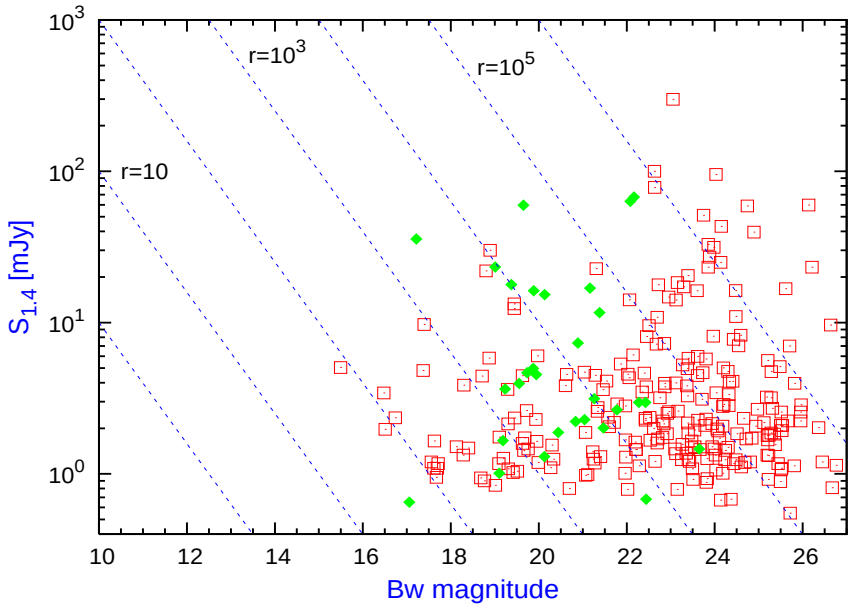

Figure 3.3: The radio flux vs. *Bw* magnitude for all FIRST radio sources identified in Boötes field. Empty squares represent sources identified as galaxies, filled diamonds indicates sources identified as point-like objects. Superimposed are the lines corresponding to constant values of the radio-to-optical ratio $r = 10, 100, 10^3, 10^4 ... 10^6$

QSOs with blue colour) dominate the region $0 < Bw - R < 1$ leaving a very small fraction of radio galaxies with blue colour ($Bw - R < 0$) characteristic of star-forming galaxies, although most star-forming galaxies actually have colours in the range $0 < Bw - R < 1$. The same results have been reported by Magliocchetti & Maddox (2002) and Magliocchetti et al. (2004) in the radio-optical study of the FIRST radio sources in the APM survey and 2dFGRS respectively.

Figure 3.8 presents colour-magnitude and colour-colour diagrams for the FIRST radio source counterparts. The stellar-like objects tend to have bluer optical colour than the galaxies. These sources are likely to be quasars in which the optical light is dominated by a central AGN– here the classification is based on morphology and not colour. A total number of 73 FIRST radio sources that are identified in the NDWFS are spectroscopically identified in the SDSS survey. There are 16/73 FIRST radio sources spectroscopically classified as quasars and 57/73 as galaxies. These are shown by circles on Figures 3.7 and 3.8 (galaxies in blue and quasars in magenta).

Figure 3.8 shows that the galaxy and quasar populations occupy a well defined region in colour-magnitude and colour-colour space and, although there is some overlap, there clearly exist large areas of colour space in which an unambiguous classification can be made. In both

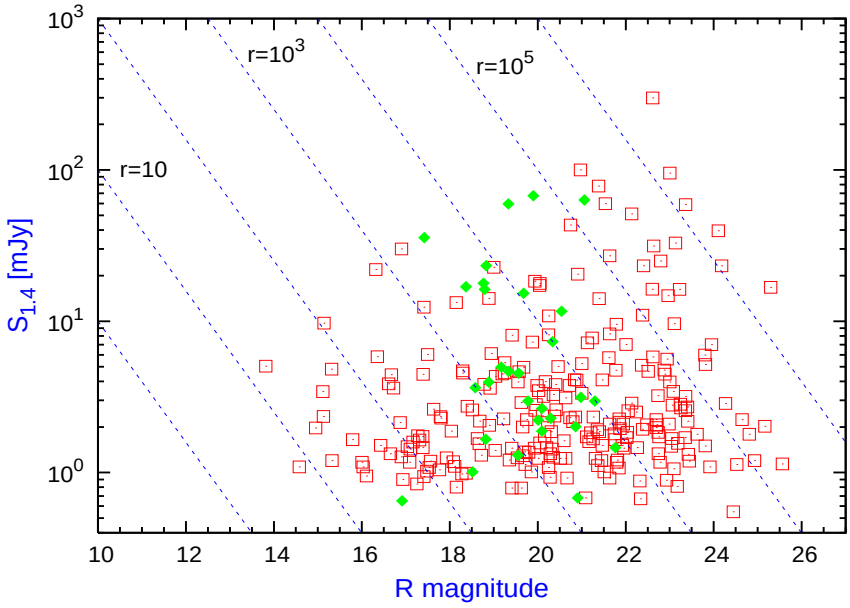

Figure 3.4: The radio flux vs. *R* magnitude for all FIRST radio sources identified in Boötes field. Empty squares represent sources identified as galaxies, filled diamonds indicates sources identified as point-like objects. Superimposed are the lines corresponding to constant values of the radio-to-optical ratio $r = 10, 100, 10^3, 10^4 ... 10^6$

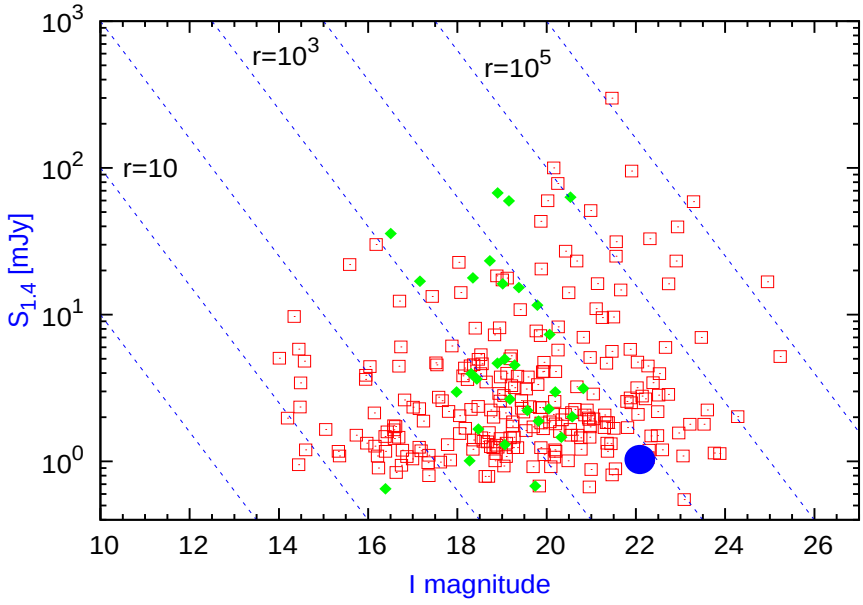

Figure 3.5: The radio flux vs. I magnitude for all FIRST radio sources identified in Boötes field. Empty squares represent sources identified as galaxies, filled diamonds indicates sources identified as point-like objects and the large filled circle represents a radio-loud quasar (McGreer et al. 2006). Superimposed are the lines corresponding to constant values of the radio-to-optical ratio $r = 10, 100, 10^3, 10^4 ... 10^6$

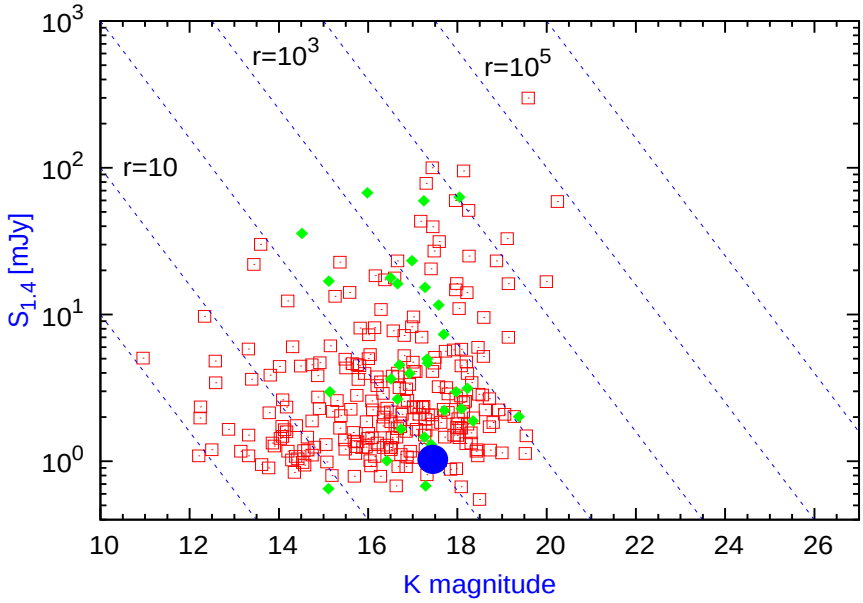

Figure 3.6: The radio flux vs. K magnitude for all FIRST radio sources identified in Boötes field. Empty squares represent sources identified as galaxies, filled diamonds indicates sources identified as point-like objects and the large filled circle represents a radio-loud quasar (McGreer et al. 2006). Superimposed are the lines corresponding to constant values of the radio-to-optical ratio $r = 10, 100, 10^3, 10^4 ... 10^6$

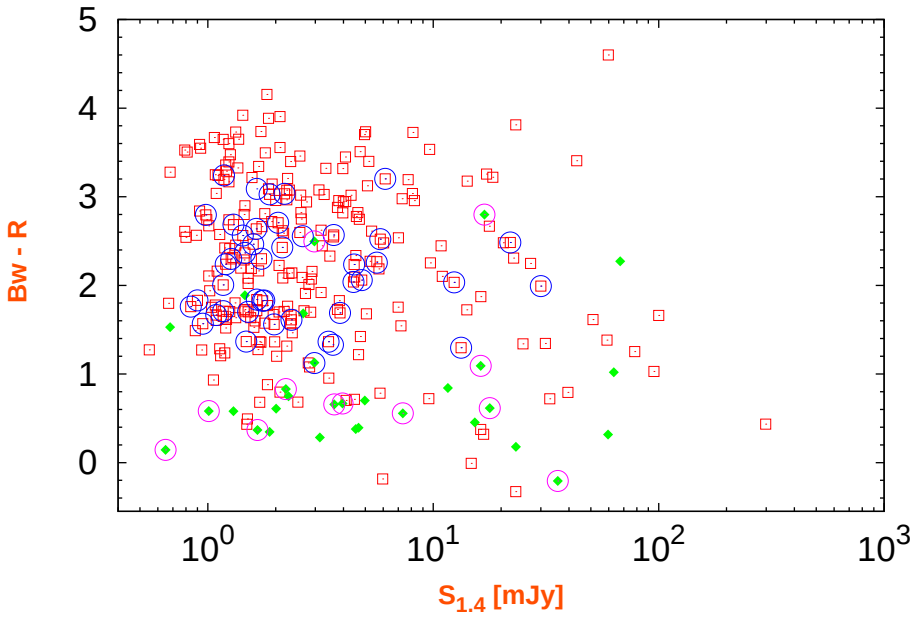

Figure 3.7: The Colour $Bw - R$ versus radio flux for all FIRST radio sources counterparts. Filled diamonds indicate sources identified as galaxies while empty squares represents stellar-like objects. Circles denotes sources spectroscopically identified in SDSS survey (galaxies in blue and quasars in magenta).

$Bw - R$ vs R and $Bw - R$ vs K diagrams the two populations are well separated over the range $R = 17 - 22$ and $K = 15 - 18$. But at fainter K and R magnitudes, the two populations become intermeshed, the $Bw - R$ colour of quasars begin to increase, while for galaxies it decreases once the 4000 Å break has been shifted out of the optical region. This is in sharp contrast to the situation in the $R - K$ vs K diagram where the two populations appear to diverge as K increases (see Figure 3.12 in section 3.6). Figure 3.8 also displays the colour-colour diagrams $Bw - R$ vs $R - I$, $R - I$ vs $I - K$, $Bw - I$ vs $I - K$, $Bw - R$ vs $R - K$. An important feature of these diagrams is that they provide an effective quasar/galaxy separation. As clearly seen from the figure the colour-colour diagrams $Bw - R$ vs $R - K$ and $Bw - I$ vs $I - K$ tend to be a good separator of the two populations with little overlap.

3.5 Properties of FIRST radio sources in the Cetus field

Cross correlating the FIRST radio sources with sources in Cetus field yielded 113/242 counterparts in the J band, 124 radio sources identified in the K band and 109 sources identified in two bands (J, K; see chapter 2). Figure 3.9 illustrates the magnitude-flux diagram for the FIRST radio sources identified in J (red empty squares) and K (green filled diamonds) bands. It is noted again that there exists an interesting shift of the population towards brighter magnitude with a small number of sources that have a radio-to-optical ratio in J band of $r \leq 100$.

Figures 3.10 and 3.11 illustrate the $J - K$ colour against K magnitude and photometric redshift respectively. There are 15 counterparts to FIRST radio sources in this field that have a red colour $J - K > 2.3$ which selects the so-called Distant Red Galaxies (DRGs, Franx et al. 2003) This latter set in turn constitutes an heterogeneous sample of galaxies going from passively evolving systems to a significant fraction of obscured star forming galaxies at $2 < z < 4.5$ with strong Balmer or 4000 Å breaks. As a comparison, Hall et al. (2001) select four galaxies with $J - K > 2.5$ with photometric redshifts $z \geq 2$, Franx et al. (2003) found 14 DRGs with $J - K > 2.3$ in a photometric redshift range from 1.92 to 4.26 (see also Takagi et al. 2007; Papovich et al. 2006).

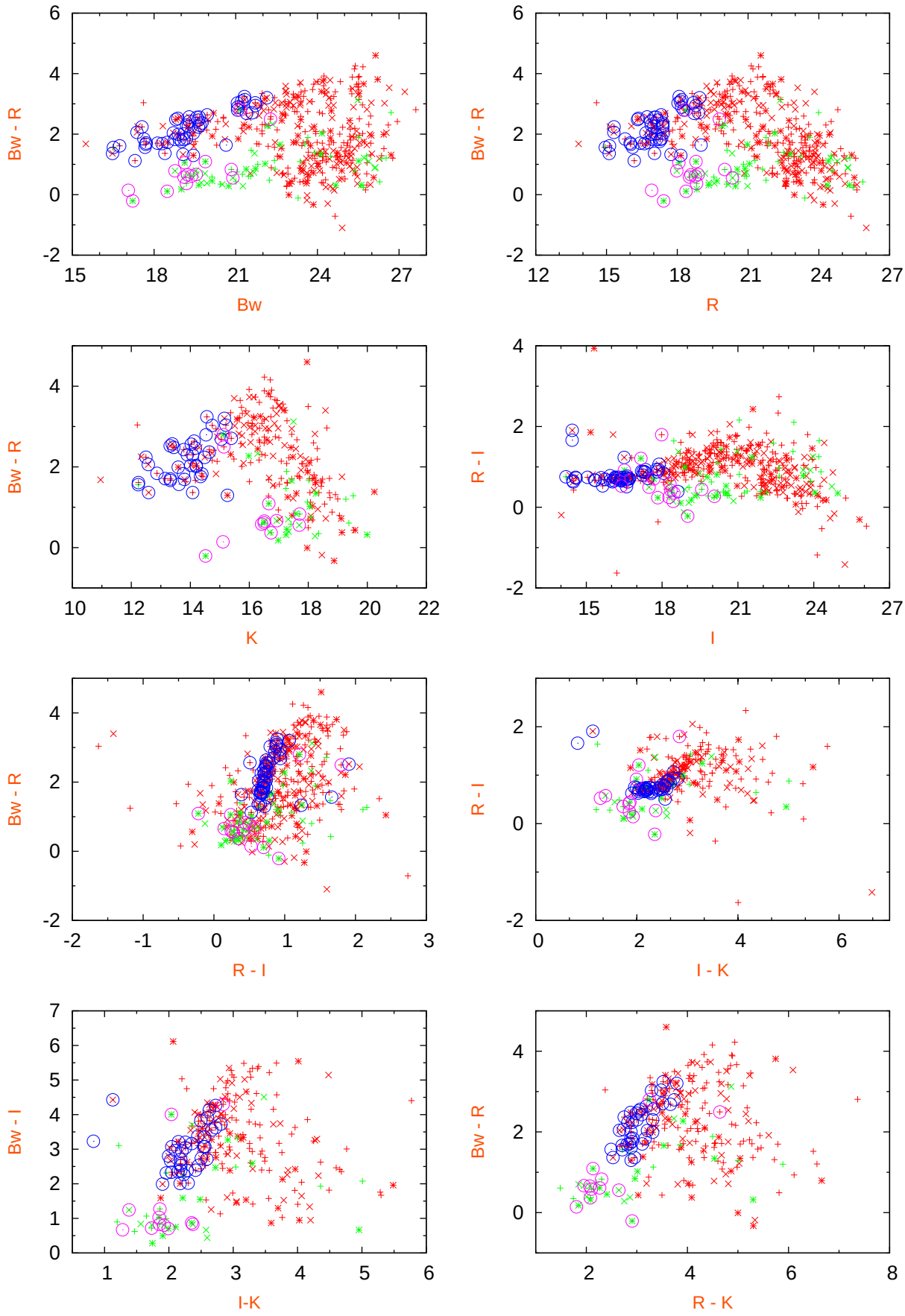

Figure 3.8: Colour-magnitude and colour-colour diagrams for the FIRST radio sources counterparts. Red symbols indicate galaxies and green symbols represent stellar-like objects (Q). Circles denote sources spectroscopically identified in the SDSS. Plus signs indicate sources with $1 < S_{1.4\ \mathrm{GHz}} \leq 3$, crosses represent sources with $3 < S_{1.4\ \mathrm{GHz}} \leq 10$ and stars denote sources with $S_{1.4\ \mathrm{GHz}} > 10$. The flux density $S_{1.4\ \mathrm{GHz}}$ is in mJy.

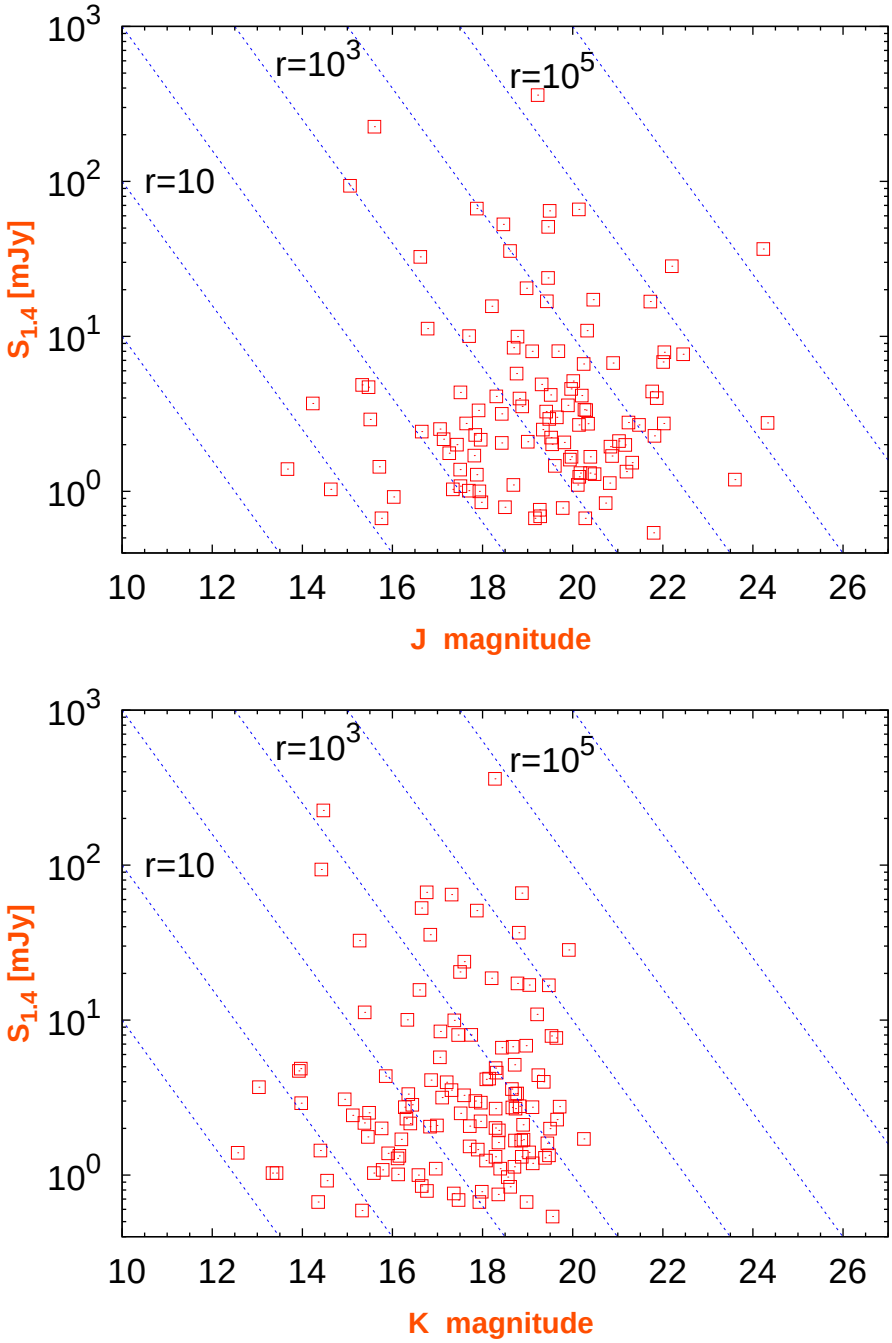

Figure 3.9: The radio flux vs. the magnitude for FIRST radio sources identified in Cetus field, in J band (top panel) and K band (bottom panel). Dashed lines correspond to constant values of the radio-to-optical ratio $r = 10, 100, 10^3, 10^4 ... 10^6$

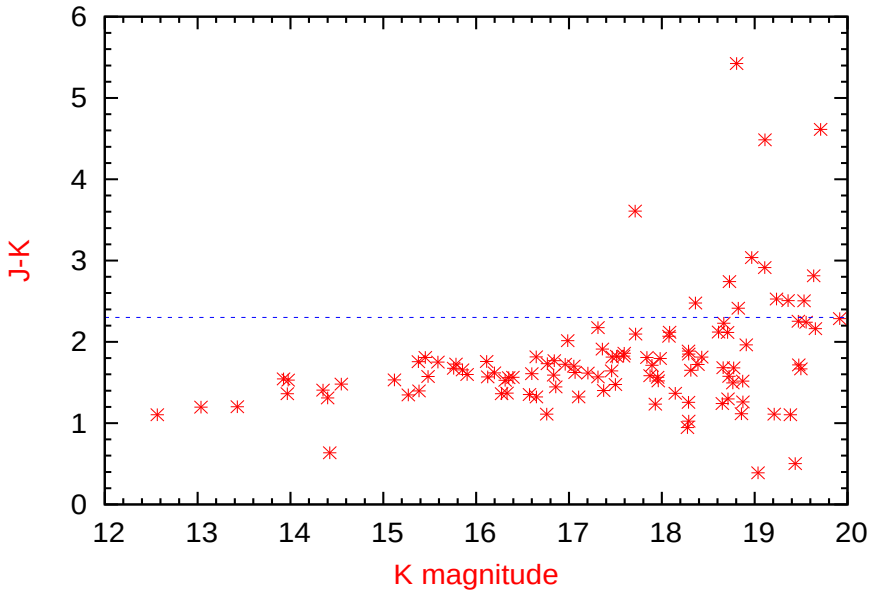

Figure 3.10: The colour magnitude sequence for all FIRST radio sources identified in Cetus field.

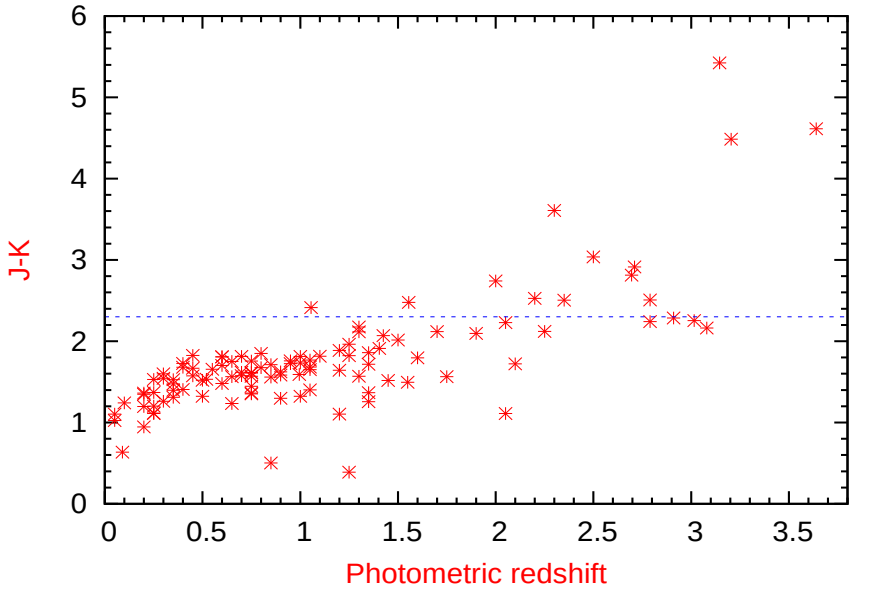

Figure 3.11: The $J-K$ colour against photometric redshift for all FIRST radio sources identified in Cetus field.

In the FIRST - Cetus sample, there are 3/15 DRG counterparts to FIRST radio sources at lower redshift ($1 \leq z \leq 2$), and 8/15 with photometric redshift ranging from 2 to 3.8 and $17 < K < 20$. Papovich et al. (2006) reported that lower redshift objects are dominated by dusty star bursts and higher redshift are objects with more complex stellar populations, these are likely to be passively evolving stellar components. Obviously spectroscopic confirmation is required before one can draw any conclusion from these results.

3.6 Extremely red objects counterparts to FIRST radio sources in Boötes field

Extremely red objects were first discovered more than 20 years ago (Elston et al. 1988) as resolved galaxies with $K \sim 16.5$ and $R - K \sim 5$; photometry and spectroscopy showed that these objects were old elliptical galaxies at $z = 0.8$ (Elston et al. 1989). EROs seem to be found everywhere; they are found in the vicinity of high redshift AGN (McCarthy et al. 1992), in a quasar field (Stockton et al. 2006; Hu & Ridgway 1994), as counterparts of faint X-ray sources (Newsam et al. 1997) and as counterparts of radio sources (Smail et al. 2002; Willott et al. 2001; De Breuck et al. 2002; Spinrad et al. 1997). Their colours are consistent with two heterogenous mix of galaxy classes: 1) Old, passively evolving elliptical galaxies at $z \geq 0.9$ where the colour is due to the lack of star formation and the large *k*-correction, 2) dust reddened star-forming galaxies or AGN (see e.g. Cimatti et al. 2003; Wold et al. 2003; Yan & Thompson 2003; Daddi et al. 2002; Smail et al. 2002; Roche et al. 2002). The identification of either type offers a potentially important deep insight into the formation and evolution of elliptical galaxies and helps to investigate the existence of a population of dusty galaxies of AGN strongly reddened by dust extinction.

Techniques to distinguish the different extragalactic ERO types include near-infrared photometric classification (Pozzetti and Mannucci 2000, Mannucci et al. 2002, Pierini et al. 2004), morphological tests (Yan et al. 2000, Yan et al 2003, Moriondo et al 2000), and an increasing number of spectroscopic discriminators (Cimatti et al. 2002, Smith et al. 2001). Near-infrared

spectroscopy of 9 EROs ($R-K>5$ and $K<19.0$) by Cimatti et al. (1999) showed neither strong emission lines nor continuum breaks. Two of their observed EROs were classified as dusty starburst candidates, because they require strong dust reddening to produce the observed global spectral energy distributions. A large sample of 30 EROs with $K \leq 19.2$ showed an almost equal distribution between old ellipticals and star-forming galaxies (Cimatti et al. 2002).

Several selection criteria have been defined for EROs, including $R-K \geq 6$, $R-K \geq 5.3$, $R-K \geq 5$ and $I-K \geq 4$ (e.g. Cimatti et al. 1999; Abraham et al. 2004, and references therin) with K-magnitude upper limits from 18 to 21 mag. All these criteria are designed to find evolved galaxies at high redshift (Cimatti et al. 1999; Abraham et al. 2004; Pozzetti & Mannucci 2000). The limit of $R-K=5$ is adopted as the definition of an ERO here. Based on this, 57 (19%) FIRST radio sources were found to have an ERO as counterpart with $R-K \geq 5$ and $16.5 \leq K \leq 20$. This fraction includes sources that have identifications in five bands (*Bw, R, I, J, K*), four bands (*Bw, R, I, K*) or less (i.e. three bands (*Bw, R, K*) or (*R, I, K*), or 2 bands (*R, K*)). A total number of 34 FIRST radio are identified in K band but not in R band, these sources are also EROs with a $R-K>7$. We will only examine the properties of EROs with identifications in R and K bands. As a comparison with ERO samples that are based on the criteria $(I-K) \geq 4$, 41 EROs were found as counterparts to FIRST radio sources, and 33 of the $(R-K) \geq 5$ EROs have $(I-K) \geq 4$. It is obvious that the R and I bands selection criteria for EROs are not equivalent. There are more $R-K \geq 5$ EROs than $I-K \geq 4$ selected ones. Figures 3.12 and 3.13 show the $R-K$ versus K and $I-K$ versus K colour-magnitude diagram respectively for FIRST radio sources with IDs in both R and K bands (305 sources). These figures show that there are no stellar-like objects (empty diamonds) that have a colour redder than $R-K \geq 5$. A total number of 30/57 sources appear to have a magnitude $K \leq 18$ and 27/57 with a magnitude $K>18$. Figure 3.14 shows the K band magnitude distribution (left panel) and photometric redshift distribution (right panel) of all 57 EROs. The median K band magnitude of these 57 EROs is $K=19.27\pm0.72$ and is equal to $K=17.97\pm0.71$ when sources with $z>2$ excluded.

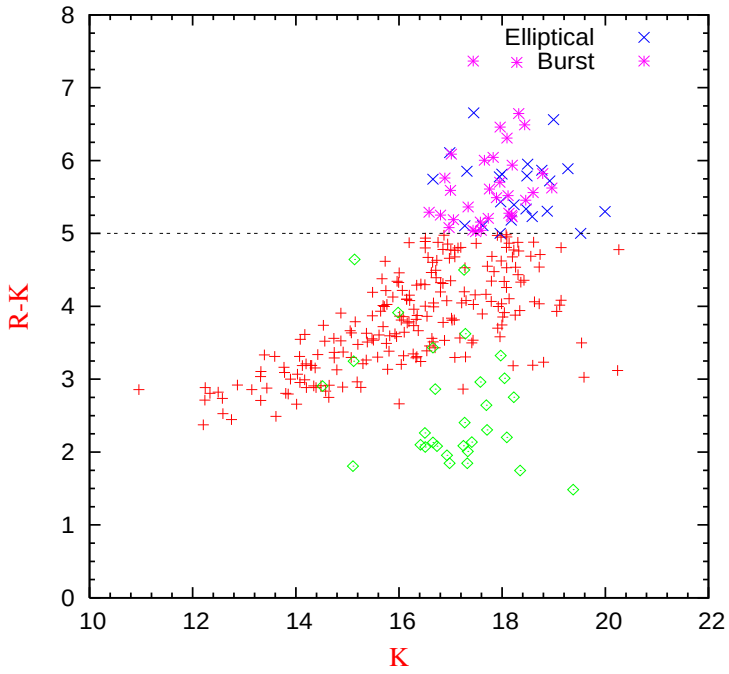

Figure 3.12: The K band magnitude vs. the $R - K$ colour. Empty diamonds indicate stellar-like objects, while the remaining crosses, stars and plus symbols indicate objects identified as galaxies. The horizontal long-dashed line corresponds to the limit adopted for the selection of the sample of ERO counterparts to FIRST radio sources in Boötes field.

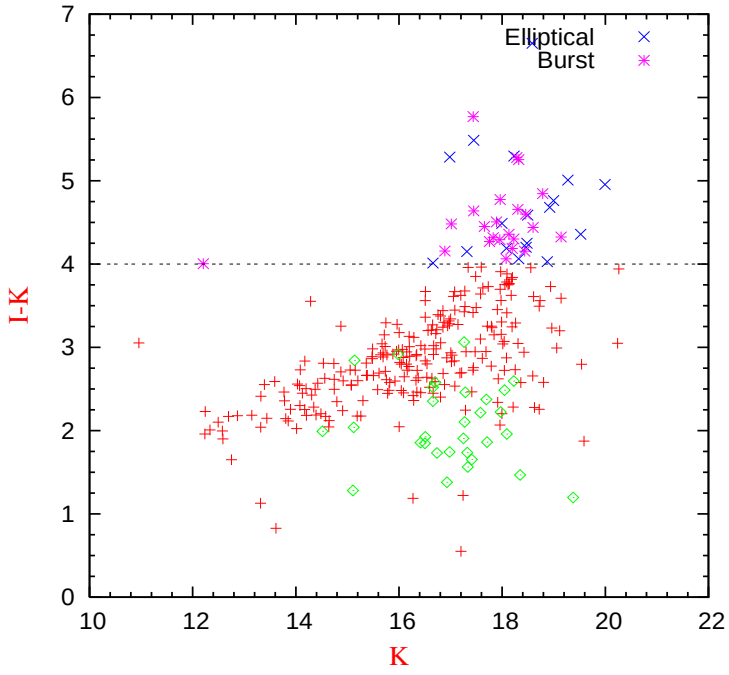

Figure 3.13: The K band magnitude vs. $I - K$ colour. Empty diamonds indicate stellar-like objects, while the remaining crosses, stars and plus for objects identified as galaxies. The horizontal long-dashed line corresponds to the limit adopted for the selection of the sample of ERO counterparts to FIRST radio sources in Boötes field.

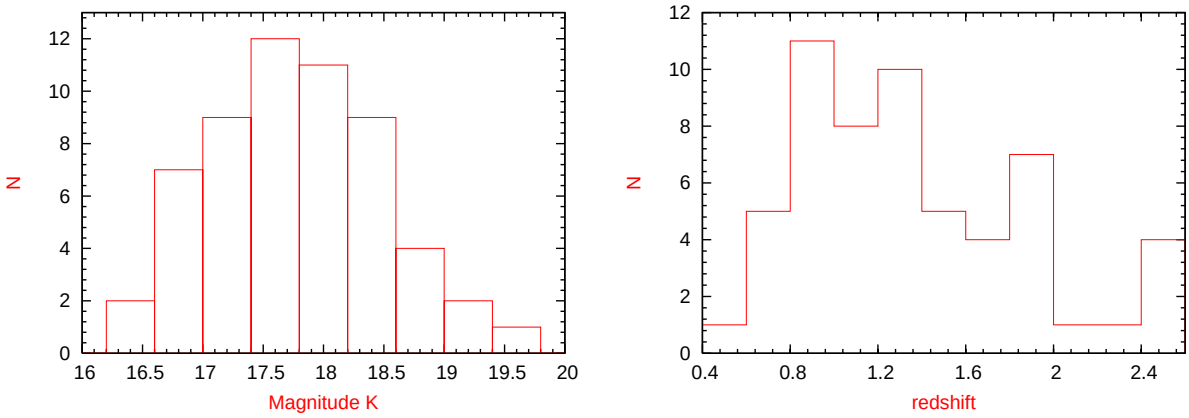

Figure 3.14: The photometric redshift and *K* band magnitude distribution for the 57 ERO counterparts (in Boötes field) in left and right panels respectively.

3.6.1 Colour-colour separation

Since EROs are composed of both passively evolving red galaxies and dusty starburst galaxies, colour is one means of breaking the degeneracy between these two groups. The SED of an elliptical galaxy at $z \sim 1$ drops off sharply at the restframe 4000 Å break between *R* and *K* bands, while the SED of a dusty starburst galaxy declines more gradually because of reddening. Therefore observations between the *R* and *K* bands, such as *I, z, J* or *H* can be used to measure the sharpness of the spectral type break and thus discriminate between these two scenarios (Pozzetti & Mannucci 2000). The $J - K$ separates EROs at $z > 1$ to bluer early type galaxies and to redder dusty EROs. As there is no *J* band data for all FIRST radio sources IDs (counterparts) I used only the EROs counterparts of FIRST radio sources identified in the second strip ($33^\circ \leq \delta < 34^\circ$) where the *J* band data are available from FLAMEX. There are 30 EROs in this strip of which 25/30 were detected in J band.

The photometric method introduced by Pozzetti & Mannucci (2000) is adopted here in order to investigate the colours of the ERO counterparts to FIRST radio sources in Boötes field. Pozzetti & Mannucci (2000) convolved a range of models and observed galaxy spectral energy distributions with *R, I, J* and *H* filters and proposed that elliptical galaxies and dusty starbursts could be separated in the $I - K$ versus $J - K$ plane and the $R - K$ versus $J - K$ plane (see also Mannucci et al. 2002). The Pozzetti & Mannucci (2000) classification criterion for EROs

defines the separation line as follows:

$$J - K = 0.36\,(I - K) + 0.46, \tag{3.2}$$

$$J - K = 0.34\,(R - K) + 0.19, \tag{3.3}$$

$$J - K = 0.33\,(H - K) + 0.20. \tag{3.4}$$

Figure 3.15 (top panel) shows the $R - K$ versus $J - K$ colour-colour scheme introduced by Pozzetti & Mannucci (2000), where elliptical galaxies lie to the left (bluer $J - K$), and dusty starburst lie to the right (redder $J - K$ colour). There are 7/25 (18%) EROs selected in the dusty starburst side of the indicator line and 18/25 (72%) appear to be elliptical galaxies.

Bergstrom & Wiklind (2004) also attempted to separate the two population using the $R - J$ vs $J - K$ colours as follows:

$$J - K = 0.34\,(R - K) + 0.19, \tag{3.5}$$

$$J - K = 0.33\,(H - K) + 0.20. \tag{3.6}$$

The bottom panel in Figure 3.15 shows the colour-colour scheme introduced by Bergstrom & Wiklind (2004) using the $(R-J)$ colour vs. $(J-K)$ colour. The results are totally consistent with the fraction emerging from Pozzetti & Mannucci (2000) $R - K$ vs $J - K$ method. However the agreement was not as good between the classification using the SED template fitting method and the optical/near-infrared colours of the sample. There are 11 sources (with $\chi^2 < 2.7$) classified as burst using *Hyperz* and classified as elliptical in the colour-colour diagram. This will be discussed further in the following section.

3.6.2 Photometric classification of EROs

As a second way to classify an ERO sample as passively evolving red galaxies, or dusty starburst galaxies, *Hyperz* was used to find the best-fit empirical galaxy template by comparing the ERO colours to two different families of SEDs: From dusty, young starburst (or AGN) or

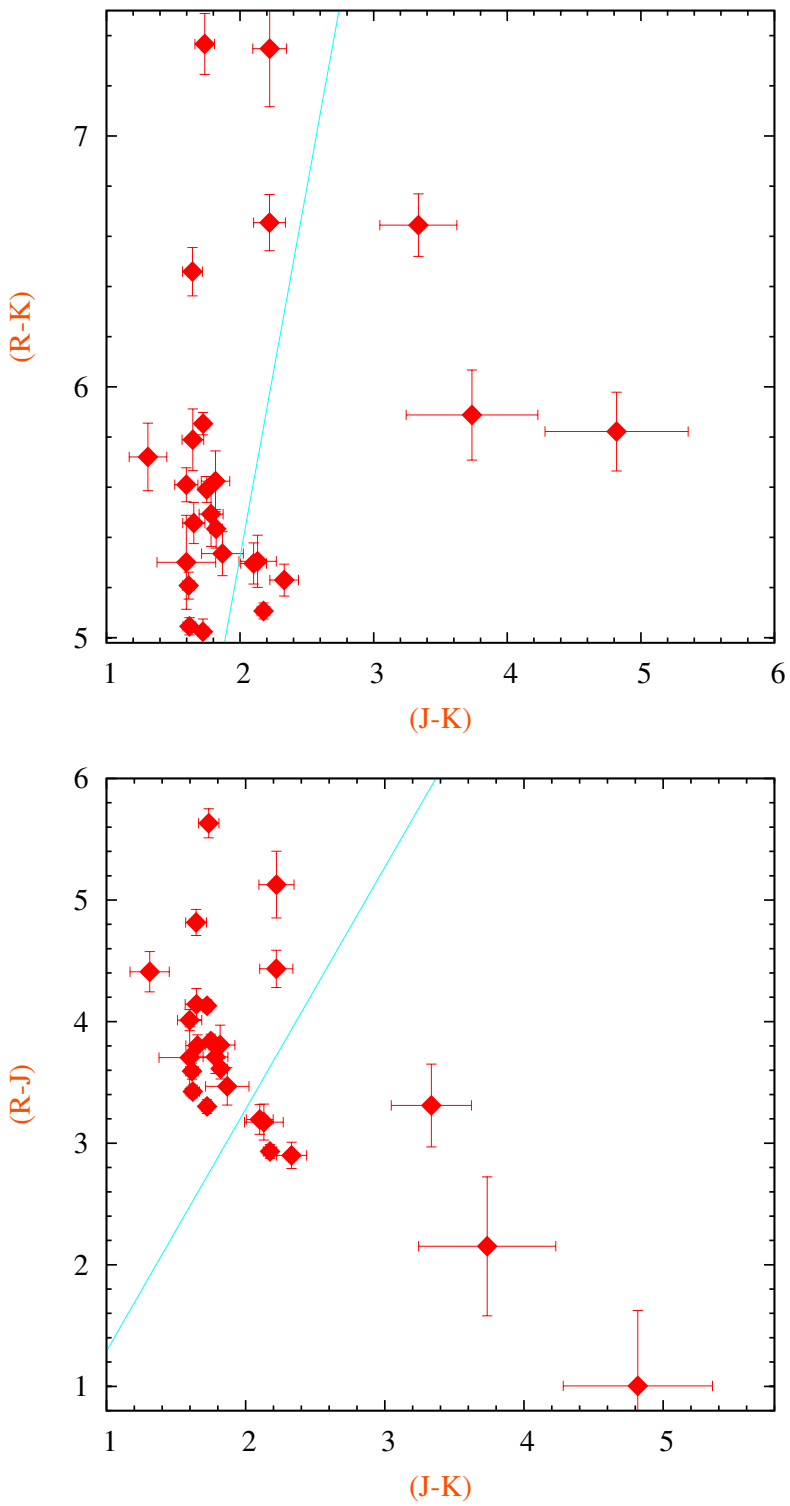

Figure 3.15: the top panel shows the $R-K$ against $J-K$ colour-colour diagram as proposed by Pozzetti & Mannucci (2000) for the 25 counterparts of FIRST radio sources that have J band data. Bottom panel shows the $R-J$ against $J-K$ scheme introduced by Bergstrom & Wiklind (2004). In both diagrams, the solid lines represent the boundary between dusty starburst and evolved, passive magnitude EROs: the dusty galaxies should lie to the right of the line (redder $(J-K)$ colours) with the evolved systems on the left.

almost dust free evolved systems. For the dusty starburst galaxies a continuous star formation model is adopted and the reddening (A_v) ranges between 1 and 4 (Cimatti et al. 2003). For the evolved galaxies, a model SED represented by an exponentially decaying star formation rate with e-folding time of 1 Gyr is adopted. The reddening for this model is required to be $A_v < 0.5$. For these model fits the Calzetti et al. (2000) reddening law is used. Since there are no *J* band data for all the sources, *Hyperz* was run for two samples: the first sample included only ERO counterparts to FIRST radio sources that have *J* band data (provided by FLAMEX; $33^\circ \leq \delta < 34^\circ$). There are 25/57 sources with *J* data and 20/25 detected in 5 bands (*Bw, R, I, J, K*) in this sample. The second sample contains 27/57 that do not have *J* band data (third and fourth strips ; $34^\circ \leq \delta < 36^\circ$) and 17/27 identified in four bands (*Bw, R, I, K*). The photometric redshift predictions of the three fits (E, Burst, all BC SED templates (E, Burst, S0, Sa, Sb, Sd)) are shown in Table 3.1. Table 3.1 presents the object name, 1.4 GHz radio flux density, colours ($R - K$ and $J - K$), the *K* band magnitude, photometric redshift and best fitting SED (either starburst or elliptical) of all ERO counterparts to FIRST radio sources.

One of the dusty sources is assigned redshift $z < 0.8$ ($z = 0.605$) lower than that expected for EROs. I note that the best-fit elliptical template has a lower photometric redshift than the best-fit starburst template. The mean photometric redshift is $z = 1.35$ and the rms scatter in the photometric redshift predictions for these three fits is $\sigma_z < 0.51$; the photometric redshifts are thus quite robust and show clearly that these EROs are $z \geq 0.8$ galaxies (except two sources, one at $z = 0.605$ classified as a dusty source using the colour-colour plot and the second one at $z = 0.55$ also classified as a dusty source with a high probability according to the template fitting). When all the SED templates are allowed, 14/57 sources cannot provide an acceptable fit (giving $\chi^2 > 2.7$), 11/57 are classified as elliptical and 31/57 as starburst. When the elliptical galaxy option is chosen 28/57 have $\chi^2 < 2.7$ and 22/57 have $\chi^2 > 2.7$ when the starburst option is chosen. One notes that broad band photometry alone cannot provide reliable information on the spectral type due to the degeneracy between age, metallicity and reddening (see Figure 1 in Bolzonella et al. 2000). Nevertheless it provides a rough SED classification at two extremes: a given object has “blue” or “red” continuum at a given *z*. As mentioned previously in chapter 2, the late type galaxies can be matched with elliptical or burst templates. These SEDs are nearly

identical (Bolzonella et al. 2000) and the best-fit *Hyperz* 'starburst' templates are evolved results of instantaneous bursts and not really dusty star-forming galaxies .

3.7 Summary

This chapter has investigated some properties of the faint radio population at the mJy level by making use of a sample of objects drawn from the joint use of the FIRST survey and the NDWFS/FLAMEX surveys introduced in chapter 2.

The population of faint radio sources is mainly dominated by early type galaxies, with radio-to-optical flux ratios between 10^2 and 10^6 and a very red colour, confirming the results found by Magliocchetti et al. (2002) who studied the optical counterparts of FIRST radio sources in the APM survey to a limiting magnitude $Bw \sim 21$ and $R \sim 20$.

A total number of 13 DRGs are found to be counterparts to FIRST radio sources in Cetus field with $J-K > 2.3$ and K magnitude < 20. Obviously deep optical imaging and spectroscopy is required to further investigate the nature of these DRGs.

Taking advantage of the infrared data provided by the FLAMEX survey in J and K bands, 91 FIRST radio sources (in Boötes field) are found to be associated with EROs with $R-K \geq 5$ (34 Firstradio sources are not identified in R band and identified in K band). Using the $J-K$ vs. Optical infrared colour-colour diagram of (Pozzetti & Mannucci 2000) to separate EROs into passively evolving and dusty star-forming galaxies, 18/25 (72%) of EROs are found to be early type galaxies with $z = 0.6-2$, 7/25 (28%) dusty star-forming galaxies, and 3/7 EROs from this latter are DRGs with $J-K > 2.3$. One should note that the total number of DRGs found in Boötes is smaller than the one found in Cetus field. This is mainly due to the samll area imaged in J band (only the second strip is covered in Boötes field) and also to the shallow K band imaging. Deep imaging are required in order to investigate this latter.

Table 3.1: Photometric redshift results for ERO sample. Col (1) Object name, col (2) flux density of each radio source, cols (3)and (4) colours, cols(5)-(6): best-fit photometric redshift and χ^2_ν for a Gissel 98 elliptical galaxy, cols(7)-(8): best-fit photometric redshift, X^2_ν for a Gissel 98 starburst model; cols (9)-(10): best-fit photometric redshift and χ^2_ν when all SED templates are included (E, burst, S0, Sa, Sb, Sc, Sd, Im) for a Gissel 98 elliptical galax, cols (11) best fit SED template.

				All SED		Starburst		Elliptical		
Object name	$S_{1.4}$	$R-K$	$J-K$	z	χ^2_ν	z	χ^2_ν	z	χ^2_ν	SED
(1)	(2)	(3)	(4)	(5)	(6)	(7)	(8)	(9)	(10)	(11)
J142439.6+3349	2.71	5.43	1.82	1.075	0.26	1.220	0.46	1.050	0.23	E
J142449.3+3343	2.02	5.89	3.73	2.435	0.61	2.445	4.63	1.395	3.86	E
J142525.2+3345	4.66	5.02	1.72	1.345	0.20	1.345	0.21	1.135	2.38	Bst
J142611.0+3339	1.70	5.30	2.10	0.880	0.36	1.215	1.56	1.030	1.64	SO
J142616.8+3309	1.09	5.46	1.65	1.800	0.85	1.800	0.85	1.255	5.97	Bst
J142643.3+3351	2.86	5.79	1.65	1.555	0.89	1.555	0.89	1.095	3.11	Bst
J142755.9+3321	16.74	5.30	1.40	1.845	1.63	1.780	8.58	1.845	1.63	E
J142843.0+3326	5.97	5.33	1.87	1.770	6.69	1.490	34.36	1.770	6.69	E
J142843.4+3355	2.41	5.82	4.82	2.945	3.24	2.945	3.24	2.495	18.38	Bst
J142910.3+3358	2.24	5.72	1.31	1.740	2.14	1.740	2.14	1.305	3.13	Bst
J142915.2+3303	1.79	7.37	1.73	1.675	13.54	1.675	13.54	1.095	67.44	Bst
J142916.1+3355	2.07	5.04	1.62	1.125	1.52	1.125	1.52	0.935	3.16	Bst
J143004.7+3302	3.18	5.61	1.60	1.580	0.46	1.580	0.46	1.095	3.58	Bst
J143116.7+3354	1.69	5.62	1.82	0.960	4.08	0.960	4.08	0.840	4.87	Bst
J143209.1+3356	1.93	5.11	2.17	0.605	2.16	0.885	4.90	0.800	4.90	E
J143226.7+3330	4.53	5.49	1.78	1.945	0.52	1.945	0.52	1.095	4.49	Bst
J143249.7+3316	1.32	5.23	2.33	1.005	6.91	1.005	6.91	0.840	12.61	Bst
J143258.3+3315	0.81	5.85	1.72	1.480	0.46	1.480	0.46	1.010	32.56	Bst
J143304.2+3334	2.95	5.59	1.75	1.595	99.42	1.595	99.42	1.395	174.09	Bst
J143347.0+3353	1.19	7.34	2.22	1.700	0.00	1.700	0.00	1.395	9.54	Bst
J143428.0+3311	23.23	5.30	2.13	1.820	9.84	1.490	30.71	1.820	9.84	E
J143435.1+3343	5.62	5.21	1.61	1.295	0.36	1.295	0.36	1.000	2.36	Bst
J143527.9+3311	39.60	6.65	2.22	1.650	1.10	1.530	16.12	1.395	7.84	E
J143646.0+3345	3.22	6.64	3.33	2.545	0.86	2.545	0.86	1.395	8.13	Bst
J143731.0+3340	2.64	6.46	1.64	1.650	1.20	1.650	1.20	1.385	12.89	Bst
J142517.2+3415	14.74	5.00	-	1.580	8.18	1.580	8.18	1.100	14.74	E
J142648.2+3458	4.46	5.70	-	1.305	0.25	1.020	1.20	1.305	0.25	Bst
J142802.4+3437	1.20	6.49	-	1.105	2.85	1.030	3.87	1.105	2.86	Bst
J142850.6+3453	2.19	5.75	-	1.015	0.11	0.840	3.29	1.015	0.11	Bst
J142905.6+3449	31.42	5.04	-	1.355	0.23	1.045	2.14	1.355	0.22	Bst
J142917.6+3437	2.56	5.25	-	0.840	3.40	0.805	5.33	0.840	3.39	Bst
J142943.8+3434	1.89	6.00	-	1.300	0.03	1.035	1.53	1.300	0.03	Bst
J143248.7+3413	0.95	5.25	-	0.555	0.05	0.735	0.72	0.555	0.05	Bst
J143259.2+3406	1.14	6.56	-	1.125	0.41	1.190	1.19	1.385	1.56	E
J143308.0+3418	7.07	5.10	-	0.805	2.45	0.795	6.11	0.805	2.44	Bst
J143430.5+3427	1.50	5.81	-	1.430	1.24	1.430	1.24	1.125	5.92	E
J143506.4+3438	3.22	5.16	-	0.935	8.67	0.840	13.65	0.935	8.67	Bst
J143539.8+3443	23.22	5.74	-	0.780	0.21	0.830	6.64	0.895	0.22	E

Table 3.1: continued...

				All SED		Starburst		Elliptical		
Object name	$S_{1.4}$	$R-K$	$J-K$	z	χ^2_ν	z	χ^2_ν	z	χ^2_ν	SED
(1)	(2)	(3)	(4)	(5)	(6)	(7)	(8)	(9)	(10)	(11)
J142440.4+3511	1.06	6.11	-	1.850	0.10	1.425	13.21	1.625	23.32	E
J142618.6+3545	2.49	5.56	-	1.860	0.02	1.070	1.14	1.860	0.02	Bst
J142628.5+3527	1.79	5.39	-	2.495	5.16	0.275	9.12	2.210	6.36	E
J142639.3+3510	2.56	5.18	-	0.850	0.10	0.870	0.00	1.070	0.20	E
J142817.2+3509	5.46	6.31	-	0.805	4.41	0.940	9.10	0.805	4.41	Bst
J143042.5+3512	5.18	5.23	-	2.495	17.63	0.260	20.76	2.415	18.45	E
J143051.3+3543	3.41	5.51	-	0.805	0.39	0.840	1.04	0.805	0.40	Bst
J143108.3+3525	2.07	5.36	-	1.335	0.07	1.020	0.32	1.335	0.07	Bst
J143112.5+3535	9.64	6.08	-	1.405	0.02	0.840	9.08	1.405	0.02	Bst
J143134.5+3515	64.12	5.94	-	0.800	0.00	1.010	1.28	0.800	0.00	Bst
J143238.0+3530	17.86	5.20	-	0.905	0.27	0.790	1.85	0.905	0.27	Bst
J143246.7+3533	2.18	5.28	-	1.825	0.05	0.605	6.61	1.825	0.05	Bst
J143313.7+3539	0.90	6.04	-	0.750	0.01	1.030	2.01	0.750	0.01	Bst
J143414.5+3541	0.55	5.95	-	1.240	0.00	1.240	0.00	1.495	0.83	E

CHAPTER 4

X-ray Identification of FIRST radio sources in Boötes field

4.1 Overview

In this chapter a brief summary of the X-ray observations for the XBoötes survey and the resulting XBoötes source catalogue is presented. The FIRST radio catalogue is correlated with the xBoötes data. The method of correlating the radio sources with the X-ray sources is explained. General properties of the radio/X-ray sample are examined.

4.2 Introduction

X-ray surveys have played a crucial role in understanding the nature of the sources that populate the X-ray universe. Early surveys like the Einstein Medium Sensitivity Survey (Gioia et al. 1990), ROSAT (Roentgen Satellite) International X-ray/optical survey (Ciliegi et al. 1997) and the ASCA (Advanced Satellite for Cosmology and Astrophysics) Large Sky Survey (Akiyama et al. 2000) showed that the vast majority of X-ray sources were AGN. In particular, in shallow wide area surveys in the soft (0.5-2 keV) X-ray band, most of the sources detected are unobscured, broad line AGN, which are characterised by a soft X-ray spectrum with a photon index $\Gamma = 1.9$ (Nandra & Pounds 1994). On the other hand, the number density of AGN iden-

tified in the hard X-ray and mid-IR bands is far greater than that is found in optical surveys of comparable depth (e.g. Bauer et al. 2002b; Stern et al. 2002b).

The advent of the XMM-Newton and Chandra satellites (e.g. Rosati et al. 2002) started a new era in X-ray astronomy. These telescopes with their superb spatial resolution and sensitivity, resolved almost entirely the X-ray background (XRB) in the 0.5-8 keV regime into discrete sources. They have resolved 90% of the soft (0.5-2 keV) X-ray background and also a significant fraction ($\sim$ 80%) of the hard (2-7 keV) X-ray background (Brandt et al. 2001; Moretti et al. 2003; Worsley et al. 2004) into discrete sources. But the small area covered by these surveys (typically $\sim$0.1 deg^2) does not allow them to obtain a statistically significant number of sources in the intermediate X-ray flux range (10^{-15} – 10^{-12} erg s^{-1} cm^{-2}) that contributes $\sim$ 60 – 70% of the XRB. Therefore, surveys covering larger volume are needed to overcome cosmic variance and to better determine the properties of the most luminous and rarest sources, such as powerful quasars, whose number densities are low. Large area and extensive multi-wavelength coverage are also necessary for detailed studies of AGN clustering and their environment.

A combination of radio data with optical and X-ray photometry provides a considerable wealth of information on the nature of the faint radio/X-ray population even in the absence of optical spectroscopy (Stocke et al. 1991), and is a convenient way to shed some light on the differences between AGNs that are strong radio-loud and radio-quiet sources. Deep radio observations represent an excellent tool to explore a number of unresolved questions regarding radio emission from galaxies. The primary emission mechanism in virtually all radio sources is synchrotron emission from relativistic electrons spiralling around the magnetic field within the host galaxy. One should also note that for many powerful AGN the majority of the emitting electrons are well outside the host galaxy. The radio emission can be related either to ongoing star-forming processes or to the accretion activity onto super-massive black hole within the galaxy. At very faint flux densities (μJy), studies have shown that the radio population is dominated by star-forming galaxies, which produce non-thermal radio continuum at 1.4 GHz through synchrotron emission from supernovae remnants. At the Jansky and mJy levels, the bulk of the radio source population is dominated by powerful AGNs. Observations of radio emission of AGNs provide clues to the accretion history of the universe, and important information in our understanding of how central black holes grow over cosmic time, as well as the physical process

behind these powerful objects, especially when combined with X-ray observations (e.g. Merloni et al. 2003). They also provide clues to some properties of the interstellar and intergalactic medium.

Previous studies on cross correlations between radio and X-ray surveys have determined a link between the star formation rate and the radio and X-ray luminosities of star-forming galaxies (e.g. Condon 1992; Ranalli et al. 2003), which can be combined to determine relationships between radio and X-ray luminosities for star-forming galaxies. Bauer et al. (2002a) have conducted a study of the faint X-ray and radio sources using 1 Ms Chandra data set and ultra deep VLA observations, finding a large overlap between faint X-ray and radio sources. These authors have showed that the X-ray and radio luminosities are correlated for nearby late type galaxies, and therefore used it to estimate the star formation rate in their sample. Other studies of the radio-X-ray correlations involve studies of the radio properties of the hard X-ray sources. For example, Barger et al. (2001), cross correlated the VLA data ($S_{1.4\ \mathrm{GHz}} = 25\ \mu$Jy), with a deep Chandra survey ($f_X(2-10\ \mathrm{keV}) = 3.8\times10^{-15}$ erg s^{-1} cm^{-2}) finding radio counterparts for 50% of their X-ray sources. Ciliegi et al. (2003), have performed a study of the radio properties of the X-ray sources detected in the HELLAS survey ($S_{5\ \mathrm{GHz}}$= 0.3 mJy; $f_X(5-10\ \mathrm{keV}) = 5-4\times10^{-14}$ erg s^{-1} cm^{-2}). They find an identification rate of the X-ray sources in the radio bands of 30% much higher than that in the soft band (0.5-2 keV). At somewhat fainter fluxes ($f_X(2-8\ \mathrm{keV})$ $= 7.7\times10^{-15}$ erg s^{-1} cm^{-2}, $S_{1.4\ \mathrm{GHz}} = 60\ \mu$Jy), Georgakakis et al. (2004) combined a single 50 ks XMM-Newton pointing with an ultra deep radio survey, finding an identification rate of $\sim$ 33%.

In the previous chapters, a detailed study on the optical/infrared identifications of FIRST radio sources in Boötes field of the NDWFS survey was performerd. A total of 688/900 FIRST radio sources have been identified in one or more bands (*Bw, R, I, K*) in Boötes field. The X-ray properties of FIRST radio sources have been studied in a few papers. For example, Brinkmann et al. (2000) compiled a large sample of X-ray selected AGN from the ROSAT All Sky Survey (Voges et al. 1999) and cross correlate this sample with the FIRST radio survey, finding a relatively tight linear correlation between the logarithmic of radio luminosity and the X-ray luminosity in the soft X-ray 0.5-2 keV band. At bright flux limits, $f_X(2-10)$ keV = 10^{-13} erg s^{-1} cm^{-2}, Akiyama et al. (2000) cross correlated the ASCA Large Sky Survey (LSS) with

the FIRST catalogue, finding an identification rate of a ∼ 35% and a fraction of radio loud hard X-ray selected sources of approximately 10%. At faint X-ray flux $f_X(0.5-2)$ keV=1.5×10^{-16} erg s^{-1} cm^{-2}, four radio sources from FIRST survey have been identified as a radio counterparts to four X-ray sources in the Large Area Lyman Alpha survey (LALA) Boötes field (Wang et al. 2004). Sánchez-Sutil et al. (2006) cross correlated the FIRST radio sources with an ULX (Ultra Luminous X-ray) catalogue, and they found 70 positional coincidence and the majority of them are associated with the galaxy nucleus. The aim of this paper is to shed light on the nature and the environment of the faint radio population (at mJy level) detected in the FIRST radio survey, to characterise their X-ray counterparts and to distinguish between different groups of AGNs. We combine data from the FIRST radio survey with a new, medium depth (5 ks/pointing) Wide field X-ray survey (known as the Chandra XBoötes) of the Boötes field of the NDWFS survey. The X-ray data reach a limiting flux of 4×10^{-15} erg s^{-1} cm^{-2} in the soft band and 8×10^{-15} erg s^{-1} cm^{-2} in the full band. Compared to the previous studies this data set, the FIRST/XBoötes, has the advantage of deep wide area optical/infrared observations, radio and intermediate in depth X-ray observations.

This chapter is organised as follows: section 4.3 presents a summary of the X-ray data. The matching procedure is described in section 4.4. Optical magnitude and optical morphology of the radio-X-ray matches are investigated in sections 4.6 and 4.5 respectively. In section 4.7 I present the photometric redshifts and the $K-z$ relation. Section 4.8 investigates the radio-X-ray luminosities. Section 4.9 is devoted to the X-ray properties of the sample and §4.10 discusses the general properties of the radio-X-ray matches. Conclusions are summarised in section 4.12. Throughout this chapter it is assumed that $\Omega_M = 0.3$, $\Omega_\Lambda = 0.7$ and H_0=70 km s^{-1} Mpc^{-1}.

4.3 X-ray data

In this section a brief introduction is given to the XBoötes catalogue as applied to the cross matching process. For thorough description of the catalogue see Kenter et al. (2005), Murray et al. (2005) and Brand et al. (2006).

4.3.1 The XBoötes catalogue

The X-ray data (Murray et al. 2005; Kenter et al. 2005) used in this thesis are from the Chandra XBoötes survey. The XBoötes catalogue contains ~ 3213 X-ray point sources and is publicly available through the NOAO Deep Wide Field Survey (NDWFS) homepage[1]. The Chandra XBoötes survey imaged a large and contiguous area of 9.3 square degrees of the Boötes field of the NDWFS survey, and is centred on RA (J2000) ~ 14^h32^m and Dec (J2000) ~ $34°06'$. The field was observed by the advanced CCD Imaging Spectrometer (ACIS-I) on the Chandra X-ray Observatory, and the data have arcsecond resolution and broad energy response up to 10 keV. The X-ray data was taken in 126 separate pointings, each observed for 5 ks. The X-ray data are filtered in the three energy bands: 0.5 – 7 keV, 0.5 – 2 keV, 2 – 7 keV with a limiting flux of $\sim 8 \times 10^{-15}$ erg s^{-1} cm^{-2} in the full band (0.2 – 7 keV) and of $\sim 4 \times 10^{-15}$ erg s^{-1} cm^{-2} in the soft band (0.5 – 2 keV). For details of the XBoötes catalogues and data processing see Murray et al. (2005).

4.4 Cross identification method

When searching for optical/infrared or X-ray counterparts of radio sources (or vice versa), one must decide on the matching criteria to be adopted, at what angular separation can one be reasonably confident that a candidate is a true counterpart of a radio/X-ray source. A compromise is required in order to maximise both the completeness (i.e. all potential radio sources are included) and the reliability (i.e all included identifications are genuine) of the data base. The best way to ensure completeness and reliability is to determine a maximum position offset which includes all possible identifications and to have some realistic estimate of the uncertainties in both the radio and X-ray positions. The FIRST radio survey provides a high positional accuracy that is around ~ 0.5″. The mean uncertainty in the X-ray positions is estimated to be ~ 1.68″. Combining these in quadrature with the radio astrometry errors defines a circle about the predicted coordinates of the source, with a radius of 1.75″ ($1\,\sigma$), within which the X-ray counterpart of the radio source is expected to be found.

I first cross correlated both FIRST and XBoötes catalogues based on simple positional co-

[1] http://www.noao.edu/noao/noaodeep/XBootesPublic/index.html

incidence, and then took all the pairs whose radio and X-ray positions differed by less than 20″. The cumulative distribution of the separations between the X-ray and radio positions is shown in Figure 4.1. The upper curve shows the distribution offset for all matches between radio and X-ray positions. The lower curve shows the differential distribution which would be expected if all identifications were chance coincidence. This is obtained by shifting all the radio positions by 3 arcminutes. As one can see from the plots, the radio-X-ray offset distribution exceed vastly the random distribution at offset $\leq 2''$, meaning that real identifications of FIRST radio sources with X-ray objects dominate at smaller offsets. Based on this Figure, a 2″ cut-off is chosen as a good compromise that radio and X-ray sources can be considered as counterparts, which results in 92 radio-X-ray matches. Furthermore, only one random identification is made at offsets smaller than the chosen matching radius of 2 arcsec, corresponding to 1% of the true matches.

Figure 4.2 shows the positional offset between the radio and their X-ray counterparts. There are 86/92 (93%) X-ray-radio matches within 1.5″ and only 6 sources lie beyond 1.5″. It is clearly seen from the figure that the sources are not centred on (0,0) and there is a small systematic offset between the radio and X-ray reference frames. The mean offsets are $\langle \Delta \mathrm{Ra} \rangle = -0.32''$ and $\langle \Delta \mathrm{Dec} \rangle = -0.27''$. I shifted the X-ray reference frame to match up to the radio using the median offset of matched objects and again ran the source matching algorithm. Correcting this small offset made no difference to the total matched sample. Bauer et al. (2002a), used a 1″ search radius for the VLA/Chandra cross correlation on the HDF-N; Barger et al. (2007) adopted a 1.5″ search radius as a good compromise for the VLA/HDF-N.

The comparison of the positions of FIRST radio sources with the XBoötes X-ray sources reveals 92 coincidence, corresponding to an identification rate of ~ 10% (92/900). This clearly shows that there is little overlap between radio and X-ray sources. A higher overlap between radio sources and X-ray sources has been found by Tozzi et al. (2009). In their cross correlation between radio sources and X-ray sources in the E-CDFS area, they found that 40% of the radio sources are associated with X-ray sources. Rovilos et al. (2007) found that the radio detection rates for the E-CDFS and CDFS X-ray sources increases from 9% to 14% in the central region of this field (which has deeper X-ray data), while the X-ray detection rates for radio sources are 21% for the E-CDFS and 33% for the CDFS field. The radio flux density limit in Tozzi et al. (2009) ranges from 42 μJy at the field centre, to 125 μJy near the field edge and

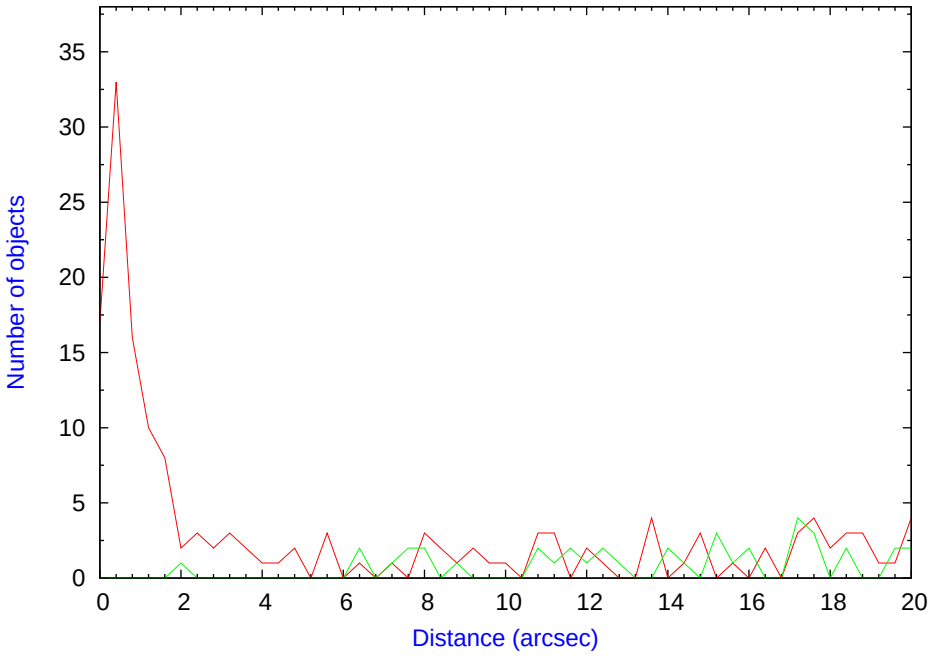

Figure 4.1: Histogram of the separations between positions of radio sources and the X-ray sources to which they have been matched. The lower plot shows the expectation of chance associations. I consider sources to be associated if the separations are < 2 arcsec.

in Rovilos et al. (2007) is 60 μJy, while the detection threshold in the FIRST survey is 1 mJy. Ciliegi et al. (2003) reported a high fraction of 36% in the HELLAS field. The identification rate measured in Akiyama et al. (2000) is 35% for the FIRST radio sources in the LSS field ($f_X(2.0-10\text{keV}) = 1\times10^{-13}$ erg s^{-1} cm^{-2}). It is interesting to note that both radio and X-ray detection rates increases with deeper observations. Ciliegi et al. (2003) have shown that the radio-X-ray association is a function of the radio/X-ray limit ratio, f_r/f_X (see their table 2), the deeper radio data compared to the X-ray flux limit, the higher the number of radio-X-ray associations. To summarise, the small fraction of radio detected X-ray sources in comparison to the previous results is due to a mismatch between the flux limit of the VLA FIRST 1.4 GHz (deep radio survey) and that of the Chandra XBoötes survey (shallow X-ray survey).

4.4.1 Optical counterparts to the radio/X-ray matches

Brand et al. (2006) presented a catalogue of the optical/infrared counterparts to the 3213 X-ray point sources detected in the XBoötes survey[2]. These authors found optical counterparts

[2]The catalogue can be obtained through the NDWFS homepage at http://www.noao.edu/noao/noaodeep/XBootesPublic

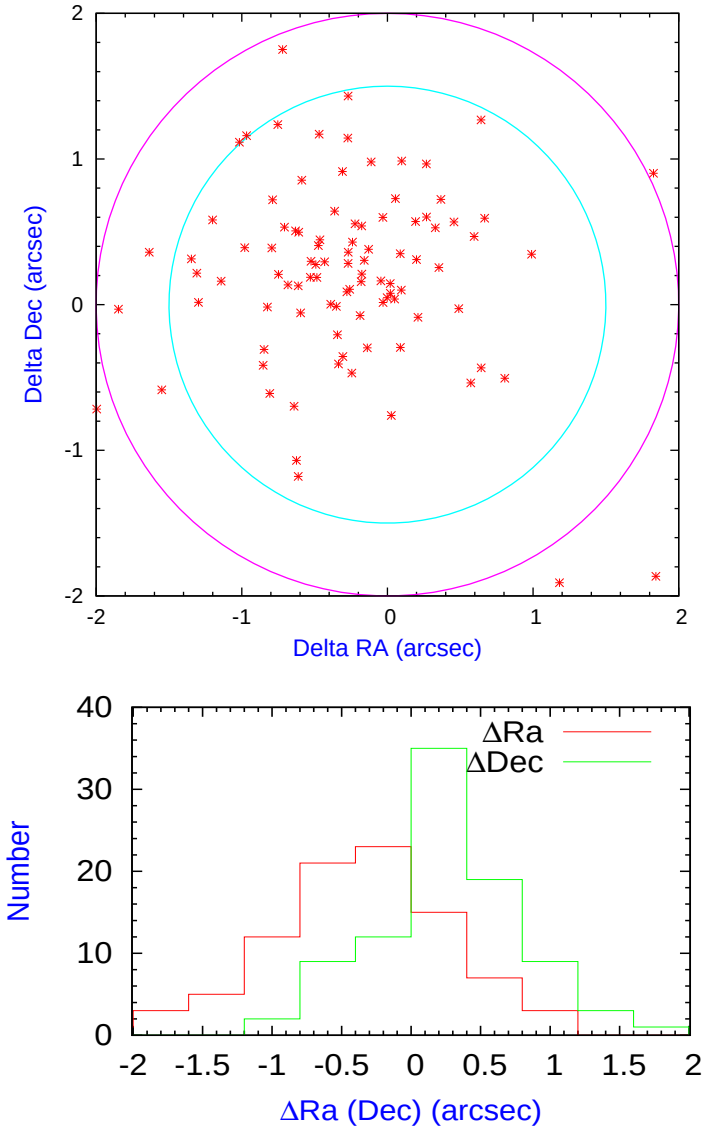

Figure 4.2: *Top panel*: Diagram of the offset in Ra and Dec (arcsec) of the FIRST radio sources and xBoötes sources with a 2″ and 1.5″ circles overlaid to show how many of the matches are separated by more than 2″. *Lower panel*: offset histograms for Δ Ra (solid histogram) and Δ Dec (dashed histogram).

for 98% of the X-ray sources using a Bayesian identification scheme. For each candidate the full catalogue provides a number of parameters containing information about the X-ray sources and their optical/infrared counterparts. A detailed analysis of the matching criteria and a full description of the catalogue is presented in Brand et al. (2006). The following provides a brief description of the parameters that have been taken into account in this analysis :

- nopt: labels the number of optical sources with $> 1\%$ probability of being the correct optical/infrared counterparts to the X-ray source in the case of multiple matches.
- optrank: labels the optical rank when the X-ray sources are multiply matched. This parameter ranges from 1 (most probable) in running order to the least probable.
- bayprob: gives the Bayesian probability of an optical object being the true counterpart to an X-ray source.
- Class: describes the optical morphology of the optical counterparts to the X-ray sources (1: point-like object; 0: galaxy (extended or resolved)).
- flag: In cases of no optical ID being the most probable identification, the flag parameter takes three values which have been applied manually (Brand et al. 2006):

    1. flag $= -3$: no optical ID, but source obscured by nearby star / missing data.
    2. flag $= -2$: no optical ID, but X-ray position is close to optically bright galaxy (source is either obscured by or associated with the galaxy.
    3. flag $= -1$: 'true' no optical ID (optical image is truly blank).

A total of 90/92 of the X-ray counterparts to FIRST radio sources have optical counterparts and the remaining two X-ray sources are associated with a blank field flag $= -1$. The majority (75%) of the X-ray candidates are associated with only one optical object (nopt = 1). In 22 cases, the X-ray candidates have more than one optical match. Ten X-ray sources each have 2 multiple matches, three X-ray candidates each have three multiple matches, five X-ray sources each are associated with 4 optical objects, one source has 5 optical counterparts, two X-ray candidates each have 6 counterparts and one is associated with 8 possible matches. In those multiple

matches, only optical matches with optrank = 1 (high probability) have been considered as real matches.

In chapter 2, I have presented a cross correlation of FIRST radio sources and the NDWFS survey (Boötes field), using both the likelihood ratio and a simple positional coincidence. The identification procedure yielded 688/900 optical counterparts to FIRST radio sources in either one or more bands (*Bw, R, I, K*). From these, 79 optical counterparts are in common to the FIRST radio sources and their X-ray candidates – recall that the Boötes field is split by declination into four strips ($32^\circ < \delta \leq 33^\circ, 33^\circ < \delta \leq 34^\circ, 34^\circ < \delta \leq 35^\circ, 35^\circ < \delta \leq 36^\circ$) and each is imaged in four bands (*Bw, R, I, K*). The Boötes field is partially covered in K band (especially the second strip), hence the infrared data (for the second strip) have been obtained from FLAMEX survey.

In summary; the cross correlation of FIRST radio sources and the XBoötes survey yielded a total of 92 X-ray counterparts of FIRST radio sources, and there are 79/92 optical/infrared counterparts in common with the radio-X-ray matches. Among the 79 radio-X-ray matches, 4 double-radio sources are identified in XBoötes field, four radio sources with three components and one source with four components. But only one component of each group that is identified in the XBoötes field, Figure 4.3 shows images of the identified double radio sources. These images are extracted from the FIRST website[3]

4.5 Morphology

Optical morphologies of these objects provide a further clue as to their nature. The source SExtractor stellarity parameter was used to classify these objects morphologically into “stellar” in appearance (i.e. unresolved) or “galaxy” (i.e. resolved or extended). As mentioned previously, the SExtractor software has difficulty in correctly classifying sources fainter than $R = 23$ in the NDWFS data (Brown et al. 2003; Brand et al. 2006). Typically, all objects brighter than $R \sim 23$ should be classified correctly and it is estimated that about 80% of the objects with $24 < R < 25$ should be correctly classified. Figure 4.4 shows the stellarity parameter against the apparent *R*-band magnitude for all the X-ray sources identified in Boötes field in the upper panel, for the

[3]http://third.ucllnl.org/cgi-bin/firstcutout

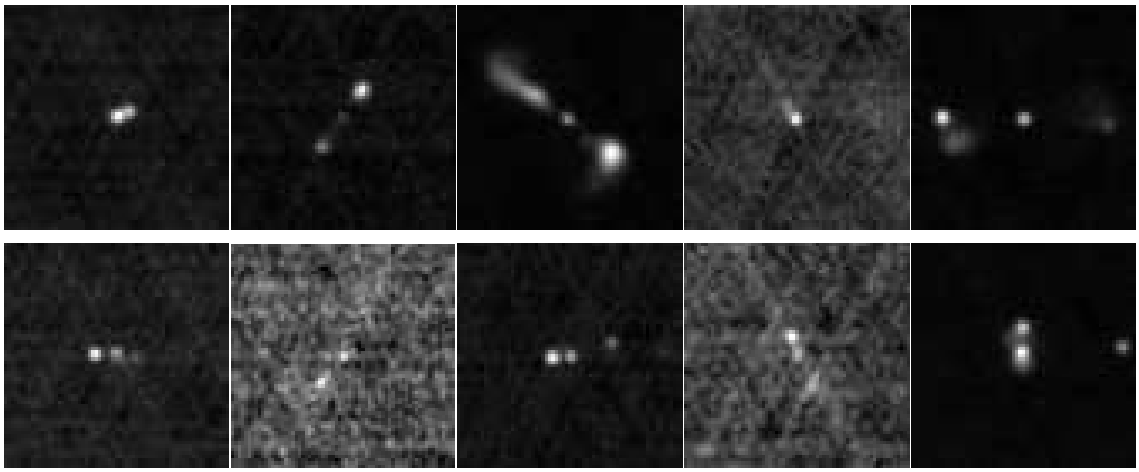

Figure 4.3: The FIRST radio sources with multiple components identified by the selection algorithm of Magliocchetti et al. (1998). Each FIRST stamp is $2' \times 2'$, normalised to the maximum intensity.

optical counterparts of FIRST radio sources in the middle panel and for all radio-X-ray matches in Boötes field in the lower panel. The majority of identifications are non-stellar. A total number of 46 (58%) sources are classified as galaxies (stellarity < 0.7), and 33 (42%) sources classified as "stellar" (i.e. mostly QSOs). Taking a crude split between stars and galaxies at stellarity level of 0.9 and 0.1 for stars and galaxies respectively; all sources with stellarity ≥ 0.9 are classified as point-like objects (mostly QSO), sources with stellarity ≤ 0.1 as galaxies and intermediate objects as sources with $0.1 <$ stellarity < 0.9. This criteria yielded 27 (34%) point-like objects, 35 (44%) galaxies and 17 (22%) intermediate objects.

The *R* band images for all the radio-X-ray matches are shown in Figure 4.5. These cut-out images have been obtained from the NOAO cut-out service: http://archive.noao.edu/ndwfs/cutout-form.html. The majority (63/75; 84%) of the radio-X-ray matches have magnitudes brighter than $R = 23$ from which 57% (36/63) have magnitudes brighter than $R = 20$ mag. These sources appear visually to be mainly elliptical, and lenticulars are also seen. A number of these sources also appear to be either an interacting or merging galaxies. At Fainter magnitudes, the sources tend to have low stellarity (see Figure 4.4) so they are likely QSOs or compact (distant) galaxies.

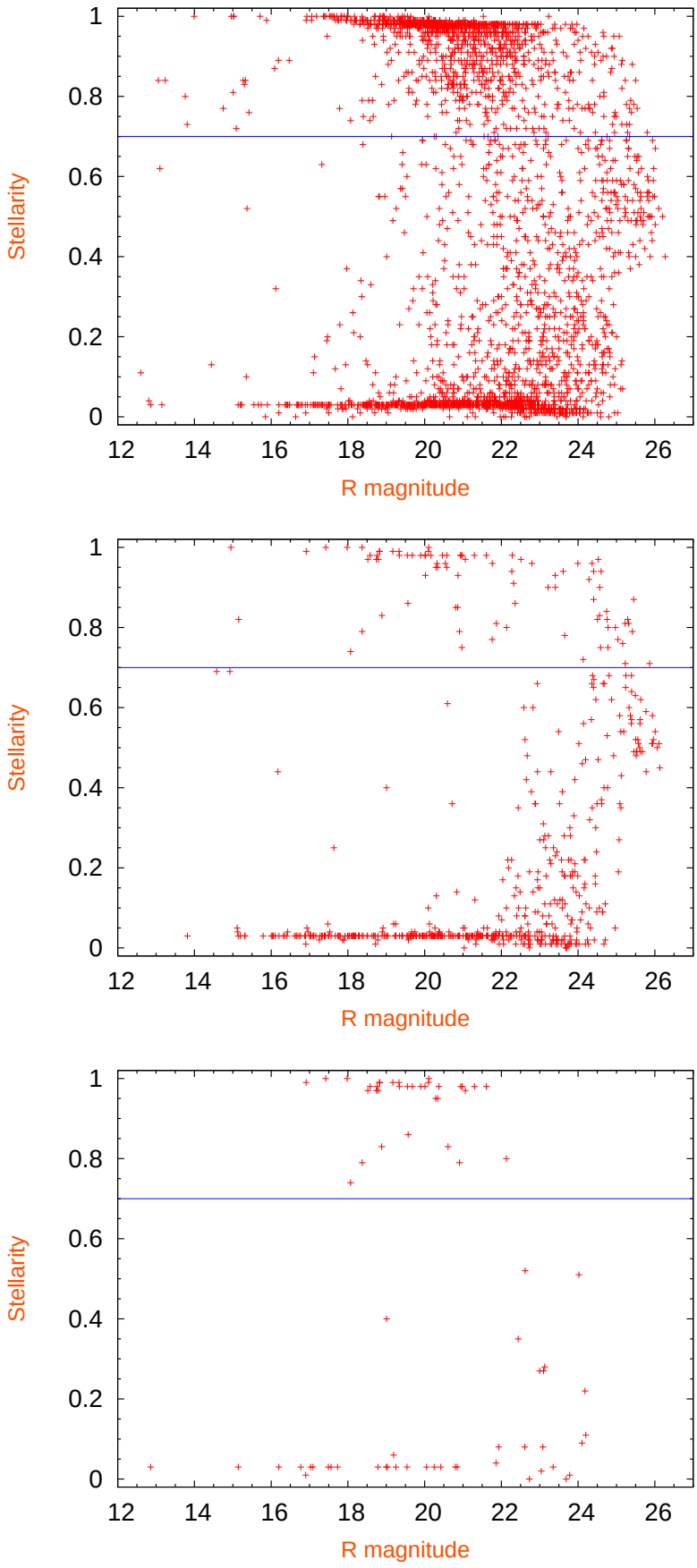

Figure 4.4: The stellarity of the optical counterparts against their *R*-band magnitude for X-ray sources (upper panel), for the FIRST radio sources (middle panel), and for both FIRST radio and X-ray sources in common (lower panel).

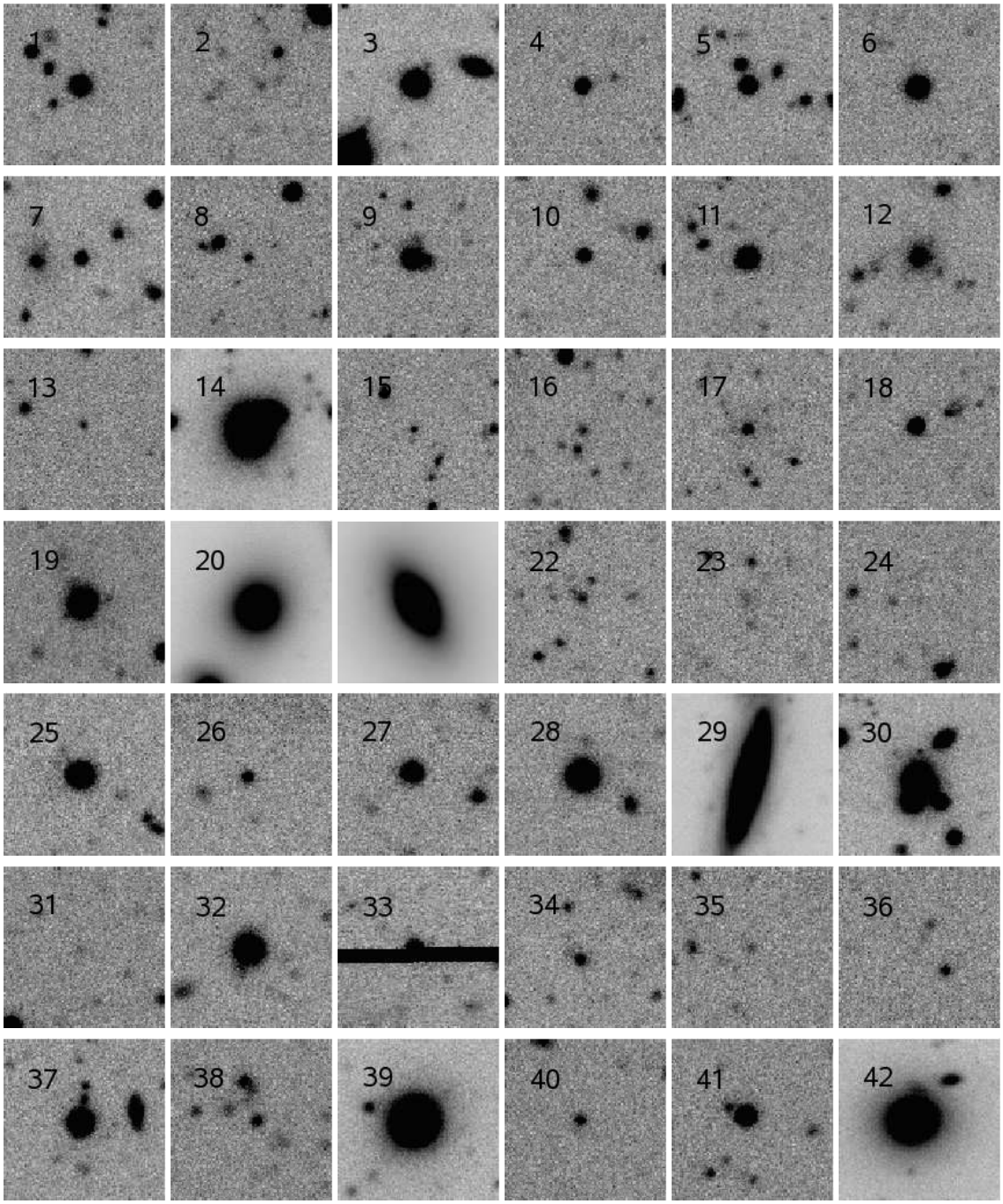

Figure 4.5: The *R* band images of all the 79 radio-X-ray matches in the 9.3 deg^2 Boötes field. All the images are centred on the FIRST radio sources. The FIRST radio sources reference number (shown in column 1 of Table 4.1) is at the top left of each image. These cut-out images have been obtained from the NOAO cut-out service: http://archive.noao.edu/ndwfs/cutout-form.html.

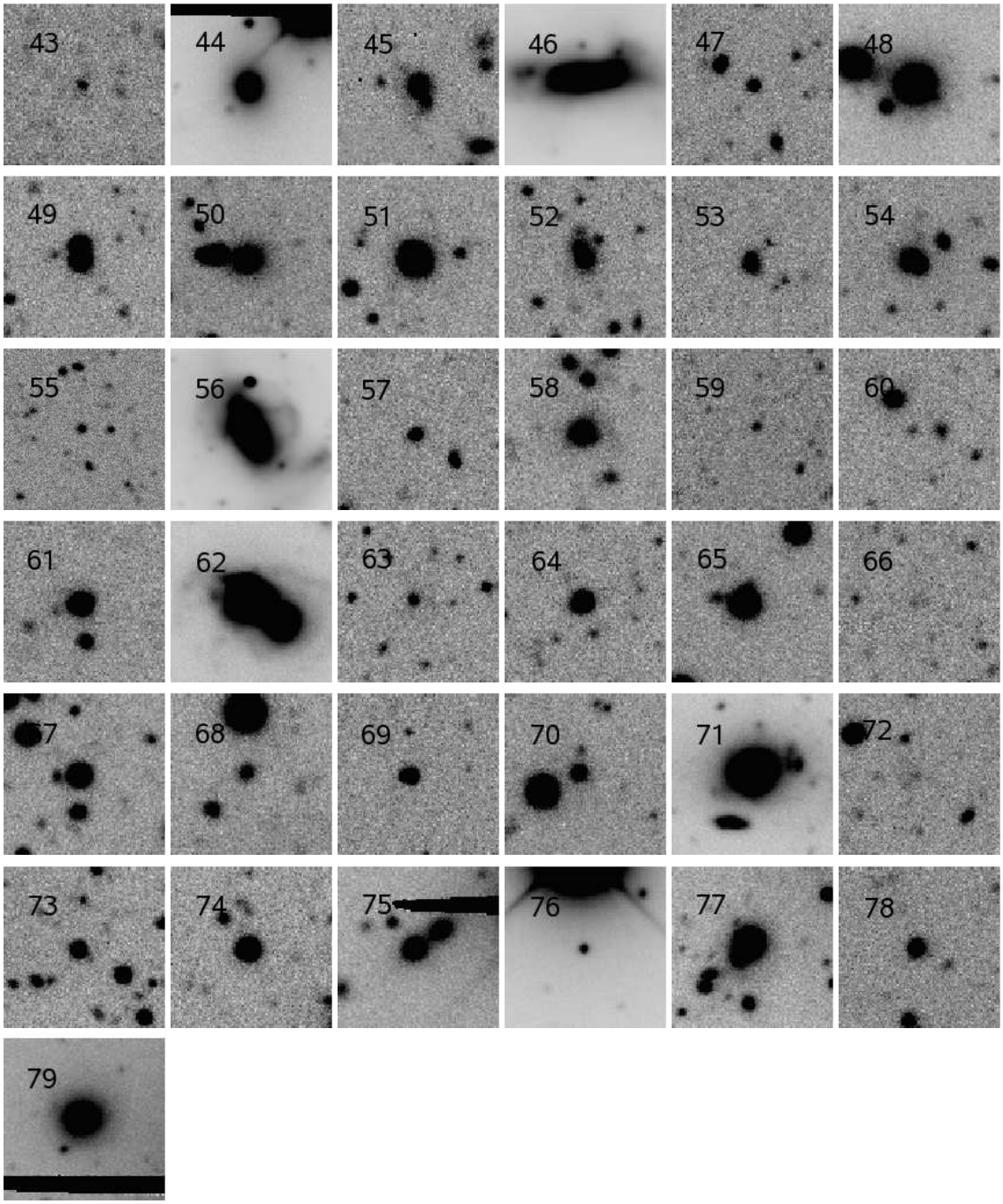

Figure 4.5: *continued*

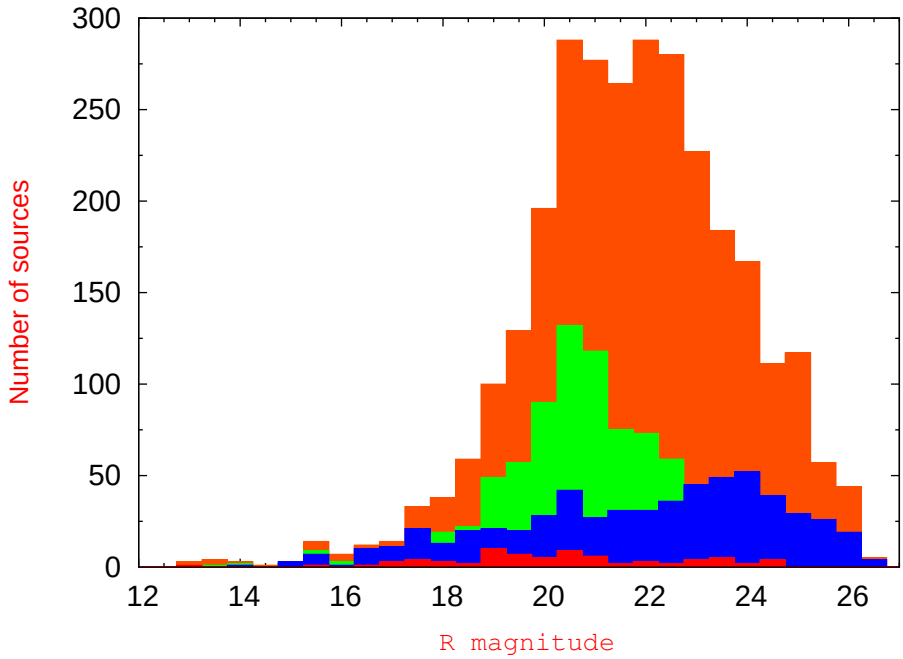

Figure 4.6: From top to bottom, the optical magnitude distribution in *R* band for: all the X-ray sources identified in Boötes field, all X-ray sources identified in four bands (*Bw, R, I, K*) in Boötes field, all FIRST radio sources identified in Boötes field and all the common optical counterparts to the radio-X-ray matches.

4.6 Optical magnitude distributions

Figure 4.6 shows the optical magnitude distributions in R band of the common optical counterparts to the radio-X-ray matches. From top to bottom the histograms shown are distributions for: 1) all X-ray sources optically identified in Boötes field, 2) all X-ray sources identified in four bands (*Bw, R, I, K*) in Boötes field, 3) all FIRST radio sources identified in the Boötes field, and 4) the optical counterparts to the radio-X-ray matches. The magnitude distribution of all X-ray sources identified in Boötes field has two apparently weak peaks (a KS test confirmed a normal distribution) with a small tail at brighter magnitudes and few counterparts at fainter magnitudes, with a small tail at brighter magnitudes and few counterparts at fainter magnitudes. The radio sample has significantly flatter distributions compared to the global optical catalogue (orange histogram) and to the X-ray sources identified in four bands (green histogram), and falls off at $R \sim 24$. The mean magnitude of the optically extended radio-X-ray matches is $R = 20.68$ with a median of 19.91. For radio-X-ray matches that are associated with point-like objects the mean magnitude is $R = 19.62$ and the median is 18.58. The mean magnitude for all radio-X-ray matches is $R = 20.16$ and the median $R = 22.13$.

4.7 Redshift estimation

4.7.1 Optical classification

Optical spectroscopic information is available for 22 out of 79 sources (28%). The spectroscopic data have been obtained from the SDSS (Sloan Digital Sky Survey). The spectroscopically identified sample comprises 14 point-like objects (13 sources show broad emission lines and one source shows a featureless spectrum) and 8 resolved radio galaxies (with emission/absorption lines). Extragalactic radio sources are known to be a mixture of two main populations: AGN and star-forming galaxies. The AGN class can be divided into two sub-classes: QSOs (often unresolved in the optical image) and objects where the AGN does not dominate the entire SED (Spectral Energy Distribution), such as type 2 QSOs, low luminosity AGN (seyfert and LINERS) and absorption line AGN. A total number of 13 point-like objects are spectroscopically classified as QSOs by the SDSS and the point-like source which shows a featureless optical spectrum could be classified as a BL Lac object. The presence of broad emission lines (width larger than 2000 km/s) like Mg_{II}, C_{III} and at large redshifts C_{IV} and Lyα classifies the source as a broad line AGN (BLAGN), type -1 AGN or QSO according to the simple unification model by Antonucci (1993). To classify emission line galaxies as star-forming or AGN, I used the line flux ratio diagram of $[O_{III}]/H\beta$ versus $[N_{II}]/H\alpha$ (BPT diagram, Baldwin et al. ????). I used an empirical criterion to segregate AGN host galaxies from star-forming galaxies: $[O_{III}]/H\beta = 0.61/([N_{II}]/H\alpha - 0.05) + 1.3$ given by Kauffmann et al. (2003). With these diagnostics, the AGN population still remained mixed. To distinguish seyferts from LINERS I used an empirical relation given by Kewley et al. (2006): $[O_{III}]/H\beta = 1.18\,[O_I]/H\alpha + 1.3$. Based on the 2 independent classification of galaxies, 3 emission lines galaxies were classified as star-forming galaxies (sources # 42, #46, #71) and four were classified as LINERS (sources #29, #39, #56, #62).

In Summary, among the spectroscopically classified sources I find: 13 BLAGNs (59% of the sample with spectroscopic redshift), one BL Lac object (source #11), 3 (14%) star-forming galaxies and four (18%) LINERS galaxies. The optical spectra of these sources are shown in Figure 4.19 with spectroscopic redshift, type and source number printed on each figure. One also notes the fair agreement (98%) between the SDSS classification and the SExtractor

stellarity parameter (provided by the NDWFS catalogue) used so far to classify the radio-X-ray matches into point-like objects and extended objects. For the remaining sources (55) without spectroscopic information I turn to photometric redshift techniques to estimate redshifts for these.

4.7.2 Photometric redshifts

Photometric redshift techniques have been applied by many authors to obtain photometric redshift for X-ray sources identified in optical/radio surveys (Barger et al. 2001, 2002; Gandhi et al. 2004; Georgakakis et al. 2004; Mobasher et al. 2004; Zheng et al. 2004). X-ray sources may have complex spectral energy distributions that arise from both the host galaxy and the AGN. Consequently estimating photometric redshifts for X-ray sources using templates for normal galaxies may be problematic. However, with the aim of studying the X-ray spatial correlation function in the NDWFS survey (Boötes field), and in the absence of spectroscopic redshifts, Gonzalez & Maccarone (2002) have studied the effectiveness of photometric redshifts based on galaxy spectral template fitting for 65 X-ray luminous objects detected by Chandra in the Caltech Faint Galaxy redshift survey(CFGRs). They used the two publicly available codes, *Hyperz*[4](Bolzonella et al. 2000) and BPZ (Bayesian photometric redshift, Benítez 2000). Gonzalez & Maccarone (2002) have shown that the two codes produce similar results when compared to spectroscopic data, and confirm that photometric redshifts based on template fitting for X-ray sources are quite robust for 90% of sources that have optical counterparts brighter than R $\sim$ 24.5 (see also Barger et al. 2002; Gandhi et al. 2004; Zheng et al. 2004). They have also shown that photometric redshift estimates agree well with spectroscopic measurements for objects in which galactic light dominates the optical flux. Using multi-wavelength photometric data from the Great Observatories Origins Deep Survey, Mobasher et al. (2004) also attempted to estimate photometric redshifts for a sample of 434 galaxies with spectroscopic redshifts in the Chandra Deep Field-South with magnitudes in the range $18 < R_{AB} < 25.5$. They have applied a bayesian method to two subsamples of galaxies: Extremely Red Objects (EROs) and AGNs. Mobasher et al. (2004) found good agreement between photometric redshifts based on template fitting and more accurate results for EROs when compared to the sample as a whole ($\sigma = 0.051$), while

[4]The code is publicly available at: http://webast.ast.obs-mip.fr/hyperz/

the results tend to be less accurate for X-ray sources (AGNs) ($\sigma = 0.104$), but still acceptable for further studies.

In this chapter, I used the publicly available code *Hyperz* to obtain photometric redshifts for the radio-X-ray matches (see chapter 2). Four filters (*Bw, R, I, K*) have been used to obtain photometric redshifts for 79 radio-X-ray matches. The majority of the radio-X-ray matches (63%) are detected in four bands. As mentioned previously, no infrared data are available for the first strip ($32^\circ \leq \delta < 33^\circ$), and 8 radio-X-ray sources are identified in this strip. In this case, spectroscopic redshift is available for four radio-X-ray matches, and for the remaining four sources, photometric redshift is estimated based on three filters (*Bw, R, I*). In 23 cases, it was not possible to assign an accurate photometric redshift in this cases($\chi^2 > 2.7$), but 12/ 23 of these sources have spectroscopic redshifts (the majority of these sources are detected either in three bands or two bands). Figure 4.7 shows the photometric redshift distribution derived for the radio-X-ray matches in the top panel and the photometric redshift vs spectroscopic redshift for sources with secure redshift (i.e. χ^2 <2.7) in the lower panel. The hatched histogram shows the spectroscopic redshift distribution for 22 radio-X-ray matches and the open histogram displays the best estimate of photometric redshifts as derived from *Hyperz*. About 72% of the sources are estimated to be at $z \leq 1$ with a small tail extending up to $z \sim 4$, and the mean photometric/spectroscopic redshift is $z \sim 0.85$.

Only a small fraction (22/79) of the optical counterparts to the radio-X-ray matches have a spectroscopically measured redshift. Comparing the z_{phot} with z_{spec}, the accuracy of the photometric redshift technique applied so far is estimated to be $\Delta z/(1 + z_{spec}) \approx 0.2$.

4.7.3 The $K - z$ diagram

It is believed that powerful radio galaxies and quasars are associated with the most massive galaxies at a wide range of redshifts. A number of studies of these objects have shown that the near infrared *K* band magnitudes follow a tight correlation with redshifts (e.g. Willott et al. 2003; Jarvis et al. 2001a). Studies of fainter radio sources at mJy level also have shown a remarkably tight correlation between the *K* magnitude and redshift (see e.g. Brookes et al. 2006;

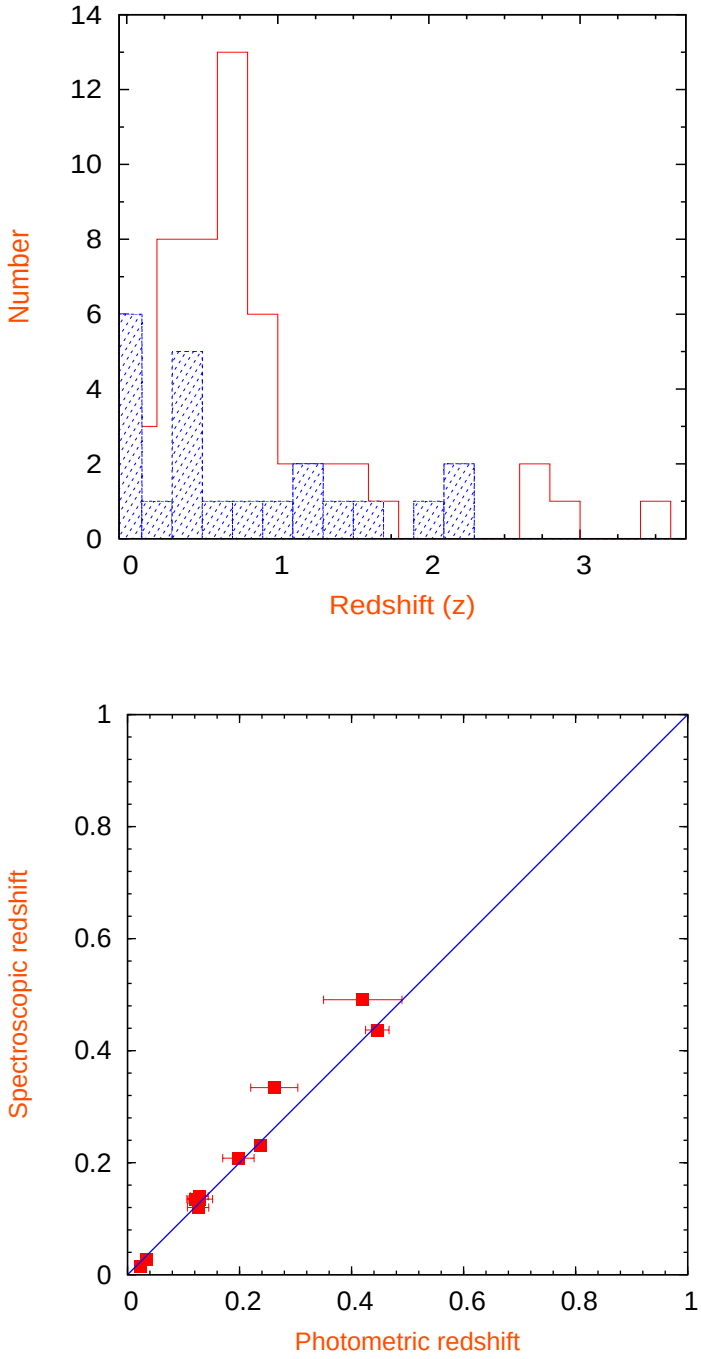

Figure 4.7: *Top panel*: Photometric redshift distribution for the optical counterparts of the radio-X-ray matches (open histogram) and spectroscopic redshift distribution for 22 radio-X-ray matches (hatched regions). *Lower panel*: Photometric redshift vs spectroscopic redshift for sources with secure redshift (i.e. χ^2 <2.7).

El Bouchefry & Cress 2007). This diagram has been widely used to study evolution of galaxies at high redshifts and is known to be an excellent tool to measure stellar masses of galaxies up to high redshifts. The K magnitude versus redshift of the optical counterparts to the radio-X-ray matches is shown in Figure 4.8; point-like objects (QSO, stellarity $\geq$ 0.7) are represented by open circles dots and filled circles denote resolved objects (galaxies; stellarity<0.7); the empty squares denote sources classified as AGN-1, empty triangles for AGN-2, empty diamonds stand for sources classifed as QSO-2, crosses represent normal galaxies (see §4.8 for the X-ray classification), cyan large circles for sources with spectroscopic measurements and yellow large circles present extremely red objects. The blue curve shows the best fit to the $K-z$ relation for the radio-X-ray matches (only extended objects with $L_X > 10^{42}$ erg s^{-1} were considered in this fit):

$$K = (17.39 \pm 0.25) + (4.32 \pm 0.40)\ \log_{10}\ z, \tag{4.1}$$

and the green line illustrates the second order polynomial best fit of Willott et al. (2003): $K = 17.37 + 4.53 \log_{10}\ z - 0.31(\log_{10}\ z)^2$. The fit for the FIRST sources is identical to Willott et al. (2003) fit at $z \geq 0.6$. It is clear that the faint radio population is possibly associated with massive and bright galactic systems, which also host very massive black holes (see e.g. Willott et al. 2003). The three upper plots show the passive stellar evolutionary tracks of an $L_\star(K)$ galaxy (where $L_\star(K)$ is the K band $L_\star$) for an instantaneous starburst at $z = 5$ and $z = 10$ as well as a no-evolution curve, as derived by Jarvis et al. (2001a). The majority of the sources lie brighter than $L_\star$.

4.7.4 Extremely red objects

Figure 4.9 shows the $R-K$ colour of the common optical counterparts to the radio-X-ray matches as a function of the R magnitude. One notes that the $R-K$ colour tend to increase to fainter magnitudes. A similar trend has been reported by several studies (e.g. Lehmann et al. 2001; Alexander et al. 2001; Mainieri et al. 2002). Galaxies (stellarity < 0.7) rapidly become redder than point-like objects (stellarity ≥ 0.7). One also notes the clear separation between the two groups. This can be seen in a more pronounced way in Figure 4.16, where the $Bw-I$ colour is plotted versus the $I-K$ colour (see section 4.10). It is important to note that this result might

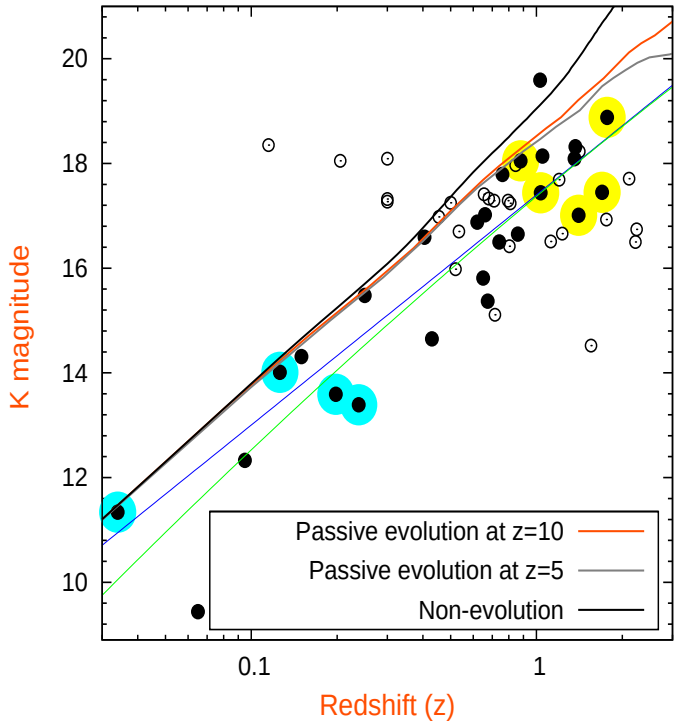

Figure 4.8: The K magnitude versus redshift z for all the optical counterparts to the radio-X-ray matches. The green line shows the best fit $K-z$ relation of Willott et al. (2003) and the blue line shows the best fit $K-z$ relation for only extended objects (point sources are not included in this fit). The three upper plots show the passive stellar evolutionary tracks of an $L_\star(K)$ galaxy (where $L_\star(K)$ is the K band $L_\star$) for an instantaneous starburst at $z=5$ and $z=10$ as well as a no-evolution curve, as derived by Jarvis et al. (2001a). Same symbols as for the radio-X-ray matches in Fig 4.9

be biased due to the fact that many sources are not detected at K band. The vertical line in Figure 4.9 shows the approximate K band completeness limit. There are 25 radio-X-ray matches don't have measured K magnitudes and will lie to the right of this line. The correlation would look somewhat different if those 25 sources had measured K magnitudes, so the result should be taken with caution. Five interesting objects are associated with bright near infrared sources with $17 < K < 19$ and their colour ($R - K > 5$) place them in the ERO population. In this subsample of the EROs, four are classified as AGN1 and one source is classified as AGN2 based on their X-ray properties. The red colour of the radio-X-ray matches can be explained by either obscured AGN or a high redshift cluster of galaxies (Lehmann et al. 2001). The extremely red colour of X-ray sources can be used as a good tracer of red galaxies at high redshifts. Near infrared spectroscopy observations have confirmed this (Cowie et al. 2001).

The ERO population is well known to be a mixture of old passively evolving ellipticals and star-forming galaxies strongly reddened by dust extinction at high redshift ($z > 1$). Photometric and spectroscopic classifications (see e.g. Cimatti et al. 2003; Smail et al. 2002) have shown that the ERO population is almost equally divided between the two components.

The photometric redshift of the four EROs range from 0.88 to 1.77 and the spectral type classify two EROs as elliptical, two as starburst galaxies and the last one as lenticular. Moreover, these sources have a high X-ray to optical flux ratio $\log(f_X/f_{opt}) > 1$ (see Figure 4.14, yellow filled circles) and this signature can be used to pick out high redshift X-ray sources. Obviously spectroscopic confirmation is required to explore this further. The X-ray luminosities in the 0.5-7 keV rest-frame energy band of the EROs are in the range $10^{43} - 10^{44}$ erg s^{-1}, suggesting that the EROs subsample is heavily dominated by sources with strong AGN activity.

4.8 X-ray and radio luminosities

In the following, the photometric redshift estimate has been used to calculate the X-ray and radio luminosities. I also used the spectroscopic redshift measurements whenever available.

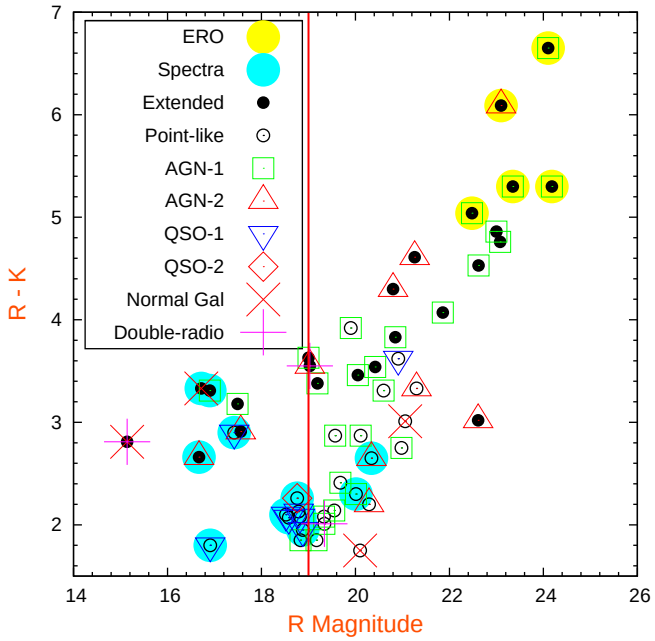

Figure 4.9: Colour magnitude diagram $R - K$ versus R-band magnitude for all radio-X-ray matches identified in both R and K bands in Boötes field. The objects are marked according to their X-ray classification: open circles are identifications with stellar profiles and small filled circles denote extended objects. Empty squares represent sources classified as AGN-1, triangles for sources classified as AGN-2, reversed triangles denote sources classified as QSO-1, diamonds for sources classified as QSO-2, cyan large circles denote sources with optical spectroscopic identification, yellow large circles represent EROs, large crosses for normal galaxies and plus signs for radio sources resolved into multi-components. The vertical line shows the approximate K band completeness limit.

4.8.1 Radio luminosity

The rest-frame radio luminosity density was calculated from the following equation:

$$L_{1.4\ \mathrm{GHz}} = 4\pi\, d_L^2\, S_{1.4\ \mathrm{GHz}}\, (1+z)^{-1+\alpha}\ 10^{-33}\ \mathrm{W\ Hz^{-1}}, \tag{4.2}$$

where d_L is the luminosity distance (in cm), $S_{1.4}$ is the 1.4 GHz flux density (in mJy), and α is the radio spectral index ($f_\nu \propto \nu^{-\alpha}$), which I take to be 0.8. In Figure 4.10 (bottom panel) I plot the 1.4 GHz luminosity as a function of redshift for all the radio-X-ray matches. Many of the objects are close to the lower radio flux limit. Many of the AGN-1 sources cluster around a redshift of $z \sim 0.7$.

4.8.2 X-ray luminosity

In Figure 4.10 I plot the X-ray (0.5 – 7 keV) luminosity (upper panel) as a function of redshift. The rest-frame X-ray luminosity was calculated from:

$$L_X = 4\pi\, d_L^2\, f_X\, (1+z)^{-2+\Gamma}\ \mathrm{erg\ s^{-1}}. \tag{4.3}$$

Here d_L is the luminosity distance (in cm), f_X is the observed full X-ray flux (in erg s^{-1} cm^{-2}). Γ is the photon index assumed to be $\Gamma = 1.8$ for all sources. Barger et al. (2002) has shown that the use of individual indices result in only small differences in the rest-frame luminosities (see also Barger et al. 2007).

In order to classify the X-ray counterparts to FIRST radio sources, I used the same procedure adopted by Szokoly et al. (2004). Following Szokoly et al. (2004) the X-ray sources can be classified based only on their observed X-ray L_X properties and the hardness ratio HR = $h - s/h + s$, where s is the number of counts detected in the 0.5-2 keV band and h is the number of counts detected in the 2-7 keV band. The X-ray luminosity L_X is derived from the 0.5 – 7 keV fluxes and spectroscopic/photometric redshifts. The criteria adopted by Szokoly et al. (2004) is as follows:

1. Galaxy: $L_X \leq 10^{42}$ erg. s^{-1} with hardness ratio $HR < -0.2$.

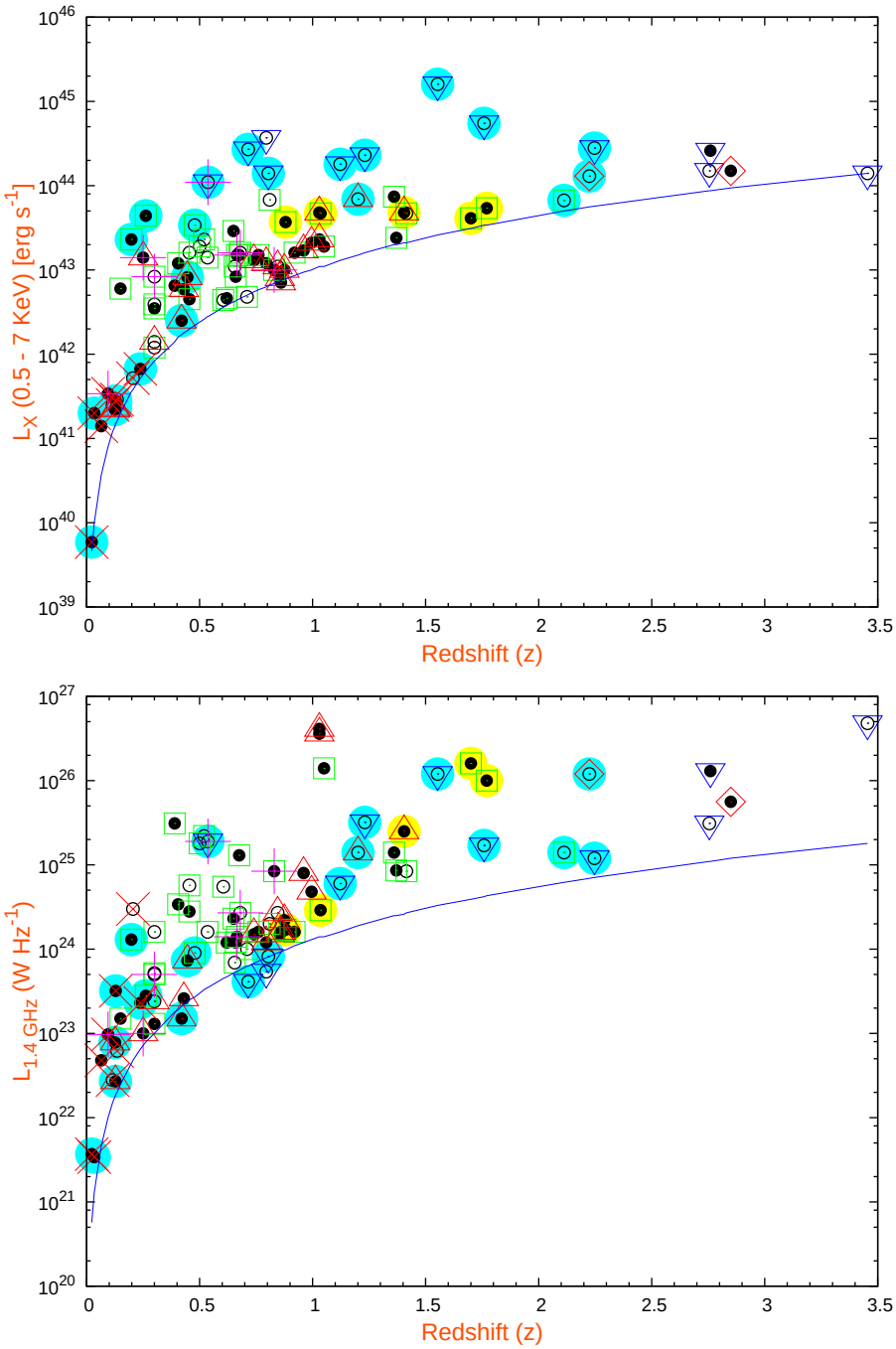

Figure 4.10: Full (0.5 – 7) keV X-ray luminosity versus redshift for the radio-X-ray matches is shown in the top panel. Solid line represents the faintest limiting X-ray luminosity for a source with a full flux of $\sim 8 \times 10^{-15}$ erg s^{-1} cm^{-2} as a function of redshift. The lower panel shows the radio luminosity as a function of redshift for all the radio-X-ray matches and the solid line corresponds to the radio flux limit of 1 mJy. Sources with spectroscopic redshift are shown with large filled circles (cyan colour). Same symbols as for the radio-X-ray matches in Fig 4.9.

2. AGN-2: $10^{41} \leq L_X < 10^{44}$ erg. s^{-1} and the hardness ratio $HR > -0.2$.

3. AGN-1: $10^{42} \leq L_X < 10^{44}$ erg. s^{-1} and the hardness ratio $HR \leq -0.2$.

4. QSO-2: $L_X > 10^{44}$ erg. s^{-1} with hardness ratio $HR > -0.2$.

5. QSO-1: $L_X > 10^{44}$ erg. s^{-1} with hardness ratio $HR < -0.2$.

The classification criteria yielded 37 radio-X-ray matches classified as AGN-1, 19 classified as AGN-2. Normal galaxies represent a small fraction of 9 sources while 12 sources were classified as QSO-1 sources and 10 sources of these are spectroscopically classified as QSOs and some of these sources are also identified in ROSAT. The QSO-2 type constitutes the smallest fraction: only two candidates are classified as QSO-2 sources. The lack of high X-ray luminosity of type 2 quasars is a well known effect, only a few sources considered as the prototype of type 2 quasars have been detected (Norman et al. 2002; Stern et al. 2002a), but many more have been identified since then (e.g. Padovani et al. 2004).

As discussed previously, different types of X-ray sources are separated in the plot of X-ray hardness ratio versus X-ray luminosity. This trend is shown in Figure 4.11, where the hardness ratio as a function of the soft X-ray luminosity is illustrated in the top panel and as a function of the hard X-ray luminosity in the lower panel.

4.8.3 X-ray-radio correlation?

At the sub-mJy and μJy levels, radio emission is known to be a highly indirect indicator of star formation rate (see the review by Condon 1992) because of the extremely tight FIR-radio correlation, which deviates by less than a factor of two over five orders of magnitude. A number of studies have investigated the radio-derived SFRs and find them to be in good agreement with the FIR derived values (e.g. Condon et al. 1991; Haarsma et al. 2000; Hopkins et al. 2001; Bell 2003). The disadvantage of this method is that it is hard to account for the contamination of the radio flux by AGNs. Moreover, star-forming and spiral galaxies are also found to be powerful X-ray emitters with luminosities that sometimes exceed 10^{42} erg s^{-1} (e.g. NGC 3265; Moran et al. 1999). This is believed to be due to a number of high mass X-ray binaries, young supernovae remnants and hot gas plasma associated with star-forming regions (see the review

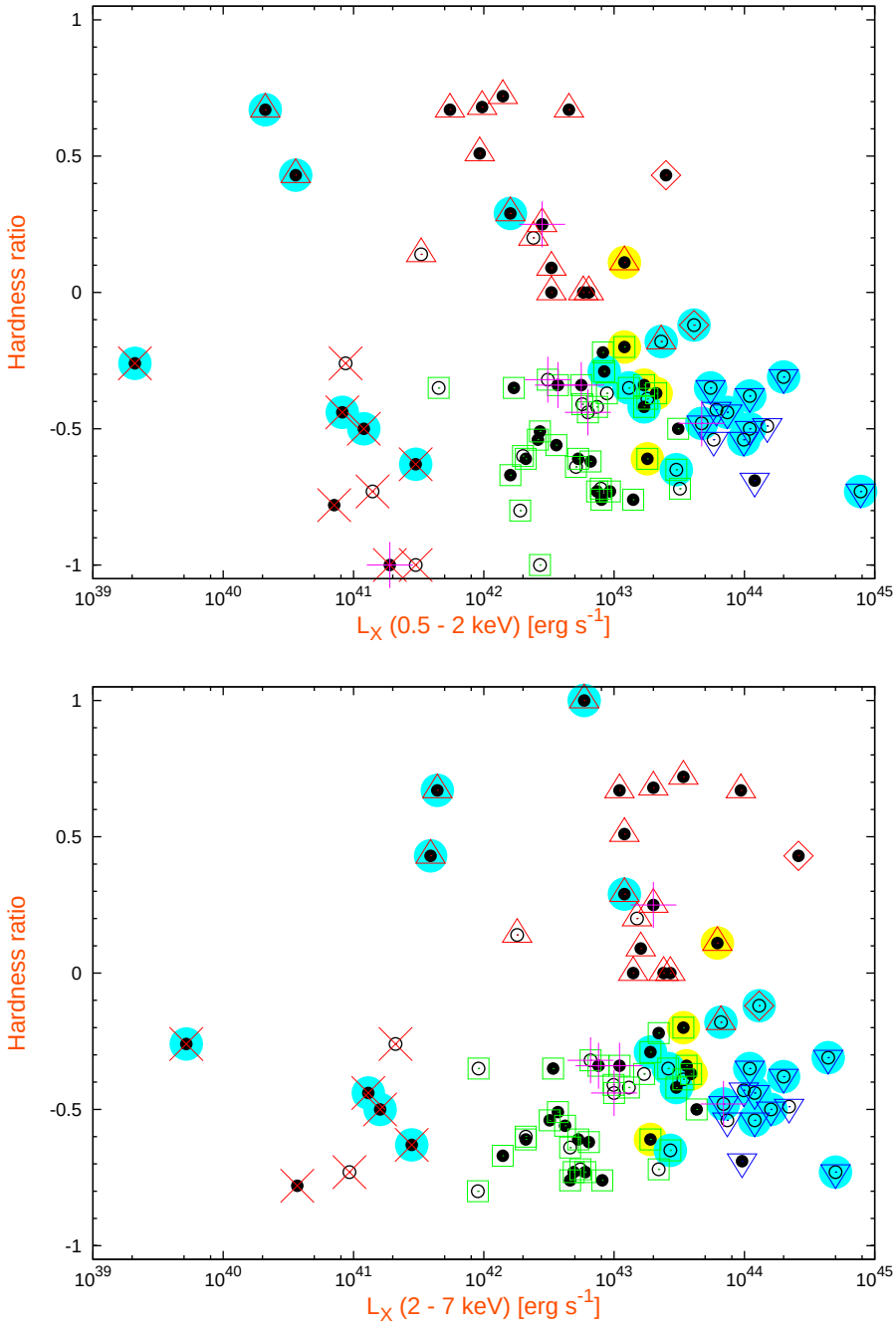

Figure 4.11: The hardness ratio as a function of the soft X-ray luminosity (top panel) and the hard X-ray luminosity (bottom panel) for the radio-X-ray matches. Same symbols as for the radio-X-ray matches in Fig 4.9.

by Fabbiano 1989). With the latest generation of X-ray satellites such as Chandra and XMM, it is now possible to study the X-ray-SFR correlation (Bauer et al. 2002a; Franceschini et al. 2003; Grimm et al. 2003; Ranalli et al. 2003). Early results show good agreement with FIR and radio estimates of the SFR.

Correlations between X-ray and radio luminosities for radio-quiet AGN have been determined by Brinkmann et al. (2000). These authors have cross correlated the FIRST radio survey ($S_{1.4\ \mathrm{GHz}} > 1$mJy) and the ROSAT ($f_X > 10^{-13}$ erg s^{-1}cm^{-2}) and shown that the X-ray and radio luminosities for radio quiet AGN follow a relatively tight linear correlation in the form:

$$\log(L_X\ \mathrm{erg\ s^{-1}}) = (-4.57 \pm 2.55) + (1.012 \pm 0.083)\ \log(L_{1.4\ \mathrm{GHz}}). \tag{4.4}$$

Simpson et al. (2006) have converted the previous correlations (found for X-ray-radio AGN) to relationships between fluxes in the form of:

$$S_{0.5-2\ \mathrm{keV}}\ (\mathrm{W\ m^{-2}}) = 10^{-15.5}\ S_{1.4\ \mathrm{GHz}}\ (\mathrm{mJy}), \tag{4.5}$$

$$S_{2-10\ \mathrm{keV}}\ (\mathrm{W\ m^{-2}}) = 10^{-15.3}\ S_{1.4\ \mathrm{GHz}}\ (\mathrm{mJy}), \tag{4.6}$$

and also converted correlations found for X-ray-radio star-forming galaxies into relations between fluxes :

$$S_{0.5-2\ \mathrm{keV}}\ (\mathrm{W\ m^{-2}}) = 10^{-18}\ S_{1.4\ \mathrm{GHz}}\ (\mathrm{mJy}), \tag{4.7}$$

$$S_{2-10\ \mathrm{keV}}\ (\mathrm{W\ m^{-2}}) = 10^{-18}\ S_{1.4\ \mathrm{GHz}}\ (\mathrm{mJy}), \tag{4.8}$$

and used these relations in their plot of X-ray flux versus radio flux density in order to determine the nature of their radio-X-ray matches, depending on which of the two correlations they are closer to (radio quiet AGNs or starburst galaxies). They suggest that 20% or more of the radio sources in their sample with $100\,\mu\mathrm{Jy} < S_{1.4\ \mathrm{GHz}} < 300\,\mu\mathrm{Jy}$ are radio quiet AGNs. They also claim that the radio-X-ray correlation found for radio quiet AGN might be biased to unusually high X-ray-luminous sources because it is derived from cross correlation of a deep radio catalogue (FIRST) and a shallower X-ray survey (ROSAT).

The top panel in Figure 4.12 shows the distribution of the full (0.5-7 keV) X-ray flux (in erg cm^{-2} s^{-1}) against radio flux density (in mJy). It is immediately clear from this plot that there is no obvious correlation between radio and X-ray fluxes. It is clearly seen from the figure that the majority of the radio-X-ray matches have a radio flux below 10 mJy. Three sources are detected below the radio flux density limit (1 mJy); two of these sources are optically star-like and X-ray bright sources of which one is spectroscopically identified as a QSO. The third source is an optically extended source and is spectroscopically identified as galaxy showing a narrow emission line. This source is classified as an AGN-2 based on its X-ray luminosity and hardness ratio. One also notes that the radio-X-ray matches span a large range in the radio-X-ray diagram which is consistent with observations of classical AGN. The scatter in the radio-X-ray diagram of AGN is not surprising considering that AGN have been found to be radio loud and radio quiet, depending on orientation, AGN activity, presence of jets etc., and also X-ray loud and X-ray quiet, depending on AGN activity, amount of absorption etc. There is also variability of objects that possibly needs to be considered as the VLA and Chandra xBoötes observations were taken more than 6 years apart. It is known that radio loud AGN vary on levels of 10-20% in flux over few months in both X-rays and radio waves. Radio variability is not so well studied for radio quiet AGN, e.g. Seyferts, but Wrobel (2000) has shown that they can vary by 20-50% over a few months which is consistent with their known X-ray variability.

The lower panel in Figure 4.12 shows the full X-ray luminosity versus the radio luminosity. From Figure 16 and Figure 17 (lower panel) galaxies extend to lower radio/X-ray luminosities from the quasar population with some overlap. The majority of the radio-X-ray matches tend to have a small radio to X-ray luminosity ratio (Figure 4.12), corresponding to radio-quiet AGN. The small sample size and incompleteness of the spectroscopy do not allow more quantitative conclusions.

4.9 X-ray-to-optical flux ratio

The X-ray-to-optical flux ratio is an important tool that can be used to explore the nature of the X-ray sources. Previous studies (e.g. Maccacaro et al. 1988; Elvis et al. 1994) have shown

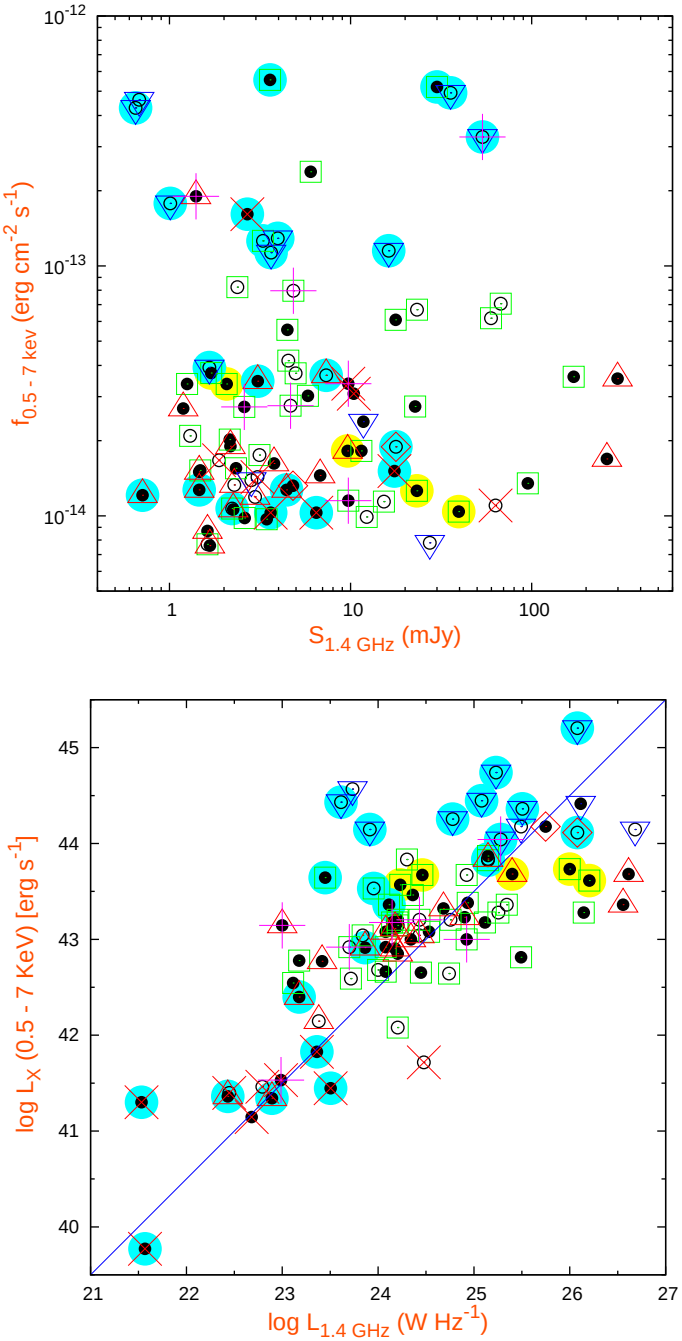

Figure 4.12: The upper panel shows the full X-ray flux as a function of radio flux density with the class of sources indicated by the symbols. The lower panel displays the full X-ray luminosity versus the radio luminosity for the radio-X-ray matches. The symbols are the same as in Fig. 4.9.

that there is an empirical relationship between X-ray and optical emission in AGN, and this can yield important information on the nature of AGN activity. In the X-ray optical plane, powerful unobscured AGNs (Stocke et al. 1991; Barger et al. 2003) typically have flux ratios of $-1 < \log f_{(2-7)\ \mathrm{keV}}/f_{\mathrm{opt}} < +1$, while star forming galaxies and low luminosity AGNs tend to have $\log f_{(2-7)\ \mathrm{keV}}/f_{\mathrm{opt}} \leq -1$ (e.g. Alexander et al. 2001; Hornschemeier et al. 2001; Giacconi et al. 2002). The X-ray-to-optical flux ratio is estimated from the relation (Hornschemeier et al. 2001):

$$\log \frac{f_X}{f_{\mathrm{opt}}} = \log f_X + 0.4\,R + 5.53, \tag{4.9}$$

where the flux is measured in units of 10^{-15} erg s^{-1} cm^{-2} in the considered X-ray band and R is the apparent R-band Vega magnitude.

In Figure 4.13 I plot the R magnitude as a function of the 0.5 – 7 keV X-ray flux for the radio-X-ray matches (top panel). The middle panel displays the 2 – 7 keV X-ray flux for the radio-X-ray matches. Also shown in this plot is the Akiyama et al. (2000) ASCA Large Sky Survey data (two clusters and one source without an optical identification have been excluded) (filled diamonds). The bottom panel shows the 0.5 – 2 keV soft X-ray flux for the radio-X-ray matches. The figures show that there is a large fraction of the sources that span the typical X-ray-to-optical flux ratio of the AGN region. The majority of the radio-X-ray matches (68%) fall within $\log f_{(2-7)\ \mathrm{keV}}/f_{\mathrm{opt}} = 0.0 \pm 1.0$. One notes that there is also a significant population ($\sim$ 23%) of sources that are X-ray over-luminous for their optical magnitudes [$\log f_{(2-7)\ \mathrm{keV}}/f_{\mathrm{opt}} > 1$]. This can be seen clearly in the full and hard bands, suggesting high redshift sources and/or dust obscuration (Alexander et al. 2001; Fiore et al. 2003; Brusa et al. 2003; Georgantopoulos et al. 2004; Mignoli et al. 2004; Gandhi et al. 2004; Georgakakis et al. 2004). Among sources with high X-ray-to-optical flux ratio five are EROs shown with yellow filled circles. Two optically non-identified sources fit within this category but are not plotted here.

Recent studies have revealed a population of optically bright X-ray faint sources. Such a population was unveiled by the Chandra deep survey (Hornschemeier et al. 2001; Tozzi et al. 2001) and appear to be at $z \lesssim 1$. These sources appear mainly at very faint X-ray fluxes ($f_X \lesssim \times 10^{-15}$ erg s^{-1} cm^{-2}), and were found to comprise star-forming galaxies, normal galaxies and low luminosity AGN (with $L_X < 10^{42}$ erg s^{-1} in the 0.5−10 keV band). However, in this analysis

7 (8%) radio-X-ray matches are found to be optically bright and X-ray faint [$\log f_{(2-7)\ \mathrm{keV}}/f_{\mathrm{opt}} < -1$]. All are extended objects in the R band image (sources # 20, # 29, #39, # 42, # 44, # 48, # 71) and their R magnitude is in the range $15 < R < 18$ (and $I < 17$). Four of these sources are classified spectroscopically as galaxies: source # 29, source # 39, source # 42 and source #71, with spectroscopic redshifts of $z = 0.128$, $z = 0.126$, $z = 0.238$ and $z = 0.129$ respectively (see their spectra in Figure 4.19). Thus, these sources should be nearby, bright normal galaxies (see e.g. Barger et al. 2001; Hornschemeier et al. 2001; Tozzi et al. 2001). In addition, two of the spectroscopically identified sources are classified as AGN2 (# 29 and # 39) with $L_X[0.5-7\ \mathrm{keV}] = 2.3\times10^{41}$ erg s^{-1}. and $L_X[0.5-7\ \mathrm{keV}] = 2.2\times10^{41}$ erg s^{-1} respectively. The other two are classified as normal galaxies (# 42 and # 71, the optical spectra of the latter source show emission lines that identify the source as a star-forming galaxy) which are however X-ray luminous: $L_X[0.5-7\ \mathrm{keV}] = 6.7\times10^{41}$ erg s^{-1}, and $L_X[0.5-7\ \mathrm{keV}] = 2.8\times10^{41}$ erg s^{-1}.

4.10 General properties of the radio-X-ray sample

4.10.1 HR-X-ray-to-optical flux ratio-colour

Figure 4.14 displays the X-ray-to-optical flux ratio (calculated using equation 4.9) as a function of the hardness ratio (upper panel) and as a function of the colour $Bw-R$ colour (lower panel). Although the radio/X-ray matches span a large range of hardness ratios, most cluster around the soft values (HR~ -0.4). The majority of these sources have point-like optical morphology and 12 of them are spectroscopically identified as QSOs with broad emission lines and high f_X/f_{opt}, while 2 sources spectroscopically are identified as galaxies showing narrow emission lines with high X-ray-to-optical flux ratio ($\log f_X/f_{opt} > -1$) with high hardness ratio, possibly suggesting high column densities. The lower panel in Figure 4.14 shows that the optically extended sources have, on average, a red colour ($Bw-R \geq 1.5$), suggesting that the optical light is dominated by the host galaxy rather than the central AGN (see e.g. Barger et al. 2003; Gandhi et al. 2004). Additional evidence that the optical/NIR light in many sources is dominated by the host galaxy can be seen in Figure 4.18 where the optical-NIR colour is plotted versus redshift and the magnitude respectively.

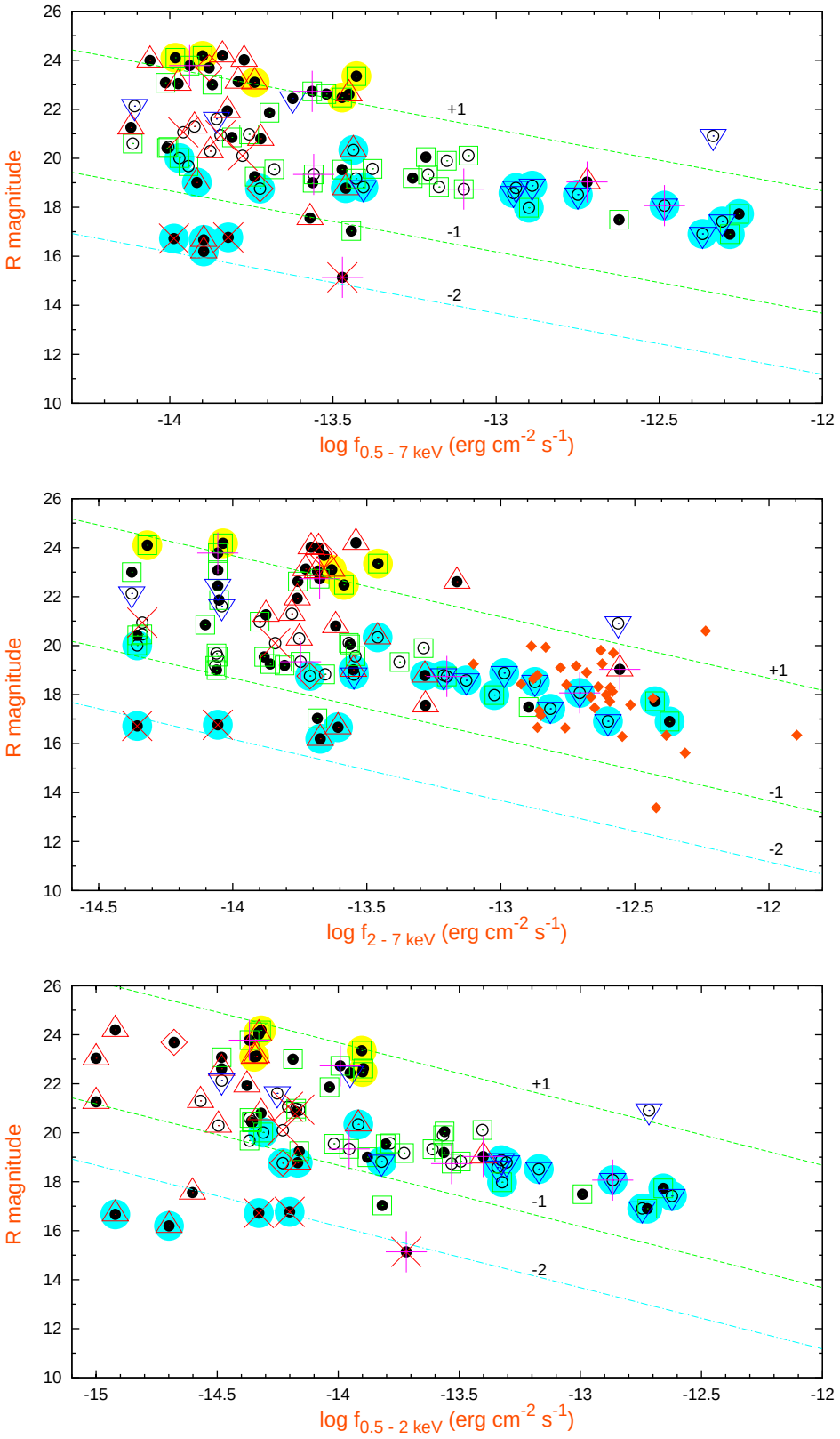

Figure 4.13: Optical *R*-band magnitude of the radio-X-ray matches plotted against the full (0.5-7 KeV) X-ray fluxes in the top panel, hard (2-7 keV) X-ray fluxes in the middle panel and soft (0.5-2 keV) X-ray fluxes in the lower panel. The filled diamonds in the middle panel correspond to the sources in Akiyama et al. (2000). The solid lines denote the location of constant X-ray-to-optical flux ratios of log f_X/f_{opt}=1, 0, -1 from top to bottom as given by equation 4.9. Same symbols as for the radio-X-ray matches in Fig 4.9.

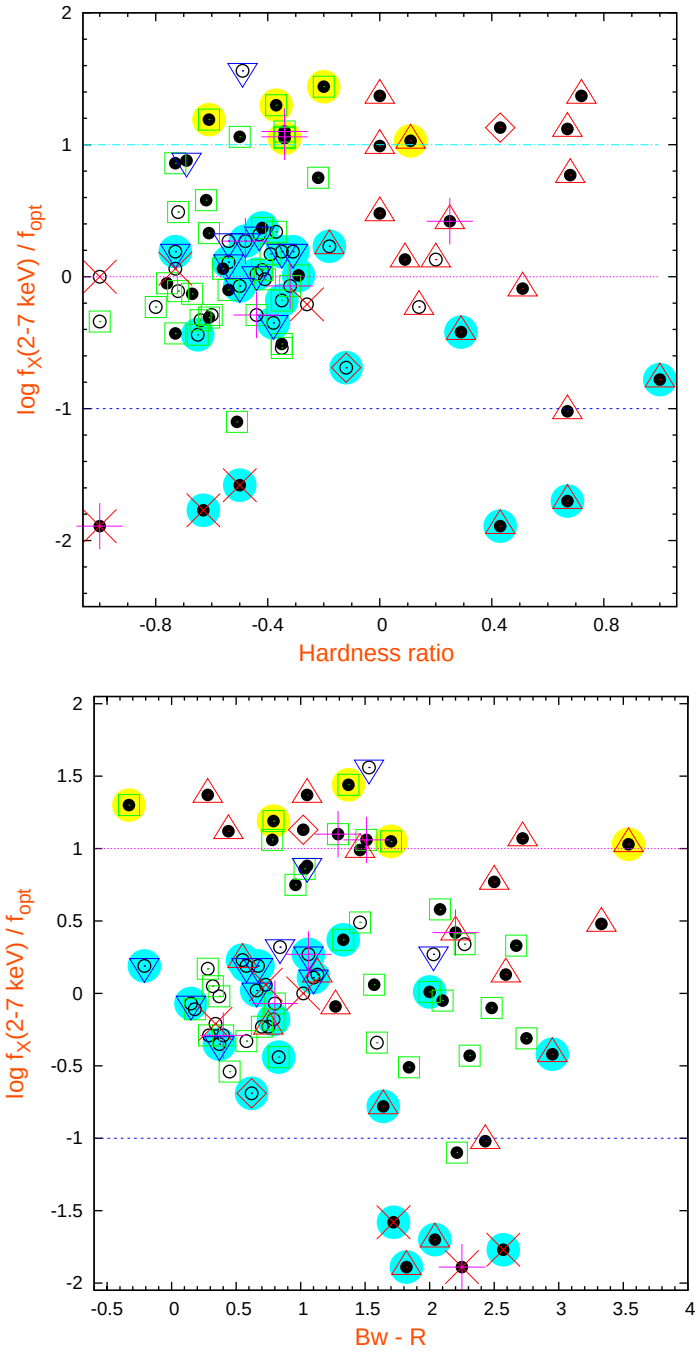

Figure 4.14: The X-ray-to-optical flux ratio as a function of the Hardness ratio HR (HR is defined as (h-s)/(h+s) where h and s are the count rates in the 0.5 keV and 2 – 7 keV bands respectively) (top panel) and as a function of the optical colour $Bw-R$ (bottom panel). Horizontal lines show location of constant X-ray-to-optical flux ratio of +1, 0, and -1. Same symbols as for the radio-X-ray matches in Fig 4.9.

Figure 4.15 illustrates the hardness ratio as function of redshift (top panel) and the optical/near-infrared colour (bottom panel). This figure shows an interesting evolution of the hardness ratio with redshift of the radio-X-ray matches. The hardness ratio declines with redshift, and the majority of the hard X-ray counterparts to FIRST radio sources are at redshift lower than 1.5. The evolution of the hardness ratio with the redshift could be due to a combination of two effects. First, the fraction of AGN which are obscured is higher at lower luminosities (equals lower redshifts in a flux-limited sample). Second, the k-correction for obscured AGN pushes the less obscuration sensistive hard X-rays into the observed band at higher redshift. The hardness ratio versus $R - K$ optical colour is presented in the lower panel of Figure 4.15. In this diagram, no clear correlation between the hardness ratio and optical colour is observed. The lack of a strong correlation can probably be explained by the differences in the intrinsic optical and X-ray spectrum for different types of sources detected in the X-ray bands, independent of the amount of obscuration present. Moreover, it is important to note that the $R - K$ colour for the quasars comes from AGN, not the galaxy. Ignoring the quasars, we see that the very hard sources all have low $R - K$. This is a consequence of the correlation of hardness ratio with redshift in the upper panel and the fact that low $R - K$ are moslty at low redshift. One should note, however, that, in general, sources optically classified as obscured AGN are redder than unobscured AGN and also tend to have higher values of HR.

4.10.2 Colour-colour diagram

Figure 4.16 displays the $Bw - I$ colour versus the $I - K$ colour. The optical point sources tend to occupy a different region from the optically extended ones in the colour-colour diagram. The clear separation between the two groups reflect the effectiveness of the SExtractor parameter to separate extended objects (galaxies) and point-like objects (stars or QSOs). The blue colour of optical point-like objects is consistent with those of quasars. In addition to the point-like objects (13 sources) spectroscopically classified as quasars (cyan filled circles), 20 of the identifications have stellar optical profiles and all of these lie in the AGN region of the X-ray optical plane (see Figure 4.13), suggesting that they are QSOs rather than stars. Figure 4.17 shows the $Bw - R$ colour as a function of R magnitude. A similar trend is shown in this Figure. In this Figure

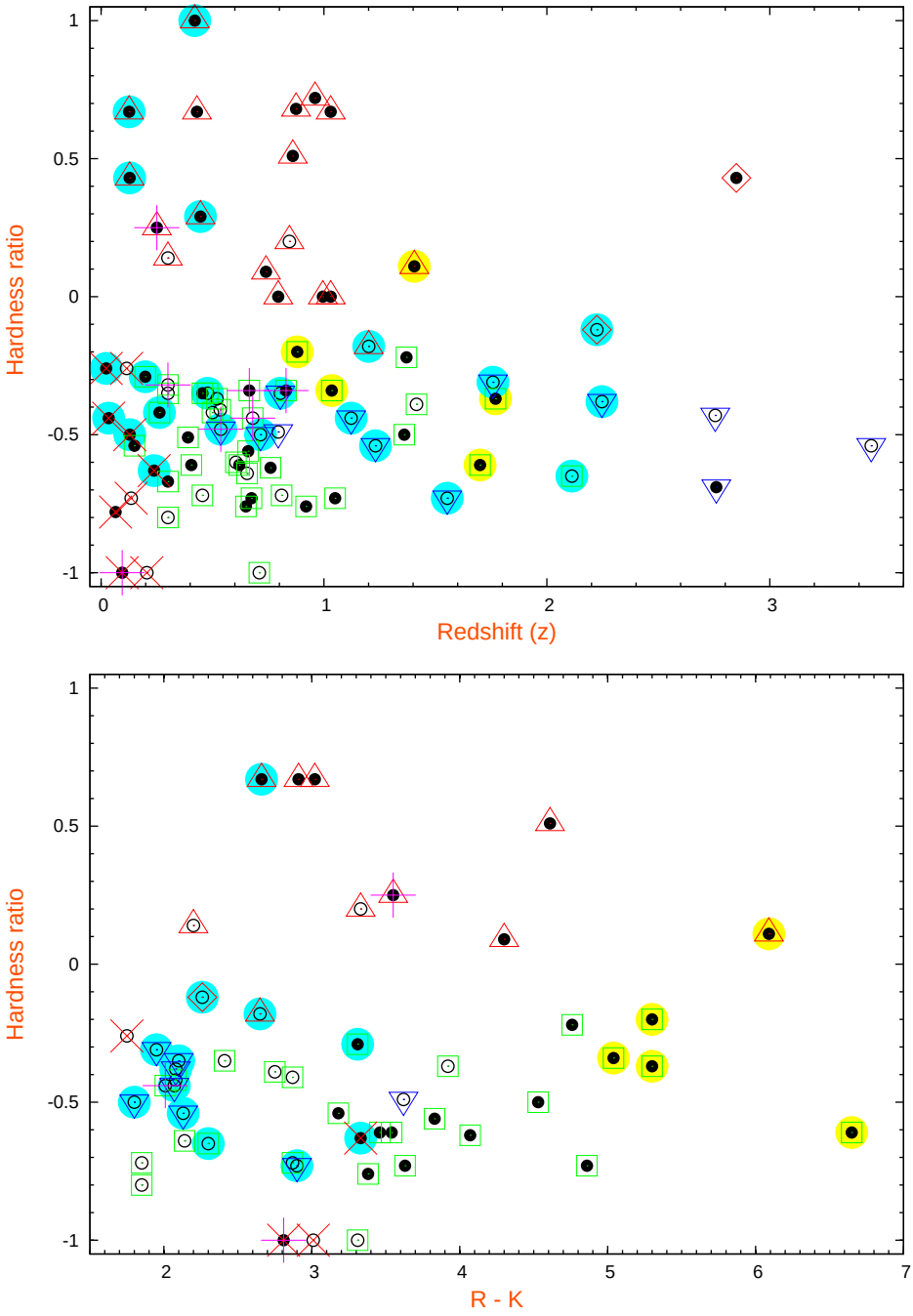

Figure 4.15: The hardness ratio as function of redshift is plotted in the top panel, and as a function of the optical/near-infrared colour is plotted in the bottom panel. Same symbols as for the radio-X-ray matches in Fig 4.9. A clear correlation between HR and the optical/near-infrared colour is not observed.

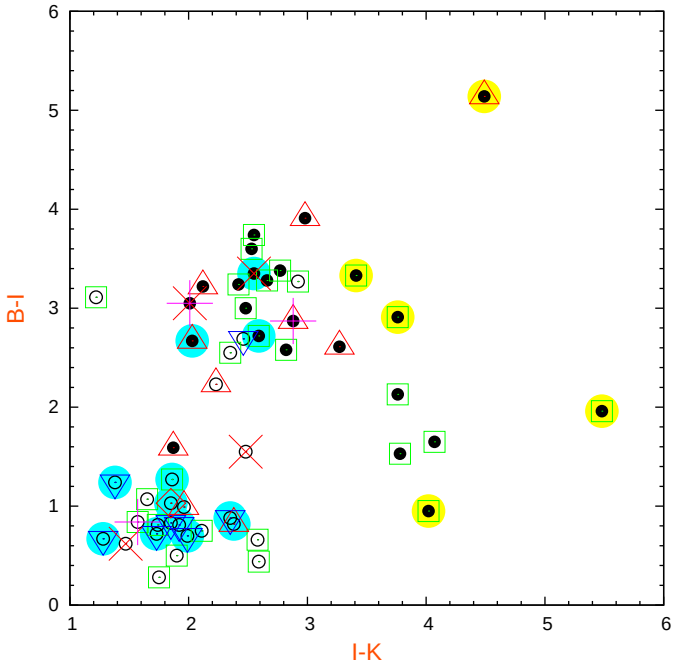

Figure 4.16: Colour-colour diagram for all radio-X-ray matches identified in *Bw, I* and *K* bands in Boötes field. Same symbols as for the radio-X-ray matches in Fig 4.9.

a group of optically extended objects tend to have a bluer colour ($Bw - R < 1$) at fainter magnitudes ($22 < R < 24$). Akiyama et al. (2000) used this criteria to select candidates of broad line AGNs in the LSS area.

Figure 4.18 displays the $R - K$ colour as a function of redshift. Overlaid are the optical/infrared colour of the mean observed spectra of three different galaxy types (E, Sbc, Scd) from Coleman et al. (1980). Broad line AGNs, most of which exhibit soft X-ray spectra, have colours consistent with the QSO template prediction, while the majority of hard X-ray-radio matches have colours which are consistent with the galaxy tracks. The figure also illustrates an interesting segregation between optically extended and point-like objects, and clearly shows that optically extended objects have a redder colour while point-like objects tend to have a blue colour.

4.11 Final data table

The final characteristics of the radio-X-ray matches are presented in Table 4.1 with the following information:

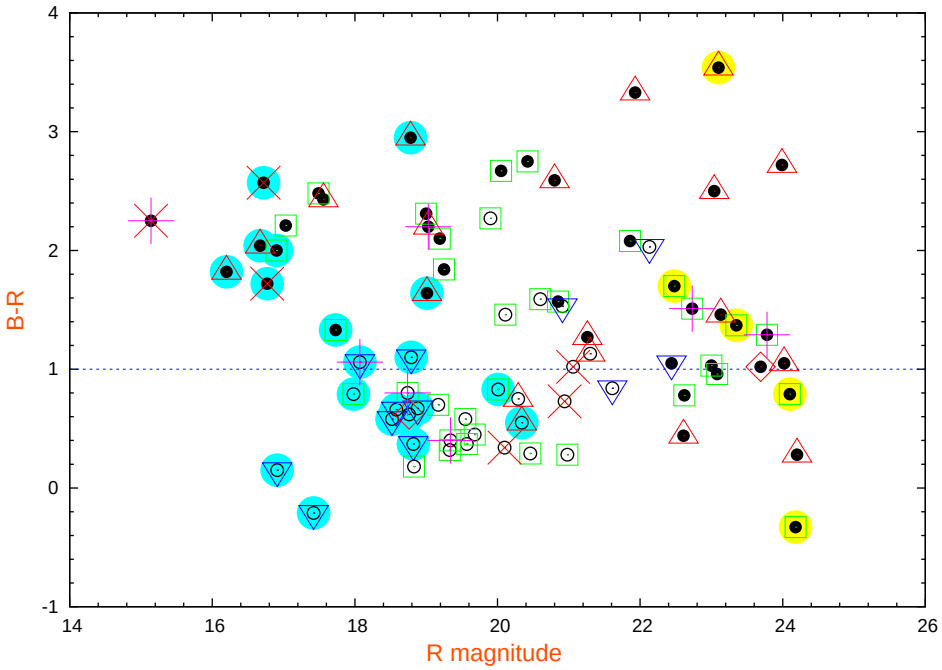

Figure 4.17: Colour magnitude diagram $Bw - R$ versus R-band magnitude for all radio-X-ray matches identified in both Bw and R bands in Boötes field. The horizontal line corresponds to $Bw - R = 1$. Same symbols as for the radio-X-ray matches in Fig 4.9.

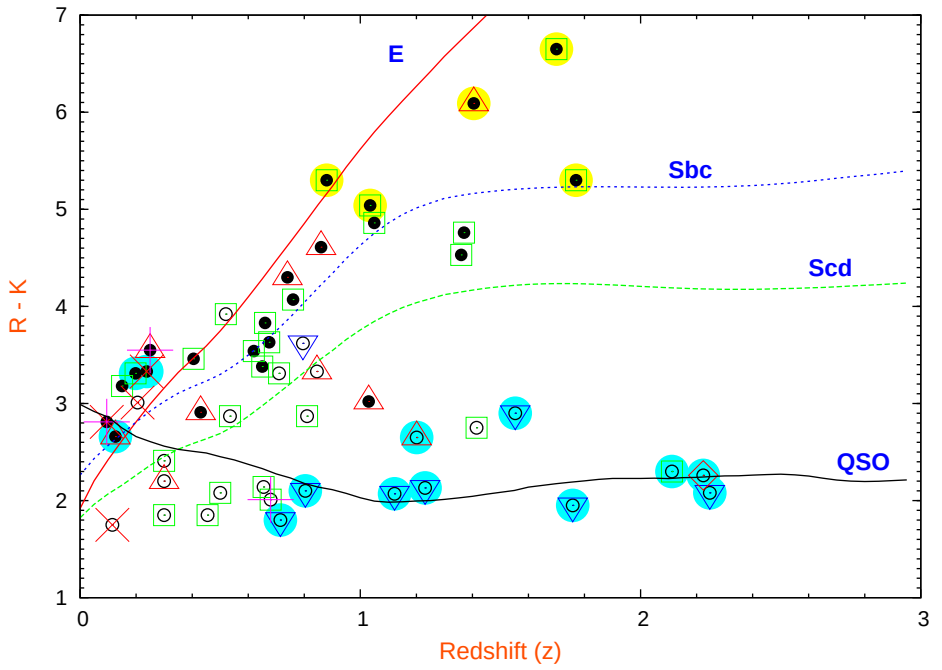

Figure 4.18: Optical/near-infrared colours as a function of photometric/spectroscopic redshift for the radio-X-ray matches. Colour tracks are shown for Coleman-Wu-Weedman (CWW) E (red line), Sbc (blue line) and Sdc (green line) empirical templates. The black line is a colour track of a QSO template obtained from a set of QSO SEDs of the LEPHARE software. Same symbols as for the radio-X-ray matches in Fig 4.9.

- (1) source ID number;
- (2) X-ray object name (X-ray counterparts to FIRST radio sources);
- (3)-(4) radio coordinates in hours, minutes and seconds;
- (5) radio flux in mJy;
- (6)-(7)-(8) the X-ray flux in the full (0.5-7) keV, soft (0.5-2) keV and hard (2-7) keV bands in units of erg s^{-1} cm^{-2};
- (9) the hardness ratio HR, derived from the 0.5-2 and 2-8 keV band counts (Kenter et al. 2005);
- (10) X-ray-to-optical flux ratio;
- (11)-(12)-(13) log of X-ray luminosity in the soft (0.5-2 keV), hard (2-7 keV) and full (0.5-7 keV) bands respectively in erg s^{-1}.

- (14) log of 1.4 GHz luminosity in Whz^{-1};
- (15) the apparent R band magnitude associated with the corresponding errors;
- (16) the optical/near-infrared colour;
- (17) the sourceExtractor stellarity parameter used to classify sources into point-like objects and extended sources;
- (18) the photometric redshift as derived from *Hyperz* with the corresponding errors. Sources with spectroscopic redshift are printed in bold face;
- (19) Classification obtained from the X-ray characteristics (based on the X-ray luminosity and the hardness ratio HR).

4.12 Discussion and Conclusions

In this chapter I have presented the broad band properties of a sample of 79 radio emitting X-ray sources, obtained from a correlation of the FIRST 1.4 GHz survey and the publicly available X-ray data of the medium depth XBoötes field. Out of ∼ 900 FIRST radio sources that lie in the Boötes field, 92 have an X-ray counterparts and 79 optical/infrareds sources are common to both radio and X-ray sources. All the 79 sources are identified in the full X-ray band (0.5-7 keV), 76 in the hard X-ray band (2-7 keV) and 77 in the soft band (0.5-2 keV).

Optical spectra were obtained from the SDSS for 22 radio-Xray matches. The optical classification have revealed different classes of objects: BLAGNs, LINERS, BL Lac and star-forming galaxies.

Photometric redshift was calculated using the public code *Hyperz*. The redshift distribution of the AGNs shows a peak at $z \sim 0.7$, supporting previous studies (Barger et al. 2003) that show that the peak formation of super-massive black holes occurred at relatively recent times ($z < 1$). This leads to the conclusion that medium depth X-ray surveys are well suited for studying and probing this epoch effectively.

X-ray luminosities have been calculated using photometric redshifts and also spectroscopic redshift wherever available. The majority (88%) of the sources have a high X-ray luminosity in the full band, $L_X > 10^{42}$ erg s^{-1}, and 11% of sources have low X-ray luminosity, $L_X < 10^{42}$ erg s^{-1}. The classification of the radio-X-ray matches based on the hardness ratio and X-ray luminosity yielded 46% AGN-1 (unobscured), 24% AGN-2 (obscured), 15% QSO-1, 3% QSO-2 and 11% normal galaxies. One should note that 13 sources were spectroscopically classified as QSO (by SDSS) and 12/13 were classified as QSO-1 based on X-ray luminosity and hardness ratio. Si it is interesting that the X-ray classification scheme is largely coincident with the classical AGN classification based on optical spectroscopic diagnostics.

The X-ray-to-optical flux ratios is a good discriminator between X-ray sources calsses down to very faint optical magnitudes and X-ray fluxes, with AGN typically falling within the region defined by the loci $\log f_X/f_{opt} = 0 \pm 1$, and star-forming galaxies and low luminosity AGNs have $\log f_X/f_{\rm opt} \leq -1$. The majority of the radio-X-ray matches (68%) are AGN ($\log f_X/f_{opt} = 0 \pm 1$). One notes again that all the sources classified as QSO (by SDSS) fall within this region.

A significant population (23%) exists with high X-ray-to-optical flux ratio (log $f_X/f_{opt} > 1$) corresponding to high redshift or dust obscuration, and 8% have low X-ray-to-optical flux ratio (log $f_X/f_{opt} \leq -1$) that comprise normal galaxies and low X-ray luminosity sources.

The $R-K$ colour of the radio-X-ray matches get redder towards fainter R magnitudes, such trend is not present between $R-K$ and the K magnitude.

Results form this study will be used to calculate the X-ray luminosity function and determine its evolution with redshift in a future study.

Table 4.1: Characterisation of Faint Radio Sources

IDs (1)	Object name (2)	Ra (3)	Dec (4)	$S_{1.4}$ (5)	flux (6)	sflux (7)	hflux (8)	HR (9)	$\log(f_X/f_{opt})$ (10)	$\log(L_X)$ (11)	$\log(L_X)$ (12)	$\log\ L_X(0.5-7)$ (13)	$\log L_{1.4\,GHz}$ (14)	R (15)	R-K (16)	Class (17)	Photo-Z (18)	Class (X-ray) (19)
1	J142449.3+340944	14 : 24 : 49.3	34 : 09 : 44.7	4.53	4.18	1.64	2.87	$-0.41^{+0.07}_{-0.07}$	-0.02	42.76	43.00	43.15	24.20	19.57 ± 0.00	2.87	0.86	$0.535^{+0.584}_{-0.381}$	AGN-1
2	J142456.3+351659	14 : 24 : 56.5	35 : 16 : 59.9	9.71	1.15	0.43	0.88	$-0.34^{+0.21}_{-0.23}$	1.10	42.57	42.88	43.00	24.92	23.78 ± 0.09	.....	0.01	$0.830^{+0.953}_{-0.692}$	AGN-1
3	J142507.3+323137	14 : 25 : 07.3	32 : 31 : 37.5	3.28	12.60	4.75	9.46	$-0.35^{+0.02}_{-0.02}$	-0.18	43.11	43.41	43.53	23.95	17.98 ± 0.00	.....	1.00	**0.478 ± 0.000**	AGN-1
4	J142516.5+345246	14 : 25 : 16.5	34 : 52 : 46.6	63.21	1.10	0.62	0.00	$-1.00^{+0.00}_{-0.40}$	0.00	41.48	.....	41.72	24.48	21.06 ± 0.01	3.01	0.97	$0.205^{+0.585}_{+0.000}$	Gal
5	J142524.2+340936	14 : 25 : 24.2	34 : 09 : 35.7	15.29	1.14	0.43	0.87	$-0.35^{+0.22}_{-0.23}$	-0.54	41.65	41.96	42.08	24.20	19.68 ± 0.00	2.41	0.98	$0.300^{+0.575}_{-0.145}$	AGN-1
6	J142532.8+330125	14 : 25 : 32.8	33 : 01 : 25.4	7.33	3.65	1.21	3.47	$-0.18^{+0.08}_{-0.08}$	0.23	43.36	43.82	43.84	25.15	20.34 ± 0.00	2.65	0.95	**1.201 ± 0.001**	AGN-2
7	J142533.5+345805	14 : 25 : 33.5	34 : 58 : 05.7	2.97	1.19	0.27	1.66	$+0.20^{+0.28}_{-0.26}$	0.13	42.38	43.18	43.04	24.43	21.30 ± 0.01	3.33	0.98	$0.845^{+0.883}_{-0.817}$	AGN-2
8	J142543.9+335534	14 : 25 : 43.9	33 : 55 : 33.2	298.44	3.54	0.33	6.86	$+0.67^{+0.08}_{-0.07}$	1.12	42.65	43.97	43.68	26.61	22.61 ± 0.05	3.02	0.08	$1.030^{+1.047}_{-0.987}$	AGN-2
9	J142552.6+340239	14 : 25 : 52.6	34 : 02 : 39.5	1.25	3.37	1.57	1.31	$-0.67^{+0.08}_{-0.08}$	-0.13	42.20	42.15	42.54	23.11	19.54 ± 0.01	.....	0.03	$0.300^{+0.685}_{+0.000}$	AGN-1
10	J142601.8+343106	14 : 26 : 01.9	34 : 31 : 07.1	3.14	1.75	0.67	1.26	$-0.39^{+0.16}_{-0.17}$	0.17	43.26	43.53	43.67	24.92	20.98 ± 0.01	2.75	0.98	$1.415^{+1.625}_{-1.295}$	AGN-1
11	J142607.7+340425	14 : 26 : 07.7	34 : 04 : 26.3	35.70	49.30	23.90	15.30	$-0.73^{+0.01}_{-0.01}$	0.19	44.89	44.70	45.20	26.08	17.42 ± 0.00	2.90	1.00	**1.553 ± 0.001**	QSO-1
12	J142611.1+354201	14 : 26 : 11.0	35 : 42 : 01.7	2.17	1.90	0.48	2.42	$+0.09^{+0.16}_{-0.16}$	0.13	42.52	43.20	43.11	24.18	20.80 ± 0.01	4.30	0.03	$0.740^{+0.760}_{-0.722}$	AGN-2
13	J142611.1+333932	14 : 26 : 11.1	33 : 39 : 32.7	1.70	3.73	1.25	3.48	$-0.20^{+0.08}_{-0.08}$	1.44	43.08	43.53	43.57	24.23	23.35 ± 0.11	5.30	0.03	$0.880^{+0.964}_{-0.848}$	AGN-1
14	J142620.3+353707	14 : 26 : 20.4	35 : 37 : 08.4	6.02	23.80	10.20	12.70	$-0.54^{+0.01}_{-0.01}$	-0.10	42.41	42.51	42.78	23.18	17.49 ± 0.00	3.18	0.03	$0.150^{+0.592}_{-0.086}$	AGN-1
15	J142624.2+334632	14 : 26 : 24.2	33 : 46 : 32.8	3.44	0.97	0.33	0.88	$-0.22^{+0.26}_{-0.28}$	0.75	42.91	43.34	43.38	24.93	23.08 ± 0.09	4.76	0.08	$1.370^{+1.662}_{-1.297}$	AGN-1
16	J142632.2+350814	14 : 26 : 32.2	35 : 08 : 14.7	95.31	1.35	0.65	0.42	$-0.73^{+0.16}_{-0.22}$	0.86	42.97	42.78	43.28	26.15	23.00 ± 0.07	4.86	0.27	$1.050^{+1.156}_{-0.987}$	AGN-1
17	J142632.6+334621	14 : 26 : 32.4	33 : 46 : 21.3	1.67	0.76	0.10	1.33	$+0.51^{+0.39}_{-0.31}$	-0.09	41.97	43.08	42.85	24.20	21.26 ± 0.03	4.61	0.03	$0.860^{+0.908}_{-0.795}$	AGN-2
18	J142633.6+333211	14 : 26 : 33.6	33 : 32 : 11.8	4.97	3.72	1.87	0.86	$-0.80^{+0.07}_{-0.08}$	-0.23	42.28	41.95	42.59	23.72	19.17 ± 0.00	1.85	0.99	$0.300^{+0.464}_{-0.230}$	AGN-1
19	J142651.5+351924	14 : 26 : 51.5	35 : 19 : 24.7	3.96	12.90	4.72	10.30	$-0.31^{+0.05}_{-0.05}$	0.19	44.30	44.64	44.74	25.23	18.88 ± 0.00	1.95	0.83	**1.758 ± 0.002**	QSO-1
20	J142659.6+341158	14 : 26 : 59.7	34 : 12 : 00.2	9.71	3.38	1.91	0.00	$-1.00^{+0.00}_{+0.00}$	-1.89	41.28	.....	41.53	22.99	15.14 ± 0.00	2.81	0.03	$0.095^{+0.154}_{-0.076}$	Gal
21	J142708.6+331508	14 : 27 : 08.7	33 : 15 : 08.9	10.42	3.08	1.53	0.79	$-0.78^{+0.07}_{-0.08}$	31.62	40.85	40.57	41.15	22.68	.....	.....	0.03	$0.065^{+7.000}_{+0.000}$	Gal
22	J142731.4+324435	14 : 27 : 31.4	32 : 44 : 34.4	2.25	1.06	0.10	2.07	$+0.68^{+0.25}_{-0.19}$	0.77	41.99	43.30	43.00	24.34	23.04 ± 0.05	.....	0.02	$0.875^{+0.932}_{-0.835}$	AGN-2
23	J142735.5+341927	14 : 27 : 35.6	34 : 19 : 28.1	2.59	2.73	1.02	2.11	$-0.34^{+0.21}_{-0.23}$	1.06	42.75	43.04	43.18	24.15	22.73 ± 0.13	.....	0.00	$0.665^{+0.728}_{-0.607}$	AGN-1
24	J142741.4+325433	14 : 27 : 41.6	32 : 54 : 32.1	1.62	0.87	0.00	2.09	$+1.10^{+0.65}_{+0.00}$	1.07	.....	43.28	42.90	24.18	23.99 ± 0.17	.....	0.04	$0.855^{+1.051}_{-0.770}$	AGN-2
25	J142744.4+333828	14 : 27 : 44.4	33 : 38 : 28.6	16.24	11.50	4.96	6.12	$-0.54^{+0.03}_{-0.03}$	0.11	44.00	44.08	44.36	25.51	18.79 ± 0.00	2.13	0.97	**1.231 ± 0.001**	QSO-1
26	J142750.4+344100	14 : 27 : 50.3	34 : 41 : 00.8	1.62	0.77	0.43	0.00	$-1.00^{+0.00}_{+0.00}$	-0.34	42.43	.....	42.68	24.00	20.60 ± 0.03	3.31	0.83	$0.710^{+0.743}_{-0.693}$	AGN-1
27	J142752.2+353031	14 : 27 : 52.2	35 : 30 : 31.8	2.28	1.33	0.32	1.77	$+0.14^{+0.19}_{-0.19}$	-0.23	41.52	42.26	42.15	23.38	20.29 ± 0.01	2.20	0.95	$0.300^{+0.511}_{-0.079}$	AGN-2
28	J142810.3+353846	14 : 28 : 10.3	35 : 38 : 47.0	1.01	17.80	6.74	13.40	$-0.35^{+0.02}_{-0.02}$	0.19	43.74	44.04	44.15	23.91	18.52 ± 0.00	2.10	0.97	**0.804 ± 0.001**	QSO-1
29	J142850.2+323248	14 : 28 : 50.3	32 : 32 : 48.8	1.46	1.27	0.20	2.12	$+0.43^{+0.26}_{-0.18}$	-1.89	40.56	41.59	41.36	22.43	16.20 ± 0.00	.....	0.03	**0.128 ± 0.000**	AGN-2
30	J142852.7+325026	14 : 28 : 52.7	32 : 50 : 27.2	3.07	3.46	0.68	5.21	$+0.29^{+0.08}_{-0.08}$	-0.42	42.20	43.08	42.91	23.86	18.78 ± 0.00	.....	0.03	**0.446 ± 0.000**	AGN-2
31	J142905.1+342640	14 : 29 : 05.1	34 : 26 : 41.1	260.41	1.69	0.47	1.96	$+0.00^{+0.17}_{-0.17}$	1.37	42.81	43.43	43.36	26.56	24.02 ± 0.16	.....	0.51	$1.030^{+1.046}_{-0.997}$	AGN-2
32	J142910.2+352946	14 : 29 : 10.2	35 : 29 : 46.9	17.81	1.89	0.59	1.94	$-0.12^{+0.15}_{-0.15}$	-0.69	43.61	44.11	44.11	26.08	18.76 ± 0.00	2.26	0.98	**2.224 ± 0.001**	QSO-2
33	J142911.1+350320	14 : 29 : 11.2	35 : 03 : 20.7	2.37	8.22	3.94	2.71	$-0.72^{+0.04}_{-0.04}$	0.49	43.51	43.34	43.83	24.30	20.11 ± 0.02	2.87	1.00	$0.810^{+0.822}_{-0.799}$	AGN-1
34	J142916.1+335536	14 : 29 : 16.1	33 : 55 : 38.8	2.07	3.37	1.26	2.60	$-0.34^{+0.21}_{-0.23}$	1.05	43.23	43.56	43.67	24.46	22.48 ± 0.04	5.04	0.04	$1.035^{+1.102}_{-1.024}$	AGN-1
35	J142917.4+332626	14 : 29 : 17.4	33 : 26 : 26.4	6.79	1.45	0.12	2.88	$+0.72^{+0.21}_{-0.16}$	1.37	42.15	43.53	43.23	24.90	24.20 ± 0.12	.....	0.11	$0.960^{+1.227}_{-0.806}$	AGN-2
36	J142922.8+351218	14 : 29 : 22.8	35 : 12 : 19.7	1.48	1.52	0.74	0.43	$-0.76^{+0.17}_{-0.22}$	31.31	42.90	42.66	43.20	24.20	..... 1.00	0.00	0.50	$0.920^{+1.102}_{-0.743}$	AGN-1
37	J142942.6+335654	14 : 29 : 42.6	33 : 56 : 55.0	3.64	11.30	4.55	7.43	$-0.44^{+0.03}_{-0.03}$	0.02	43.87	44.08	44.26	24.78	18.58 ± 0.00	2.07	0.98	**1.122 ± 0.0001**	QSO-1
38	J142955.6+353707	14 : 29 : 55.7	35 : 37 : 07.6	11.78	2.38	1.12	0.88	$-0.69^{+0.12}_{-0.14}$	0.88	44.08	43.98	44.41	26.11	22.44 ± 0.04	.....	0.35	$2.760^{+3.001}_{-2.424}$	QSO-1
39	J143003.1+340649	14 : 30 : 03.1	34 : 06 : 51.3	4.43	1.27	0.12	2.47	$+0.67^{+0.21}_{-0.19}$	-1.70	40.32	41.64	41.34	22.89	16.67 ± 0.00	2.66	0.31	**0.126 ± 0.000**	AGN-2
40	J143008.8+344713	14 : 30 : 08.9	34 : 47 : 13.8	27.38	0.78	0.33	0.42	$-0.54^{+0.29}_{-0.37}$	0.27	43.76	43.87	44.15	26.68	22.13 ± 0.04	.....	0.80	$3.455^{+3.552}_{-3.184}$	QSO-1
41	J143011.5+350019	14 : 30 : 11.5	35 : 00 : 19.7	4.66	2.76	1.11	1.79	$-0.44^{+0.10}_{-0.10}$	-0.29	42.80	43.00	43.20	24.43	19.34 ± 0.00	2.01	0.98	$0.680^{+0.781}_{-0.601}$	AGN-1
42	J143103.6+334541	14 : 31 : 03.4	33 : 45 : 41.6	3.62	1.03	0.47	0.44	$-0.63^{+0.23}_{-0.30}$	-1.77	41.48	41.45	41.83	23.36	16.72 ± 0.00	3.33	0.03	**0.238 ± 0.000**	Gal
43	J143112.4+353527	14 : 31 : 12.5	35 : 35 : 27.3	9.64	1.82	0.45	2.34	$+0.11^{+0.15}_{-0.15}$	1.03	43.08	43.79	43.68	25.40	23.10 ± 0.05	6.09	0.27	$1.405^{+1.447}_{-1.044}$	AGN-2
44	J143114.4+323225	14 : 31 : 14.3	32 : 32 : 25.6	170.73	3.60	1.52	2.07	$-0.51^{+0.07}_{-0.07}$	-1.10	42.43	42.57	42.81	25.49	17.03 ± 0.00	.....	0.03	$0.390^{+0.481}_{-0.344}$	AGN-1
45	J143121.8+344046	14 : 31 : 21.9	34 : 40 : 46.6	1.40	19.00	3.97	27.80	$+0.25^{+0.03}_{-0.03}$	0.42	42.45	43.30	43.15	23.00	19.03 ± 0.00	3.55	0.03	$0.250^{+0.319}_{-0.156}$	AGN-2
46	J143125.0+331350	14 : 31 : 25.3	33 : 13 : 48.3	6.47	1.03	0.36	0.90	$-0.26^{+0.28}_{-0.30}$	31.14	39.32	39.72	39.77	21.57	.....	.....	0.04	**0.023 ± 0.000**	Gal

Table 4.1: *Continued...*

IDs	Object name	Ra	Dec	$S_{1.4}$	flux	sflux	hflux	HR	$\log(f_X/f_{opt})$	$\log L_X$	$\log L_X$	$\log L_X$	$\log L_{1.4\,GHz}$	R	R-K	Class	Photo-Z	Class (X-ray)
				(mJy)	$\times 10^{-15}$ (ergs^{-1}m^{-2})					(0.5-2) keV	(2-7) Kev	(0.5-7) Kev	(W Hz^{-1})					
(1)	(2)	(3)	(4)	(5)	(6)	(7)	(8)	(9)	(10)	(11)	(12)	(13)	(14)	(15)	(16)	(17)	(18)	(19)
47	J143127.7+343740	14 : 31 : 27.9	34 : 37 : 40.9	2.83	1.39	0.56	0.91	$-0.43^{+0.18}_{-0.20}$	0.32	43.79	44.00	44.18	25.49	21.61 ± 0.02	.....	0.98	$2.755^{+2.902}_{-2.353}$	QSO-1
48	J143131.1+342721	14 : 31 : 31.1	34 : 27 : 22.1	1.19	2.69	0.25	5.23	$+0.67^{+0.12}_{-0.11}$	-1.02	41.74	43.04	42.77	23.41	17.56 ± 0.00	2.91	0.03	$0.430^{+0.441}_{-0.417}$	AGN-2
49	J143152.3+323213	14 : 31 : 52.3	32 : 32 : 13.4	4.83	7.96	2.94	6.29	$-0.32^{+0.03}_{-0.03}$	-0.07	42.49	42.82	42.92	23.70	18.74 ± 0.00	-80.26	0.97	$0.300^{+0.355}_{-0.263}$	AGN-1
50	J143156.4+325137	14 : 31 : 56.4	32 : 51 : 37.8	0.71	1.21	0.00	2.82	$+1.00^{+0.35}_{+0.00}$	-0.78	.....	42.77	42.40	23.18	19.01 ± 0.00	.....	0.40	**0.420 ± 0.001**	AGN-2
51	J143157.9+341649	14 : 31 : 57.9	34 : 16 : 50.3	0.65	42.90	18.00	25.10	$-0.50^{+0.01}_{-0.01}$	-0.07	44.04	44.20	44.43	23.61	16.91 ± 0.00	1.80	0.99	**0.715 ± 0.001**	QSO-1
52	J143214.3+342605	14 : 32 : 14.3	34 : 26 : 05.7	17.75	6.09	2.75	2.74	$-0.61^{+0.04}_{-0.04}$	0.33	42.72	42.72	43.08	24.53	20.05 ± 0.01	3.46	0.03	$0.405^{+0.505}_{-0.345}$	AGN-1
53	J143308.1+353151	14 : 33 : 08.1	35 : 31 : 51.4	2.33	1.55	0.67	0.79	$-0.56^{+0.14}_{-0.16}$	0.06	42.56	42.62	42.92	24.08	20.85 ± 0.01	3.83	0.03	$0.660^{+0.675}_{-0.582}$	AGN-1
54	J143311.0+335828	14 : 33 : 11.1	33 : 58 : 28.8	22.72	2.74	1.32	0.87	$-0.73^{+0.09}_{-0.10}$	-0.43	42.87	42.69	43.18	25.11	19.00 ± 0.00	3.63	0.03	$0.675^{+0.685}_{-0.647}$	AGN-1
55	J143315.7+332858	14 : 33 : 15.7	33 : 28 : 58.4	5.81	3.02	1.27	1.75	$-0.50^{+0.08}_{-0.09}$	1.06	43.49	43.63	43.87	25.15	22.62 ± 0.03	4.53	0.52	$1.360^{+1.548}_{-1.297}$	AGN-1
56	J143318.5+344404	14 : 33 : 18.5	34 : 44 : 04.3	2.69	16.10	6.51	10.40	$-0.44^{+0.02}_{-0.02}$	32.34	40.91	41.11	41.30	21.53	.....	.....	0.03	**0.034 ± 0.001**	Gal
57	J143355.1+340933	14 : 33 : 55.2	34 : 09 : 34.3	3.06	1.43	0.69	0.46	$-0.73^{+0.16}_{-0.22}$	0.06	41.15	40.97	41.46	22.79	20.94 ± 0.01	.....	0.98	$0.135^{+0.236}_{+0.000}$	AGN-1
58	J143413.9+345506	14 : 34 : 13.8	34 : 55 : 06.2	2.60	0.98	0.44	0.44	$-0.61^{+0.23}_{-0.30}$	-0.31	42.32	42.32	42.66	24.08	20.42 ± 0.01	3.54	0.03	$0.620^{+0.640}_{-0.592}$	AGN-1
59	J143423.3+342610	14 : 34 : 23.4	34 : 26 : 09.9	3.78	1.62	0.46	1.87	$+0.00^{+0.17}_{-0.17}$	0.99	42.76	43.38	43.32	24.68	23.13 ± 0.06	.....	0.28	$0.995^{+1.039}_{-0.870}$	AGN-2
60	J143428.0+331102	14 : 34 : 28.0	33 : 11 : 02.0	23.23	1.26	0.48	0.92	$-0.37^{+0.22}_{-0.24}$	1.30	43.32	43.59	43.73	26.00	24.18 ± 0.11	5.30	0.22	$1.770^{+1.802}_{-1.753}$	AGN-1
61	J143434.2+351009	14 : 34 : 34.2	35 : 10 : 09.5	67.51	7.06	2.71	5.15	$-0.37^{+0.04}_{-0.04}$	0.34	42.94	43.23	43.36	25.34	19.90 ± 0.00	3.92	0.98	$0.520^{+0.543}_{-0.449}$	AGN-1
62	J143445.3+332820	14 : 34 : 45.3	33 : 28 : 20.6	30.03	52.00	18.90	42.60	$-0.29^{+0.00}_{+0.00}$	0.01	42.92	43.28	43.36	24.11	16.90 ± 0.00	3.31	0.01	**0.198 ± 0.001**	AGN-1
63	J143513.2+333117	14 : 35 : 13.3	33 : 31 : 18.3	2.15	2.02	0.92	0.89	$-0.62^{+0.13}_{-0.15}$	0.58	42.82	42.81	43.18	24.20	21.86 ± 0.04	4.07	0.04	$0.760^{+0.782}_{-0.747}$	AGN-1
64	J143527.3+331240	14 : 35 : 27.3	33 : 12 : 40.1	1.30	2.09	0.96	0.88	$-0.64^{+0.11}_{-0.13}$	-0.33	42.71	42.66	43.04	23.84	19.55 ± 0.00	2.14	0.98	$0.655^{+0.701}_{-0.598}$	AGN-1
65	J143527.9+350928	14 : 35 : 27.9	35 : 09 : 28.3	1.66	3.92	1.51	2.83	$-0.38^{+0.07}_{-0.07}$	-0.35	44.04	44.30	44.45	25.08	18.82 ± 0.00	2.08	0.99	**2.247 ± 0.002**	QSO-1
66	J143528.0+331145	14 : 35 : 28.0	33 : 11 : 45.5	39.60	1.04	0.47	0.48	$-0.61^{+0.23}_{-0.29}$	1.19	43.26	43.28	43.61	26.20	24.10 ± 0.15	6.65	0.09	$1.700^{+1.802}_{-1.595}$	AGN-1
67	J143528.4+331931	14 : 35 : 28.4	33 : 19 : 31.5	23.27	6.68	3.21	2.21	$-0.72^{+0.04}_{-0.04}$	-0.11	42.90	42.74	43.20	24.76	18.83 ± 0.00	1.85	0.99	$0.455^{+0.529}_{-0.234}$	AGN-1
68	J143541.6+345055	14 : 35 : 41.6	34 : 50 : 55.3	1.46	1.50	0.42	1.74	$+0.00^{+0.17}_{-0.17}$	0.48	42.52	43.15	43.08	24.08	21.93 ± 0.03	.....	0.08	$0.795^{+0.816}_{-0.781}$	AGN-2
69	J143547.6+335310	14 : 35 : 47.6	33 : 53 : 09.9	2.22	1.07	0.49	0.44	$-0.65^{+0.24}_{-0.31}$	-0.44	43.48	43.43	43.83	25.15	20.01 ± 0.00	2.30	0.98	**2.112 ± 0.001**	AGN-1
70	J143608.7+350613	14 : 36 : 08.7	35 : 06 : 13.8	0.68	46.20	19.20	27.40	$-0.49^{+0.01}_{-0.01}$	1.56	44.18	44.34	44.57	23.73	20.91 ± 0.01	3.62	0.79	$0.795^{+0.819}_{-0.779}$	QSO-1
71	J143623.4+352710	14 : 36 : 23.4	35 : 27 : 10.8	17.48	1.51	0.63	0.88	$-0.50^{+0.16}_{-0.18}$	-1.58	41.08	41.20	41.45	23.51	16.77 ± 0.00	.....	0.03	**0.129 ± 0.000**	Gal
72	J143644.2+350626	14 : 36 : 44.2	35 : 06 : 27.1	4.81	1.32	0.21	2.19	$+0.43^{+0.20}_{-0.18}$	1.13	43.40	44.41	44.18	25.75	23.69 ± 0.09	.....	0.00	$2.850^{+3.284}_{-1.916}$	QSO-2
73	J143651.3+333909	14 : 36 : 51.3	33 : 39 : 10.2	1.88	1.67	0.59	1.44	$-0.26^{+0.17}_{-0.17}$	-0.21	40.94	41.32	41.40	22.45	20.10 ± 0.00	1.75	0.99	$0.115^{+0.143}_{+0.000}$	Gal
74	J143713.5+350553	14 : 37 : 13.6	35 : 05 : 54.8	59.62	6.18	2.45	4.19	$-0.42^{+0.05}_{-0.05}$	0.05	42.87	43.11	43.28	25.26	19.33 ± 0.00	2.08	0.99	$0.500^{+0.557}_{-0.206}$	AGN-1
75	J143715.3+340652	14 : 37 : 15.3	34 : 06 : 52.5	4.48	5.55	2.73	1.56	$-0.76^{+0.04}_{-0.04}$	-0.05	43.15	42.91	43.46	24.36	19.19 ± 0.00	3.38	0.06	$0.650^{+0.660}_{-0.624}$	AGN-1
76	J143752.0+351939	14 : 37 : 52.0	35 : 19 : 40.1	11.48	1.82	0.69	1.38	$-0.35^{+0.15}_{-0.16}$	-0.51	42.23	42.53	42.65	24.45	19.25 ± 0.00	.....	0.03	$0.455^{+0.469}_{-0.443}$	AGN-1
77	J143756.4+351936	14 : 37 : 56.5	35 : 19 : 36.5	53.48	32.80	13.60	19.70	$-0.48^{+0.01}_{-0.01}$	0.27	43.67	43.84	44.04	25.28	18.07 ± 0.00	.....	0.74	**0.537 ± 0.01**	QSO-1
78	J143821.8+344000	14 : 38 : 21.8	34 : 40 : 01.1	12.28	0.99	0.44	0.46	$-0.60^{+0.23}_{-0.29}$	-0.29	42.30	42.32	42.64	24.74	20.46 ± 0.00	.....	0.98	$0.605^{+0.727}_{-0.499}$	AGN-1
79	J143830.2+353915	14 : 38 : 30.2	35 : 39 : 15.9	3.59	55.50	22.00	37.60	$-0.42^{+0.01}_{-0.01}$	0.37	43.23	43.48	43.64	23.45	17.73 ± 0.00	.....	0.03	**0.262 ± 0.001**	AGN-1

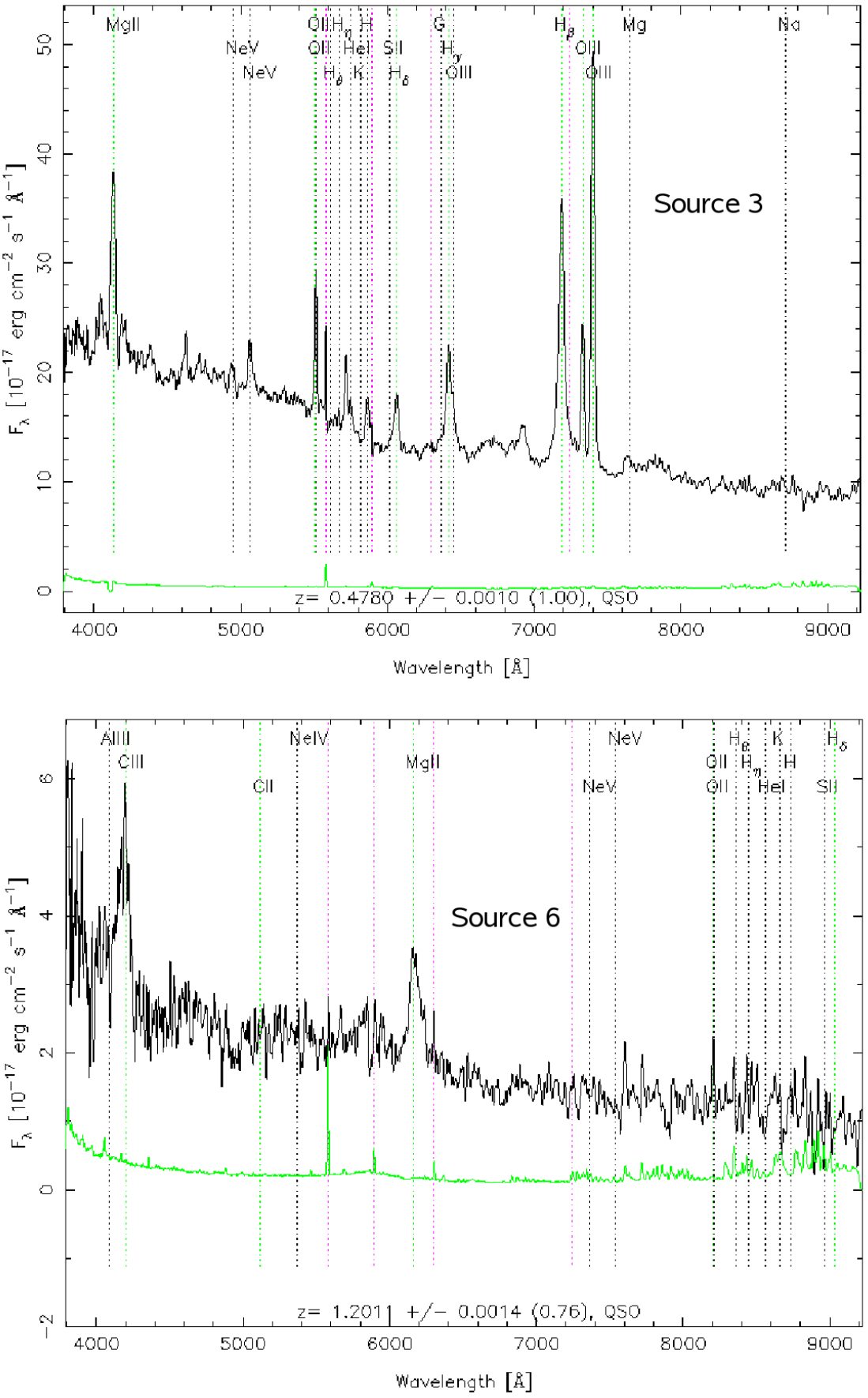

Figure 4.19: Optical spectra of 22 radio-X-ray matches obtained from the SDSS survey. The spectrum of each object is shown with the identification label (shown in column 1 of Table 4.1), spectroscopic redshift and classification.

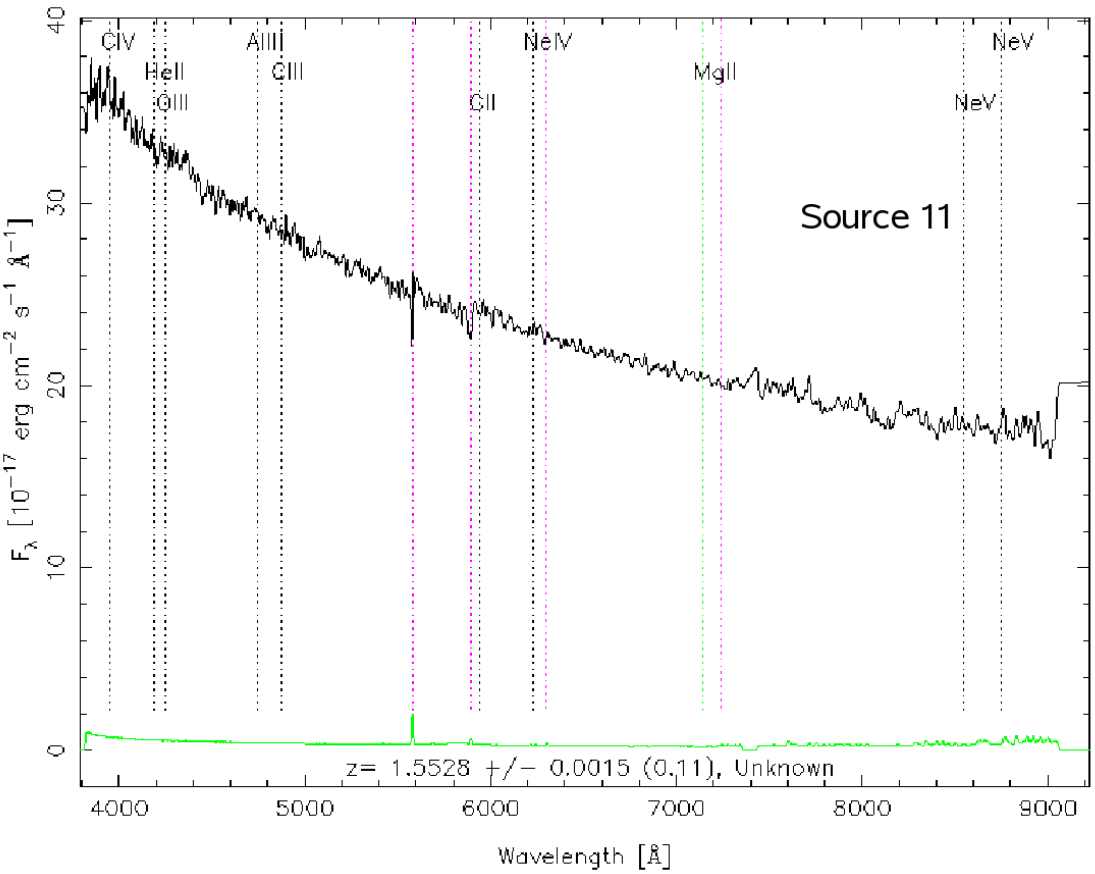
CIV
HeII
OIII
AlIII
CIII
CII
NeIV
MgII
NeV
NeV
Source 11
z= 1.5528 +/- 0.0015 (0.11), Unknown
F_λ [10^{-17} erg cm^{-2} s^{-1} Å^{-1}]
Wavelength [Å]

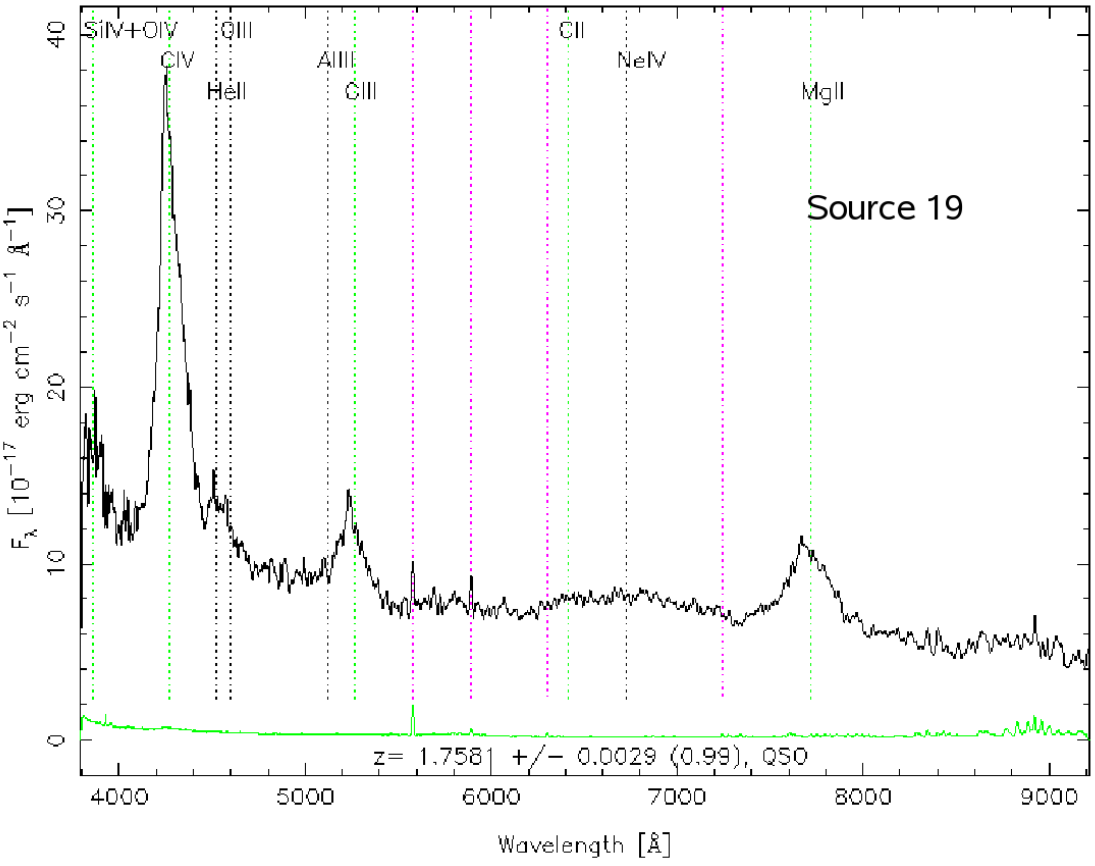
SiIV+OIV
CIV
OIII
HeII
AlIII
CIII
CII
NeIV
MgII
Source 19
z= 1.7581 +/- 0.0029 (0.99), QSO
F_λ [10^{-17} erg cm^{-2} s^{-1} Å^{-1}]
Wavelength [Å]

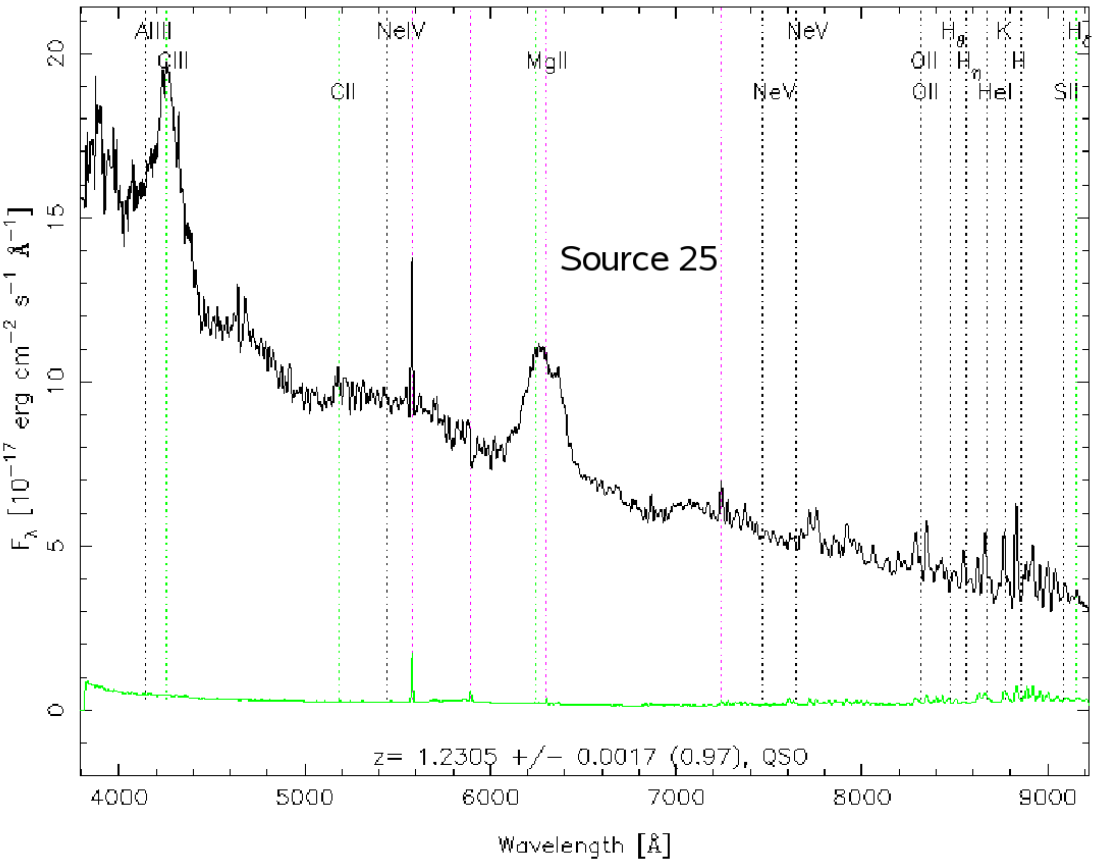
AlIII
CIII
CII
NeIV
MgII
NeV
NeV
OII
OII
H_η
K
H
HeI
SII
H_δ
Source 25
z= 1.2305 +/- 0.0017 (0.97), QSO
F_λ [10^{-17} erg cm^{-2} s^{-1} Å^{-1}]
Wavelength [Å]
0
5
10
15
20
4000
5000
6000
7000
8000
9000

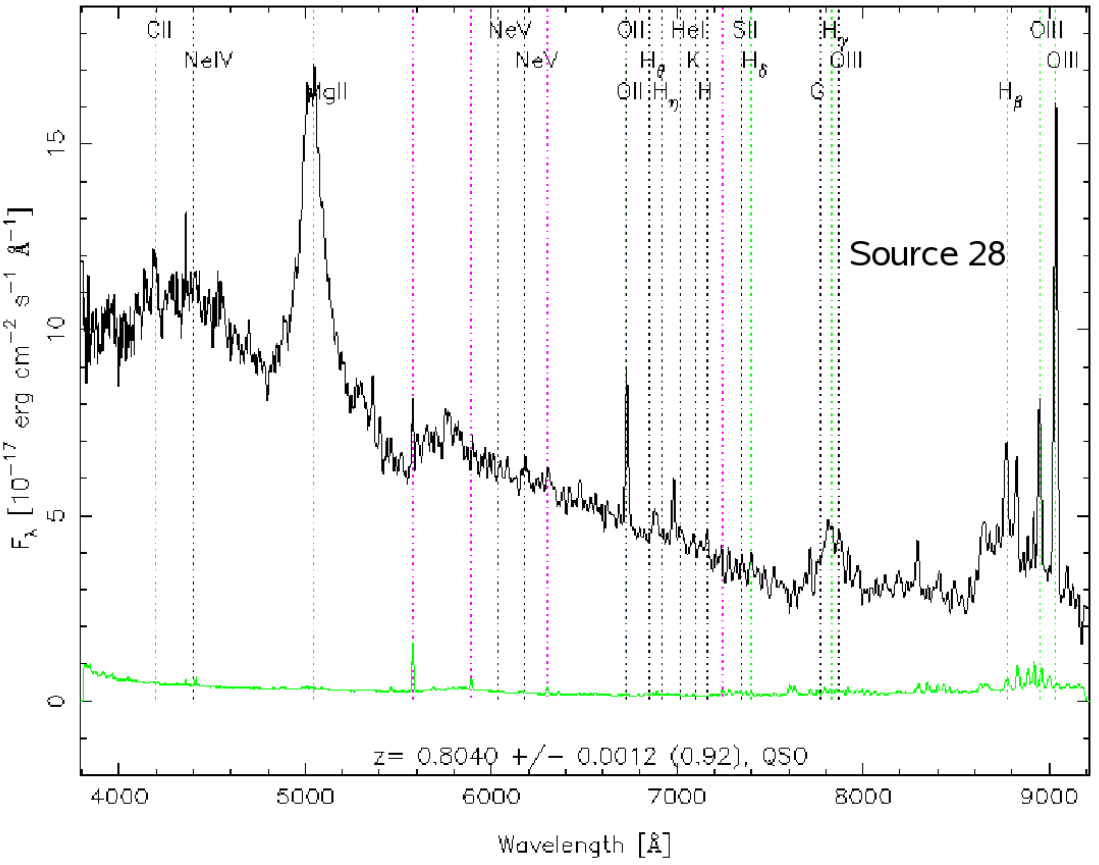
CII
NeIV
MgII
NeV
NeV
OII
OII
H_θ
H_η
HeI
K
H
SII
H_δ
H_γ
G
OIII
H_β
OIII
OIII
Source 28
z= 0.8040 +/- 0.0012 (0.92), QSO
F_λ [10^{-17} erg cm^{-2} s^{-1} Å^{-1}]
Wavelength [Å]
0
5
10
15
4000
5000
6000
7000
8000
9000

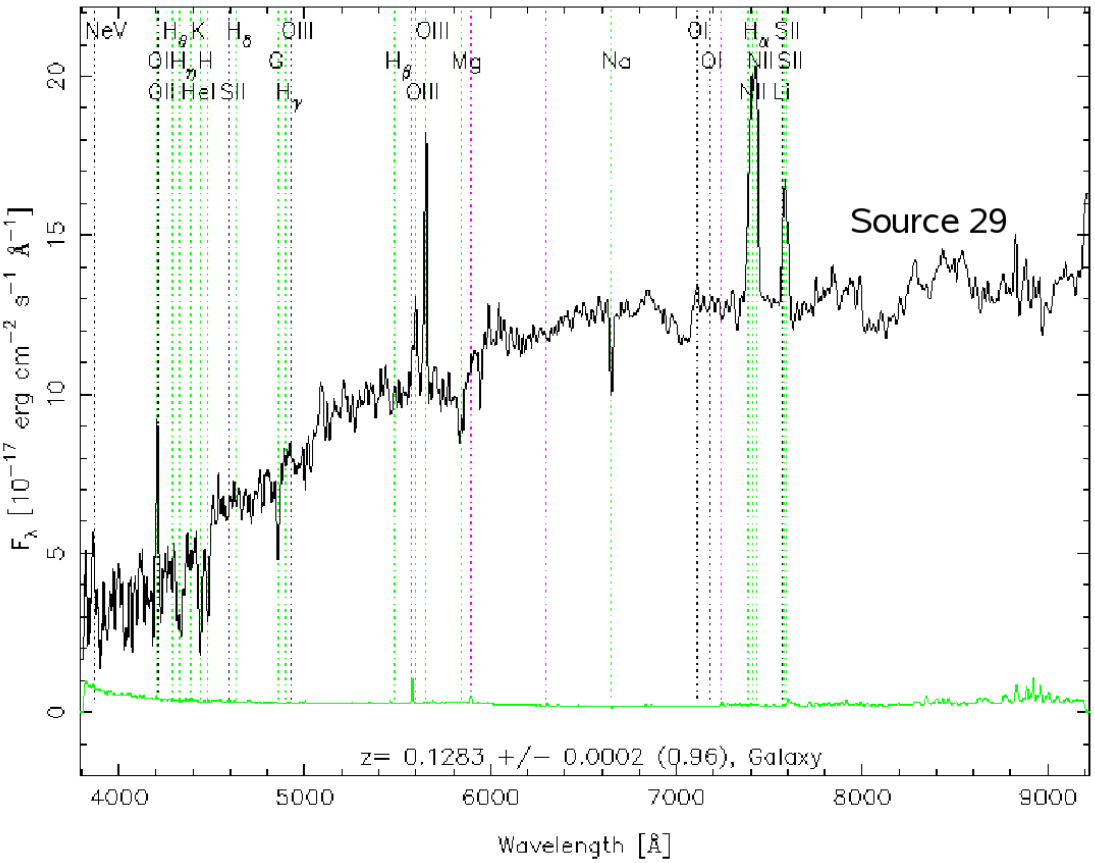
NeV
OII
H
K
H
G
OIII
OIII
H
Mg
Na
OI
H
SII
OII
HeI
SII
H
OIII
OI
NII
SII
NII
Source 29
z= 0.1283 +/- 0.0002 (0.96), Galaxy
Wavelength [Å]

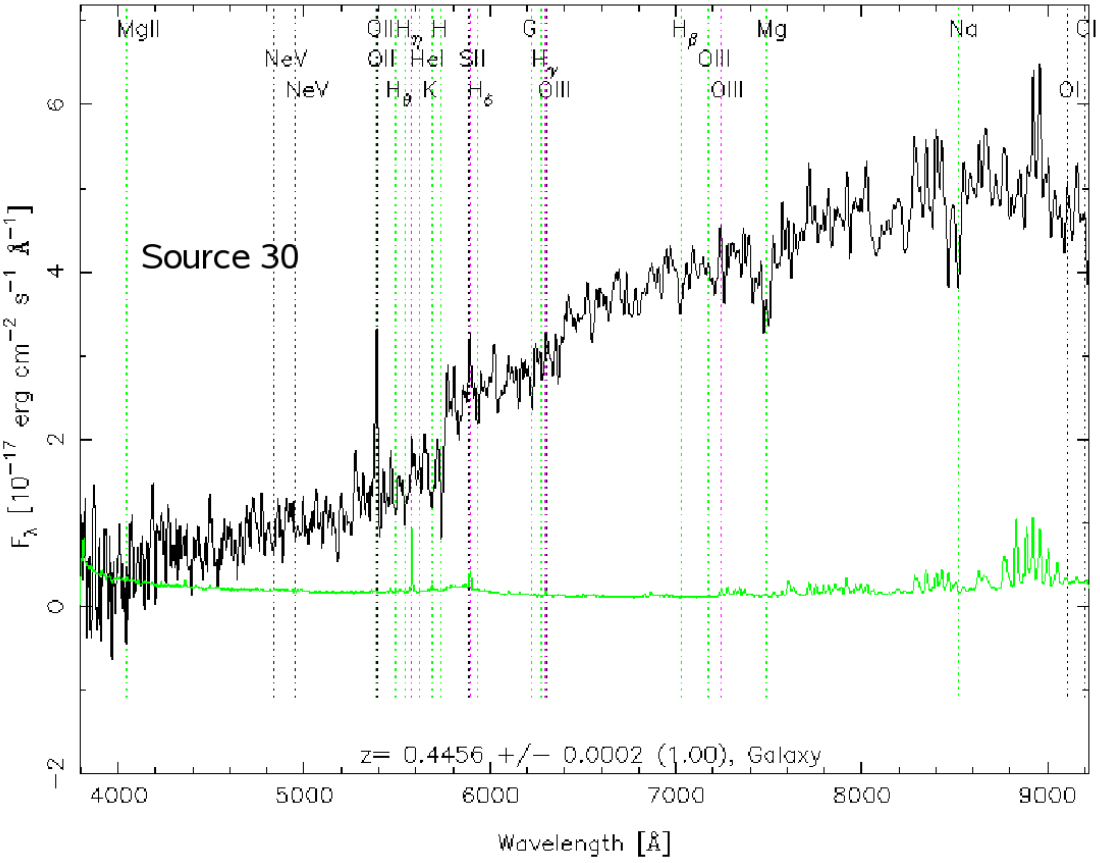
MgII
NeV
NeV
OII
H
HeI
SII
G
H
H
K
H
OIII
OIII
Mg
Na
OI
Source 30
z= 0.4456 +/- 0.0002 (1.00), Galaxy
Wavelength [Å]

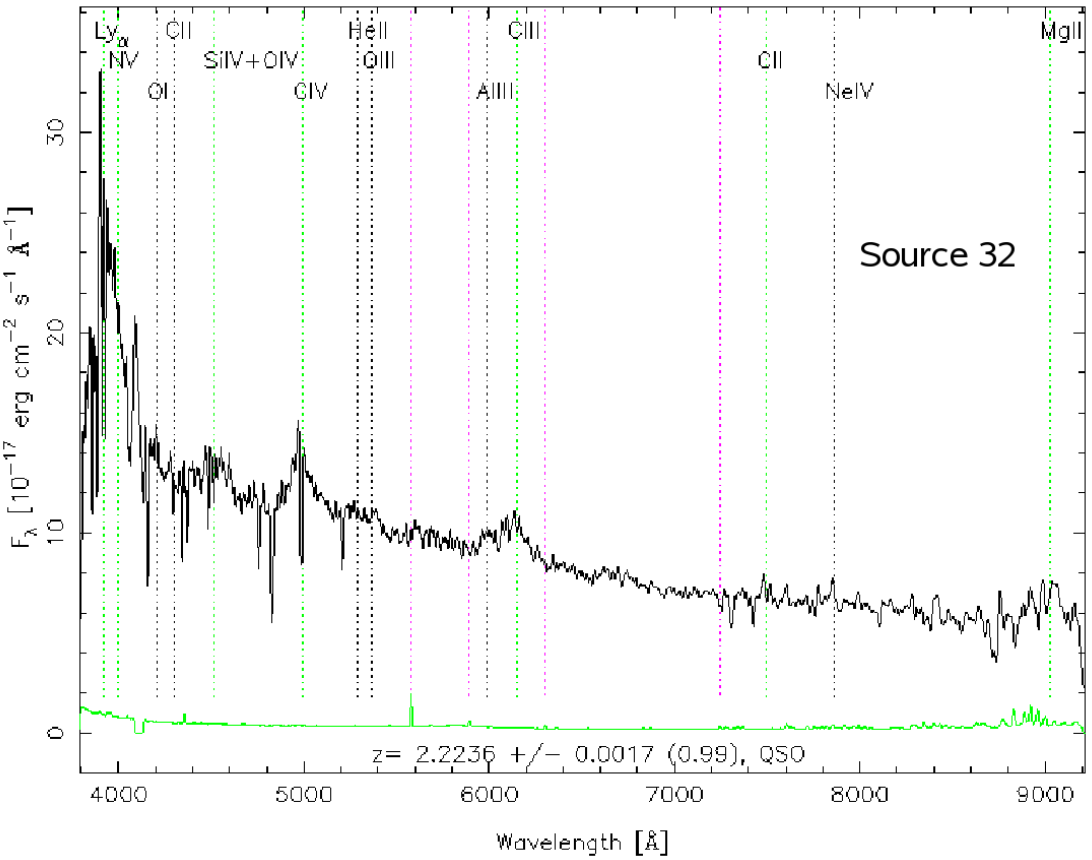
Ly$_\alpha$
NV
OI
CII
SiIV+OIV
CIV
HeII
OIII
AlIII
CIII
CII
NeIV
MgII
Source 32
z= 2.2236 +/- 0.0017 (0.99), QSO
F_λ [10^{-17} erg cm^{-2} s^{-1} Å^{-1}]
Wavelength [Å]

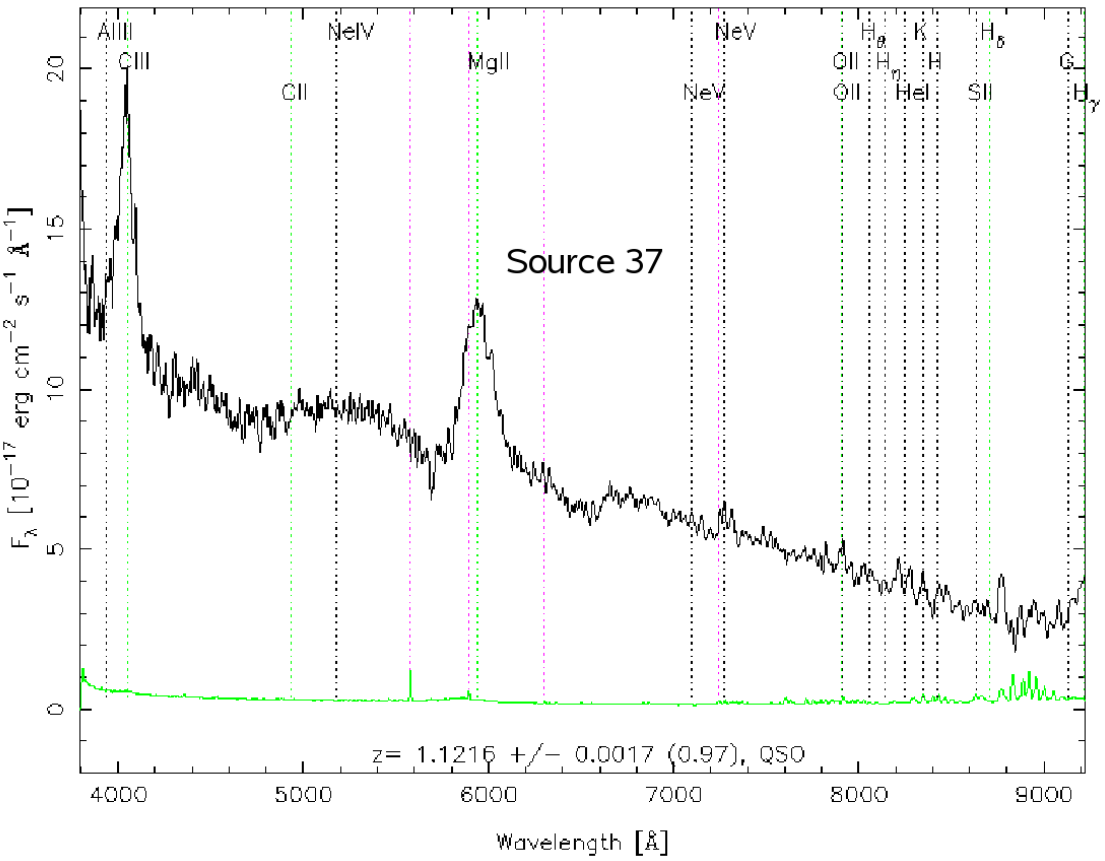
AlIII
CIII
CII
NeIV
MgII
NeV
NeV
OII
OII
H_θ
H_η
K
H
HeI
H_δ
SII
G
H_γ
Source 37
z= 1.1216 +/- 0.0017 (0.97), QSO
F_λ [10^{-17} erg cm^{-2} s^{-1} Å^{-1}]
Wavelength [Å]

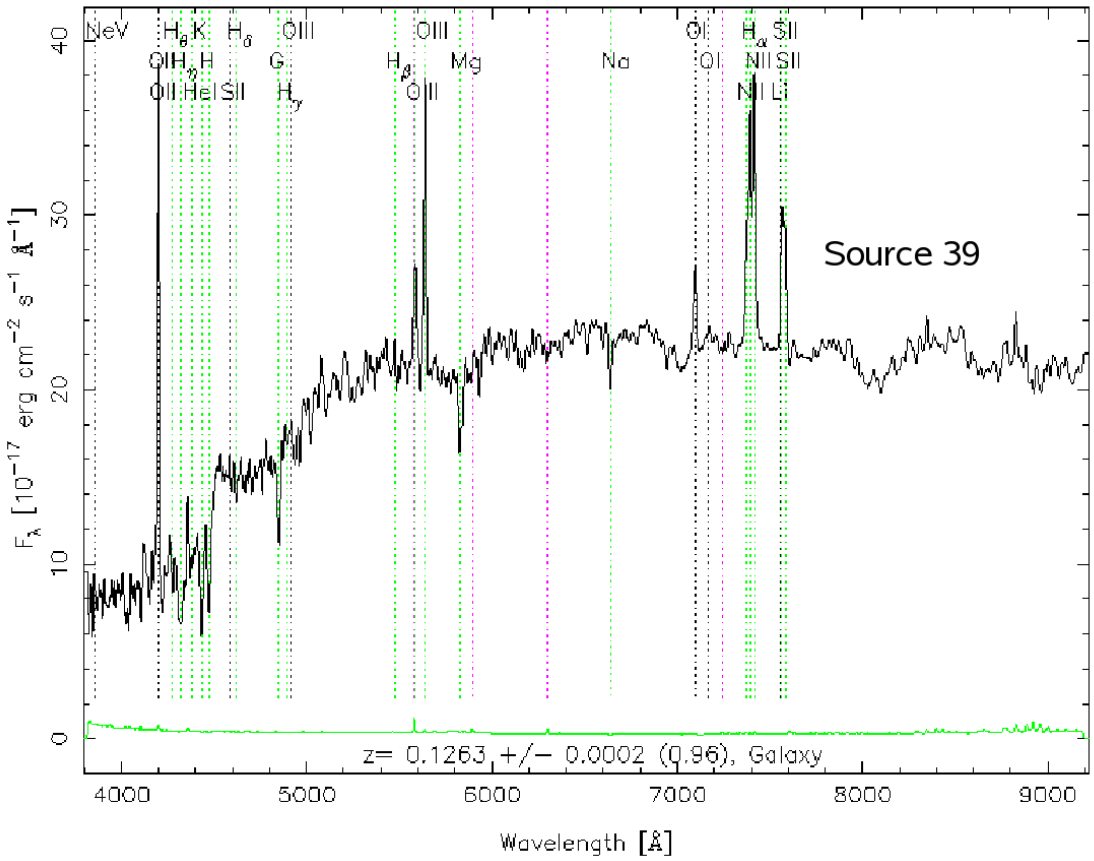
NeV
Hθ K
Hδ
OIII
OIII
OI
Hα SII
OII H9 H
G
Hβ
Mg
Na
OI
NII SII
OII HeI SII
Hγ
OII
NII L
Source 39
z= 0.1263 +/- 0.0002 (0.96), Galaxy
Wavelength [Å]

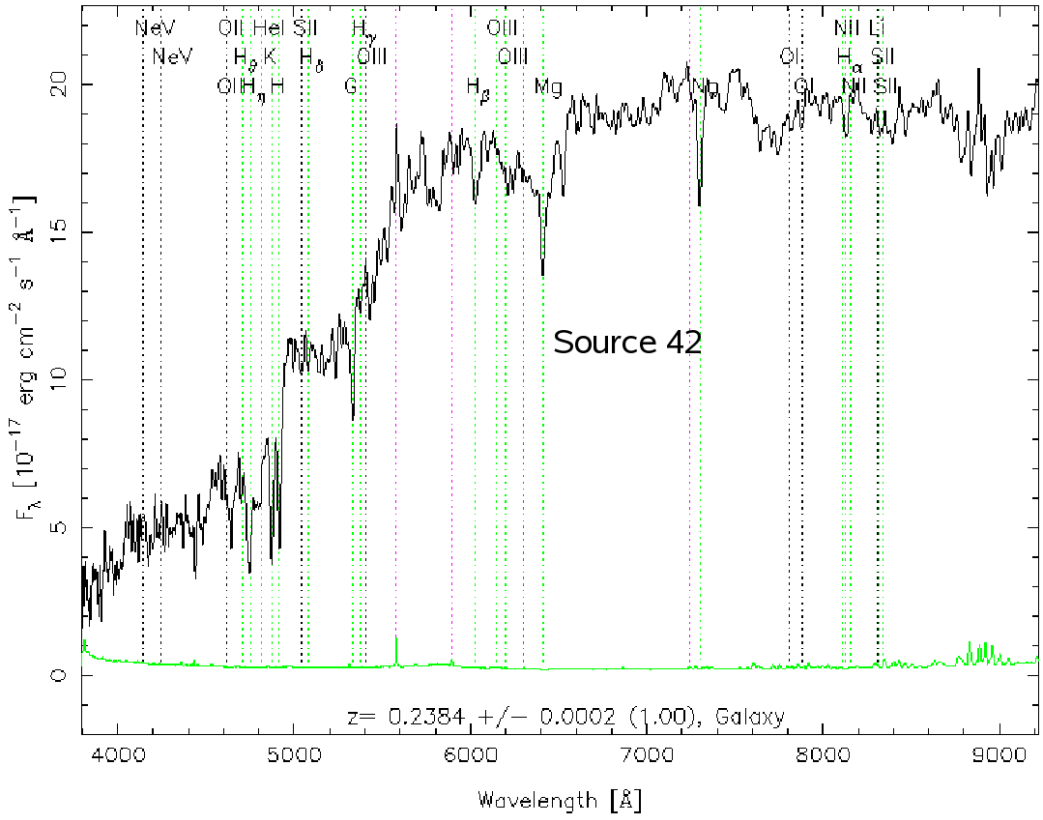
NeV
NeV
OII HeI SII
Hγ
OIII
OIII
OI
NII L
Hθ K
Hδ
OIII
OI
Hα SII
OII H9 H
G
Hβ
Mg
Na
NII SII
Source 42
z= 0.2384 +/- 0.0002 (1.00), Galaxy
Wavelength [Å]

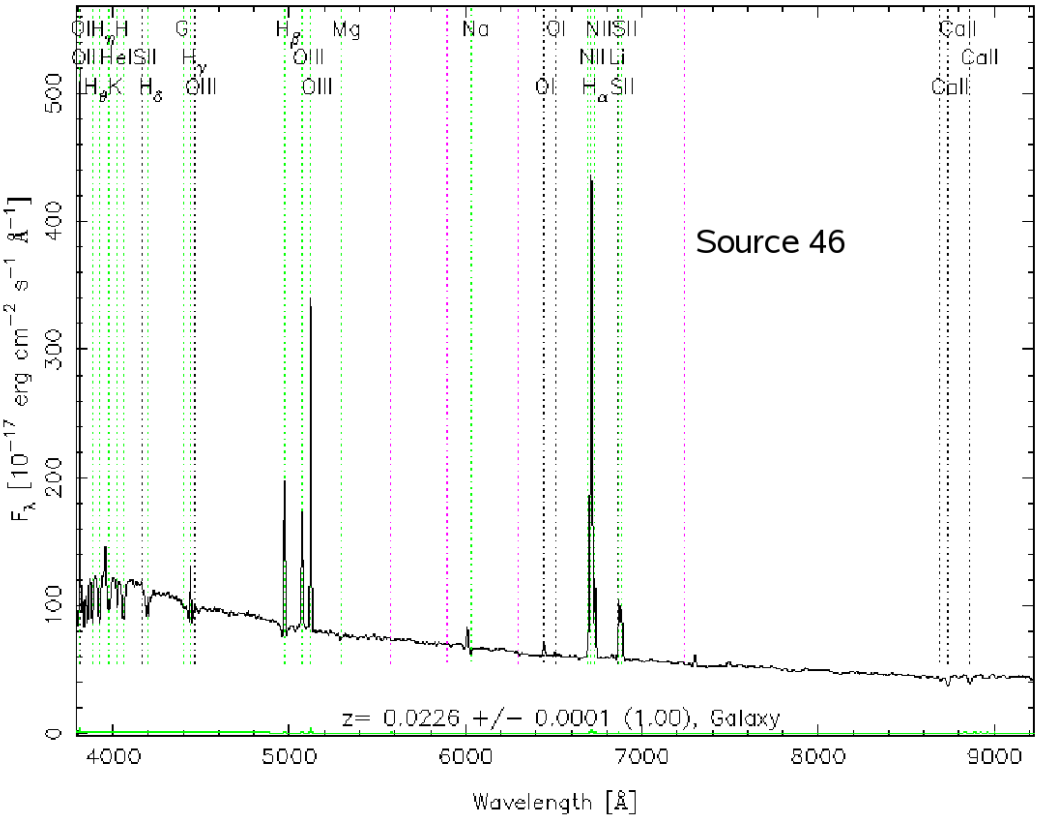
OIIH$_\eta$ H
OII HeI SII
H$_\theta$ K H$_\delta$
G
H$_\gamma$
OIII
H$_\beta$
OIII
OIII
Mg
Na
OI
NII SII
NII Li
OI H$_\alpha$ SII
CaII
CaII
CaII
Source 46
z= 0.0226 +/- 0.0001 (1.00), Galaxy
F$_\lambda$ [10^{-17} erg cm^{-2} s^{-1} Å^{-1}]
0
100
200
300
400
500
4000
5000
6000
7000
8000
9000
Wavelength [Å]

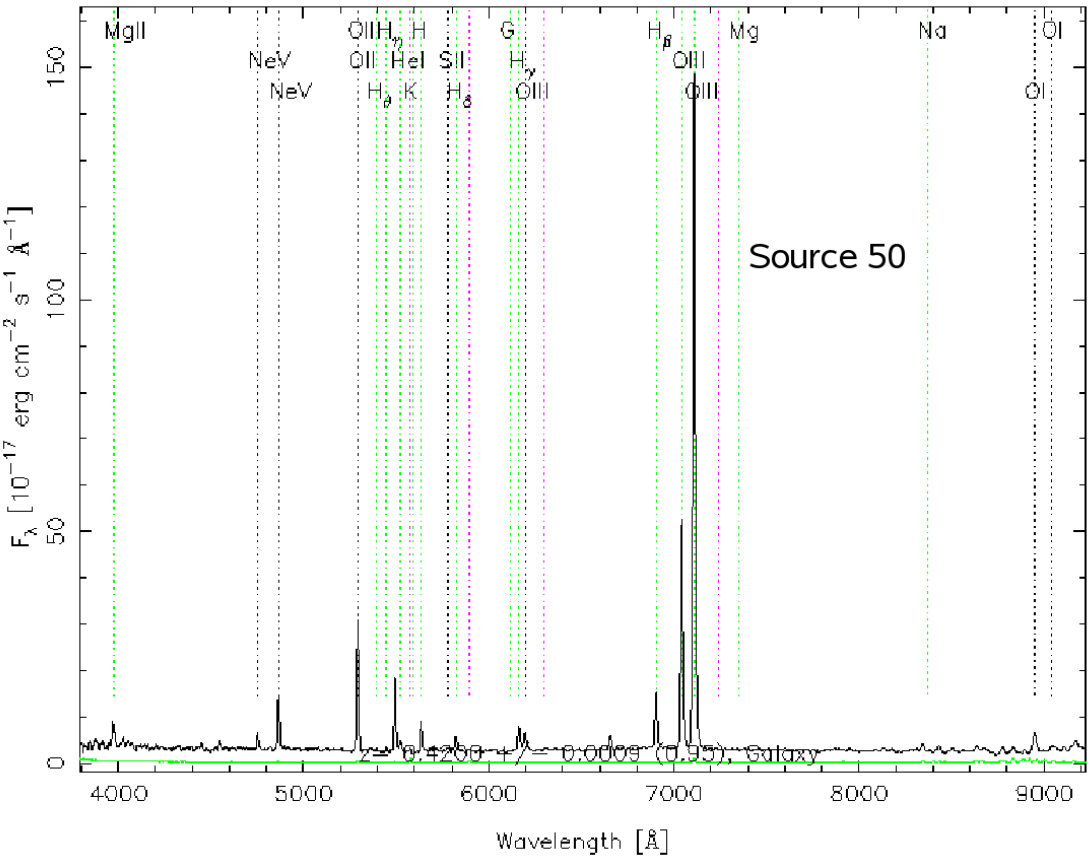
MgII
NeV
NeV
OIIH$_\eta$ H
OII HeI SII
H$_\theta$ K H$_\delta$
G
H$_\gamma$
OIII
H$_\beta$
OIII
OIII
Mg
Na
OI
OI
Source 50
z= 0.4280 +/- 0.0009 (0.95), Galaxy
F$_\lambda$ [10^{-17} erg cm^{-2} s^{-1} Å^{-1}]
0
50
100
150
4000
5000
6000
7000
8000
9000
Wavelength [Å]

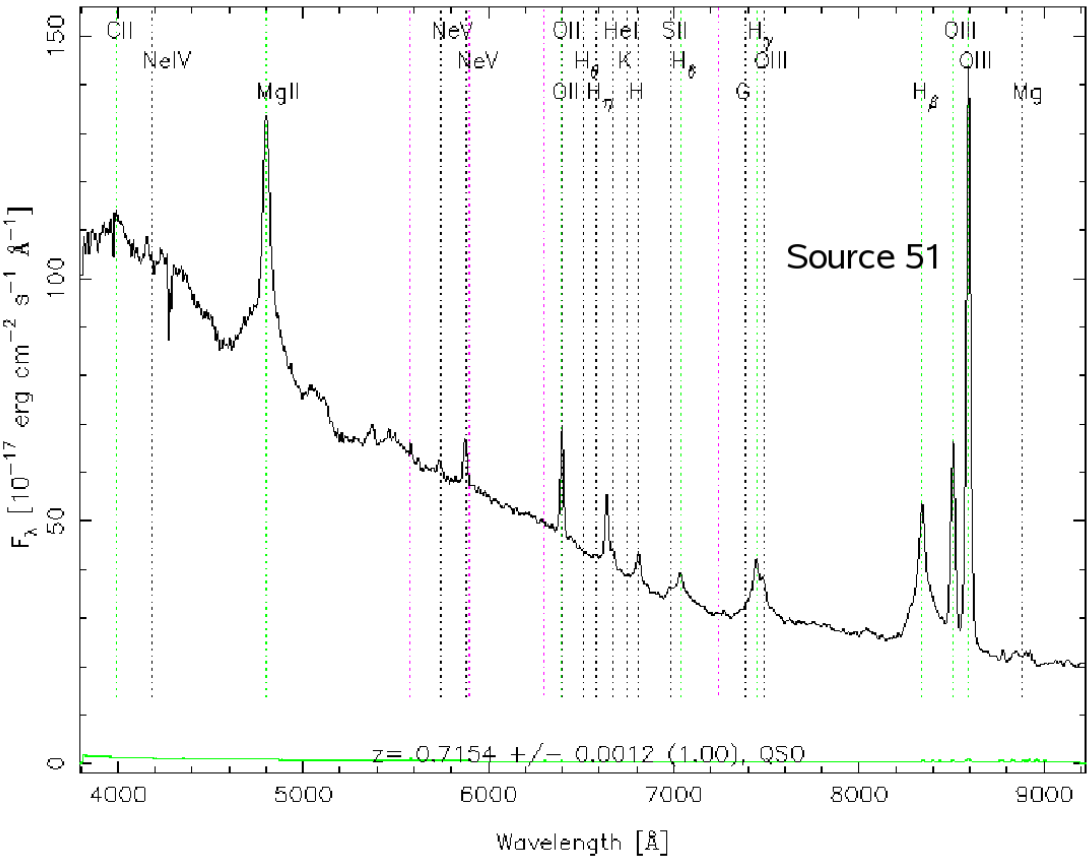
CII
NeIV
MgII
NeV
NeV
OII
Hε
OII
Hη
HeI
K
H
SII
Hδ
Hγ
OIII
G
Hβ
OIII
OIII
Mg
Source 51
z= 0.7154 +/- 0.0012 (1.00), QSO
F_λ [10^-17 erg cm^-2 s^-1 Å^-1]
Wavelength [Å]

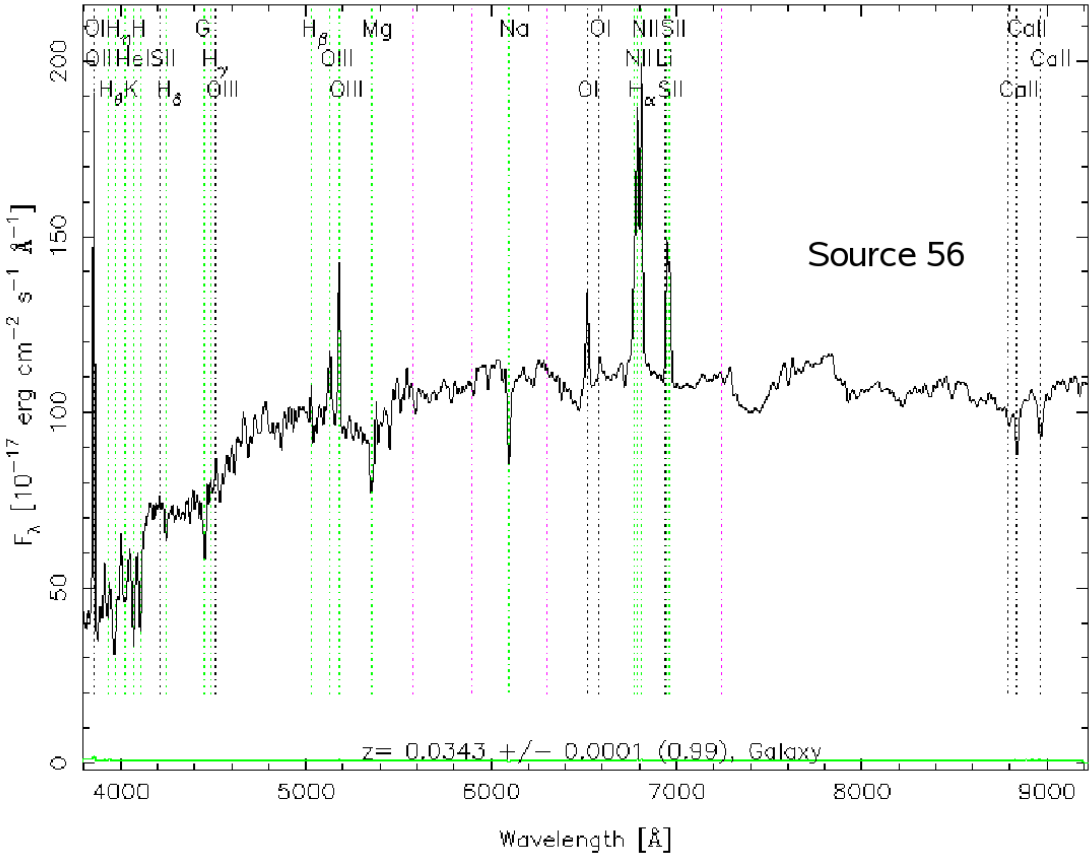
OI
Hη
H
G
Hβ
Mg
Na
OI
NII
SII
CaII
CaII
OII
HeI
SII
Hγ
OIII
OIII
NII
G
CaII
Hθ
K
Hδ
OIII
Hα
SII
Source 56
z= 0.0343 +/- 0.0001 (0.99), Galaxy
F_λ [10^-17 erg cm^-2 s^-1 Å^-1]
Wavelength [Å]

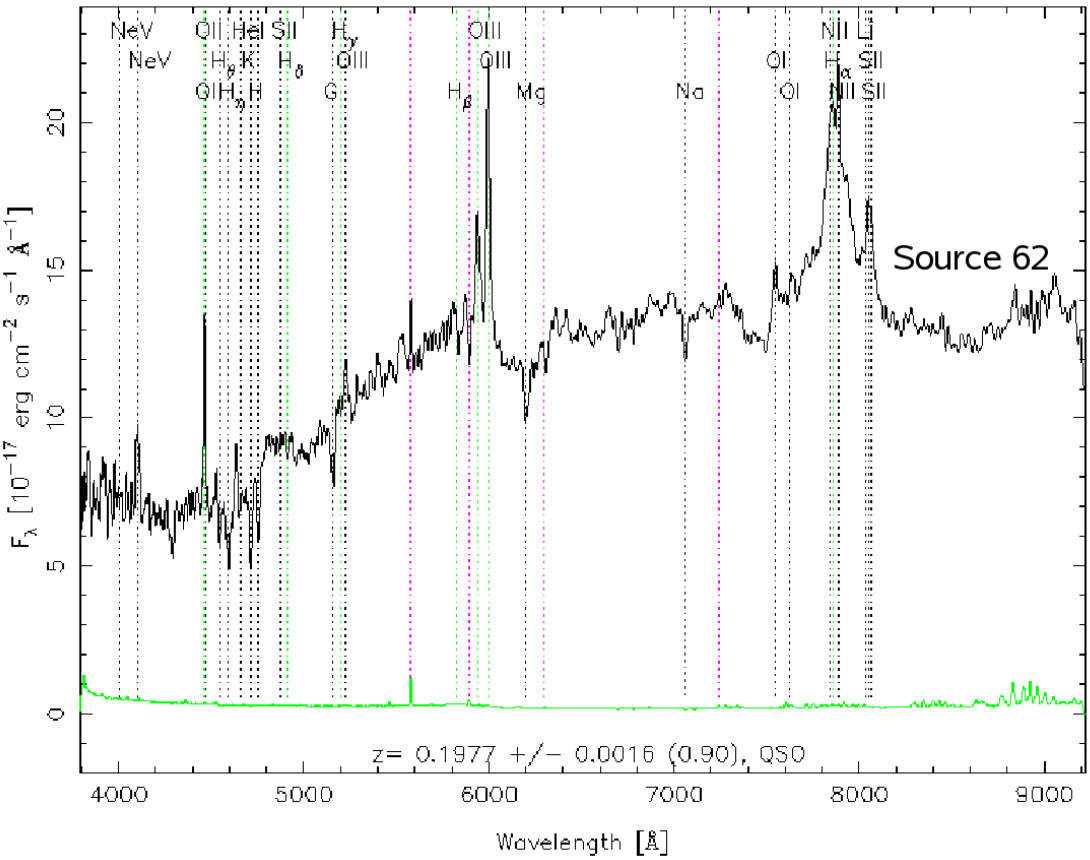
NeV
NeV
OII
HeI
SII
Hγ
OIII
OIII
NII
Hβ
K
Hδ
OIII
Hα
SII
G
Hβ
Mg
Na
OI
OI
NII
SII
Source 62
z= 0.1977 +/- 0.0016 (0.90), QSO
Wavelength [Å]

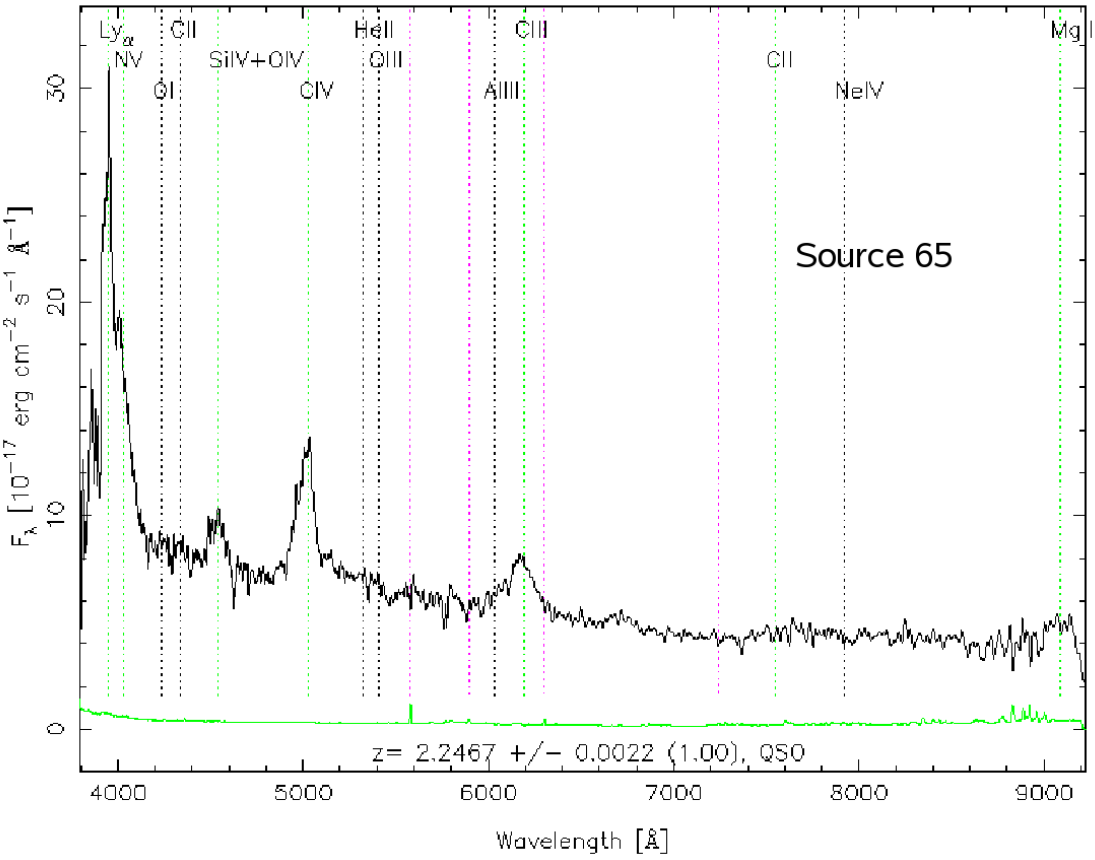
Lyα
NV
CII
OI
SiIV+OIV
CIV
HeII
OIII
CIII
AlIII
CII
NeIV
MgII
Source 65
z= 2.2467 +/- 0.0022 (1.00), QSO
Wavelength [Å]

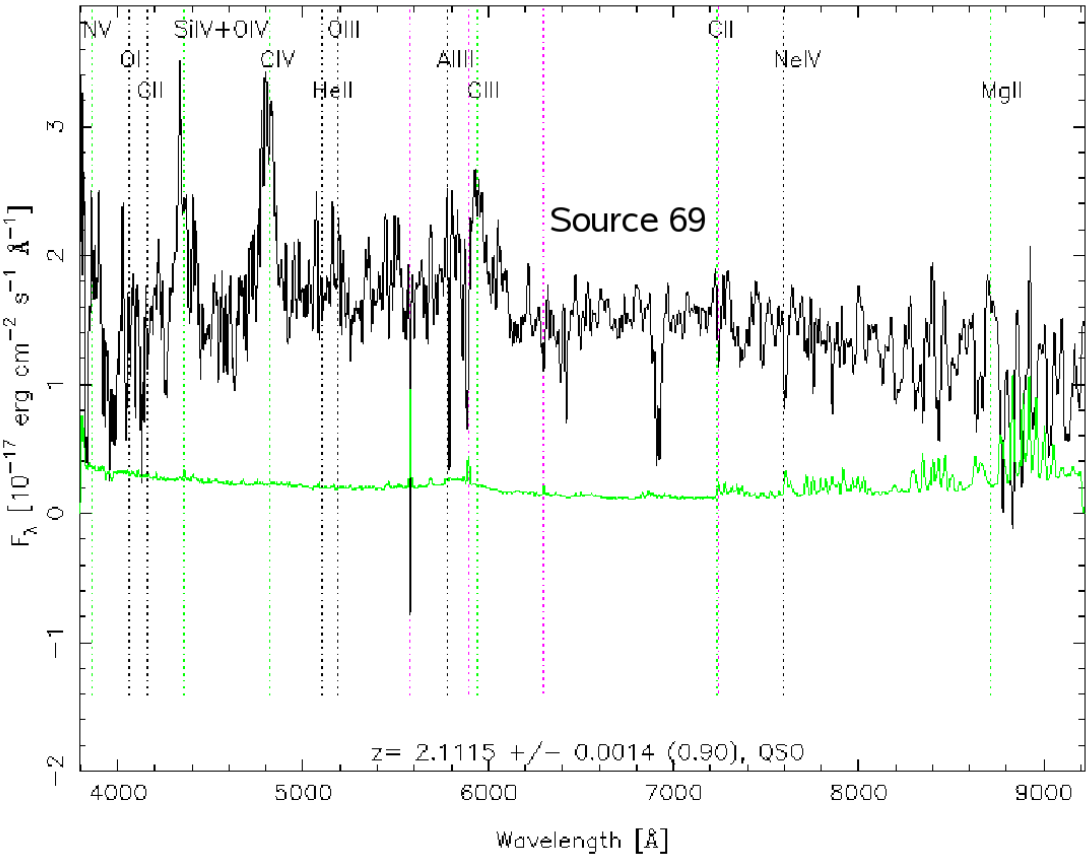
NV
OI
CII
SiIV+OIV
CIV
HeII
OIII
AlIII
CIII
CII
NeIV
MgII
Source 69
z= 2.1115 +/- 0.0014 (0.90), QSO
F_λ [10^{-17} erg cm^{-2} s^{-1} Å^{-1}]
Wavelength [Å]

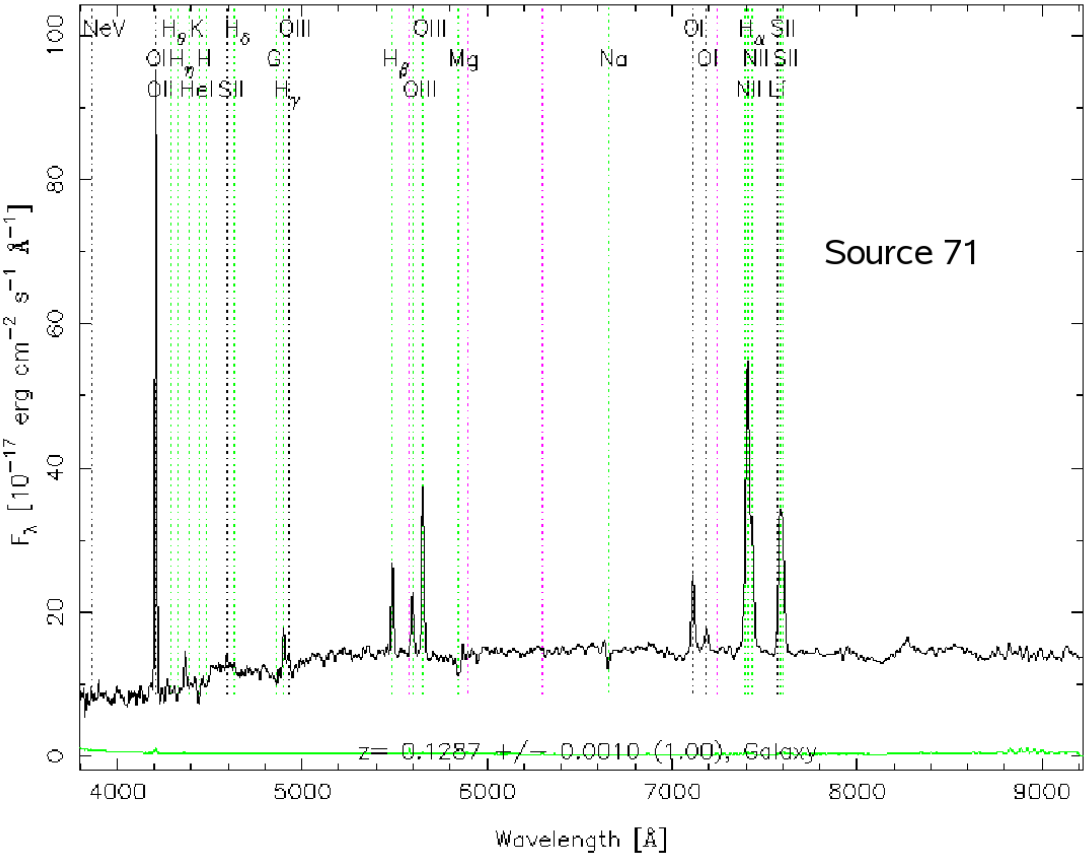
NeV
OII
HeI
SII
G
OIII
Mg
Na
OI
NII
Source 71
z= 0.1287 +/- 0.0010 (1.00), Galaxy
F_λ [10^{-17} erg cm^{-2} s^{-1} Å^{-1}]
Wavelength [Å]

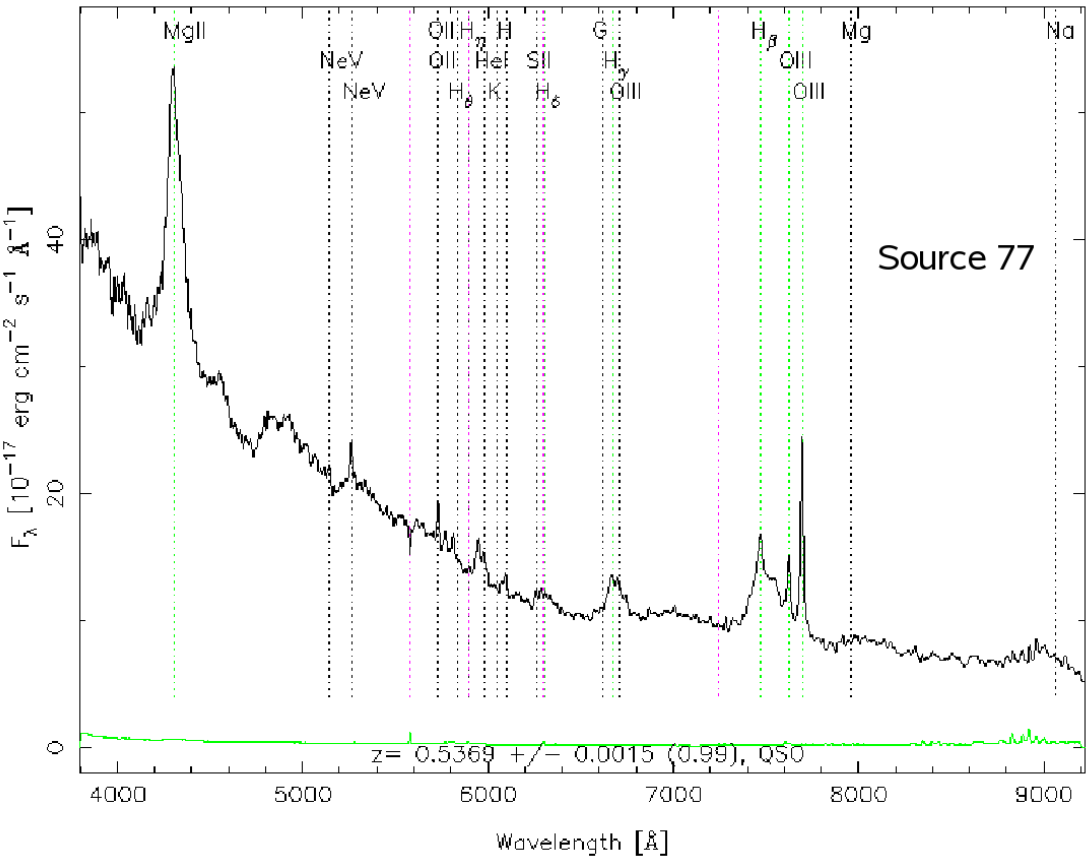
MgII
NeV
NeV
OII
OII
H8
H
HeI
K
SII
Hδ
G
Hγ
OIII
Hβ
OIII
OIII
Mg
Na
Source 77
z= 0.5369 +/- 0.0015 (0.99), QSO
Fλ [10−17 erg cm−2 s−1 Å−1]
Wavelength [Å]

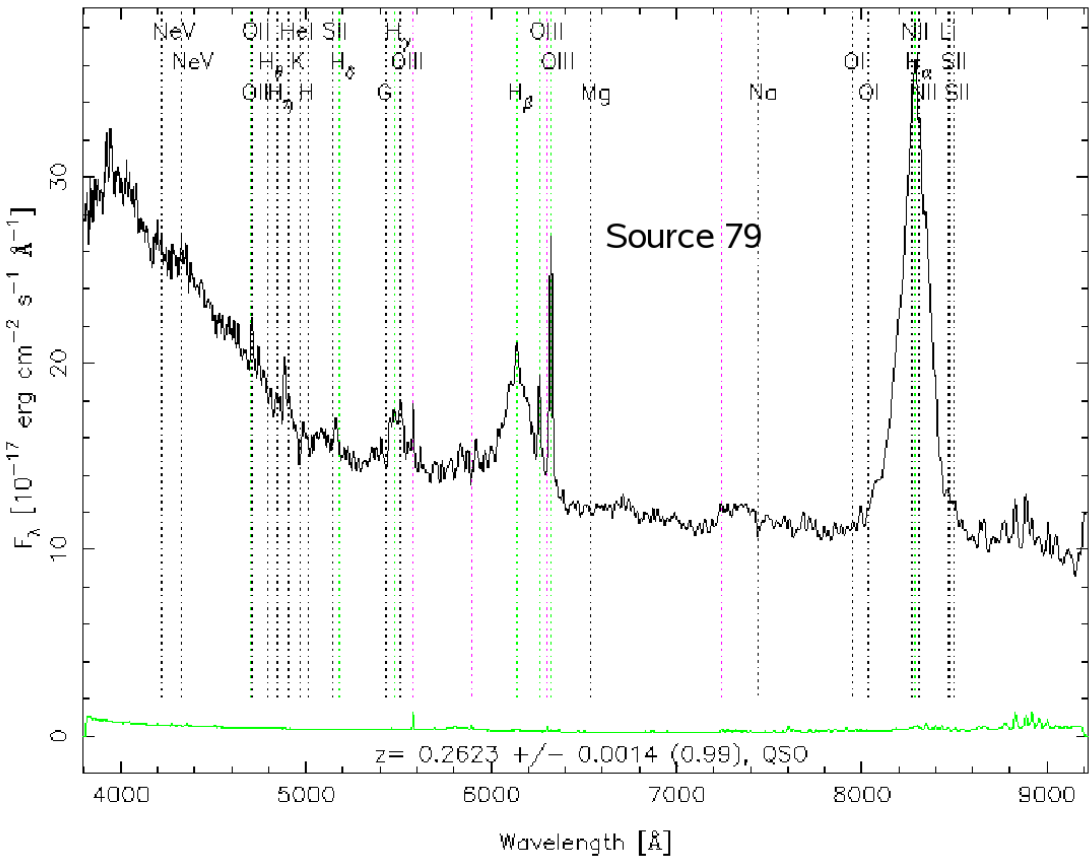
NeV
NeV
OII
H8
K
Hδ
SII
Hγ
OIII
OIII
H8
H
G
Hβ
OIII
Mg
Na
OI
OI
Hα
NII
NII
SII
SII
Source 79
z= 0.2623 +/- 0.0014 (0.99), QSO
Fλ [10−17 erg cm−2 s−1 Å−1]
Wavelength [Å]

CHAPTER 5

Clustering statistics of FIRST radio sources identified in SDSS DR6 survey

5.1 Overview

In this chapter, I cross correlate the FIRST radio survey with the Sloan Digital Sky Survey (SDSS) sixth Data Release (DR6). The FIRST survey was designed to study the region of the sky that will be observed by the SDSS, and therefore overlaps with the SDSS very closely. The imaging data set covers the north galactic cap and the survey also provides spectra for ~ 1.27 million objects, covering an area of 7425 deg^2. This chapter presents a brief analysis of the clustering properties of radio sources optically identified in the SDSS DR6 survey, and examines the evolution of the clustering properties of galaxies. Clustering properties are determined via the two point angular correlation function, $\omega(\theta)$.

5.2 Introduction

One of the principal challenges in modern cosmology is understanding how structures form and evolve in the universe. The form and evolution of the large scale structure can be used to probe

the density of the underlying dark matter distribution and constrain fundamental cosmological parameters e.g., the matter density and baryon density. The generally accepted picture is that tiny fluctuations in the matter density, seeded by quantum fluctuations during an inflating era in the early universe, evolved and grew under gravity until the gravitational instability eventually caused overdense regions to collapse and form structures. If fluctuations arise from inflationary processes their Fourier modes have random phases. The central limit theorem then implies that the initial density field will be gaussian. In this case the higher order moments of the field vanish and one can give a full statistical description of the density field by using the two point (auto) correlation function. Non linear gravitational collapse does create nongaussian fluctuations in the large scale structure distribution on small scales–in this case higher order correlations are also important.

Galaxies are often treated as tracers of the underlying matter distribution, and observations of the distributions of galaxies are used to infer cosmological parameters, which govern the matter distribution. However, since galaxy formation is a complex process, the distribution of galaxies does not necessarily follow that of the matter. Galaxy bias, which is the difference between the galaxy distribution and the underlying matter distribution, is usually regarded as an obstacle to deriving cosmological parameters with clustering data from galaxy redshift surveys. On the other hand, the existence of galaxy bias can be used to test theories of galaxy formation, if galaxy bias can be determined from the data.

With the recent release of mJy level radio surveys covering large fractions of the sky, such as the NRAO VLA Sky Survey (NVSS; Condon et al. 1998), Westerbork Northern Sky Survey (WENSS; Rengelink 1998), Sydney University Molongolo Sky Survey (SUMSS; Mauch et al. 2003) and Faint Images of the Radio Sky at Twenty cm (FIRST; Becker et al. 1995), it has become possible to study the large-scale structure using the spatial distribution of radio galaxies down to a limiting flux density of a few mJy over large fractions of the celestial sphere. The population of radio sources at these flux densities includes a mixture of AGNs and star-forming galaxies. Measurements of the angular two-point correlation function, $\omega(\theta)$, have been made for all these surveys (Negrello et al. 2006; Blake et al. 2004b; Overzier et al. 2003; Blake & Wall 2002a,b; Magliocchetti et al. 1998; Cress et al. 1996). However, de-projecting the angular two-point correlation function to estimate the spatial two-point correlation function $\xi(r)$ is difficult

as the redshift distribution $N(z)$ of mJy radio sources is poorly determined out to the median redshift of most radio surveys ($z \sim 0.8$). A simple way to alleviate the problem of the poorly-determined $N(z)$ is to compute redshift distributions using the Dunlop & Peacock (1990) radio luminosity functions (see e.g Peacock & Nicholson 1991; Overzier et al. 2003; Negrello et al. 2006).

Obtaining redshifts for a large sample of radio sources has recently become possible with the release of large optical redshift surveys such as the 2 degree Field Galaxy Redshift Survey (2dFGRS; Colless et al. 2001), Sloan Digital Sky Survey (SDSS; York et al. 2000) and 6 degree Field Galaxy Survey (6dFGRS; Jones et al. 2004). All of these surveys provide redshifts for a large number of galaxies over large areas of sky and can be used in concert with the large-area radio surveys mentioned above to obtain redshifts of many radio sources in the local universe. Magliocchetti et al. (2004) have done this by crossmatching FIRST radio sources down to 1 mJy with the 2dFGRS. They obtained a sample of 826 radio sources with optical spectra and redshifts from which they determined the two point correlation function in both redshift space and real space. Having the source spectra allows the physical source of radio emission to be determined so that the correlation functions of different types of galaxies can be studied separately (e.g AGNs and star-forming galaxies). This chapter presents preliminary clustering results for different subsamples of FIRST radio sources optically identified in the SDSS DR6 imaging area, and is the first part of an ongoing effort to measure the evolution of clustering in different populations of faint radio sources.

5.3 The SDSS DR6 survey

The Sloan Digital Sky Survey (SDSS; York et al. 2000) sixth Data Release (DR6) is a digital photometric and spectroscopic survey. This data set covers the north Galactic cap, containing photometric information of $\sim$ 287 million objects over 9583 deg^2. Around 1.27 million objects were selected for spectroscopy, covering an area of 7425 deg^2 on the sky. A technical summary of the survey is given in York et al. (2000) and there are also descriptions at http://www.sdss.org/dr6. Detailed information about the SDSS DR6 can be found in Adelman-McCarthy et al. (2008). Here a brief overview is given.

The SDSS is the largest survey of the nearby universe publicly available. The survey uses a dedicated, wide-field, 2.5 m telescope (Gunn et al. 2006) at Apache Point Observatory, New Mexico, equipped with a 54-CCD imaging and astrometric camera (Gunn et al. 1998) and a two dual fibre-field spectrograph (Newman et al. 2004). The imaging uses a drift scanning camera (Gunn et al. 1998) with 30 2048 CCDs at the focal plane which image the sky in five broad filters (*ugriz*; see Figure 5.1) at 3553, 4686, 6165, 7481 and 8931 Å (Fukugita et al. 1996; Stoughton et al. 2002) to limiting magnitudes of 22.0, 22.2, 22.2, 21.3, and 20.5 respectively. The magnitude scale is placed on the AB system. The PSF width is 1.4 arcsec, the photometric calibration is accurate to 2.3% (depending on waveband) and the astrometry has an RMS accuracy of less than 0.1 arcsec per coordinate. The limiting magnitude for the spectra is $r < 17.77$, which is substantially brighter than that for the imaging to ensure that the spectroscopic completeness is almost 100%. A typical signal to noise value is > 4 per pixel and the spectral resolution is 1800. The redshifts have an RMS accuracy of $\pm 30\,\mathrm{km\,s^{-1}}$ and up to 5760 spectra can be observed in one night. There is also a survey of three stripes in the Southern Galactic cap: the Legacy survey, the SEGUE (Sloan Extension for Galactic Understanding and Exploration) survey, and the Supernovae survey. The equatorial strip is repeatedly scanned to give flux limits about two magnitudes deeper than the nothern survey.

5.4 Matching procedure

The SDSS provides numerous properties measured from 5-colour imaging data, such as astrometry, photometry, and morphological information, as well as high-quality spectra – recall that the SDSS astrometry is very accurate (~ 0.1 arcsec; Pier et al. 2003), which significantly simplifies the matching algorithm. The cross correlation between the two catalogues was performed using SQL (Structured Query Language) in the SDSS database (Cas Jobs). The query written in the language SQL is given in Appendix B. In order to avoid congestion on the server, the upload file is limited to a size of 80KB. Consequently, the FIRST radio catalogue was divided into subsamples of 1 deg in declination and 1 hour in right ascension. Then each of the subsamples was imported into SQL, and the cross matches were performed with one subset at a time. The matching radius was determined by analysing the distribution of the distances between the

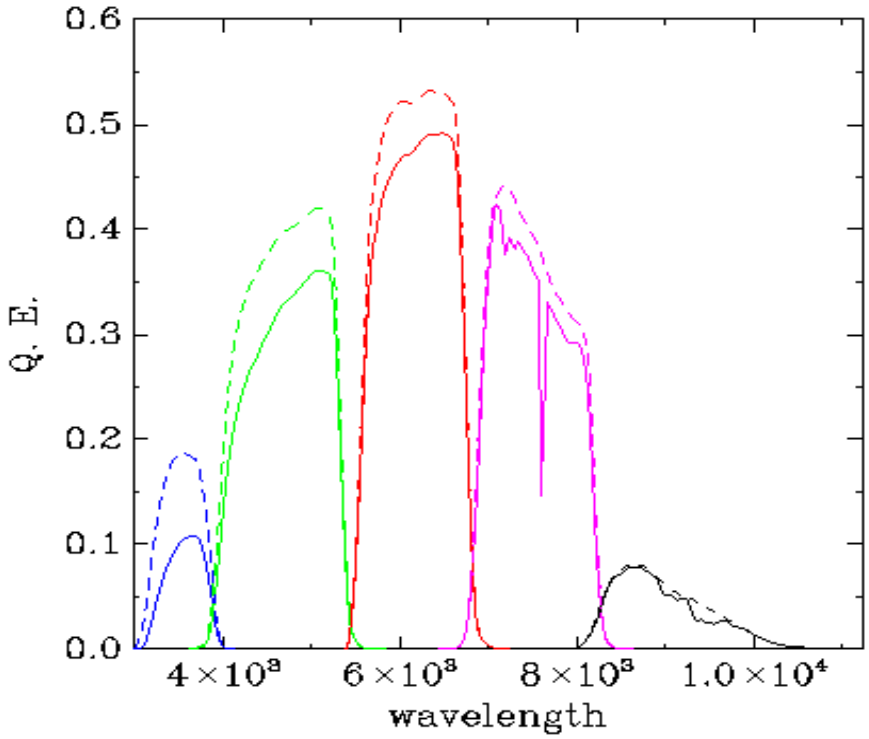

Figure 5.1: Response function of the SDSS photometric system. Dashed curves indicate the response function including atmospheric transmission at 1.2 airmass at the altitude of Apache Point Observatory. From left to right, the bands u, g, r, i and z

quoted position in the FIRST catalogue and the SDSS position, and corresponds to a 3σ cutoff. The distribution of the distance between the SDSS data and FIRST positions is shown in Figure 5.2, the upper curve shows the offset distribution for all FIRST radio sources identified in the SDSS DR6, the middle curve for all FIRST radio sources classified morphologically as resolved (or galaxy), and the lower curve for FIRST radio sources classified as unresolved (or 'stellar-like') objects (for a discussion of star-galaxy separation see section 5.4.1). As is evident, the two distributions are similar.

The FIRST radio sources were cross correlated with SDSS objects in the **PhotoPrimary** view of the SDSS DR6 Catalogue Archive Server (CAS) with 'clean' photometry i.e. rejecting objects with magnitude errors >0.2 in all five bands *ugriz*, or flagged as 'BRIGHT', 'SATURATED', 'EDGE', 'BLENDED', 'CHILD'. Because of the exclusion of 'CHILD' objects (objects which are the product of deblending a blended object), in all cases there is one optical object per radio source. In total 221504 FIRST radio sources were identified in the SDSS DR6 catalogue. The matching contamination rate is typically ~ 10% (Ivezić et al. 2002; Obrić et al.

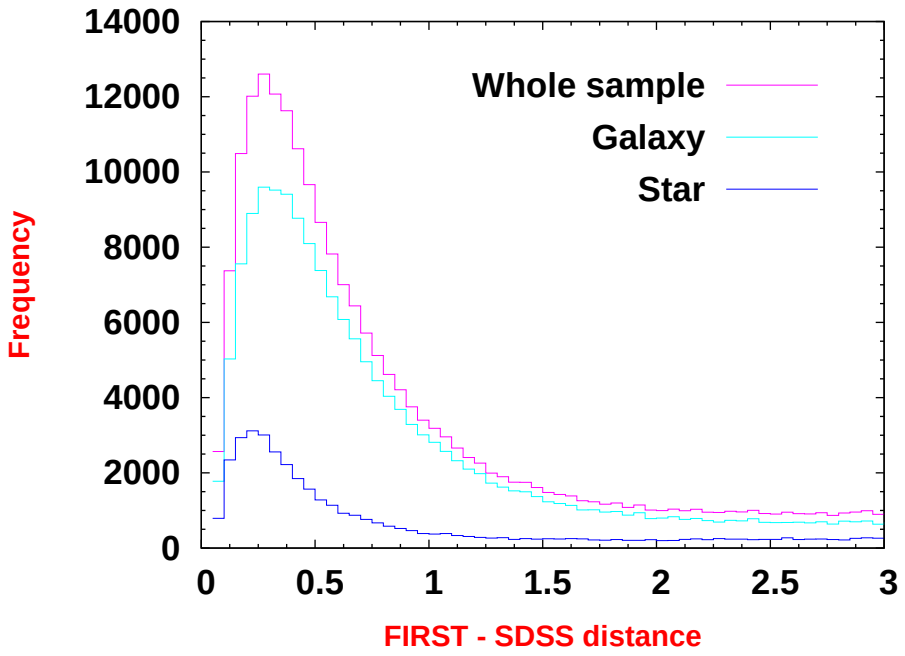

Figure 5.2: The distribution of the distance between SDSS and FIRST positions for all radio sources identified in SDSS, for FIRST radio sources optically unresolved and resolved. The three distributions are similar.

2006). Figure 5.3 displays the full area covered by the FIRST radio survey. Figure 5.4 shows the projected distribution of FIRST radio sources identified in the imaging era in the top panel, and the projected distribution of FIRST radio sources identified in the spectroscopic era in the lower panel.

5.4.1 Morphology

Morphology is one of the most important criteria used to classify objects. Star-galaxy separation in the SDSS is performed within the SDSS photometric pipeline (Lupton et al. 2002). An object is classified as extended, and hence a galaxy, if $psfMAG - cmodelMag > 0.145$. Here psfMag is the point spread function magnitude and cmodelMag is a combination of the best fitting de Vaucouleurs and exponential profiles. psfMag is described further in Stoughton et al. (2002) and cModelMag in Abazajian et al. (2004). The star-galaxy separation is reliable to better than 90% for sources with $r \sim 21$ and to better than 95% for sources with $20 < r < 21$ (Lupton et al. 2002). Additional star-galaxy classifications have been performed on SDSS data e.g., Scranton et al. (2002) performed a Bayesian star-galaxy separation via differences between the r band

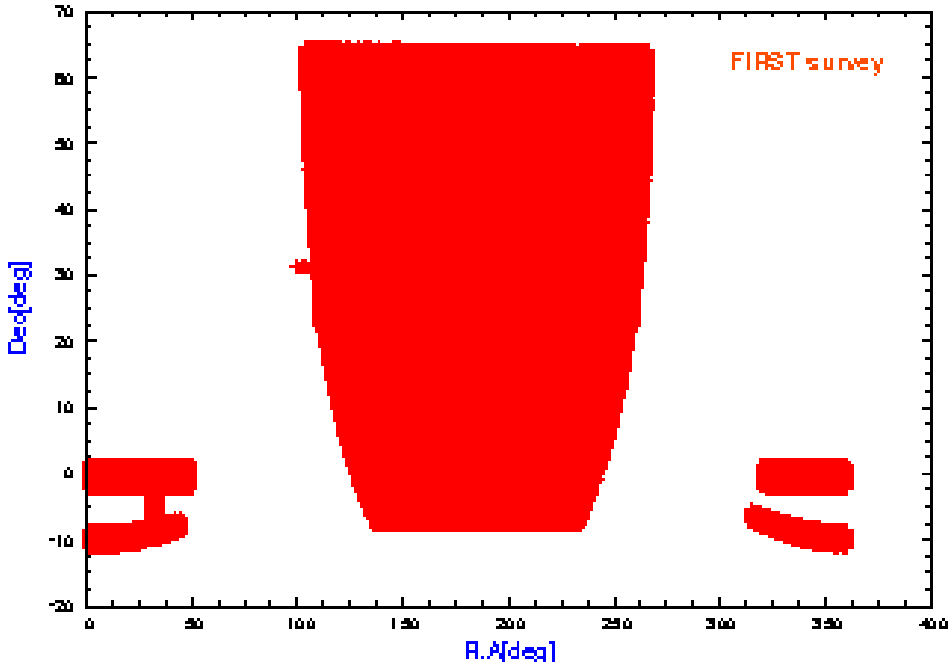

Figure 5.3: The full area coverd by the FIRST radio survey.

psfMag and modelMag (for more details see Scranton et al. 2002).

For FIRST radio sources with DR6 spectra, the parameter **SpecClass** provided by the SDSS pipeline was used to classify objects as galaxies or quasars. The distribution of SDSS spectral types for the object with DR6 spectra, as quoted in **SpecObj** view of CAS, is given in Table 5.1. For FIRST radio sources that do not have optical spectra, the parameter **type** (**type** = galaxy or star) in the **PhotoPrimary** view was used to classify objects into galaxy or star type.

Table 5.1: SDSS classification of the FIRST-SDSS DR6 matches having SDSS spectra

Spectral type	Objtype	SpecClass	Number
Galaxy	0	2	17114
Low and high redshift quasar	1	3 and 4	3035
SERENDIPITY FIRST QSO	17	3 or 4	864
SERENDIPITY FIRST galaxy	17	2	649
SERENDIPITY_ROSAT_D	15	3 or 4	77
SERENDIPITY_BLUE	16	3 0r 4	221
SERENDIPITY_DISTANT	19	3 or 4	12
SERENDIPITY_RED	18	3	1
Star_CATY_VAR	17	6	2
Stars	17	1	14
Unknown	—	0	552

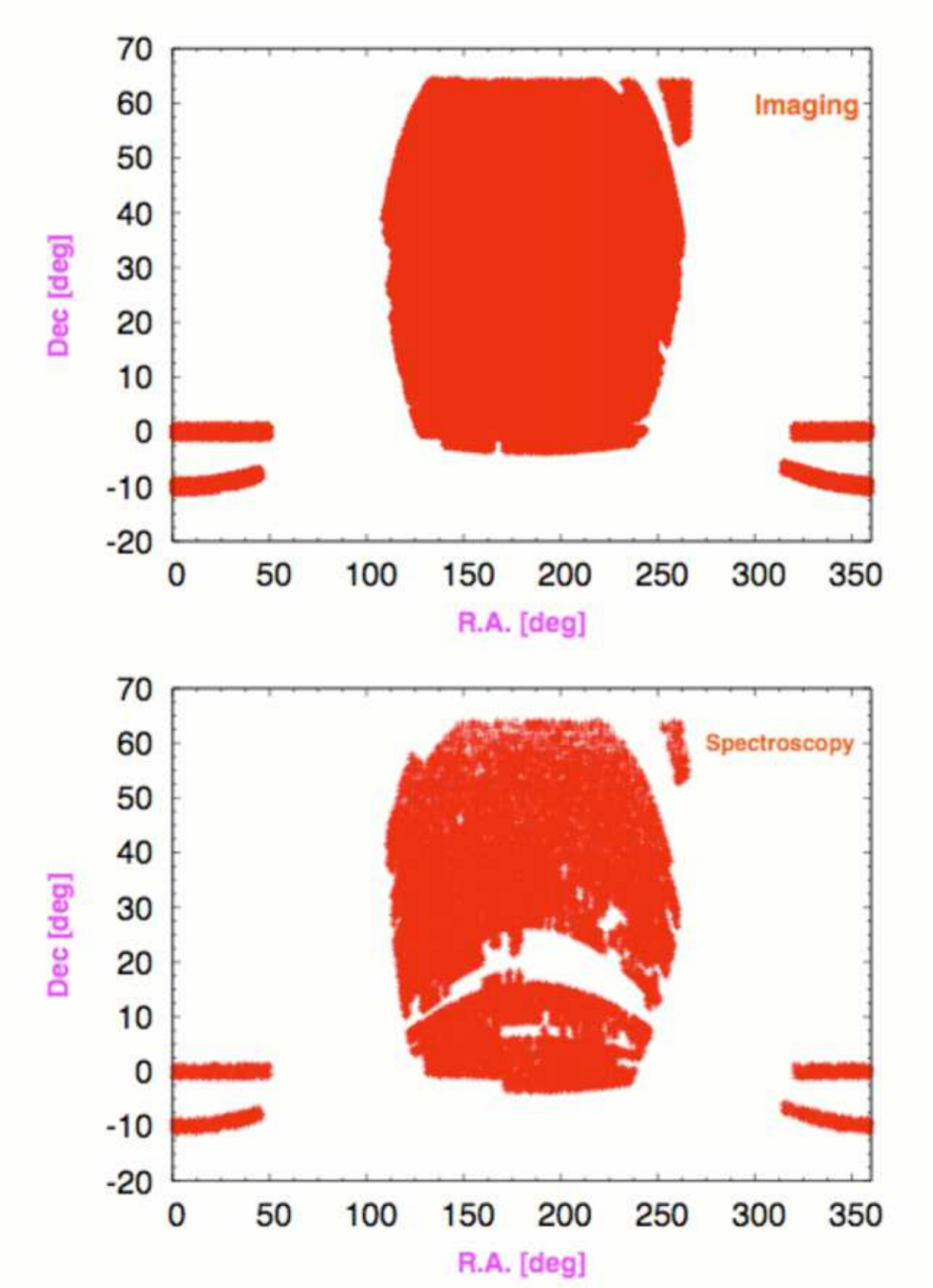

Figure 5.4: Projected distribution of FIRST radio sources optically identified in SDSS DR6. Projected distribution of FIRST radio sources identified in SDSS DR6 that have spectra with SpecZ >0

5.5 The two point angular correlation function of FIRST radio sources identified in SDSS DR6

5.5.1 Definition

One of the most widely used statistics to measure the clustering properties of a 2-D distribution of sources is the angular correlation function, $\omega(\theta)$. Following the definition from Peebles (1980), the angular two-point correlation function is defined as the joint probability δP of finding sources within the solid angle elements $\delta\Omega_1$ and $\delta\Omega_2$, separated by an angle θ, in the form:

$$\delta P = N^2(1 + \omega(\theta))\,\delta\Omega_1\,\delta\Omega_2, \tag{5.1}$$

where N is the mean surface density of galaxies. The n-point correlation function for a statistical ensemble is given by:

$$\omega(\theta) =< \delta(x)\ \delta(x+\theta)\ >, \tag{5.2}$$

where δ represents the density perturbation field and is written as:

$$\delta(x) = \frac{\rho(x) - <\rho>}{<\rho>}, \tag{5.3}$$

where $<\rho>$ is the mean density of galaxies. If galaxies are uniformly distributed on the sky then $\omega(\theta) = 0$. If they are clustered, $\omega(\theta)$ will have some non-zero value. Therefore, the angular correlation function provides a measure of galaxy density excess over that expected for a random distribution.

The angular correlation function is a projection of the spatial correlation function, $\xi(r)$, where r is physical distance, onto the plane of the sky. Even if galaxies are strongly clustered in space, when the third dimension of depth is lost to projection, a part of the clustering signal is lost too. Galaxies which are quite distant from each other in space, and hence uncorrelated, may end up quite close together in projection. The deeper the sample is, the greater the loss in clustering signal will be and the closer $\omega(\theta)$ will be to zero.

Another popular choice used to describe the amount of clustering on a given length scale

is the power spectrum, which is the Fourier transform of the correlation function $\xi(r)$ for an infinite volume:

$$\xi(r) = \frac{V}{(2\,\pi)^3} \int P(k)\, \frac{sin(k\,r)}{k\,r}\, 4\,\pi\,k^2\, dk, \tag{5.4}$$

If $P(k) \propto k^n$ (i.e. a power law), this implies that, $\xi(r) \propto r^{-3+n}$, is also a power law.

5.5.2 Method

Various methods for estimating $\omega(\theta)$ have been introduced in the literature (e.g. Infante 1994). Both geometrical and pairwise estimators have been suggested. The basic idea is to generate a set of random points in an area identical to the area of sky that was surveyed. The correlation function is measured by comparing the number of pairs of data galaxies with a given angular separation to the corresponding number for the random points. Let N_d be the number of data galaxies, N_r be the number of random points, and N_{dd}, N_{rr} and N_{dr} be respectively the numbers of data-data, random-random, and data-random pairs in a bin. The appropriately normalised versions of these values are *DD*, *RR*, and *DR* respectively:

$$DD = \frac{2\,N_{dd}(\theta)}{N_d\,(N_d - 1)}, \tag{5.5a}$$

$$RR = \frac{2\,N_{rr}(\theta)}{N_r\,(N_r - 1)}, \tag{5.5b}$$

$$DR = \frac{N_{dr}(\theta)}{N_r\,N_d}. \tag{5.5c}$$

The most commonly used estimators have the form:

$$\omega(\theta) = \frac{DD}{RR} - 1, \text{ or} \tag{5.6a}$$

$$\omega(\theta) = \frac{DD}{DR} - 1. \tag{5.6b}$$

These estimators have the advantage that no N_{rr} terms are included, which significantly reduces computer time, but is limited in its use in dealing with the interactions of the sample data with the boundaries of the sampling space. The random set behaves differently near the boundaries than the data set, which can be taken into account through the number of data-random pairs in the estimator. Infante (1994) and Hewett (1982) emphasised the importance of correcting for

any spurious cross correlation between the random and the galaxy catalogues when using the above estimators. The corrected form of the estimator is then:

$$\omega(\theta) = \frac{DD}{DR} - \frac{RD}{RR}, \tag{5.7}$$

where *RD* is the number of random-data pairs, taking the random points as centres (Infante 1994). The current popular choice for the correlation function estimator is the Landy-Szalay estimator (Landy & Szalay 1993);

$$\omega(\theta) = \frac{DD - 2\,DR + RR}{RR} - 1. \tag{5.8}$$

The advantage of this estimator is that it minimises the variance of $\omega(\theta)$ (it has a nearly Poisson variance), reduces the edge effects from which both the estimators 5.6a and 5.6b suffer, and is accurate even for small number counts. Moreover, it has similar properties (Landy & Szalay 1993, hereafter LS) to that introduced by Hamilton & Helfand (1993):

$$\omega(\theta) = \frac{DD\,.\,RR}{DR\,.\,DR} - 1. \tag{5.9}$$

In the present study, the angular correlation function has been calculated using estimators 5.8 and 5.9. The results agree well. Therefore, only the results from the LS estimator are presented.

5.5.3 Uncertainty estimates in $\omega(\theta)$

The statistics that are measured in galaxy clustering analyses are all based on pair counting. This causes large correlations in the results because the same galaxy affects the measurements over all scales, and so each data point is not independent. Therefore it is essential to estimate these uncertainties reliably, in a manner which takes proper account of the correlated character. The errors in the calculation of the angular correlation function are dominated by Poisson noise. The uncertainty in $\omega(\theta)$, in each bin, is determined using the following expression (Baugh et al. 1996):

$$\delta\omega(\theta) = \sqrt{\frac{1 + \omega(\theta)}{DD}}, \tag{5.10}$$

where, in this case, *DD* is the total number of galaxy-galaxy pairs (not normalised). Errors calculated using this equation are comparable to the errors obtained from a bootstrap resampling technique (Ling et al. 1986).

5.5.4 The random catalogue

For a given radio galaxy sample, a total of 16 random catalogues were generated, each having the same number of points as the original data set. The random sets were cross-correlated with the galaxy catalogue, giving an average value for $\omega(\theta)$ at each angular separation. In producing random sets of points, the SDSS DR6 imaging masks[1] have been taken into account. For both real (matched sources) and random data, the mangle software provided by A. Hamilton (Hamilton & Tegmark 2004) was used to locate the polygon ID for each real and random data against the SDSS imaging masks. The vast majority of FIRST radio source counterparts were in the SDSS imaging area, with only 0.1% in the masked regions. Given that this fraction is so small, these sources have been ignored.

5.5.5 Multiple component effects

A complication in the analysis of radio sources clustering is the signal at small angular separations (below a few arcminutes) caused by resolved galaxies. The true cosmological $\omega(\theta)$ can be affected or even dominated by resolving these galaxies into their various components, such as lobes, hot spots and cores. Earlier studies (e.g. Magliocchetti et al. 1998) attempted to correct $\omega(\theta)$ for the contribution of multicomponent radio sources by means of component combination algorithms. To identify groups of sources that are likely to be subcomponents of a single source, a percolation technique is adopted where all sources within a given radius are replaced by a single source at an appropriate centroid (Magliocchetti et al. 1998). Following the method developed by Magliocchetti et al. (1998), the link-length was varied in the percolation procedure according to the flux of each source. In that way, bright sources were combined, even if their angular separation was large, whereas faint sources were left as single objects. This technique is based on the $\theta \propto \sqrt{S}$ relation found by Oort (1987).

[1] http://sdss.physics.nyu.edu/vagc/

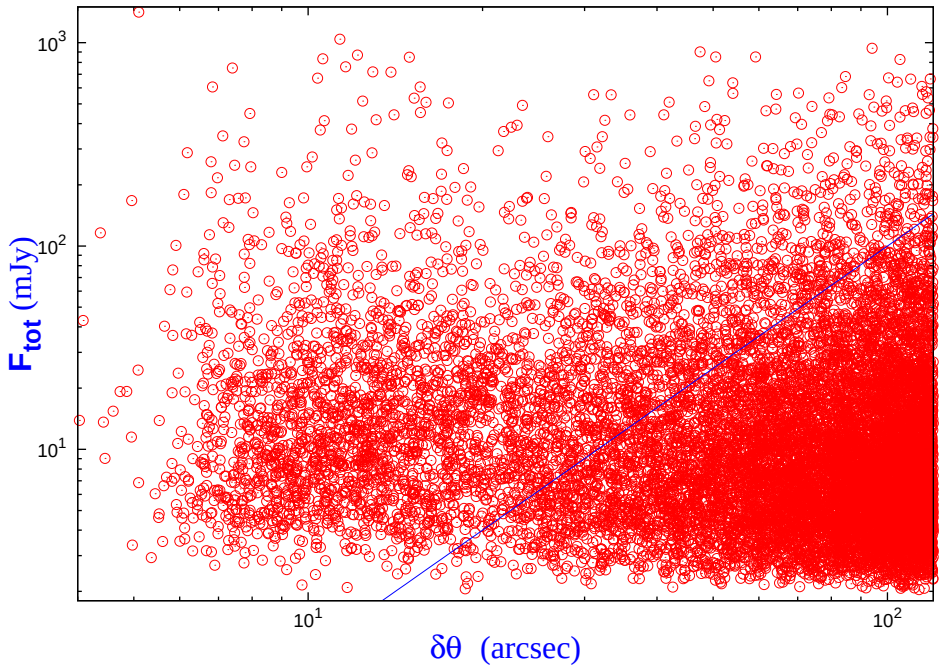

Figure 5.5: Angular separation against total flux density of double sources. The dashed line represents the maximum link-length, for a given flux density, used in the percolation technique.

To define the relation between flux density and link-length, the angular separation of double sources versus their total fluxes is plotted in Figure 5.5, out to a separation of 180″. Visual inspection has confirmed that the pairs on the left in Figure 5.5 were predominantly subcomponents of a single source. Accordingly, the maximum link-length was set to:

$$\theta_{\rm link} = 100 \left(\frac{F_{\rm total}}{100}\right)^{0.5} \text{ arcsec}, \tag{5.11}$$

where $F_{\rm total}$ is the total flux of each group. This is shown by the dashed line in Figure 5.5 and effectively removes the majority of visually identified doubles. Furthermore, only doubles whose individual component flux differ by less than a factor of four were collapsed (since lobes of a single radio source are expected to have correlated flux densities; Magliocchetti et al. 1998). This procedure was repeated until no new groups were found. The final catalogue consists of 198409 objects to the limit of 1 mJy. In the following the angular two-point correlation function is measured over the region $1^\circ < \delta < 60^\circ$ and $128^\circ < \alpha < 235^\circ$ that has a simple geometric form. This area covers ∼ 6420 square degrees and contains 120409 sources.

5.6 Results

Following the procedures described earlier, the two point angular correlation functions were computed for all FIRST radio sources identified as galaxies (in the region $128^\circ < \alpha < 235^\circ$, $1^\circ < \delta < 60^\circ$) for different flux limited samples (with flux density cutoffs at 2, 3, 5, 7 and 10 mJy), for various magnitude limited samples (with $r < 17$, $r < 18$, $r < 19$, $r < 20$, $r < 21$, $r < 22$), and for early ($u - r > 2.22$) and late-type ($u - r < 2.22$) galaxies, in equally-spaced logarithmic bins of width $\Delta \log(\theta) = 0.1$. The results are shown in Figures 5.7, 5.8, 5.9, and 5.10. The angular correlation function is parametrised as a power-law (Peebles 1980):

$$\omega(\theta) = A_\omega \left(\frac{\theta}{\theta_0}\right)^{-\delta}, \tag{5.12}$$

where the amplitude A_ω, normalised at $\theta_0 = 1^\circ$, measures the strength of the clustering, the slope, $1 - \gamma$, measures its scale-dependence, and θ is measured in degrees. The slope, $1 - \gamma = \delta$, is generally found to be $0.7 - 0.8$ for galaxies at optical wavelengths (e.g. Connolly et al. 2002; Maddox et al. 1990) although the amplitude depends on the bias of the galaxy type. At radio wavelengths, there are two different values of the slope measured in previous studies; $\delta = 0.8$ (Peacock & Nicholson 1991) and $\delta = 1.1$ (Cress et al. 1996).

To test the significance of the results, I constructed catalogues of randomly distributed points and calculated the correlation function from a region with the same geometry as the real data. The estimated amplitudes were found to be consistent with zero within the Poisson standard deviation. This is shown in Figure 5.6.

The upper panel of Figure 5.7 shows the results for $\omega(\theta)$ of the whole ID sample (i.e. FIRST-SDSS matches). As already mentioned, error bars are given by Poisson estimates for the catalogue under consideration. The solid line shows a power-law fit to these data over angular scales from 0.001° to 1°. Using a simple colour criteria determined by Strateva et al. (2001) to separate early ($u - r > 2.22$) and late ($u - r < 2.22$) galaxies in SDSS photometric data, the FIRST-SDSS matches were separated into early and late-type galaxies. The lower panel in Figure 5.7 compares the angular correlation function in the early and late-type galaxies subsamples. No consistent difference was found in the amplitude of $\omega(\theta)$.

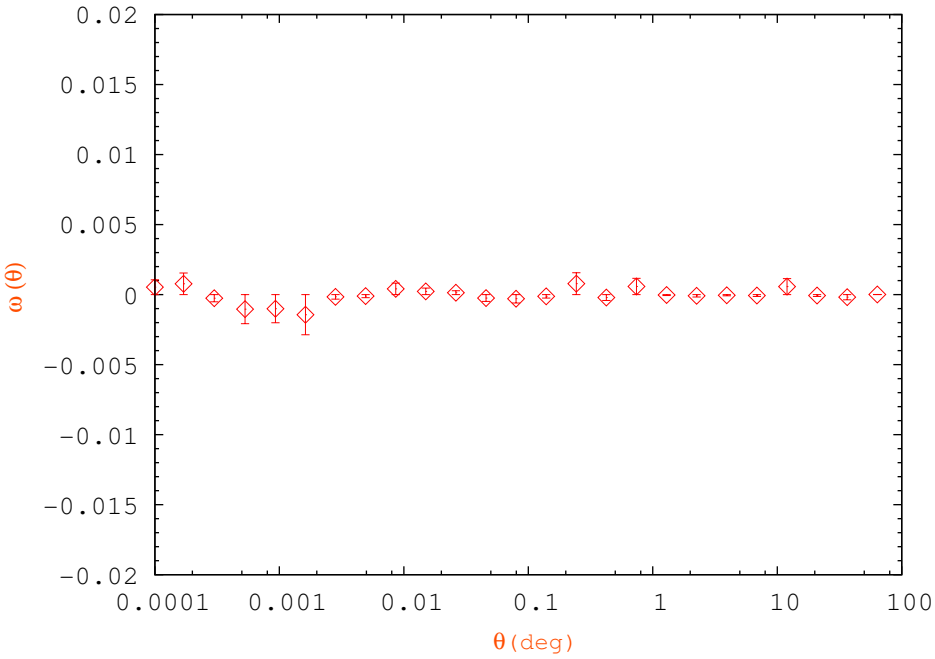

Figure 5.6: The angular correlation function of a random sample of points. The error bars are Poisson estimates.

The scaling of the correlation function with limiting magnitude is given in Figure 5.8 for the magnitude limits $r < 17$, $r < 18$, $r < 19$, $r < 20$, $r < 21$ and $r < 22$. The amplitude of the correlation function decreases toward fainter magnitudes, as would be expected from Limber's equation (e.g Scranton et al. 2002; Maddox et al. 1990). The mean amplitude for the six subsamples are close to the full sample results at all limiting magnitudes. The angular correlation function was calculated for various flux density limits 2, 3, 5, 7 and 10 mJy. The amplitude of the correlation function was found to increase with increasing flux density limits of the subsamples (see Figures 5.9 and 5.10). This is simply due to the fact that lower flux density threshold does not correspond to a deeper survey as it does for optically selected sources. This effect has been seen in previous work (e.g Overzier et al. 2003; Wilman et al. 2003; Cress et al. 1996). Overzier et al. (2003) also found that the amplitude of $\omega(\theta)$ increases with flux density limits in their calculation of $\omega(\theta)$ for both FIRST and NVSS. Blake & Wall (2002a) calculated the angular correlation function for the NVSS survey and reported that both the clustering amplitude and the slope of the clustering power-law does not depend on flux threshold. They found an amplitude, $A_w = 1.04 \pm 0.09 \times 10^{-3}$, and a slope, $\delta = 0.85 \pm 0.1$. The number of FIRST-SDSS sources in each subsample, the calculated amplitudes associated with their Poissonian errors

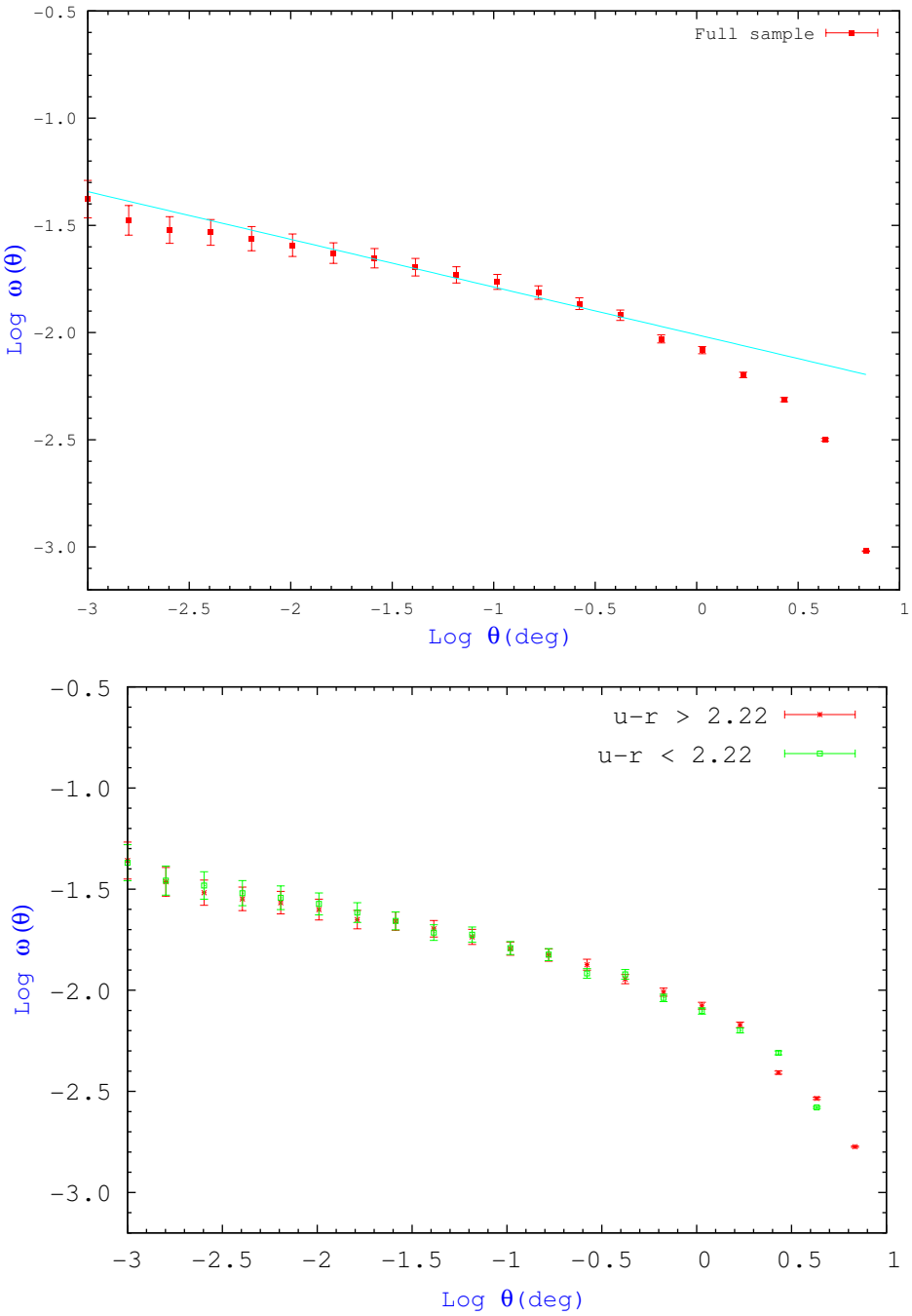

Figure 5.7: Angular correlation function from the FIRST-SDSS matches for the whole sample shown in the upper panel. The fit to the data is shown by the solid line. The lower panel displays the angular correlation function for both early ($u-r > 2.22$) and late-type ($u-r < 2.22$) FIRST-SDSS galaxies. The error bars are Poisson estimates.

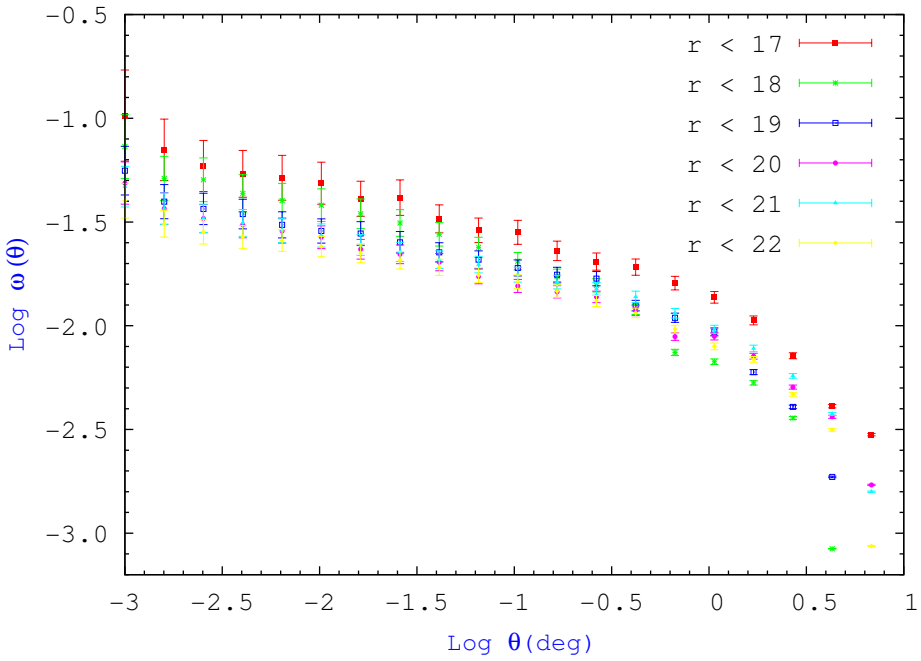

Figure 5.8: Angular correlation function from the FIRST-SDSS matches as a function of magnitude. Correlation function for different magnitude limits: $r < 17$, $r < 18$, $r < 19$, $r < 20$, $r < 21$, $r < 22$.

and the slopes are listed in Table 5.2.

The first clustering analyses of the FIRST radio sources was done by Cress et al. (1996). These authors measured the two-point angular correlation function for different subsamples (see Table 5.3), and found an amplitude of $A = 2.00 \pm 0.30 \times 10^{-3}$ and a slope of $\delta = 1.26 \pm 0.04$. Cress et al. (1996) reported that the angular correlation function shows an 'unexpected bump' at $\theta = 0.1^{\circ}$ when including sources flagged as sidelobes in the catalogue, and the bump decreases when flagged sources are removed. The analysis of the FIRST radio sources clustering was repeated by Magliocchetti et al. (1998) who attempted to remove double sources using an algorithm different from the one adopted by Cress et al. (1996). Their results were in good agreement with Cress et al. (1996).

Magliocchetti & Maddox (2002) cross correlated the FIRST radio sources with the APM survey and obtained the two point angular correlation function for FIRST radio sources identified in the APM survey. Magliocchetti & Maddox (2002) calculated the angular correlation function for three samples: all FIRST radio sources identified in the APM survey, FIRST radio sources identified as galaxies and FIRST radio sources identified as point-like objects. They

Table 5.2: The χ^2 best fitting parameters of equation 5.12 to the angular correlation function for the whole sample and different subsmaples.

Sample	N_{gals}	$10^3 A$	δ
		Full sample	
Full sample	106452	10.6 ± 0.5	1.18 ± 0.01
		Flux limited samples	
$S > 2$ mJy	70851	9.7 ± 0.3	1.20 ± 0.07
$S > 3$ mJy	50049	11.4 ± 0.5	1.18 ± 0.01
$S > 5$ mJy	31154	14.7 ± 0.7	1.17 ± 0.01
$S > 7$ mJy	22797	11.9 ± 0.7	1.18 ± 0.01
$S > 10$ mJy	16100	14.0 ± 0.1	1.19 ± 0.01
$S < 2$ mJy	35883	11.8 ± 0.6	1.17 ± 0.01
$S < 3$ mJy	56549	10.1 ± 0.5	1.19 ± 0.01
$S < 5$ mJy	75354	9.6 ± 0.5	1.18 ± 0.01
$S < 7$ mJy	83681	9.7 ± 0.5	1.18 ± 0.01
$S < 10$ mJy	90366	9.2 ± 0.4	1.19 ± 0.01
		Magnitude limited samples	
$r < 17$	11258	13.6 ± 0.1	1.27 ± 0.02
$r < 18$	19935	10.9 ± 0.1	1.26 ± 0.01
$r < 19$	32045	11.1 ± 0.9	1.21 ± 0.01
$r < 20$	47125	9.3 ± 0.6	1.22 ± 0.01
$r < 21$	67264	11.1 ± 0.5	1.19 ± 0.01
$r < 22$	93581	10.2 ± 0.5	1.18 ± 0.01
		Red galaxies	
$u - r > 2.22$	69318	9.9 ± 0.5	1.19 ± 0.01
		Blue galaxies	
$u - r < 2.22$	37134	10.1 ± 0.4	1.20 ± 0.01

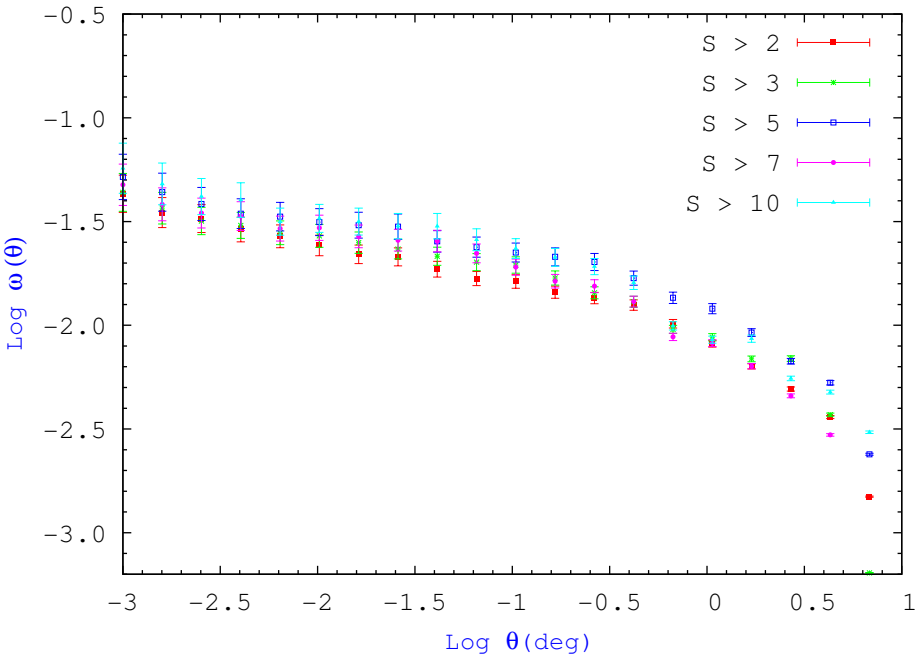

Figure 5.9: Angular correlation function from the FIRST-SDSS matches as a function of flux density limit. Correlation function for different flux density limits: $S > 2$ mJy, $S > 3$ mJy, $S > 5$ mJy, $S > 7$ mJy, $S > 10$ mJy.

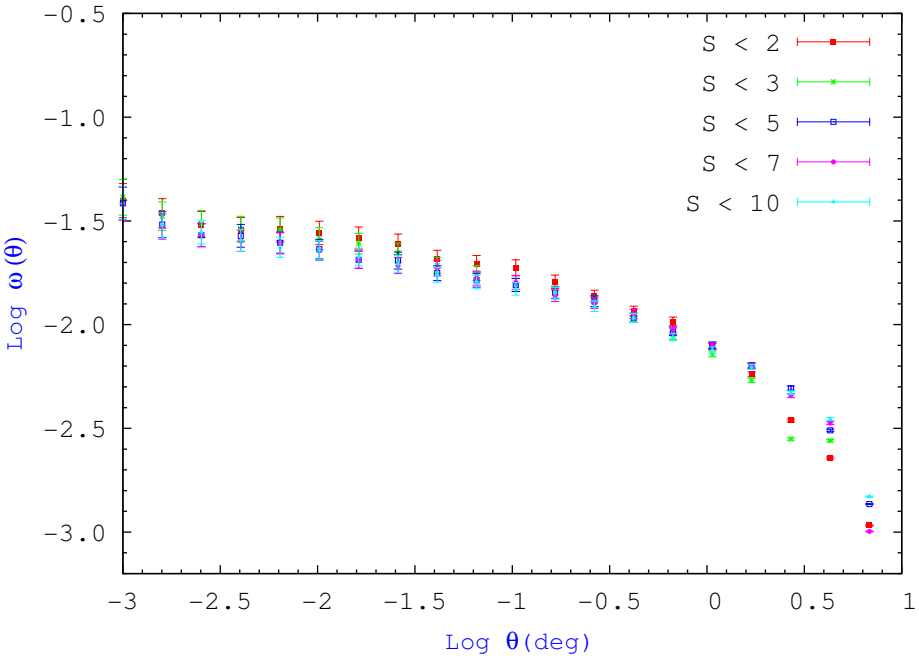

Figure 5.10: Angular correlation function from the FIRST-SDSS matches as a function of flux density limit. Correlation function for different flux density limits: $S < 2$ mJy, $S < 3$ mJy, $S < 5$ mJy, $S < 7$ mJy, $S < 10$ mJy.

found values of $\delta = 0.3$, $A = 0.018$ for the sample as a whole, and $\delta = 1.1$, $A = 0.03$ for sources identified as galaxies.

Blake & Wall (2002a) and Overzier et al. (2003) measured the angular correlation $\omega(\theta)$ of both NVSS and FIRST radio sources. They found that the angular correlation function below 6 arcmin is dominated by multi-component sources and that the true cosmological clustering amplitude is essentially constant at $\simeq 10^{-3}$ from 3 mJy to 50 mJy. These authors fitted the data with a sum of two power law functions, one dominant at $\theta < 0.1^{\circ}$, which was due to multiple component effects and another due to clustering at larger scales, with a clear break in $\omega(\theta)$ between these scales. At flux densities $S > 200$ mJy Overzier et al. (2003) found a sudden increase in the correlation signal of NVSS radio sources at $\theta = 0.2^{\circ}$. Overzier et al. (2003) argued that the cause of the bump is unclear and is unlikely to be caused by side-lobes as suggested by Cress et al. (1996). They argued that it is unlikely that the NVSS catalogue contains any such bright side-lobes. They also examined the contour maps of several tens of source pairs (with $S > 500$mJy) that contribute to $\omega(\theta)$ at $\theta = 0.2^{\circ}$, finding that the pairs are consistent with unresolved peaks without signs of diffuse, extended emission or side-lobe contamination.

Comparing the results for our FIRST-SDSS matches to Overzier et al. (2003), the amplitude is found to be higher and the slope is steeper. Rather, our measured amplitudes of $A_{\omega} \approx 0.01$ for the FIRST-SDSS matches are not consistent with the results of Magliocchetti & Maddox (2002) for the FIRST-APM matches who measured an amplitude of $A_{\omega} \approx 0.03$. Moreover, there is no clear break caused by multiple component sources in the angular correlation function as has been reported in previous studies. It is likely that this effect has been alleviated once the radio sources are optically identified. Our results in comparison to the results found in the literature are summarised in Table 5.3.

Table 5.3: Comparison of results with previous work on radio galaxies

Survey	Flux density (mJy)	Amplitude A ($\times 10^{-3}$)	Slope δ	Amplitude B ($\times 10^{-6}$)
FIRST-SDSS (This work)	> 1	10.6 ± 0.5	1.18 ± 0.01	-
NVSS (Blake & Wall 2002a)	> 15	1.04 ± 0.09	0.85 ± 0.1	-
NVSS (Blake & Wall 2002b)	> 10	1.08 ± 0.09	0.83 ± 0.05	-
SUMSS (Blake et al. 2004b)	> 10	2.04 ± 0.38	1.24 ± 0.16	-
NVSS (Overzier et al. 2003)	> 10	1.00 ± 0.20	fixed to 0.8	1.5 ± 0.10
WENSS (Wilman et al. 2003)	> 35 (peak)	1.01 ± 0.35	1.22 ± 0.33	-
FIRST (Overzier et al. 2003)	> 10	1.90 ± 0.30	fixed to 0.8	1.4 ± 0.10
FIRST (Magliocchetti et al. 1998)	-	1.06 ± 0.10	1.50 ± 0.10	-
FIRST-APM (Magliocchetti & Maddox 2002)	Whole sample	18	0.3	-
FIRST-APM (Magliocchetti & Maddox 2002)	Galaxies	30	1.10	-
FIRST (Cress et al. 1996)	whole sample	2.00 ± 0.30	1.26 ± 0.04	-
FIRST (Cress et al. 1996)	$S < 2$	5.60 ± 0.60	1.97 ± 0.04	-
FIRST (Cress et al. 1996)	$S > 3$	2.60 ± 0.80	1.20 ± 0.10	-

5.7 Conclusion

This chapter has presented a brief introduction to the clustering properties of FIRST radio sources identified in the SDSS DR7 survey. The angular two point correlation function has been measured for all FIRST radio sources identified as galaxies, and for various magnitude limited samples. The amplitude was found to be higher and the slope steeper compared to previous results (e.g. Overzier et al. 2003), rather, our measured amplitudes of $A_\omega \approx 0.01$ for the FIRST-SDSS matches are consistent with the results of Magliocchetti & Maddox (2002) for the FIRST-APM matches who measured an amplitude of $A_\omega \approx 0.03$. We also found that the angular correlation scales with the depth of the optical survey SDSS as expected. The amplitude of the angular correlation function increases as the flux increases.

CHAPTER 6

Spectral energy distribution of radio sources in nearby galaxy clusters

The following chapter is similar to the article: *Spectral Energy Distribution of Radio Sources in Nearby Clusters of Galaxies: Implications for Sunyaev-Zel'dovich Effect Surveys*, Lin, Y., Partridge, B., Pober, J. C., **El Bouchefry, K.**, Burke, S., Klein, J., Coish, J., Huffenberger, K., 2008, submitted to ApJ, astro-ph/0805.1750. My contribution to this work is described in the publications declaration that appears in the front matter of this thesis.

The text is as it appears in the submitted article with minor changes for consistency of spelling and style.

Abstract

To explore the high frequency radio spectra of galaxies in clusters, we used NRAO's Very Large Array at four frequencies, 4.9 – 43 GHz, to observe 139 galaxies in low redshift ($z < 0.25$), X-ray detected, clusters. The clusters were selected from the survey conducted by Ledlow & Owen, who provided redshifts and 1.4 GHz flux densities for all the radio sources. We find that more than half of the observed sources have steep microwave spectra as generally expected ($\alpha < -0.5$, in the convention $S \propto \nu^{\alpha}$). However, 60 – 70% of the unresolved or barely resolved sources have flat or inverted spectra. Most of these show an upward turn in flux at $\nu > 22$ GHz, implying a higher flux than would be expected from an extrapolation of the lower frequency flux measurements. Our results quantify the need for careful source subtraction in increasingly sensitive measurements of the Sunyaev-Zel'dovich effect in clusters of galaxies (as currently being conducted by, for instance, the Atacama Cosmology Telescope and South Pole Telescope groups).

6.1 Introduction

The Sunyaev-Zel'dovich effect (SZE; Sunyaev & Zeldovich 1970) is a powerful method for detecting clusters from observations of the cosmic microwave background (CMB). The hot electrons in the intracluster medium inverse-Compton scatter the CMB photons, distorting the CMB spectrum as seen in the direction of a cluster. Because the SZE is redshift independent and is caused by the presence of dense gas deep within the potential well of dark matter halos, SZE surveys can effectively detect high redshift clusters (see e.g., Carlstrom et al. 2002, for a recent review) and are less confused by large scale structure than optical surveys.

Several microwave background experiments with mJy level sensitivity and 1–10 arcminute beams, including the Atacama Cosmology Telescope (ACT[1];Fowler et al. 2007), the South Pole Telescope (SPT[2]; Ruhl et al. 2004), the Arcminute Microkelvin Imager (AMI[3]; AMI Collabora-

[1]www.physics.princeton.edu/act/index.html
[2]pole.uchicago.edu/
[3]www.mrao.cam.ac.uk/telescopes/ami/index.php

tion et al. 2006), the Atacama Pathfinder Experiment SZ survey (APEX-SZ[4]), and *Planck*[5], will yield thousands of SZE clusters in the next few years; in particular, all four ground experiments were already operational in 2007. The data from these surveys will permit study of the mass function of clusters over cosmic epochs, a measurement which can elucidate the role of dark energy because structure growth slows during dark energy domination.

As a probe of precision cosmology, a SZE survey has to control its systematics, particularly regarding the correlation between the SZE flux and cluster mass (e.g., Lin & Mohr 2003). Radio point sources often found at or near cluster centres pose serious challenges in this regard (Carlstrom et al. 2002). Powerful sources can overwhelm the cluster SZE signature (Cooray et al. 1998; Coble et al. 2007), and weaker, unresolved sources can collectively contaminate the SZE signal (Pierpaoli & Perna 2004). Clusters missed or affected this way would distort the measurements of cosmological parameters from SZE surveys, and it is therefore crucial to estimate the degree of contamination due to radio sources.

Although at low frequencies (1.4–5 GHz) there have been extensive studies of the radio galaxy population in clusters (e.g., Ledlow & Owen 1996; Miller & Owen 2001; Morrison & Owen 2003; Lin & Mohr 2007), it is not clear at present how these sources behave at the frequencies ($\geq$ 15 GHz) and flux levels ($\sim$ mJy) of on-going SZE surveys. Most of the forecasts for future surveys therefore rely on large extrapolations either in frequency or in flux level, and often both, from existing data (e.g., Toffolatti et al. 1998; Knox et al. 2004; White & Majumdar 2004; de Zotti et al. 2005; however see Sadler et al. 2008 for recent observations at 95 GHz). For example, Lin & Mohr (2007, hereafter LM07) use the observed spectral energy distribution (SED) and spectral index distribution (SID) from 1.4 to 4.85 GHz to estimate SZE survey contamination from the observed 1.4 GHz cluster radio luminosity function. At 150 GHz, they estimate that about 10% of clusters of mass 10^{14} – $10^{15} M_{\odot}$ may host AGNs whose total fluxes exceed that of the SZE flux. Although the AGN contribution can be detected and subtracted by combining observations at different frequencies used in a SZE survey, a more critical issue is to be able to quantify the uncertainty about the fraction of clusters being lost or contaminated at few percent level (Lima & Hu 2005). This extrapolation over two orders of magnitude in

[4]bolo.berkeley.edu/apexsz/
[5]www.rssd.esa.int/Planck/

frequency (i.e., from 1.4 GHz to 150 GHz) is highly uncertain, and points out the importance of understanding the actual frequency dependence of these cluster sources.

An extensive follow up of the 15 GHz 9C survey from 1.4 to 43 GHz (Bolton et al. 2004) clearly demonstrates that the SED of radio sources is highly non-trivial, but does not focus on cluster radio sources. With sensitive observations toward 89 clusters over $0.1 \leq z < 1$, Coble et al. (2007) determine the SID between 1.4 and 28.5 GHz. This is a major step toward understanding of the nature of the radio sources in intermediate- to high-z clusters. However, we note that their sample is effectively selected against clusters hosting bright radio sources. Furthermore, only a few of the radio sources are spectroscopically confirmed cluster members. Therefore it is not clear whether their sample is representative of the cluster radio source population as a whole.

Here we present a systematic study of the spectral energy distribution of *cluster* radio sources from 4.86 to 43.3 GHz, conducted with the Very Large Array (VLA). 139 radio galaxies associated with 110 clusters at $z < 0.25$ are observed at three or four frequency bands *nearly simultaneously*, allowing better determination of the spectral shape. Photometric data from the Sloan Digital Sky Survey (SDSS), where available, are used to examine correlations (if any) between the SID/SED and properties of the host galaxy and cluster, such as colour, luminosity and clustercentric distance. Our survey improves upon previous studies in several aspects, including the selection of cluster member galaxies based on available redshifts, the large sample size, and the near-simultaneous measurement of fluxes in all four bands.

The plan of the chapter is as follows. In §6.2 we describe our cluster and radio galaxy sample. The details of the observations and data reduction are provided in §6.3 and §6.4, respectively. As the angular resolution of the observations at different frequencies is quite different, we pay particular attention in comparing the fluxes in different bands; the procedure is reported in §6.5. We present the SED and SID of the sources in §6.6, and the properties of the host galaxies and clusters in §6.8. Based on these new results, we forecast the possible contamination due to radio sources of SZE surveys in §6.9. We conclude by summarising our main findings and suggesting directions for further work in §6.10.

Throughout this chapter, we employ a flat ΛCDM cosmological model where $\Omega_M = 1 - \Omega_\Lambda = 0.3$ and $H_0 = 70h_{70}\,\mathrm{km\,s^{-1}Mpc^{-1}}$.

6.2 Cluster and radio galaxy sample selection

Ledlow & Owen conducted a 1.4 GHz survey of radio galaxies in $\sim$ 400 clusters at $z < 0.25$ with a limiting sensitivity of 10 mJy, and provided extensive redshift measurements for the host galaxies (Ledlow & Owen 1995, 1996; Owen et al. 1995; Owen & Ledlow 1997). Their cluster sample was drawn from the Abell catalogs (Abell 1958; Abell et al. 1989), and was restricted to area with reddening at *R*-band of less than 0.1 mag. We further limited ourselves to 110 clusters that are detected in the X-rays. The main reasons for this requirement are: (1) as our ultimate goal is to make predictions for the radio source contamination in SZE surveys, it is preferable to work with a cluster sample that is selected in a similar fashion as the SZE; and (2) the X–ray emission provides a rough estimate of the cluster mass, which is an important ingredient in our forecast for the SZE surveys. As radio galaxies are rare, to maximise the sample size, we did not set any X-ray flux limit as we compiled our cluster sample. Based on Ledlow & Owen's redshift catalogue, 139 galaxies associated with these clusters were selected as our radio galaxy sample. We note that Ledlow & Owen surveyed the galaxies within 0.3 Abell radius of the cluster centre (i.e., $\approx 0.64 h_{70}^{-1}$ Mpc), irrespective of the size (mass) of the clusters. Given the high concentration in the spatial distribution of radio sources within clusters (LM07), their approach should include the majority of the sources associated with the clusters, thus providing us with a representative initial sample of radio galaxies. In some cases we detect galaxies not in our initial sample that we could confirm are cluster members on the basis of common redshift (see §6.6.1 below).

6.3 Observations

Measurements in all four spectral bands were made at default VLA frequencies, cantered at 43.3, 22.4, 8.5 and 4.9 GHz[6]. The observations discussed here were made in late October, 2005, with the VLA in a hybrid DnC configuration. In this configuration, the north-south baselines are on average longer than the east-west baselines, and as a consequence the synthesized beam is highly elliptical except for sources observed near the meridian at low elevation. During our

[6]Throughout the paper we refer to these frequency bands as Q, K, X, and C bands, respectively. Note that the 1.4 GHz channel is denoted as the L band.

runs, several antennas had been removed for repair or refitting; on average we had only 22 available, resulting in a ∼ 20% reduction in sensitivity from the full array of 27. The first run, during the night Oct. 23-24, was carried out in mostly cloudy weather with poor atmospheric phase stability. We consequently elected to defer the 43 GHz observations to later runs. The high frequency Q-band observations were concentrated in a short run on Oct. 28 and a much longer run on Oct. 29-30 – the latter in excellent, clear weather. The final short run on the night of Oct. 31 was used to obtain fill-in measurements on sources missed earlier at various frequencies.

6.3.1 Calibration

For all but the Oct. 31 run, our flux density scale was based on 1331+305 (3C286), for which NRAO specifies flux densities of 1.4554, 2.5192, 5.205 and 7.485 Jy at 43.3, 22.4, 8.5 and 4.9 GHz, respectively. 3C286 was not visible during our short run on Oct. 31; for these data we employed 3C48 as the primary flux calibrator, and carefully intercompared the flux densities obtained for sources and secondary calibrators observed in common on this day and earlier ones.

In the case of the two highest frequency bands, we employed standard software in the AIPS software package to import a model of the primary calibrators to take account of slight resolution effects in K and Q bands.

A variety of secondary (phase) calibrators were employed; we in general selected calibrator sources with reasonably flat spectra so that the same source could be used for observations in all four bands. Calibrators generally were within ∼ 15° of all of our cluster sources.

Additional information on some instrumental parameters is provided in Table 6.1. Note that the values for the synthesized beam shape are approximate, since the beam geometry depends on the declination and hour angle of the source.

6.3.2 Fast switching

In the case of the 43 GHz observations, we employed fast switching between the source of interest and a nearby phase calibrator source. The integration times on source and calibrator

Table 6.1: Instrumental parameters

Frequency (GHz)	Integration time (seconds)	Typical Sensitivity (mJy)	Image Pixel size (arcsec)	Synthesized beam (approx)
4.86	80	2.0	1.0	$8'' \times 13''$
8.46	50	0.5	0.6	$4'' \times 8''$
22.46	120	1.0	0.2	$2'' \times 3''$
43.34	~ 300[a]	0.8	0.2[b]	$2'' \times 3''$[b]

[a] fast switching employed (see §6.3.2).
[b] for tapered images (see §6.5.1).

were set to be approximately equal to or less than the atmospheric phase coherence time at 43 GHz. Rather than adjusting these integration times on the fly, we set them to be 100 sec on sources between calibrations, and 40 sec on nearby calibrators. For each galaxy observed, this cycle is repeated 3 times.

6.4 Data reduction, Analysis and Imaging

The raw amplitude and phase data are flagged for shadowing of one antenna by another, interference, noisy correlators, weak antennas, and so on. In general, this flagging process removes only a few percent of the raw data. When data from the available antennas in the array are combined, the data are weighted by the inverse of the variance in the average signal.

Each source at each of the four frequencies is imaged using standard NRAO procedures in the AIPS software package. In forming the images, the pixel or cell size initially employed is 0.1″, 0.2″, 0.6″ and 1.0″ at 43.3, 22.5, 8.5, and 4.9 GHz, respectively. These values allow complete sampling of the synthesized beam even along its minor axis. In all cases, we make 1024^2 images. The raw images are lightly cleaned of side lobes ($\sim$ 200 iterations) again using standard NRAO procedures in AIPS. In most cases, when a source or sources are evident in the raw image, we clean first in a small area containing the source(s), then lightly clean the entire 1024^2 pixel image. If no source is evident in the initial image, we simply clean lightly over the entire area. We have experimented with different levels of cleaning, and found no significant

change in the flux densities of sources.

6.4.1 Flux density of Unresolved or barely resolved sources

Flux densities of evident, and unresolved or barely resolved, sources are determined by fitting a two-dimensional Gaussian to each image, using a standard process in AIPS (specifically, IMFIT). We report the integrated flux for each source. When no source is evident at or near the specified position, we compare 4σ (σ is the local noise rms) to 2σ added onto the brightest flux per beam near the image centre (within 50 pixels), and present the greater as an upper limit.

6.5 Effects of resolution

As expected, many cluster radio sources show evident, resolved, structure at one or more of our observing frequencies. For resolved or irregular sources it is more difficult to obtain accurate fluxes; more importantly, the flux densities of resolved and complex sources are difficult to compare at different frequencies. For instance, the lobes of some of the classical FRII radio sources in our list are well delineated at 4.9 GHz, but only isolated hot spots in the lobes are visible at higher frequencies. In addition, the angular resolution of the VLA synthesized beam in the DnC configuration vary from $\sim 2''$ to $\sim 13''$ depending on frequency; much of the flux of extended sources is resolved out at higher frequencies. The loss of flux at higher frequencies (higher resolution) implies that our derived spectral indices are lower limits (that is, sources could have flatter spectra than we determine because we "miss" flux at the higher frequency).

6.5.1 Tapered 43 GHz Images

Since we are most interested in the highest frequencies, 22 and 43 GHz, flux densities and the 22-43 GHz spectral index, we convolve our 43 GHz images with an elliptical Gaussian weighting profile to broaden the synthesized beam to match approximately the larger size of the synthesized beam at 22 GHz. This is done by applying a Gaussian weighting function to the $u - v$ data before imaging, again using a standard procedure in the AIPS task IMAGR. A $u - v$ taper of $45k\lambda$ and $135k\lambda$ provides a good overall match to the 22 GHz beam. For these

tapered images we employ 0.2″ cells, as for the 22 GHz images. By approximately matching the 22 and 43 GHz synthesized beams, we eliminate or reduce the problem of resolution and are able to compare fluxes from matched areas of the sky. Thus our 22-43 GHz spectral indices are unbiased values, not lower limits.

Unless otherwise noted, all flux densities at 43 GHz are derived from these tapered images.

Because of the larger frequency ratio between 8.5 and 22 GHz, tapering the 22 GHz images to match the 8.5 GHz synthesized beam produces very noisy images (much of the $u-v$ data was strongly down-weighted), so we elect not to taper the 22 GHz images; see §6.6.4 for further details. Hence spectral indices based on fluxes at 8.5 (or 4.9) GHz are lower limits, as noted above.

6.5.2 Flux Density of Resolved or Irregular Sources

In the case of irregularly shaped or clearly extended sources, we estimate the flux density within a rectangular region including all of the visible emission. These are figures cited in Table 6.5. Relatively few of the 22 and 43 GHz sources are complex enough to require this treatment.

6.6 Observational Results

We have observed 139 galaxies, and detected 136 in at least one band. The three that show no sign of a source at any of the frequencies are 0053−102B, 1108+410A, and 1657+325B. These three are not included in our analysis. We note that the first and last of these three are weak 21 cm sources in Ledlow & Owen's catalogue. On the other hand, 1108+410A has a flux of 116 mJy in their catalogue, but is very extended. In our 4.9 GHz image, we see faint traces of a source, but it is almost entirely resolved out even at $\sim 12''$ resolution.

For 111 galaxies we are able to measure flux in at least three bands. This subsample will allow better determination of the spectral shape, and will be the focus of this section. Some of these galaxies have multiple components, and in total we detect 140 radio sources associated with them. Table 6.2 records the detection statistics of our sources. In Table 6.5 we provide flux measurements of all the sources.

Table 6.2: Detection statistics

	all morphologies		core/point-like	
detection[a]	components	galaxies	components	galaxies
all 4	87	75	57	57
$\geqslant 3$	140	111	73	73
$\geqslant 2$	185	133	83	83
$\geqslant 1$	192	136	86	85
total	195	139	86	85

[a] number of bands the sources are detected.

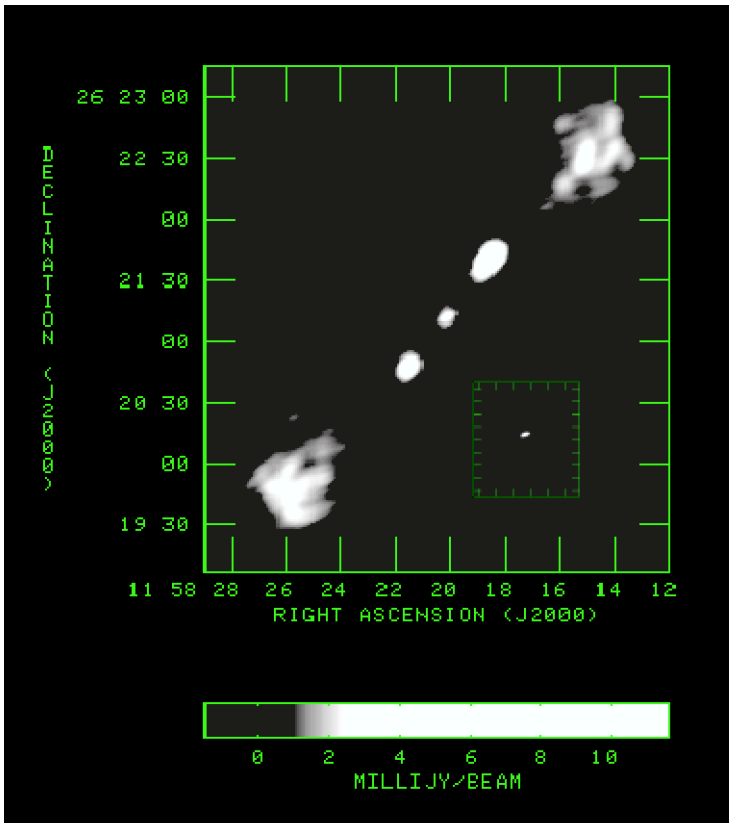

Figure 6.1: Main figure: the source 1155 + 266 imaged at 8.5 GHz. Insert (to same scale): the same source at 22 GHz, showing no evidence for emission from the lobes; the core remains.

6.6.1 "Background" Sources

In many of our images, especially those at low frequencies with their correspondingly larger solid angle, we by chance detect sources at a distance from the centre of the field (or pointing position). Since our target galaxies are all at low redshift, these peripheral sources are presumably mostly background radio sources. We exclude from our analysis of the statistical properties of cluster radio galaxies all such "background" sources. Four of these "background" sources, however, have catalogued redshifts which show they are cluster members. These 4 are added to our sample of cluster galaxies in the subsequent analysis.

6.6.2 Overall Properties of Cluster Radio Galaxies

We now focus on the 111 cluster radio galaxies for which the spectral shape can be reliably traced, since we have measurements at $\geq$ 3 frequencies. At the lowest frequency, 4.9 GHz, virtually all of the sources have complex structure. In $\sim$ 75% of the sources, a clear core or small, barely resolved jet, is visible. Even in these cases however, there is generally additional extended emission. In other sources, the cores or other resolved or barely resolved structures visible in higher frequency, higher resolution, images are unresolved or merged with diffuse structure in the 4.86 GHz images. Examples are shown in Fig. 6.2 ((a), (b) and (c)). This makes it difficult to isolate the cores at our lowest frequency, and to determine their flux densities for comparison with measurements at higher frequencies. In some cases, our best option is to compare the 4.9 GHz flux of an entire source with the sum of the flux densities of its components at the next highest frequency.

At the next highest frequency, 8.5 GHz, with a $4'' \times 8''$ beam, cores and jets are more frequently resolved and isolated. On the other hand, we are resolving out some of the flux of extended features seen in the lower resolution 4.9 GHz image. As already noted, that means that the 8.5 GHz flux densities may be underestimated for large, extended sources and hence our calculated values of the 4.9-8.5 GHz spectral index are generally lower limits. On the other hand, the flux density determination for isolated, barely resolved cores and jets are more accurate and less influenced by background emission than is the case at 4.9 GHz.

At the two highest frequencies, because of the higher resolution, most of the extended struc-

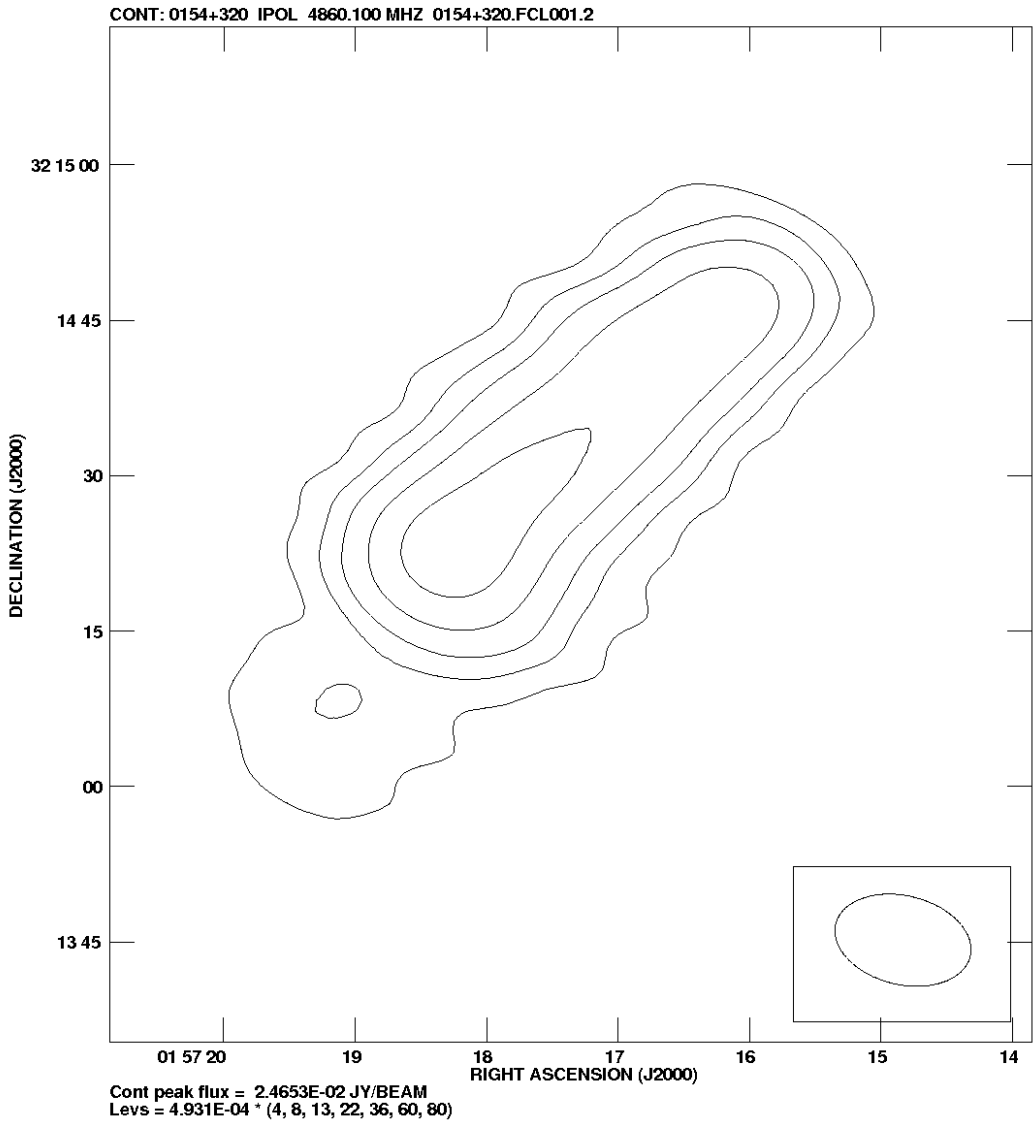

Figure 6.2: (a) A source (0154+320) imaged at C band showing the loss of flux due to resolution; beam profiles at each frequency are shown in the small box on the lower right of each panel. Contours are selected to reveal the main source properties.

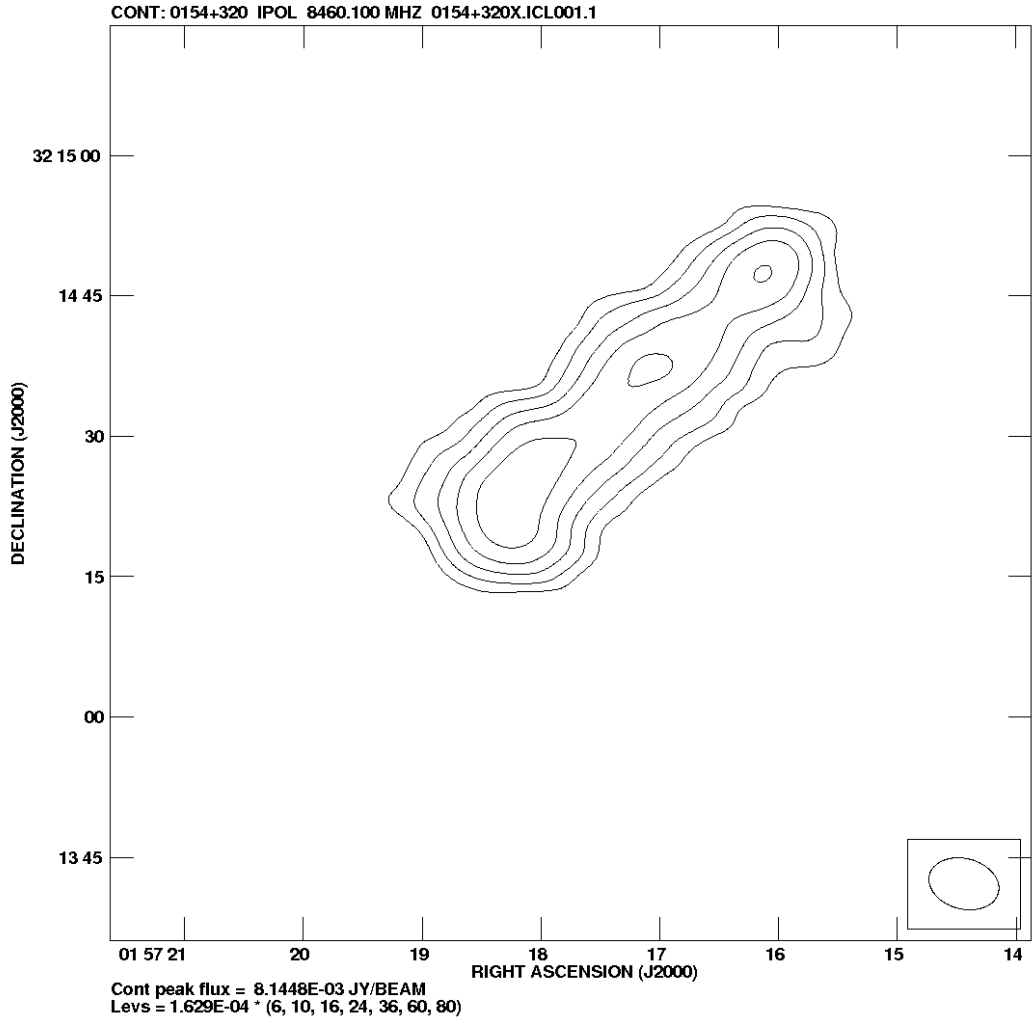

Figure 6.2: (b) A source (0154+320) imaged at X band, showing the loss of flux due to resolution; beam profiles at each frequency are shown in the small box on the lower right of each panel. Contours are selected to reveal the main source properties.

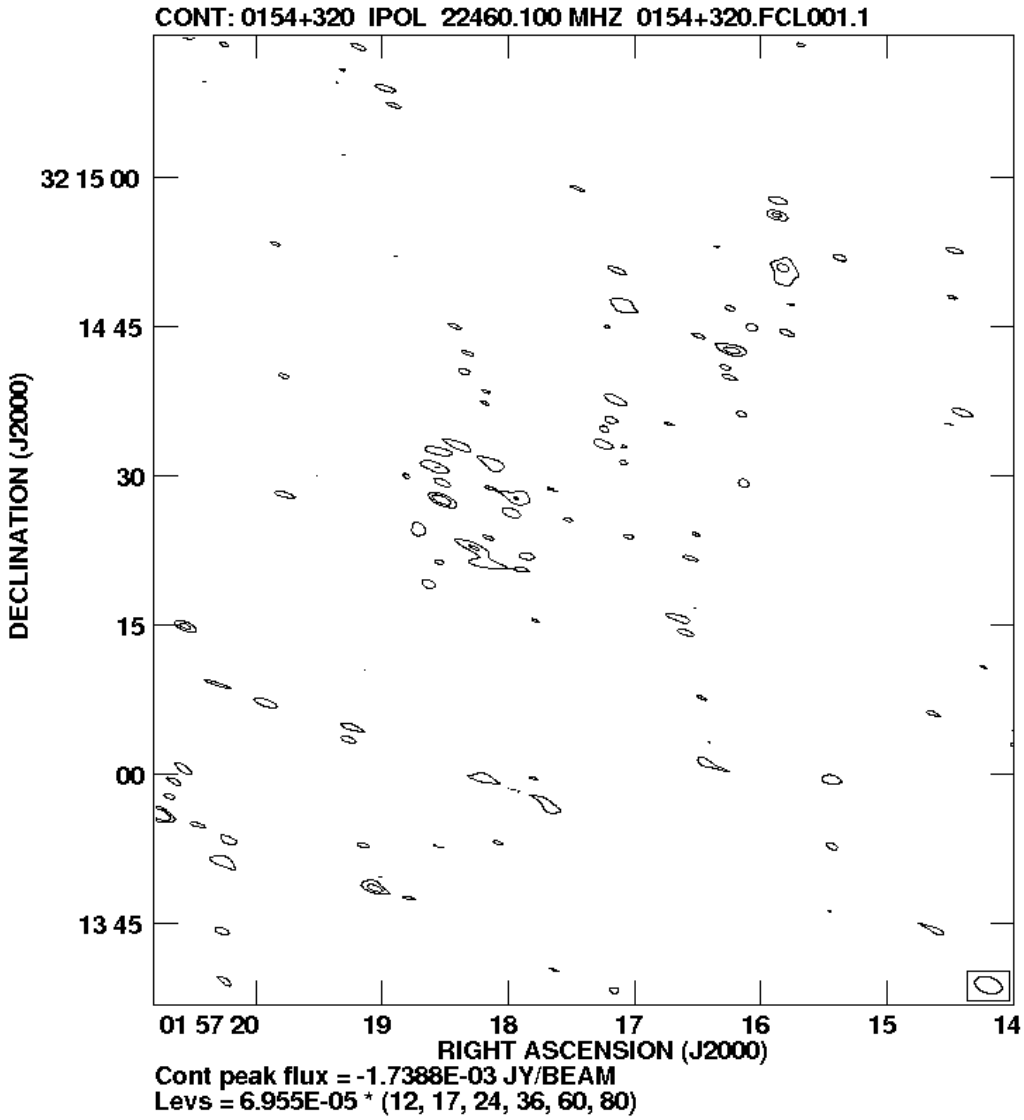

Figure 6.2: (c) A source (0154+320) imaged at K band showing the loss of flux due to resolution; beam profiles at each frequency are shown in the small box on the lower right of each panel. Contours are selected to reveal the main source properties.

ture seen at the two lower frequencies is resolved out and barely visible or not apparent (see Fig. 6.1). As noted in §6.5.1 above, we convolve the 43 GHz images to produce a synthesized beam matching that at 22 GHz. Thus we can fairly intercompare flux densities at the two higher frequencies, but it remains the case that spectral indices involving flux densities at either of the two lower frequencies will be lower limits.

6.6.3 SEDs of Cores and Other Point-like or Barely Resolved Sources

The very different resolution of our images at different frequencies makes it difficult to compare flux densities directly, and hence to determine SEDs, especially for complex or resolved sources. We therefore elect to concentrate on unresolved or barely resolved sources or the obvious cores within more complex structure. These sources are flagged in column 4 of Table 6.5 with a "C" indicating a well defined core or "P" indicating an unresolved or barely resolved "point-like" source. We are not claiming that these sources are necessarily unresolved at $\sim 1''$ scale, but rather that they are sufficiently isolated and regular in appearance that accurate flux densities can be obtained. It is still the case that the calculated values of the spectral index from 4.9 to 8.5 or 22 GHz, or from 8.5 to 22 GHz will be lower limits because of the overresolution effects described above.

Of the 140 cluster sources for which the determination of a SED is possible, 73 or 52% are either point-like or barely resolved in one or more of our three highest frequency images or have a clearly identifiable core at one or more of these same frequencies.

6.6.4 SEDs of Extended Sources

Because of the resolution effects discussed in §6.5.1, our SEDs and spectral indices for extended sources are less certain. In general, as expected (e.g., de Young 2002), the lobes and diffuse structure show steep spectral indices. In a few cases, as an experiment, we convolve the 8.5 GHz images to match the resolution of the 4.9 GHz images to allow direct comparison of fluxes. The results are shown in Table 6.3. From the table, it is clear that in these sample cases, at least, resolution is not significantly affecting the 8.5 GHz fluxes in major ways, except for the few clearly resolved sources.

Table 6.3: Effect of tapering on X-band flux measurements

Source	Extended	X flux (un-tapered) (mJy)	X Flux(tapered) (mJy)	C Flux (mJy)	α_{CX}(tapered)
0036-226B		59.850 ± 0.430	61.770 ± 0.520	74.330 ± 0.733	−0.334
0037+292		2.910 ± 0.320	3.110 ± 0.340	6.200 ± 0.500	−1.245
0039-095B		7.040 ± 0.240	7.230 ± 0.290	13.260 ± 0.644	−1.094
0100–221A		4.495 ± 0.520	3.180 ± 0.260	6.110 ± 0.570	−1.178
0119+193(1)		8.785 ± 0.320	8.480 ± 0.300	11.880 ± 0.610	−0.608
0124+189	Yes	75.440 ± 1.910	132.90 ± 2.830	310.000 ± 4.260	−1.528
0139+073A		4.898 ± 0.230	4.710 ± 0.320	6, 270 ± 1.40	−0.516
0909+161		10.430 ± 0.340	11.380 ± 0.410	16.410 ± 0.910	−0.660
1058+107		7.935 ± 0.290	9.920 ± 0.480	9.957 ± 0.390	−0.007
1130+148		8.820 ± 0.390	9.630 ± 0.560	13.680 ± 0.410	−0.633
1132+492		31.860 ± 0.740	34.640 ± 0.900	30.380 ± 0.830	+0.237
1201+282		1.870 ± 0.430	1.680 ± 0.550	2.930 ± 0.310	−1.003
1301+195		13.700 ± 0.270	12.790 ± 0.290	22.510 ± 0.280	−1.020
1433+553	Yes	16.810 ± 0.550	21.870 ± 0.710	73.920 ± 1.020	−2.197
1435+249 (1)		9.210 ± 0.390	10.160 ± 0.500	11.800 ± 0.560	−0.270
2228-087		14.480 ± 0.312	11.190 ± 0.320	10.893 ± 0.670	−0.049
2333+208 (1)		6.601 ± 0.270	7.680 ± 0.290	11.410 ± 0.330	−0.714
2348+058		3.022 ± 0.240	3.400 ± 0.250	8.490 ± 0.290	−1.651

If only emission from lobes and extended structure is involved, the generally steep spectra would ensure that most cluster radio sources would present minimal problems for SZE measurements carried out at frequencies above, say, 90 GHz. The second-to-last column of Table 6.5 lists estimated 90 GHz flux densities based on the X band flux, assuming that the spectral index between 4.9 and 8.5 GHz can be directly extrapolated to 90 GHz. The last column of the Table is the estimate based on the Q band flux where available, using the spectral index between 22 and 43 GHz.

6.6.5 SEDs of Cores

However, we find that the cores and other unresolved or barely resolved structures generally have flatter spectra, and in particular that many sources exhibit a substantial change in spectral index at frequencies above 22 GHz. This means that cluster radio sources may present a larger problem for sensitive SZE measurements than might be expected from the extrapolation of low frequency measurements (e.g., LM07). For that reason, as well as because of the difficulty of obtaining the fluxes of extended sources, we concentrate on cores and other unresolved or barely resolved components. We will focus on the 73 sources that are detected in three or more

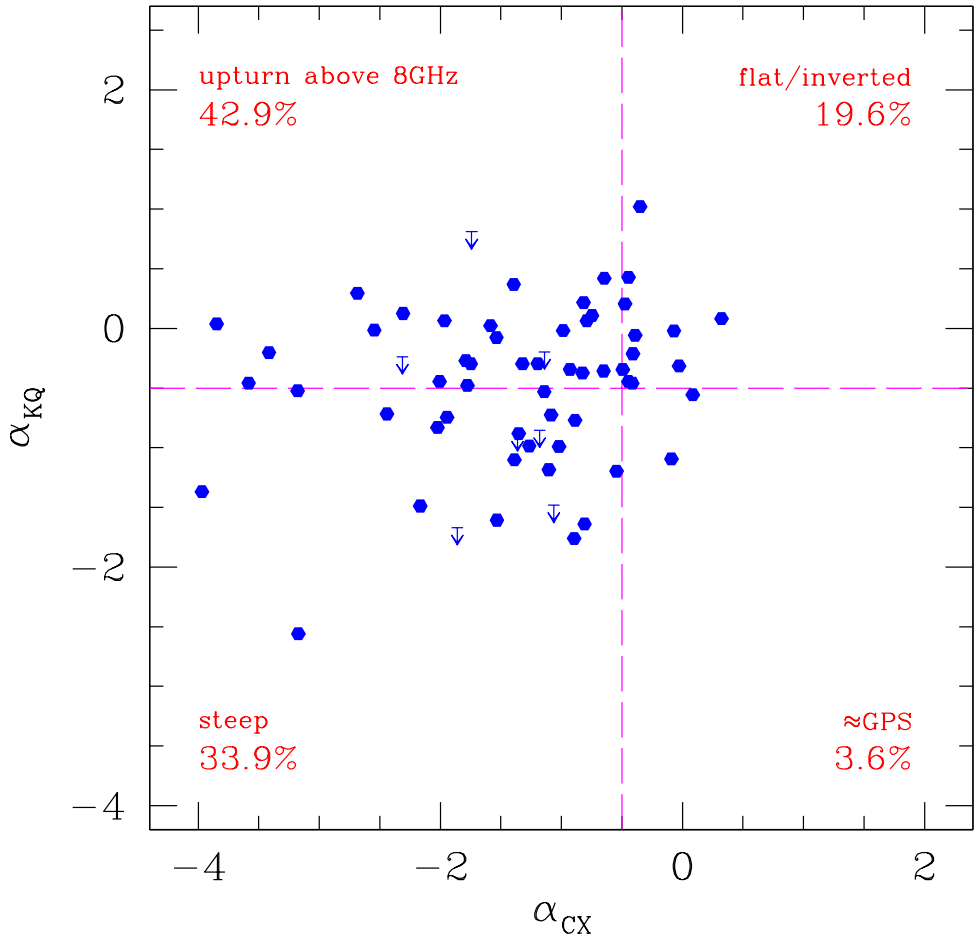

Figure 6.3: The distribution of the spectral indices provides a way to quantify the relative proportions of different spectral shapes, as indicated in the four quadrants. We list the percentage of each type of the spectral shape in the corresponding quadrants. Note that a large fraction of sources exhibit curvature in their spectra (e.g., the "upturn" type).

bands with these morphologies. It is important to recall, however, that even for these relatively small and uncomplicated sources, resolution effects could cause us to underestimate the flux at our two lower frequencies; we emphasise that the low frequency spectral indices are only lower limits.

An efficient way to quantify the distribution of the spectral shapes is through the "two-colour" plot (Sadler et al. 2006), shown in Fig. 6.3, where the spectral index between the C & X bands (α_{CX}) is plotted against that between the K & Q bands (α_{KQ}). Throughout our analysis, we adopt the notation for the spectral index such that a power-law spectrum is described as $S_\nu \propto \nu^\alpha$. Following the common practice of referring to sources with $\alpha < -0.5$ as "steep",

Table 6.4: Mean spectral indices

bands	All sources	Cores/point-like
5-8	-1.64 ± 0.10	-1.31 ± 0.10
8-22	-1.20 ± 0.07	-0.88 ± 0.09
22-43	-0.98 ± 0.11	-0.62 ± 0.10

and "flat/inverted" otherwise, the $\alpha_{CX} - \alpha_{KQ}$ space is divided into four quadrants, as delineated by the two dashed lines in Fig. 6.3. Starting from the first quadrant (upper-right corner) and going counterclockwise, the quadrants contain sources with flat/inverted spectra, with spectra that show a upturn above 8 GHz, with steep spectra, and with spectra that peak at around 10 or so GHz [which we refer to as "approximately gigahertz peaked spectrum" ($\approx$ GPS) sources], respectively.

With $\sim$ 100 sources detected at 18 GHz with the Australian Telescope Compact Array (ATCA), Sadler et al. (2006) study the distribution of the spectral shapes with the two-colour plot, where their low and high frequency indices are based on 0.8 & 5 GHz, and 8 & 18 GHz fluxes, respectively. We note that they separate the flat/inverted sources from steep ones at $\alpha = 0$; adopting the same definition, we find that the great majority of our sources become steep (73%) and upturn (23%). This seems to suggest that our cluster sources exhibit steeper spectra than theirs. However, the fact that the two samples are selected at very different frequencies (1.4 v.s. 18 GHz) needs to be taken into consideration. In addition, although the majority of their sources are likely QSOs and BL Lac objects, most of them lack redshift information, which makes it difficult to make a fair comparison (e.g., the nature of the sources, the environments, as well as the possible cosmological evolution). Nevertheless, we agree with their conclusion that extrapolation of fluxes to high frequencies (e.g., $\gtrsim$ 10 GHz) based on low frequency observations is not reliable.

6.7 Spectral Index Distribution

Here we quantify the spectral index distribution in the $5-8$, $8-22$, and $22-43$ GHz bands. An important aspect in estimating the SIDs is to deal with sources for which only an upper limit in

flux in one of the bands is available, which leads to upper or lower limits of the spectral index. To accommodate such cases, we calculate the distribution with the ASURV package (Feigelson & Nelson 1985; Isobe et al. 1986), which is based on survival statistics, a branch of statistics developed in actuarial estimates of human survival and mortality (see e.g., Feigelson & Nelson 1985 for a review). The resulting SIDs are shown in Fig. 6.4, where the solid histogram is for sources with core/point-like morphology, and the dashed histogram is for all sources. We record the mean values of the indices in Table 6.4. As expected, the SIDs based on all the sources have a mean that is more negative.

A recent study presents the spectral indices between 1.4 & 28.5 GHz for 95 probable cluster radio sources (Coble et al. 2007). They find that the mean of the index is ~ -0.7. Because of the differences between the beam size of the 1.4 GHz observations made by Ledlow & Owen (1996) and ours, we do not attempt to calculate an analog to their spectral index (e.g., α_{LK}). Furthermore, as the spectral shape tends to be complicated, it is not clear how much predictive power an index spanning such a wide range in frequency would have.

6.8 Correlation of Spectral Indices and Properties of the Host Galaxies and Clusters

Next we examine if there is any correlation between the spectral indices (from sources of core/point-like morphology) and the properties of the host galaxies or of the clusters. In particular, we consider the optical and radio luminosities, as well as the optical colour, of the host galaxies. As for the cluster-related properties, we look at the mass and redshift of the clusters, and the projected radial distance to the cluster centre, which is determined from the emission peak of the intracluster gas.

In Fig. 6.5 we show scatter plots between α_{CX}/α_{KQ} and the galaxy properties. Fig. 6.6 is the corresponding plot for the cluster properties. A few points are worth commenting on both Figures. First, we note that the host galaxies are of moderate optical luminosity (recall that $M_* = -20.8$ in the V-band), and are red in colour ($u - r > 2.2$). Inspecting the optical images of the host galaxies from SDSS confirms that most of the galaxies are early type, of elliptical

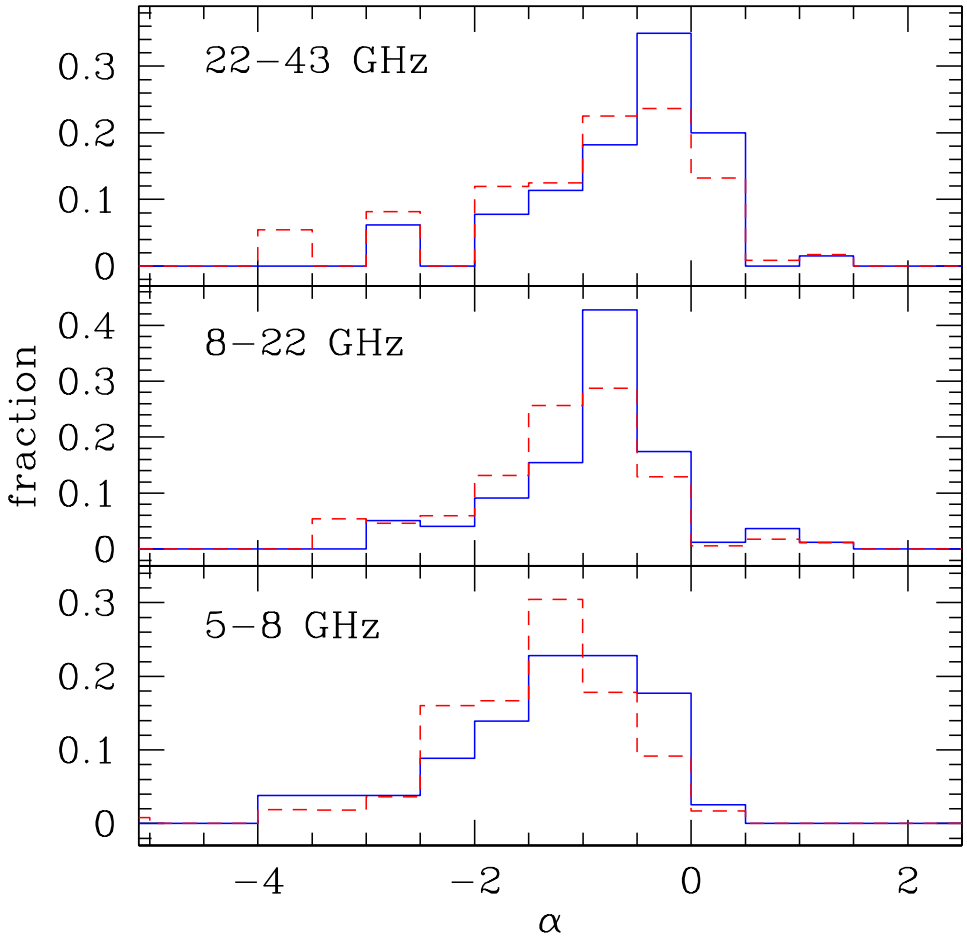

Figure 6.4: The spectral index distribution in three frequency bands. The solid histogram is the result when only sources with core/point-like morphology are used. The dashed histogram is obtained when all sources are included.

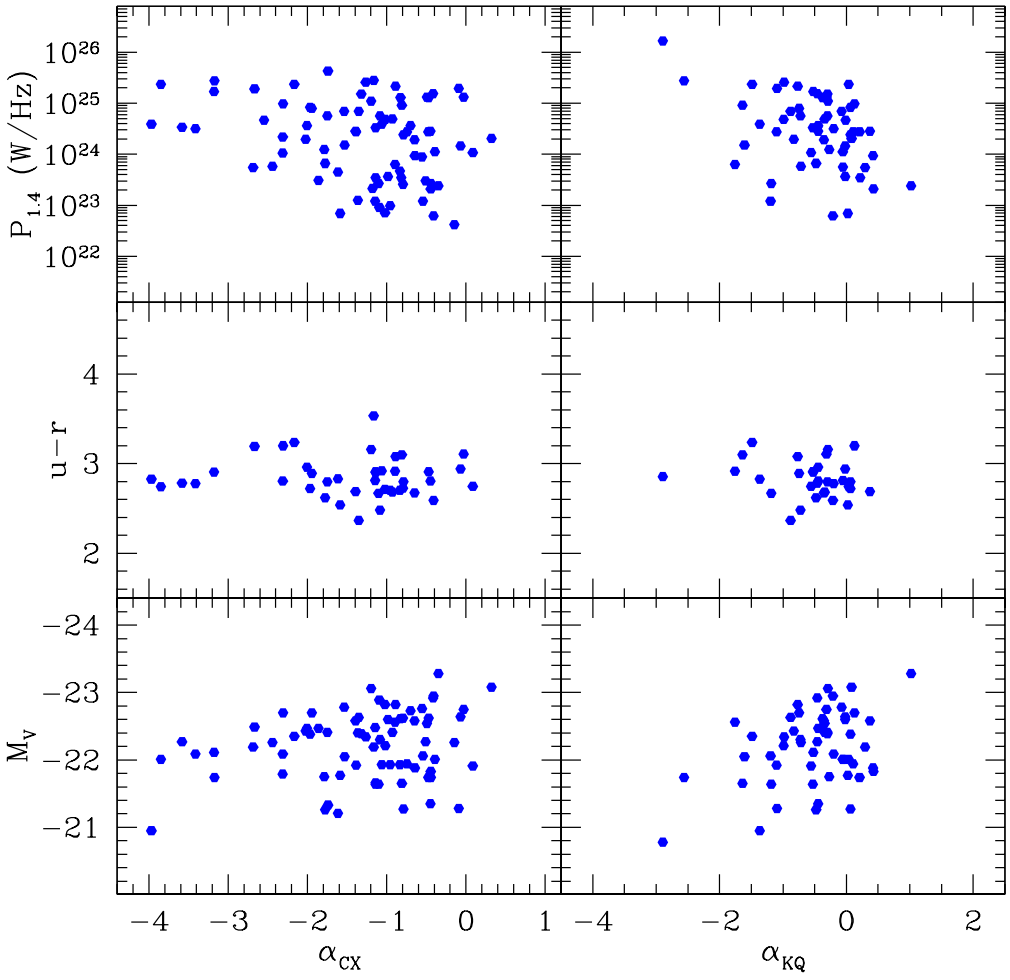

Figure 6.5: Distribution of the spectral indices with respect to properties of host galaxies. We consider the absolute optical (V-band) magnitude, the optical colour ($u-r$), and the radio power at 1.4 GHz of the hosts. No apparent correlation is found.

morphology. The distribution of the 1.4 GHz luminosities ($P_{1.4}$) suggests that these galaxies are likely FRI-type radio-loud AGNs.

The cluster mass M_{200} is estimated from the X-ray luminosity (L_X)–virial mass relation (Reiprich & Böhringer 2002). M_{200} is defined as the mass enclosed by r_{200}, a radius within which the mean overdensity is 200 times the critical density. Because of the scatter in the L_X–M_{200} relation, our mass estimate is only accurate to $\lesssim 50\%$ (Reiprich & Böhringer 2002). Nevertheless, it is shown that L_X is a unbiased mass indicator (Reiprich 2006). As our main purpose is to find correlations with the cluster mass, L_X should suffice as a proxy for mass. For each radio source, we normalise its clustercentric distance by r_{200}, to account for the difference in cluster mass. As Fig. 6.6 suggests, our clusters span a range > 20 in mass. The majority of the sources are concentrated toward the cluster centre, which confirms several earlier findings (e.g., Morrison & Owen 2003; LM07).

It is interesting to see that there appears to be no strong correlations between the spectral indices and the host galaxies/clusters. The Spearman's rank correlation coefficients for all cases we examine are between -0.1 and -0.34, indicating no significant correlations. The pair of properties that shows the strongest correlation is that between α_{KQ} and $P_{1.4}$ (correlation coefficient $= -0.34$). But this is mainly driven by a couple of sources that have the most negative spectral index.

Coble et al. (2007) do not find any difference between the spectral indices for sources in the inner and outer parts of the clusters, suggesting lack of correlation with clustercentric distance, which is consistent with our finding here. Considering the fact that spatial distribution of the low-power radio galaxies is very concentrated towards cluster centre (LM07), this seems to suggest that although the centre of massive halos increases the probability of accretion onto the supermassive blackholes (e.g., high gas density or/and pressure from the intracluster medium), the resulting emission is dominated by the small scale physics of the nucleus rather than by the cluster environment.

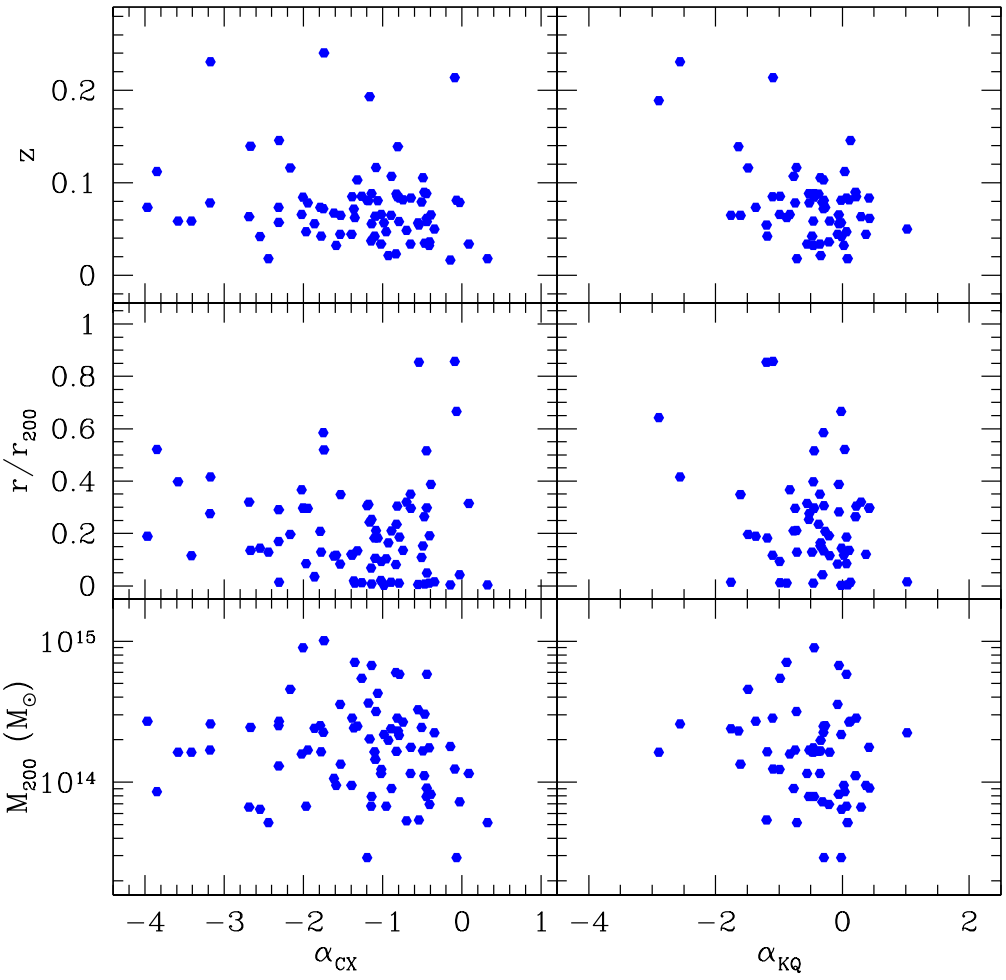

Figure 6.6: Distribution of the spectral indices with respect to properties of host clusters. We examine the mass of the clusters, the distance to the cluster centre (normalised by the virial radius of the cluster, r_{200}), and the redshift. As expected, radio sources concentrate towards cluster centre. Similar to Fig. 6.5, we do not find significant correlations.

6.9 Implications for SZE Surveys

The main motivation to conduct the present study is to characterise the SED/SID of radio sources associated with galaxy clusters, which can be used to assess their effect on the detection and characterisation of clusters through the SZE. Simply put, the SIDs can be used to extrapolate the observed radio luminosity function (RLF) at low frequencies to the frequency of an SZE experiment, which in turn provides an estimate of the abundance and effect of radio sources.

Our approach is similar to that of LM07, and we refer the reader to that paper for more details (§7 therein). We will only provide an overview of the method here. The basic idea is to use the (observed) RLF within clusters and groups to predict the number and flux of radio sources expected in massive halos of given mass and redshift. Specifically, the RLF gives the number density of radio sources which, when multiplied by the volume of the halo, becomes the number of sources expected. One can draw (Poisson) random numbers from it, and assign radio luminosities according to the RLF. By repeating this procedure for a large number of halos of the same mass and redshift, one produces a radio galaxy catalogue in a Monte Carlo fashion. In §6.9.1 we describe our scheme for extrapolating the RLFs, and in §6.9.2 we present our estimates of the contamination of SZE due to cluster radio sources.

6.9.1 Extrapolation of the Radio Luminosity Function

The main ingredients in our method include: the 1.4 GHz RLF of radio sources residing in massive halos, the SIDs between several frequencies, and a model for the redshift evolution of the RLF. The 1.4 GHz RLF in units of space density is measured in LM07, and we give in §6.8 the distributions for α_{CX}, α_{XK}, and α_{KQ}. For SZE surveys operating at $\sim$ 150 GHz (e.g., ACT and SPT), our modelling requires a factor of $\sim$ 4 extrapolation of the radio spectra in frequency (i.e., from 43 GHz), which represents a dramatic improvement from that of LM07, which adapted an SID from 1.4 and 4.85 GHz measurements. However, because of the mismatch between the angular resolutions in our images at C, X, and K bands, the spectral indices we determine between these bands may be lower limits, and thus the SIDs of α_{CX} and α_{XK} may be biased towards negative values. To assess the effects of the choices of SIDs, we will utilise other

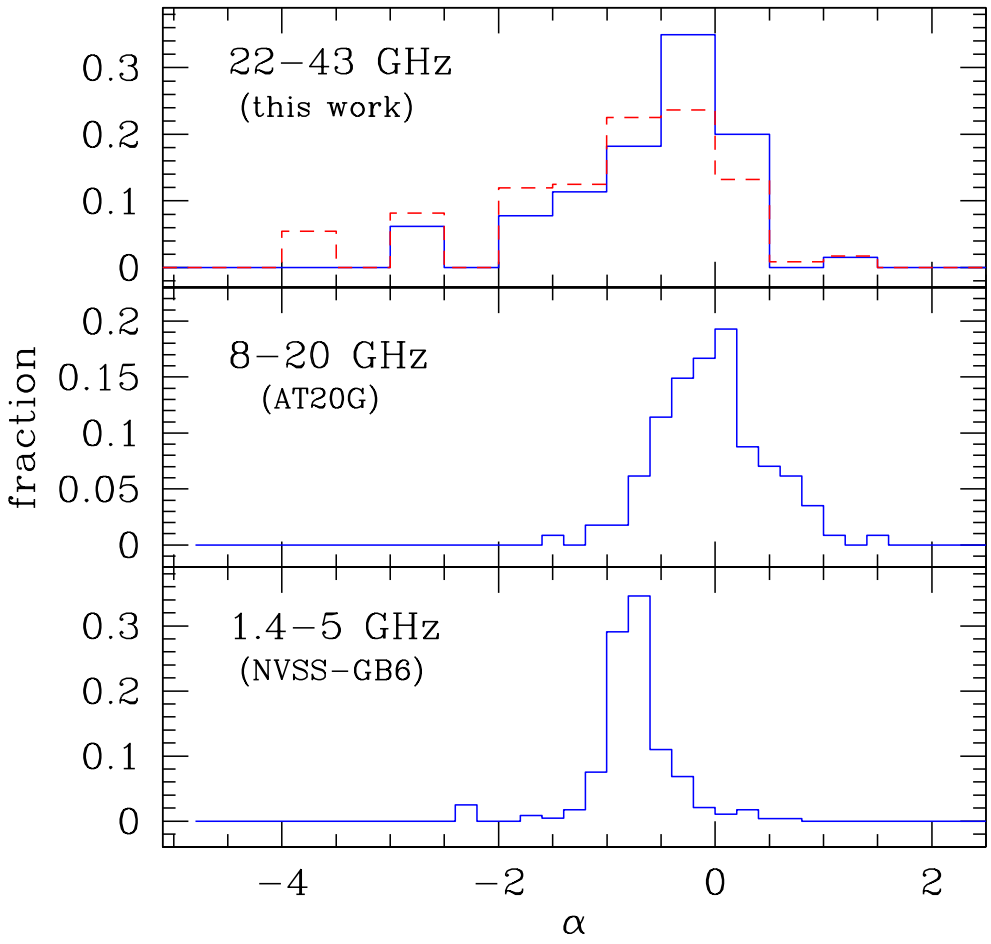

Figure 6.7: The spectral index distribution in three frequency bands. *Top*: the SID in 22 – 43 GHz band as determined from our VLA data; this is identical to that shown in the top panel of Fig. 6.4. *Middle*: the 8 – 20 GHz SID determined from the AT20G survey, using data presented in Sadler et al. (2006). The mean of the distribution is $\alpha_{XK,AT20G} = -0.028 \pm 0.046$. *Bottom*: the 1.4 – 5 GHz SID based on data from the NVSS and GB6 surveys. The mean is $\alpha_{LC,NVSS/GB6} = -0.754 \pm 0.024$. The details of the construction of SID(8 – 20, AT20G) and SID(1.4 – 5, NVSS/GB6) are described in the Appendix C. Compared to the middle and bottom panels in Fig. 6.4, the SIDs in this figure are more positive. In particular, as AT20G is a 20 GHz survey, the resulting SID is biased towards flat-spectrum sources.

data sets to determine the SIDs at $\nu \lesssim 20$ GHz. To this end, we combine the catalogs from the NVSS (Condon et al. 1998) and GB6 (Gregory et al. 1996) surveys to measure the 1.4 – 4.85 GHz SID, and use the results from the AT20G survey (Sadler et al. 2006) to measure the 8.5 – 20 GHz SID. We describe the construction of the matched NVSS/GB6 sample, as well as the AT20G data, in the Appendix C. As the beam sizes of both NVSS and GB6 surveys are large (45″ and 3.5′, respectively), the flux, and in turn the spectral index α_{LC} measurements, should be reliable except for very extended sources. On the other hand, the AT20G survey selects sources at 20 GHz, and the resulting sample would be biased towards flat-spectrum sources. These SIDs are shown in the middle and lower panels in Fig. C.1. The mean values of $\alpha_{LC,NVSS/GB6}$ and $\alpha_{XK,AT20G}$ are -0.754 ± 0.024 and -0.028 ± 0.046, respectively. Using the SID(1.4 – 4.85, NVSS/GB6) and SID(8 – 20, AT20G) rather than those presented in §6.8 will produce extrapolated RLFs with higher amplitude (i.e., more radio sources), resulting in higher estimates of the contamination of SZE signals. We caution that the SIDs from NVSS/GB6 and AT20G are not limited to radio sources *in* groups and clusters (although the NVSS/GB6 sources are constrained to be at $z < 0.4$). However, incorporating these SIDs allows us to explore the degree of AGN contamination of the SZE to a fuller extent.

LM07 determine the 1.4 GHz RLF for cluster radio sources. We transform that RLF to higher frequencies by convolving it with the spectral index distribution via (LM07)

$$\phi_2 (\log P_2) = \int \phi_1 (\log P_2 + \alpha \log(\nu_1/\nu_2))\, f(\alpha_{12}) d\alpha_{12}, \tag{6.1}$$

where $\phi \equiv dn/d\log P$ is the RLF, and subscripts refer to two frequencies 1 & 2 ($\nu_2 > \nu_1$). The function $f(\alpha_{12})$ is the SID between the two frequencies. We have measured SIDs in several frequency bands: 1.4 – 5 (or 5 – 8), 8 – 20 (or 8 – 22), and 22 – 43. Depending on the frequency of the SZE experiment, we may need to apply Eq. 6.1 in several steps. For example, the RLF at 145 GHz is obtained by extrapolating the 22 GHz RLF with $f(\alpha_{22,43})$, which is similarly extrapolated from the 8 GHz RLF with $f(\alpha_{8,20})$ [or with $f(\alpha_{8,22})$]. Finally, the 8 GHz RLF itself results from an extrapolation of the 1.4 GHz RLF with $f(\alpha_{1.4,5})$ [or $f(\alpha_{5,8})$].

It is certainly preferable to utilise the full spectral shape from 5 to 43 GHz of our sources for the extrapolation of the RLFs. We elect not to do so in the current analysis, as our determination

of spectral shape below 22 GHz may not be reliable. Instead, we treat the spectral indices at different frequency bands as independent, and extrapolate the RLFs in a piecewise fashion. This is justified given the lack of correlation of spectral indices in the radio two-colour diagram (Fig. 6.3).

Ideally, one would extrapolate the RLF separately for the compact and extended components of radio sources. However, the 1.4 GHz RLF presented by LM07 is based on fluxes from both the core and extended structures. Given that at low frequencies, the lobes usually dominate in flux over the cores (e.g., Fig. 6.1), the core-only RLF would have a smaller amplitude than the combined RLF. However, to determine the relative proportion of the core-only and the lobe-only RLFs, one needs to carefully examine all radio sources that contribute to the RLF, which is beyond the scope of the current analysis. We simply caution that without the ability to separate the core and extended components of the 1.4 GHz RLF, the amplitude of our extrapolated RLFs would be upper limits.

6.9.2 Results

The $z \sim 0$ extrapolated RLFs at several frequencies are shown in Fig. 6.8. The two panels show the effect of using the two SIDs in the 8 – 20 GHz band: while the upper panel is based on the SID from the AT20G survey, the lower panel is obtained from the SID presented in §6.8. In both panels we use the SID from NVSS/GB6 for extrapolation up to 8 GHz. As noted before, using the SID(8 – 20, AT20G) results in RLFs with higher amplitudes (about a factor of 2 – 3 towards the luminous end of the luminosity function) compared to the case where SID(8 – 22, this work) is used instead. We regard the RLFs presented in the upper panel as our "pessimistic" estimates, and those shown in the lower panel as the "optimistic" estimates. Combining both SID(5 – 8, this work) and SID(8 – 22, this work) results in the RLFs of even lower amplitudes, which likely represent the lower limits to both the RLF and the contamination; for example, at 145 GHz, the extrapolated RLF is about a factor of 2 (8 – 9) lower in amplitude compared to the "optimistic" ("pessimistic") estimate.

Compared to a similar plot presented in LM07 (Fig. 13 therein), a dramatic change in the amplitudes of the extrapolated RLFs is seen. At 145 GHz, at the luminous end, the amplitude

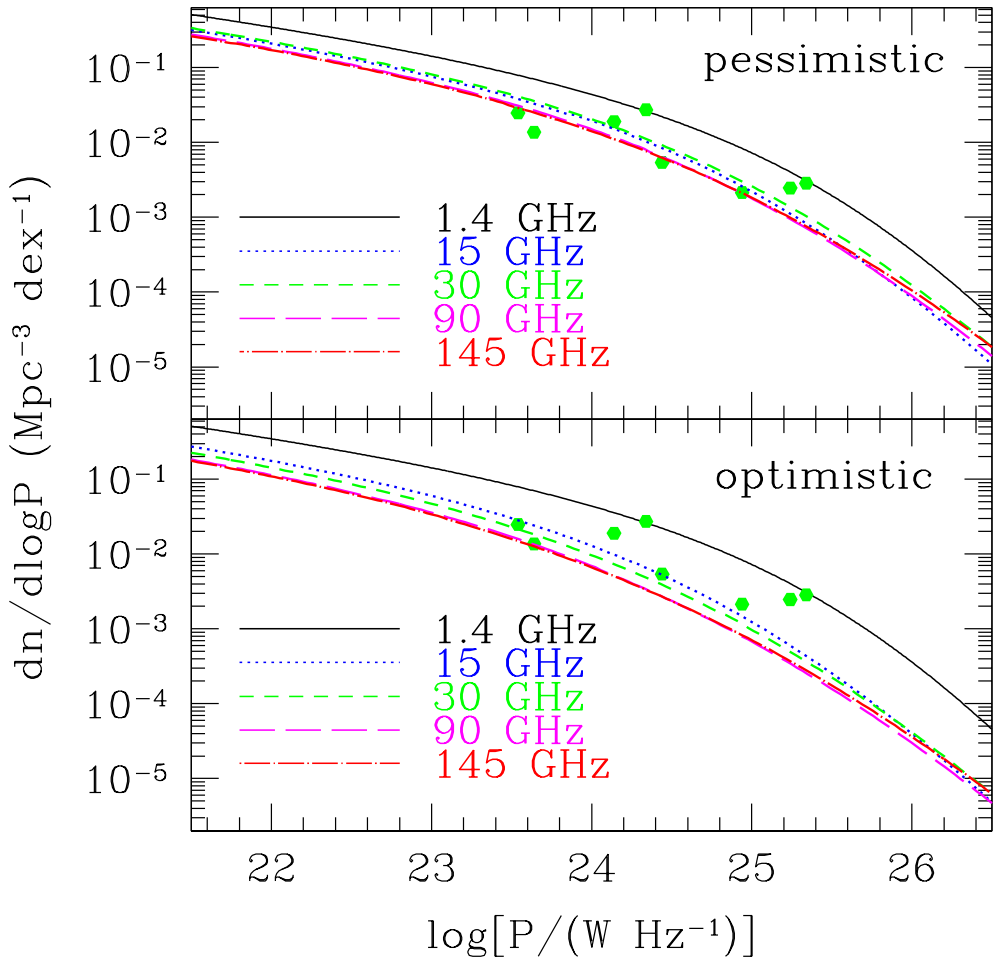

Figure 6.8: Radio luminosity function (RLF) of radio loud AGN at several frequencies. We transform the 1.4 GHz cluster AGN RLF from LM07 (solid line) to 15, 30, 90, and 145 GHz (dotted, short-dashed, long-dashed, and dot-dashed, respectively), using Eq. 6.1. The top and bottom panels show the results when SID(8−20, AT20G) and SID(8−22, this work) are used for the extrapolation of the RLF, respectively. In both panels, we use the SID(1.4 − 5, NVSS/GB6) and SID(22 − 43, this work) for further extrapolations. Compared to the similar plot presented in LM07 (Fig. 13 therein), our extrapolated RLFs have much smaller amplitude. Also shown as points is an estimate of the 30 GHz cluster RLF, as determined by LM07, based on data from Coble et al. (2007).

of our "pessimistic" RLF is about a factor of 50 less than that estimated in LM07. This is due to the combined effect of (1) the use of several SIDs in different frequency bands in the present analysis (so that the results are not strongly dependent on one single SID), and (2) that the SID used in LM07 may be biased to positive indices, as non-detections at 4.85 GHz during the matching of sources between 1.4 and 4.85 GHz were not properly taken into account (see Appendix for more discussion).

The data points in both panels show an estimate of the cluster RLF at 30 GHz, based on data from Coble et al. (2007), as determined by LM07. Although the uncertainty in this empirical determination of the RLF is large, it seems to agree with our "pessimistic" 30 GHz RLF (upper panel of Fig. 6.8, short dashed curve).

We note that the redshift evolution of radio sources in clusters is an unresolved issue. Our sample is limited to $z < 0.25$, and currently there is no consensus as how radio galaxies evolve in massive halos (see LM07 for discussion). We have acquired C, X, and K band data for a sample of radio galaxies in ~ 10 intermediate-redshift clusters. Better constraints on the redshift evolution based on these new data will be presented in a future publication. In the current analysis, we will simply assume a pure density evolution of the form $\phi(z) \propto \phi(z = 0)(1 + z)^{\gamma}$, with $\gamma = 2.5$, which corresponds to a factor of ~ 5 increase of the density at $z \approx 1$.

Now, given the mass and redshift of a dark matter halo, we can estimate the degree of contamination as follows. For a halo, we denote the total fluxes from radio sources as S_{AGN}, and the SZE flux as S_{SZE}. Using our Monte Carlo scheme to generate a large number of radio sources in massive halos, the fraction of halos for which S_{AGN} is a significant fraction q of $|S_{SZE}|$ can be calculated. We consider two cases, $q = 0.2$ and $q = 1$, corresponding to 20% and "total" contamination. We show in Fig. 6.9 the resulting AGN contamination fraction at 145 GHz, which is the proportion of the clusters expected to host radio galaxies whose flux is $S_{AGN} \geq q|S_{SZE}|$, as a function of cluster mass. The solid (open) points refer to the case of $q = 1$ ($q = 0.2$). The circles, squares, and triangles correspond to halos at $z = 0.1, 0.6$, and 1.1, respectively. Based on the cluster redshift distribution, we expect the majority of the clusters detected by the SZE experiments to be at $z \sim 0.6$. Similar to the format of Fig. 6.8, in the upper and lower panels we show the results when the SID(8 – 20, AT20G) and SID(8 – 22, this work) are used. In our "pessimistic" case (upper panel), $< 10\%$ of the clusters more massive

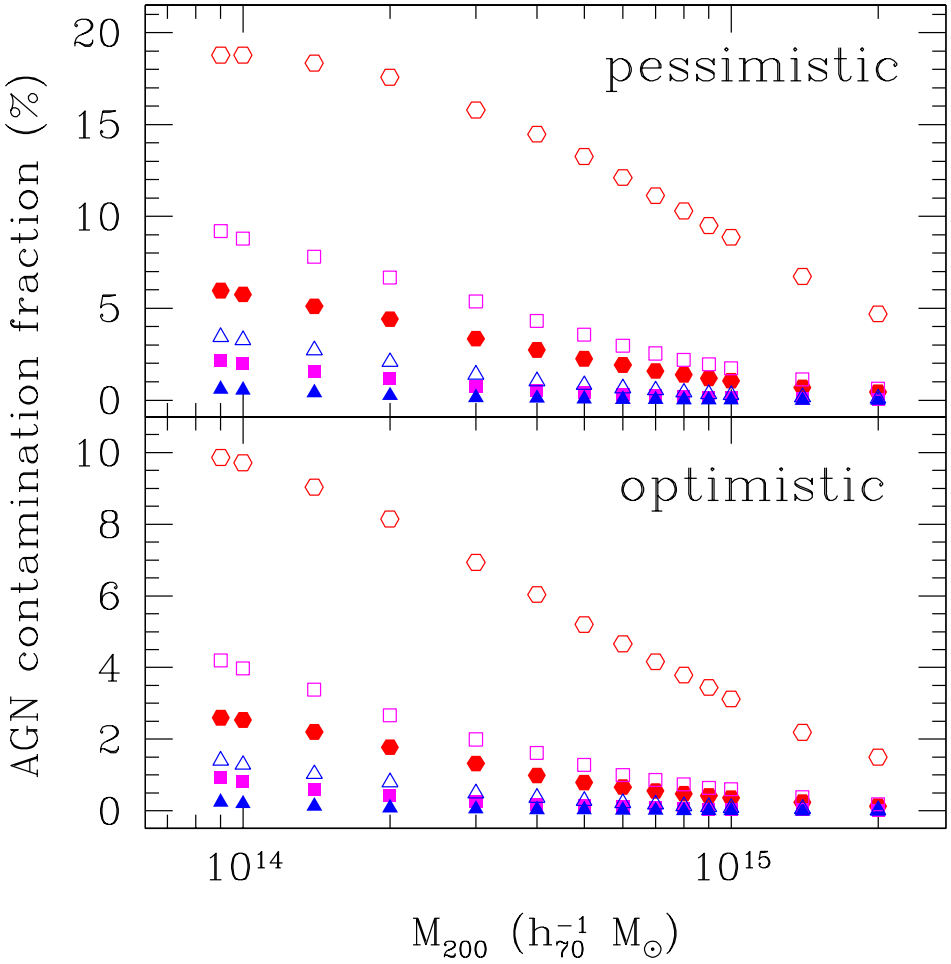

Figure 6.9: Fraction of clusters which host enough radio loud AGNs such that their SZE flux measurements at 145 GHz may be contaminated. We consider cases where the fluxes of the AGNs are at least a fraction q of the SZE flux, $S_{AGN} \geq q|S_{SZE}|$ (for the case where SZE signal is a temperature decrement), with $q = 0.2$ (open symbols) and $q = 1$ (solid symbols). We examine clusters at three redshifts: $z = 0.1$ (circles), 0.6 (squares), and 1.1 (triangles). The two panels show the results when the 145 GHz RLF from the corresponding panels in Fig. 6.8 are used in our Monte Carlo estimation.

than $10^{14} M_{\odot}$ would be affected by radio-loud AGNs to the 20% level (open squares). The corresponding fraction in the optimistic case (lower panel) is < 4%. The proportion of clusters that are affected by AGNs to 100% is a factor of 2 – 3 smaller than the above estimates (solid squares).

For completeness, we note that with our pessimistic estimate of the RLFs, about 5 – 10% (15 – 20%) of clusters in the mass range $10^{14} - 10^{15} M_{\odot}$ at $z \sim 0.6$ may be contaminated to 10% (5%) level (i.e., $q = 0.1$ and 0.05, respectively).

We have provided a framework for estimating the abundance of radio loud AGNs in halos. To better determine the impact of radio sources in SZE surveys, however, it is necessary to carry out mock observations that take into account the properties of the telescope and receiver system (e.g., angular resolution, sensitivity; see Sehgal et al. 2007), as well as the auxiliary observations (e.g., availability of multiwavelength data).

6.10 Summary and Future Work

We have presented a study of the spectral energy distribution of radio sources in a large sample of nearby clusters ($z < 0.25$). For 139 sources selected at 1.4 GHz and spectroscopically confirmed to be members of the clusters, we use VLA to measure the fluxes at 4.9, 8.5, 22, and 43 GHz (C, X, K, and Q bands) nearly simultaneously, and determine the distribution of the SED. Sources with extended morphology may be resolved out at high frequencies (i.e., reduction in flux due to the higher angular resolution of interferometer), making the determination of the spectral shape nontrivial. We have downgraded the resolution of our 43 GHz images to match the resolution at 22 GHz, thus enabling reliable comparisons of fluxes at these two frequencies (§6.5.1); it is more difficult to match the resolution between the other frequency intervals, and therefore our measurements of the spectral indices involving the two lower frequencies (e.g., between 8.5 and 22 GHz, α_{XK}, where $S \propto \nu^{\alpha}$) are *lower* limits. The flux measurement of point-like (or barely resolved) sources, or "cores" embedded in extended sources, on the other hand, is more straightforward.

Our main findings are the following:

1. For $\sim$ 70 core/point-like sources that are detected in at least three frequencies, we study

the distribution of the spectral shape via the "two-colour" diagram (Fig. 6.3), and find that the spectral shape cannot be described by simple power-laws for the bulk of the sources. About 60% of sources have $\alpha_{KQ} > \alpha_{CX}$, indicating a flattening of the spectral shape above 8 GHz or so; only $1/3$ of the sources have steep spectra from 4.9 to 43 GHz.

2. We determine the spectral index distribution using survival statistics that take non-detections (upper limits) into account. The results are shown in Fig. 6.4 and Table 6.4. The compact sources are found to have "flatter" spectral shape than the extended sources.

3. The spectral indices do not correlate with properties of host galaxies or clusters, such as the colour and luminosity of the galaxies, the radio luminosity at 1.4 GHz, the distance of the host galaxy to the cluster centre, and the mass of the host clusters. This result agrees with previous studies, and suggests that the radio emission may be dominated by the small scale physics of the nucleus, rather than by the cluster environment.

4. In an attempt to estimate the contamination of the SZE signal due to radio point sources in cluster surveys, we make use of the spectral index distributions in several frequency bands to extrapolate the well-measured RLF at 1.4 GHz to the frequencies employed by several on-going radio/millimeter wave experiments. As the extrapolation depends on the SIDs employed, we bracket the possible range of the predicted RLFs by using SIDs in intermediate frequency bands (e.g., 8 – 20 GHz) that are known to be biased in opposite ways. The amplitude of the resulting RLFs at $\nu \geq 30$ GHz is in general 3 – 10 times lower compared to the 1.4 GHz one. Under the assumption that the RLF follows a pure density evolution with redshift of the form $\phi(z) \propto \phi(z=0)(1+z)^{\gamma}$, such that the abundance of sources at $z = 1$ is 5 times the local value, we find that the fraction of clusters that may be seriously affected by point sources is small; at the cluster mass scales close to the detection limits of the on-going surveys (e.g., $2 - 3 \times 10^{14} M_{\odot}$), and at the redshift where we expect the experiments to detect most of the clusters (i.e., $z \sim 0.6$), $\lesssim 8\%$ of the clusters will be contaminated to 20% level or above (that is, the total fluxes from AGNs are at least 20% of the SZE flux).

There are two aspects that need to be improved for a better forecast within our analysis framework. Currently, the largest uncertainty in our modelling is the redshift evolution of cluster radio galaxies. If not properly accounted for, any unexpected evolution of the radio sources may be misinterpreted as changes in the cluster mass function, and cause errors in the determination

of the properties of the dark energy. With our on-going VLA survey of cluster radio galaxies at intermediate redshift ($0.3 \leq z \leq 0.8$), we plan to address this issue in a future publication.

In addition, in our forecast, it is implicitly assumed that the number of radio galaxies (N_{RG}) a cluster can host is proportional to the cluster mass (M_{200}). If, instead, $N_{RG} \propto M_{200}^{s}$ with $s < 1$, we would overestimate the AGN contribution in high mass clusters. To check this assumption, one needs to determine the halo occupation distribution for radio galaxies. To this end, we have attempted to construct the halo occupation distribution of radio galaxies, using a large sample of radio galaxies in the local Universe (Lin et al. in preparation).

Table 6.5: Cluster Radio Sources

Name[a]	RA (J2000)	Dec (J2000)	Type[b]	z[c]	f_L[d] (mJy)	f_C (mJy)	f_X (mJy)	f_K (mJy)	f_Q (mJy)	α_{CX}	α_{XK}	α_{KQ}	$f_{90,CX}$[e] (mJy)	$f_{90,KQ}$[f] (mJy)
0036-226B	9.784167	−22.333833	C	0.0654	129	74.33 ± 0.733	59.85 ± 0.43	39.12 ± 0.95	37.68 ± 1.16	−0.39	−0.44	−0.06	23.77	36.12
0037+209	9.939667	21.225556	-1	0.0622	143	10.43 ± 2.05	< 0.66	< 1.77	< 1.49	< −4.97	···	···	···	···
0037+292	10.118042	29.556083	P/C	0.0716	12	6.20 ± 0.5	2.91 ± 0.32	2.55 ± 0.95	< 1.43	−1.36	−0.14	< −0.88	0.12	···
0039+211	10.422958	21.402639	C	0.1030	670	101.70 ± 2.2	48.84 ± 0.55	24.70 ± 0.65	20.34 ± 0.8	−1.32	−0.70	−0.30	2.15	16.35
0039-095B	10.460333	−9.303111	C	0.0556	55	13.26 ± 0.644	7.04 ± 0.24	2.11 ± 0.48	< 1.85	−1.14	−1.24	< −0.20	0.47	···
0039-095A	10.450875	−9.284000	-1	0.0556	48	20.98 ± 2.09	5.20 ± 0.9	< 2.57	< 1.48	−2.51	< −0.72	···	0.01	···
0039-097	10.459208	−9.429556	C	0.0556	82	···	6.86 ± 0.32	4.10 ± 0.48	3.95 ± 0.79	···	−0.53	−0.06	···	3.79
0043+201(1)	11.623292	20.467139	C	0.1053	563	19.63 ± 1.56	14.93 ± 0.5	< 1.68	2.20 ± 0.76	−0.49	< −2.24	···	4.65	···
0043+201(2)	11.622250	20.468083	C	0.1053	563	19.63 ± 1.56	14.93 ± 0.5	10.63 ± 0.48	8.48 ± 0.65	−0.49	−0.35	−0.35	4.65	6.58
0046+011	12.166500	1.430167	C	0.0632	68	25.57 ± 0.88	5.76 ± 0.46	2.63 ± 0.57	3.19 ± 0.98	−2.68	−0.80	0.29	0.01	3.96
0047+241	12.424542	24.445111	C	0.0818	200	25.23 ± 1.08	16.68 ± 0.41	7.01 ± 0.53	7.52 ± 1.07	−0.75	−0.89	0.11	2.86	8.14
0047+242A(1)	12.436542	24.500278	-1	0.0818	24	11.86 ± 1.29	5.62 ± 0.57	1.03 ± 0.45	< 2.12	−1.35	−1.74	< 1.10	0.23	···
0047+242A(2)	12.434833	24.500806	C	0.0818	24	11.86 ± 1.29	4.82 ± 0.49	1.89 ± 0.54	< 2.12	−1.35	−0.96	< 0.18	0.20	···
0050-220(1)	13.362875	−21.750333	-1	0.0587	97	11.80 ± 1.36	6.78 ± 0.55	···	···	−1.00	···	···	0.64	···
0050-220(2)	13.356667	−21.736639	-1	0.0587	97	25.57 ± 0.89	13.94 ± 0.51	6.73 ± 0.71	3.21 ± 0.76	−1.09	−0.75	−1.13	1.05	1.40
0053+261A(1)	13.962375	26.406500	-1	0.1971	1327	82.20 ± 1.79	21.74 ± 0.68	< 2.40	< 2.21	−2.40	< −2.26	···	0.08	···
0053+261A(2)	13.957958	26.413111	-1	0.1971	1327	81.37 ± 2.06	24.13 ± 0.95	< 2.06	< 2.21	−2.19	< −2.52	···	0.14	···
0053-102B	13.966833	−9.984750	-1	0.0534	28	< 1.95	< 0.45	< 2.40	< 1.85	···	···	···	···	···
0053-015	14.106792	−1.262333	C	0.0444	1764	104.00 ± 4.3	44.33 ± 1.16	19.94 ± 1.15	18.98 ± 0.75	−1.54	−0.82	−0.08	1.17	17.96
0053-016	14.007417	−1.343000	-1	0.0444	1095	282.00 ± 8	106.53 ± −1	7.77 ± 1.74	< 1.62	−1.75	−2.69	< −2.40	1.68	···
0100-221A	15.687958	−21.904139	P	0.0566	138	6.11 ± 0.571	4.50 ± 0.52	< 3.22	···	−0.55	< −0.34	···	1.22	···
0108+173	17.764875	17.652083	P	0.0638	12	6.44 ± 0.612	3.51 ± 0.28	< 1.96	< 1.90	−1.09	< −0.60	···	0.26	···
0110+152	18.248333	15.491250	C	0.0444	719	31.50 ± 0.6	14.53 ± 2.84	4.97 ± 0.65	6.33 ± 0.6	−1.39	−1.10	0.37	0.54	8.30
0119+193(1)	20.586750	19.588056	P	0.0544	20	11.88 ± 0.61	8.79 ± 0.32	5.25 ± 0.46	2.40 ± 0.54	−0.54	−0.53	−1.20	2.43	0.99
0122+084	21.281917	8.699417	P	0.0498	51	4.03 ± 0.61	3.32 ± 0.32	1.24 ± 0.57	2.42 ± 0.47	−0.35	−1.01	1.02	1.45	5.13
0123-016A	21.434500	−1.379472	C	0.0180	910	77.60 ± 11.5	20.02 ± 1.67	10.93 ± −1	6.84 ± 0.57	−2.44	−0.62	−0.72	0.06	4.04
0123-016B	21.502750	−1.345111	P	0.0180	3270	107.53 ± 9.16	128.70 ± 3.61	121.70 ± 1.4	128.38 ± 1	0.32	−0.06	0.08	276.79	136.33
0124+189	21.726625	19.214500	C	0.0420	1345	310.00 ± 4.26	75.44 ± 1.91	24.98 ± 1.23	24.75 ± 0.96	−2.55	−1.13	−0.01	0.18	24.49
0139+073A	25.497708	7.680639	P	0.0616	43	6.27 ± 1.04	4.90 ± 0.23	2.07 ± 0.636	2.74 ± 0.81	−0.44	−0.88	0.43	1.71	3.76
0139+073B(2)	25.518333	7.650556	-1	0.0616	27	9.67 ± 1.84	3.28 ± 0.38	2.23 ± 0.84	< 1.51	−1.95	−0.40	< −0.60	0.03	···
0149+359(1)	28.193167	36.151833	-1	0.0163	81	22.42 ± 1.09	10.78 ± 0.47	5.64 ± 0.88	5.40 ± 0.64	−1.32	−0.66	−0.07	0.48	5.14
0149+359(2)	28.165000	36.171444	P	0.0163	81	5.98 ± 1.36	5.51 ± 0.55	···	···	−0.15	···	···	3.89	···
0154+320(1)	29.325708	32.240028	-1	0.0894	372	91.00 ± 2	40.37 ± 1.4	< 6.40	< 1.67	−1.46	< −1.89	···	1.26	···
0154+320(2)	29.317500	32.246472	C	0.0894	372	91.00 ± 2	16.98 ± 0.92	3.15 ± 1.08	< 1.59	−1.46	−1.73	< −1.04	0.53	···
0304-122(1)	46.722958	−12.109111	-1	0.0788	501	86.06 ± 2.7	40.07 ± 1.89	12.73 ± 2.3	2.35 ± 1.08	−1.38	−1.18	−2.58	1.54	0.35
0304-122(2)	46.718417	−12.105722	-1	0.0788	501	87.75 ± 2	45.55 ± 1.53	11.67 ± 1.4	6.56 ± 1.35	−1.18	−1.40	−0.88	2.79	3.43
0304-122(3)	46.719292	−12.106111	C	0.0788	501	87.75 ± 2	45.55 ± 1.53	4.93 ± 1.44	2.93 ± 0.86	−1.18	−2.28	−0.80	2.79	1.63
0306-237	47.067833	−23.563778	-1	0.0665	117	55.70 ± 1.2	33.71 ± 0.51	16.80 ± 0.59	14.15 ± 1.06	−0.90	−0.71	−0.26	3.97	11.67

Table 6.5: Cluster Radio Sources

0431-134(1)	68.543375	−13.370078	-1	0.0327	1160	106.00 ± 3.5	33.06 ± 0.98	23.10 ± 0.73	16.96 ± 0.74	−2.10	−0.37	−0.47	0.23	11.98
0445-205	72.012542	−20.444028	P	0.0734	95	15.50 ± 2	4.29 ± 0.52	2.30 ± 0.8	< 1.97	−2.31	−0.64	< −0.24	0.02	···
0446-205	72.043083	−20.415972	C	0.0734	119	46.90 ± 1.6	17.37 ± 0.52	10.24 ± 0.63	8.58 ± 0.97	−1.79	−0.54	−0.27	0.25	7.03
0717+559	110.339917	55.809056	-1	0.0381	16	7.16 ± 1.17	2.29 ± 0.64	< 2.12	< 1.46	−2.05	< −0.08	···	0.02	···
0810+665	123.720708	66.447639	-1	0.1380	266	79.90 ± 1.5	38.21 ± 0.66	9.18 ± 1.3	6.17 ± 0.99	−1.33	−1.46	−0.61	1.65	3.95
0816+526(1)	124.949208	52.536833	-1	0.1890	2020	281.00 ± 2.3	140.29 ± 2.33	48.30 ± 4.32	19.62 ± 1.8	−1.25	−1.09	−1.38	7.27	7.12
0816+526(2)	124.947958	52.540833	C	0.1890	2020	···	145.40 ± 4.38	23.90 ± 6.3	3.59 ± 1.07	···	−1.85	−2.90	···	0.43
0816+526(3)	124.947083	52.544972	-1	0.1890	2020	497.10 ± 2.8	260.00 ± 3	59.24 ± 4.12	35.33 ± 2.4	−1.17	−1.52	−0.79	16.43	19.75
0836+290	129.816042	28.844083	P	0.0788	1022	156.00 ± 2.34	153.60 ± 0.91	117.06 ± 1.25	95.22 ± 1.18	−0.03	−0.28	−0.32	143.78	75.48
0909+162(1)	138.146250	15.999833	C	0.0851	183	25.00 ± 2	11.57 ± 1.45	2.94 ± 0.83	1.43 ± 0.64	−1.39	−1.41	−1.10	0.43	0.64
0909+162(2)	138.140792	15.995806	-1	0.0851	183	34.75 ± 1.35	18.25 ± 1.1	< 2.50	< 1.89	−1.16	< −2.04	···	1.17	···
0909+161	138.127417	15.924417	P	0.0851	23	16.41 ± 0.91	10.43 ± 0.34	6.56 ± 0.57	7.56 ± 0.63	−0.82	−0.48	0.22	1.51	8.87
1058+107	165.239250	10.505472	P	0.0360	24	9.96 ± 0.39	7.93 ± 0.29	4.85 ± 0.68	4.22 ± 0.74	−0.41	−0.50	−0.21	3.02	3.61
1108+289A	167.698958	28.660139	C	0.0321	34	9.50 ± 1.3	3.94 ± 0.72	2.55 ± 0.57	2.59 ± 1.01	−1.59	−0.45	0.02	0.09	2.63
1108+411(1)	167.914458	40.838000	-1	0.0794	771	235.00 ± 2	67.54 ± 1.21	16.30 ± 2.17	8.59 ± 2.57	−2.25	−1.46	−0.98	0.33	4.18
1108+411(2)	167.914417	40.840611	C	0.0794	771	235.00 ± 2	37.70 ± 0.82	13.37 ± 1.65	3.76 ± 1.03	−2.25	−1.06	−1.94	0.19	0.90
1108+411(3)	167.911958	40.839083	C	0.0794	771	235.00 ± 2	71.01 ± 1.46	10.37 ± 2.17	···	−2.25	−1.97	···	0.35	···
1108+410A	-99.000000	−99.000000	-1	0.0794	116	< 4.35	< 1.21	< 2.37	< 1.46	···	···	···	···	···
1108+410B	167.931875	40.820972	P	0.0794	23	6.99 ± 1.08	5.27 ± 0.79	< 2.44	< 1.49	−0.51	< −0.79	···	1.59	···
1113+295B(1)	169.119167	29.285972	-1	0.0471	22	15.92 ± 4.15	< 4.86	4.14 ± 1.05	2.16 ± 0.66	< −2.14	···	−1.00	···	1.04
1113+295B(2)	169.094542	29.252278	P	0.0471	22	54.08 ± 4.67	31.78 ± 4.06	···	···	−0.96	···	···	3.30	···
1113+295C	169.143833	29.254694	C	0.0471	1888	289.90 ± 6.1	97.35 ± 2.9	35.72 ± 1.95	37.28 ± 1.07	−1.97	−1.03	0.07	0.93	39.12
1129+562	173.096042	55.967750	-1	0.0531	39	8.22 ± 0.494	2.60 ± 0.59	< 2.00	< 2.33	−2.07	< −0.27	···	0.02	···
1130+148	173.256083	14.534583	C	0.0834	167	13.68 ± 0.41	8.82 ± 0.39	3.42 ± 0.76	3.56 ± 1.08	−0.79	−0.97	0.06	1.36	3.73
1130-037	173.271333	−4.013264	P	0.0484	791	158.51 ± 2.1	107.40 ± 1.37	62.13 ± 0.86	···	−0.70	−0.56	···	20.45	···
1131+493	173.496708	49.062194	C	0.0338	835	131.25 ± 2	91.44 ± 1.32	52.85 ± 1.1	41.84 ± 0.92	−0.65	−0.56	−0.36	19.60	32.17
1132+492	173.694042	48.956167	C	0.0338	475	30.38 ± 0.83	31.86 ± 0.74	26.76 ± 0.88	18.59 ± 0.86	0.09	−0.18	−0.56	39.02	12.34
1132+493	173.705625	49.077917	P	0.0338	31	12.61 ± 0.49	7.15 ± 0.43	< 2.45	1.81 ± 0.83	−1.02	< −1.10	···	0.64	···
1141+466(1)	175.914583	46.354917	P	0.1162	814	149.40 ± 0.5	44.90 ± 0.66	3.47 ± 1.04	1.31 ± 0.73	−2.17	−2.63	−1.49	0.27	0.44
1141+466(2)	175.915833	46.356361	C	0.1162	814	149.40 ± 0.5	66.15 ± 0.62	11.35 ± 1.4	0.95 ± 0.56	−2.17	−1.81	−3.79	0.39	0.06
1141+676	176.152625	67.405972	P	0.1164	196	68.94 ± 0.47	37.75 ± 0.51	16.84 ± 1.2	10.48 ± 0.95	−1.08	−0.83	−0.72	2.90	6.15
1142+198	176.270875	19.606417	C	0.0214	5450	723.75 ± 9.55	432.27 ± 4.22	215.48 ± 2.7	172.11 ± 2.3	−0.93	−0.71	−0.34	48.08	133.66
1153+736	178.996458	73.415361	P	0.0836	64	27.66 ± 0.59	19.33 ± 0.75	3.01 ± 1.09	3.96 ± 1.74	−0.65	−1.91	0.42	4.20	5.39
1155+266	179.583875	26.353306	C	0.1120	880	13.80 ± 6.7	1.63 ± 0.73	6.92 ± 0.93	7.09 ± 0.64	−3.85	1.48	0.04	0.00	7.29
1159+583(1)	180.514250	58.033681	-1	0.1035	765	110.00 ± 1	53.15 ± 0.88	19.66 ± 2.335	8.70 ± 1.7	−1.31	−1.02	−1.25	2.40	3.48
1159+583(3)	180.520333	58.037333	-1	0.1035	765	124.00 ± 1.1	54.62 ± 0.86	23.74 ± 3	12.50 ± 2.1	−1.48	−0.85	−0.98	1.66	6.07
1201+282	180.902792	27.944250	C	0.1390	215	2.93 ± 0.31	1.87 ± 0.43	4.94 ± 0.86	1.69 ± 0.74	−0.81	1.00	−1.64	0.28	0.51
1201+026(1)	181.030333	2.409903	C	0.0844	244	120.00 ± 1	29.82 ± 1.32	3.75 ± 1.5	···	−2.01	−2.13	···	0.26	···

Table 6.5: Cluster Radio Sources

1201+026(2)	181.026375	2.411758	C	0.0844	244	120.00 ± 1	39.40 ± 1.4	8.11 ± 0.965	6.06 ± 0.9	−2.01	−1.62	−0.45	0.34	4.37
1201+026(3)	181.272292	2.413469	C	0.0844	244	120.00 ± 1	25.65 ± 1.06	···	···	−2.01	···	···	0.22	···
1207+722	182.580833	71.999250	C	0.1226	256	···	47.53 ± 2.4	6.56 ± 2.09	< 2.58	···	−2.03	< −1.43	···	···
1221+615(1)	185.876167	61.247250	-1	0.2308	321	69.15 ± 0.57	34.34 ± 0.89	12.50 ± 1.485	3.89 ± 1.35	−1.26	−1.04	−1.78	1.74	1.05
1221+615(2)	185.873958	61.252111	-1	0.2308	321	49.46 ± 0.54	24.78 ± 0.69	5.98 ± 1.55	< 2.58	−1.24	−1.46	< −1.28	1.30	···
1224+091	186.826375	8.843056	C	0.0896	48	< 3.40	5.05 ± 0.68	< 2.39	< 2.91	···	< −0.77	···	···	···
1225+636(1)	186.968667	63.383958	-1	0.1459	210	70.32 ± 0.82	19.53 ± 0.65	11.80 ± 4.8	< 1.66	−2.31	−0.52	< −3.00	0.08	···
1225+636(2)	186.963417	63.384778	C	0.1459	210	70.32 ± 0.82	22.41 ± 0.63	5.04 ± 1.27	5.47 ± 1	−2.31	−1.53	0.13	0.10	6.00
1231+674	188.308458	67.128944	C	0.1071	879	18.00 ± 1	11.00 ± 1.33	7.33 ± 1.23	4.43 ± 0.84	−0.89	−0.42	−0.77	1.35	2.51
1232+414(1)	188.625042	41.159917	C	0.1908	689	< 17.00	19.51 ± 2.4	< 2.67	< 1.39	···	< −2.04	···	···	···
1232+414(2)	188.614250	41.166778	-1	0.1908	689	105.30 ± 1.5	48.94 ± 0.71	19.85 ± 2.5	12.67 ± 1.35	−1.38	−0.93	−0.69	1.87	7.65
1233+169	189.033792	16.641361	P	0.0784	630	189.00 ± 2.5	64.22 ± 1.16	33.21 ± 0.99	20.39 ± 0.96	−1.94	−0.68	−0.75	0.65	11.78
1233+168	189.107875	16.538361	C	0.0784	1338	65.00 ± 12	11.13 ± 2.4	4.62 ± 1.17	3.28 ± 0.9	−3.18	−0.90	−0.52	0.01	2.23
1238+188	190.251083	18.553722	C	0.0718	537	48.35 ± 1.41	18.32 ± 0.8	5.77 ± 1.03	4.75 ± 0.91	−1.75	−1.19	−0.30	0.29	3.82
1243+699	191.472625	69.658250	C	0.2307	220	38.76 ± 1.39	6.66 ± 0.6	4.27 ± 1.26	0.80 ± 0.43	−3.17	−0.46	−2.56	0.00	0.12
1256+281	194.846167	27.911194	C	0.0231	450	59.69 ± 1.39	37.62 ± 1.53	< 2.56	< 1.85	−0.83	< −2.76	···	5.26	···
1257+282(1)	194.896375	27.957917	-1	0.0231	215	39.83 ± 0.89	22.64 ± 0.45	7.83 ± 1.94	3.00 ± −1	−1.02	−1.09	−1.47	2.04	1.02
1257+282(2)	194.900167	27.961000	-1	0.0231	215	50.20 ± 1	23.19 ± 0.47	7.54 ± 1.18	2.82 ± 0.71	−1.39	−1.15	−1.50	0.86	0.93
1301+195	195.944167	19.271500	P	0.0649	74	22.51 ± 0.28	13.70 ± 0.27	6.20 ± 0.75	1.96 ± 0.55	−0.89	−0.81	−1.76	1.65	0.54
1300+677	195.668625	67.478028	-1	0.1055	298	137.20 ± 0.6	87.48 ± 0.77	15.90 ± 0.9	< 3.00	−0.81	−1.75	< −2.55	12.86	···
1320+584(1)	200.732083	58.167528	-1	0.1932	325	78.62 ± 1.02	50.00 ± 1	13.94 ± 1.33	···	−0.82	−1.31	···	7.27	···
1320+584(2)	200.726750	58.171083	C	0.1932	325	53.21 ± 0.81	27.87 ± 0.67	< 2.85	···	−1.16	< −2.34	···	1.77	···
1333+412(1)	203.835000	40.999861	-1	0.2290	797	169.70 ± 0.9	63.05 ± 0.62	22.77 ± 1.4	···	−1.78	−1.04	···	0.93	···
1333+412(2)	203.831958	41.002444	-1	0.2290	797	161.30 ± 0.9	62.34 ± 0.64	18.44 ± 1.21	···	−1.71	−1.25	···	1.09	···
1339+266A	205.455167	26.373778	-1	0.0724	40	15.90 ± 0.64	6.39 ± 0.67	< 1.63	< 1.59	−1.64	< −1.40	···	0.13	···
1339+266B	205.460625	26.371500	-1	0.0724	287	91.95 ± 0.61	41.04 ± 0.64	1.87 ± −1	< 1.59	−1.45	−3.17	< −0.25	1.32	···
1346+268A	207.218583	26.592806	P	0.0622	883	234.60 ± 0.5	110.74 ± 0.84	21.79 ± 1.02	12.24 ± 0.67	−1.35	−1.67	−0.88	4.52	6.40
1346+268B	207.247375	26.559389	-1	0.0622	35	10.75 ± 0.67	12.05 ± 1.17	4.14 ± 0.957	< 1.50	0.21	−1.10	< −1.55	19.60	···
1415+084(1)	214.380333	8.208444	C	0.0570	331	29.83 ± 1.66	8.27 ± 0.72	3.60 ± 0.59	···	−2.31	−0.85	···	0.03	···
1415+084(2)	214.382625	8.210083	C	0.0570	331	29.83 ± 1.66	5.88 ± 0.82	< 0.78	···	−2.31	< −2.07	···	0.02	···
1418+253(1)	215.173083	25.149944	-1	0.0780	116	22.27 ± 0.507	9.45 ± 0.75	1.28 ± 0.5	1.70 ± 0.71	−1.54	−2.05	0.43	0.24	2.34
1418+253(2)	215.174708	25.146111	-1	0.0780	116	< 26.70	6.63 ± 0.76	2.03 ± 0.656	3.76 ± 0.84	···	−1.21	0.94	···	7.53
1418+253(3)	215.175833	25.143778	C	0.0780	116	< 26.70	6.65 ± 0.79	2.15 ± 0.802	< 1.56	···	−1.16	< −0.49	···	···
1418+253(4)	215.176750	25.140778	-1	0.0780	116	21.03 ± 0.594	6.36 ± 0.65	< 1.74	< 1.84	−2.15	< −1.33	···	0.04	···
1424+169(1)	216.642167	16.750667	-1	0.0528	97	9.55 ± 0.584	8.20 ± 0.73	···	···	−0.27	···	···	4.28	···
1424+169(2)	216.631292	16.763333	-1	0.0528	97	7.94 ± 0.7	1.92 ± 0.63	···	···	−2.56	···	···	0.00	···
1424+167(1)	216.822083	16.554778	-1	0.0528	103	11.93 ± 0.567	7.15 ± 0.44	4.75 ± 1.32	···	−0.92	−0.42	···	0.81	···
1435+249(1)	219.312583	24.759056	C	0.0883	175	11.80 ± 0.56	9.21 ± 0.39	7.72 ± 0.61	5.77 ± 0.58	−0.45	−0.18	−0.45	3.20	4.16

Table 6.5: Cluster Radio Sources

1435+249(2)	219.316750	24.765250	-1	0.0883	175	11.69 ± 0.88	5.54 ± 0.71	< 1.98	···	−1.35	< −1.06	···	0.23	···
1435+250	219.320000	24.869278	C	0.0883	206	23.03 ± 0.73	12.22 ± 0.45	6.53 ± 1.1	4.62 ± 0.835	−1.14	−0.64	−0.53	0.82	3.12
1433+553	218.868750	55.131056	C	0.1396	447	73.92 ± 1.02	16.81 ± 0.55	7.95 ± 0.834	···	−2.67	−0.77	···	0.03	···
1435+038(0)	219.599333	3.672889	C	0.2240	801	103.16 ± 0.78	11.25 ± 0.85	< 16.06	···	−1.40	< 0.37	···	0.41	···
1435+038(1)	219.594583	3.671333	-1	0.2240	801	103.16 ± 0.78	47.29 ± 0.54	12.21 ± 2.13	···	−1.40	−1.39	···	1.70	···
1435+038(2)	219.588625	3.670222	-1	0.2240	801	114.12 ± 0.73	55.45 ± 0.51	15.91 ± 1.61	···	−1.30	−1.28	···	2.56	···
1435+038(4)	219.595958	3.671361	-1	0.2240	801	89.03 ± 1.37	< 2.54	< 2.93	···	< −6.41	···	···	···	···
1452+188	223.631167	18.642306	P	0.0579	38	11.99 ± 0.23	7.71 ± 0.25	2.11 ± 0.56	···	−0.80	−1.33	···	1.17	···
1508+059(1)	227.733917	5.744556	-1	0.0767	489	60.51 ± 0.46	21.31 ± 0.42	4.07 ± 1.03	···	−1.88	−1.70	···	0.25	···
1508+065(1)	227.863042	6.347222	-1	0.0817	552	127.65 ± 0.72	54.79 ± 0.66	18.02 ± −1	···	−1.52	−1.14	···	1.49	···
1508+065(2)	227.858375	6.350306	-1	0.0817	552	127.44 ± 0.7	56.48 ± 0.62	15.35 ± 2.17	···	−1.47	−1.34	···	1.76	···
1508+182(1)	227.789292	18.030028	-1	0.1163	346	74.34 ± 0.88	30.50 ± 0.65	< 9.33	···	−1.60	< −1.22	···	0.68	···
1508+182(2)	227.784667	18.032639	-1	0.1163	346	68.61 ± 0.96	26.85 ± 0.61	6.90 ± 1.51	···	−1.69	−1.39	···	0.49	···
1510+076(1)	228.140500	7.424889	-1	0.0451	17	10.59 ± 1.54	2.76 ± 0.55	< 2.87	···	−2.42	< 0.04	···	0.01	···
1510+076(2)	228.142667	7.431806	C	0.0451	17	10.59 ± 1.54	1.97 ± 0.45	1.57 ± 0.7	···	−2.42	−0.23	···	0.01	···
1514+072	229.185375	7.021556	P	0.0348	5390	897.61 ± 2.89	691.40 ± 2.7	393.16 ± 5.7	···	−0.47	−0.58	···	227.36	···
1520+087	230.771917	8.609361	-1	0.0355	13	5.59 ± 0.47	2.11 ± 0.37	< 2.30	···	−1.75	< 0.09	···	0.03	···
1525+290	231.935000	28.918278	C	0.0656	224	88.69 ± 0.64	28.84 ± 0.779	5.70 ± 0.84	3.31 ± 0.9	−2.02	−1.66	−0.83	0.24	1.80
1530+282	233.186000	28.063139	C	0.0734	352	133.24 ± 1.03	14.71 ± 0.69	4.87 ± 0.82	1.99 ± 1.13	−3.97	−1.13	−1.37	0.00	0.73
1531+312(1)	233.313208	31.128500	-1	0.0670	49	6.89 ± 0.37	2.81 ± 0.32	< 2.17	< 1.61	−1.62	< −0.27	···	0.06	···
1531+312(2)	233.313667	31.130694	C	0.0670	49	6.89 ± 0.37	1.28 ± 0.32	< 2.17	< 2.80	−1.62	< 0.54	···	0.03	···
1531+312(3)	233.316917	31.133056	-1	0.0670	49	8.53 ± 0.38	4.39 ± 0.45	< 2.17	< 2.25	−1.20	< −0.72	···	0.26	···
1555+356(2)	239.425792	35.507556	-1	0.1579	216	57.62 ± 0.63	14.60 ± 0.41	7.02 ± 1.85	3.03 ± 0.9	−2.47	−0.75	−1.28	0.04	1.18
1555+356(3)	239.426750	35.509361	C	0.1579	216	23.70 ± 0.44	16.80 ± 0.44	5.38 ± 0.909	3.58 ± 1.04	−1.27	−1.17	−0.62	0.83	2.26
1556+274	239.558500	27.272306	-1	0.0896	130	30.38 ± 0.41	16.97 ± 0.36	7.97 ± 1.59	< 1.92	−1.05	−0.77	< −2.18	1.42	···
1559+161(1)	240.570292	15.974472	-1	0.0354	17	6.83 ± 0.36	4.97 ± 0.42	< 1.80	···	−0.57	< −1.04	···	1.28	···
1602+178B(1)	241.287208	17.731444	-1	0.0368	780	116.48 ± 1.62	76.02 ± 2.36	10.84 ± 1.27	···	−0.77	−2.00	···	12.34	···
1602+178B(1.5)	241.287500	17.729875	-1	0.0368	780	···	···	10.75 ± 1.26	···	···	···	···	···	···
1602+178B(2)	241.288042	17.726972	-1	0.0368	780	213.70 ± 1.75	139.80 ± 2.39	< 4.73	···	−0.76	< −3.47	···	22.92	···
1603+165	241.371667	16.435750	C	0.0372	44	9.04 ± 0.35	4.78 ± 0.33	2.48 ± 0.69	···	−1.15	−0.67	···	0.32	···
1610+296(2)	243.145625	29.481417	C	0.0320	119	38.00 ± −1	< 0.59	2.83 ± 0.86	< 1.66	−6.22	···	< −0.82	···	···
1626+396	247.159417	39.551306	-1	0.0299	3480	440.00 ± −1	185.00 ± −1	···	···	−1.56	···	···	4.61	···
1638+468	250.092500	46.713083	-1	0.2070	212	74.10 ± 0.73	44.70 ± 0.84	···	···	−0.91	···	···	5.19	···
1657+325A	254.754542	32.494139	-1	0.0628	171	22.00 ± −1	1.18 ± 0.3	< 3.28	< 1.82	−5.27	< 1.05	···	0.00	···
1657+325B	-99.000000	−99.000000	-1	0.0628	12	···	< 0.62	< 2.86	···	···	···	···	···	···
1707+344(1)	257.413125	34.428306	-1	0.0806	680	100.38 ± 0.81	56.81 ± 1.53	22.00 ± 3.2	13.90 ± −1	−1.03	−0.97	−0.70	5.02	8.29
1707+344(2)	257.409583	34.433583	-1	0.0806	680	108.22 ± 0.74	62.07 ± 1.29	23.00 ± 2.5	7.00 ± 2.8	−1.00	−1.02	−1.82	5.81	1.84
1708+345	257.497208	34.511972	P	0.0806	16	9.53 ± 0.67	4.95 ± 0.81	3.83 ± 1.77	< 2.19	−1.18	−0.26	< −0.85	0.30	···

Table 6.5: Cluster Radio Sources

1709+397B	257.736417	39.692639	C	0.0656	543	106.15 ± 0.7	60.28 ± 0.75	23.20 ± 2.5	12.13 ± 2.5	−1.02	−0.98	−0.99	5.41	5.85
1712+640	258.097375	64.033444	C	0.0808	290	82.50 ± 1	45.76 ± 1.15	4.67 ± 0.77	< 1.77	−1.06	−2.34	< −1.48	3.71	···
1712+641(1)	258.269875	64.115667	-1	0.0808	66	26.93 ± 0.99	8.41 ± 0.8	3.59 ± 1.23	< 1.87	−2.10	−0.87	< −1.00	0.06	···
1712+641(2)	258.266125	64.117722	C	0.0808	66	26.93 ± 0.99	8.80 ± 0.54	1.28 ± 0.41	< 1.87	−2.10	−1.98	< 0.58	0.06	···
1713+641(1)	258.366667	1.897222	-1	0.0808	250	39.60 ± 85.1	0.66 ± 37.21	0.56 ± 9.33	1.44 ± 4.84	−7.37	−0.17	1.44	0.00	4.17
1713+641(2)	258.370625	64.045722	C	0.0808	250	85.10 ± 0.66	48.83 ± 0.81	7.26 ± 0.79	5.02 ± 0.79	−7.37	−1.96	−0.56	0.00	3.31
1713+641(3)	258.373542	64.050250	-1	0.0808	250	70.30 ± 0.65	37.34 ± 0.67	4.26 ± 0.88	< 1.86	−1.14	−2.23	< −1.27	2.52	···
1706+786	255.867583	78.632139	-1	0.0581	157	42.81 ± 0.69	23.50 ± 0.58	5.98 ± 1.11	< 1.78	−1.08	−1.40	< −1.85	1.82	···
1705+786	255.760375	78.599250	-1	0.0581	62	26.00 ± −1	6.91 ± 0.73	< 2.30	< 1.83	−2.39	< −1.13	···	0.02	···
1706+787	255.866792	78.666000	P	0.0581	39	5.06 ± 0.6	3.96 ± 0.53	< 1.01	< 1.99	−0.44	< −1.40	···	1.39	···
1703+787	255.217583	78.690139	-1	0.0581	10	2.14 ± 0.45	1.25 ± 0.36	< 2.32	< 3.48	−0.97	< 0.63	···	0.13	···
1820+689	274.926042	68.947639	C/P	0.0880	801	83.27 ± 1.61	52.65 ± 1.54	31.11 ± 1.12	24.36 ± 0.78	−0.83	−0.54	−0.37	7.47	18.50
1826+747(1)	276.234875	74.730806	-1	0.1271	244	38.53 ± 1.11	21.63 ± 0.71	1.44 ± 0.647	1.85 ± 0.65	−1.04	−2.78	0.38	1.85	2.46
1826+747(2)	276.215333	74.731639	-1	0.1271	244	44.98 ± 1.27	16.27 ± 0.54	3.68 ± 1.3	2.14 ± 0.76	−1.83	−1.53	−0.83	0.21	1.16
1849+702(1)	282.325625	70.353528	C	0.0899	163	18.83 ± 0.54	14.47 ± 0.34	8.28 ± 0.49	9.48 ± 0.65	−0.47	−0.57	0.21	4.71	11.04
1857+799	283.467833	80.047361	P	0.2139	180	2.80 ± 0.51	2.66 ± 0.27	5.34 ± 1.44	2.61 ± 0.6	−0.09	0.71	−1.09	2.15	1.17
2124-124(1)	321.741375	−12.215361	-1	0.1760	251	96.09 ± 1.1	38.45 ± 1.1	< 2.43	< 2.10	−1.65	< −2.83	···	0.78	···
2124-124(2)	321.738417	−12.214361	C	0.1760	251	96.09 ± 1.1	26.53 ± 0.58	8.96 ± 1.13	8.38 ± 0.81	−1.65	−1.11	−0.10	0.54	7.77
2142-202	326.314250	−19.995167	-1	0.0576	351	2.45 ± 1.27	< 0.70	2.28 ± 1.06	< 1.74	< −2.26	···	< −0.41	···	···
2149-158C(1)	327.999000	−15.638417	C	0.0646	176	29.88 ± 1.8	12.76 ± 1.03	5.24 ± 1.07	1.83 ± 0.75	−1.53	−0.91	−1.61	0.34	0.56
2149-158C(2)	327.979625	−15.626250	-1	0.0646	176	64.00 ± 3.4	14.67 ± 1.7	< 2.93	···	−2.65	< −1.65	···	0.03	···
2154-080A(1)	329.253250	−7.847417	-1	0.0584	460	81.60 ± 1.14	51.47 ± 2.65	36.00 ± −1	···	−0.83	−0.37	···	7.22	···
2154-080A(2)	329.256917	−7.839750	C	0.0584	460	81.20 ± 1.13	11.11 ± 1.055	5.45 ± 0.53	4.04 ± 0.71	−3.58	−0.73	−0.46	0.00	2.88
2154-080A(3)	329.263458	−7.836250	-1	0.0584	460	73.43 ± 1.06	46.53 ± 2.41	18.00 ± −1	···	−0.82	−0.97	···	6.66	···
2154-080B	329.389583	−7.794306	C	0.0584	430	92.43 ± 1.16	13.88 ± 0.71	6.47 ± 0.92	5.67 ± 0.96	−3.42	−0.78	−0.20	0.00	4.89
2228-087	337.870125	−8.484917	P	0.0810	107	10.89 ± 0.67	10.48 ± 0.312	6.39 ± 0.72	6.30 ± 0.62	−0.07	−0.51	−0.02	8.89	6.20
2229-086	337.930167	−8.408833	C	0.0810	812	64.79 ± 2.52	33.38 ± 1.13	20.42 ± 0.85	16.84 ± 0.7	−1.19	−0.50	−0.29	1.98	13.56
2247+106B	342.581792	10.903444	-1	0.0768	14	2.44 ± 0.24	0.99 ± 0.28	3.07 ± 1.08	< 1.11	−1.62	1.16	< −1.55	0.02	···
2321+164	350.976167	16.680417	-1	0.0416	46	20.40 ± 0.574	9.95 ± 0.44	6.96 ± 0.105	2.30 ± −1	−1.29	−0.37	−1.69	0.47	0.66
2322+143A(1)	351.133917	14.639556	C	0.0421	187	65.59 ± 1.36	24.47 ± 0.8	6.75 ± 0.92	4.94 ± 0.78	−1.78	−1.32	−0.48	0.37	3.47
2322+143B(1)	351.154833	14.642528	C	0.0421	76	25.85 ± 0.95	14.01 ± 0.54	6.84 ± 1.05	3.15 ± 0.71	−1.10	−0.74	−1.18	1.03	1.32
2322-123	351.332417	−12.124111	P	0.0852	1699	415.59 ± 0.91	205.83 ± 0.66	59.58 ± 1.22	31.26 ± 0.99	−1.27	−1.27	−0.99	10.31	15.13
2332+270(2)	353.756958	27.371417	-1	0.0617	61	9.23 ± 0.45	< 1.02	< 1.47	< 1.90	< −3.97	···	···	···	···
2333+208(1)	354.127042	21.146583	P	0.0569	55	11.41 ± 0.33	6.60 ± 0.27	4.30 ± 0.62	4.25 ± 0.74	−0.99	−0.44	−0.02	0.64	4.19
2333+208(3)	354.165417	21.102111	P	0.0569	55	2.33 ± 0.51	···	···	···	···	···	···	···	···
2335+267(1)	354.622542	27.031444	C	0.0321	7650	267.48 ± 15.6	212.63 ± 5.08	139.12 ± 2.16	102.95 ± 1.33	−0.41	−0.44	−0.46	79.97	73.37
2335+267(2)	354.633042	27.024417	-1	0.0321	7650	316.87 ± 22.3	184.23 ± 12.6	< 109.90	···	−0.98	< −0.53	···	18.27	···
2348+058	357.710708	6.149528	P	0.0556	50	8.49 ± 0.29	3.02 ± 0.24	5.28 ± 1.88	< 1.77	−1.86	0.57	< −1.67	0.04	···

Table 6.5: Cluster Radio Sources

2352+261(1)	358.851875	26.404722	C	0.2404	311	3.89 ± 0.84	1.48 ± 0.57	1.91 ± 0.823	< 3.25	−1.74	0.26	< 0.81	0.02	···
2352+261(3)	358.824667	26.416167	-1	0.2404	311	28.44 ± 1.58	12.30 ± 0.85	···	···	−1.51	···	···	0.35	···

[a] Source name from Owen & Ledlow (1997), which is based on B1950 positions; Parentheses denote multiple components.

[b] Morphology of the sources: "−1" denotes extended source; "C" means core; "P" refers to point-like.

[c] Redshift taken from Owen & Ledlow (1997).

[d] 1.4 GHz flux from Owen & Ledlow (1997).

[e] Predicted flux at 90 GHz based on the fluxes at C & X bands.

[f] Predicted flux at 90 GHz based on the fluxes at K & Q bands.

CHAPTER 7

Conclusion

In this thesis we have presented a multi-wavelength study of the FIRST radio sources. In the first part of the thesis a cross correlation analysis of FIRST radio sources with optical data for the NDWFS and infrared data from FLAMINGOS survey was performed.

The results of multi-wavelength identification of FIRST radio sources in both the Boötes and Cetus fields have been presented in the second chapter. The optical *B R I K* imaging covers an area of 9.2 deg^2 to $Bw = 26.5$, $R = 25.8$, $I = 25.5$ and $K = 19.5$ in Boötes field, and 4.7 deg^2 in Cetus field to $J = 21.4$ and $K = 19.9$. With this optical/infrared imaging, robust counterparts for FIRST radio sources have been identified based on the positional coincidence and the likelihood ratio techniques (688/900 and 109/242 in Boötes and Cetus fields, respectively). Photometric redshifts have been derived for all radio sources optically identified in Boötes and Cetus fields using the public code *Hyperz*. The redshift distribution of FIRST radio sources counterparts peaks at $z \sim 0.737$ with 68% of the population estimated to be at $z < 1.5$. The photometric redshifts derived for FIRST radio source identified in Boötes and Cetus fields (based on the multi-wavelength *Bw R I J K* bands) have been used to investigate the near infrared Hubble diagram of the faint radio population at high frequency (1.4 GHz) to a limiting flux-density of 1 mJy level. It is found that there is a remarkably tight correlation in the Hubble $K - z$

diagram of FIRST radio source counterparts in Boötes and Cetus fields. The $K-z$ relation obtained is similar to that obtained for brighter sources investigated by Willott et al. (2003) and Brookes et al. (2006). The $K-z$ relation for FIRST radio sources is well fitted by a second order polynomial between K magnitude and $\log_{10}\ z$ (in Boötes and Cetus fields) as

$$K(z) = 17.52 + 4.34\ \log_{10}\ z + 0.86\,(\log_{10}\ z)^2. \tag{7.1}$$

A composite $K-z$ diagram of FIRST radio sources and low-frequency selected radio samples (3CRR, 6CE, 7CRs and the EIS-NVSS) with progressively fainter flux-density limits was presented. The majority of the FIRST radio population tends to lie at fainter magnitudes possibly indicating that the galaxy luminosity is correlated with radio power (Willott et al. 2003; McLure & Jarvis 2004).

Multi-wavelength properties of the faint radio population at the mJy level have been investigated in the third chapter by making use of a sample of objects drawn from the joint use of the FIRST survey and the NDWFS/FLAMEX surveys introduced in the second chapter. The population of faint radio sources is mainly dominated by early type galaxies, with radio-to-optical flux ratios between 10^2 and 10^6 and a very red colour, $Bw-R\ \sim 4.6$. Similar results have been reported by Magliocchetti et al. (2002) who studied the optical counterparts of FIRST radio sources in the APM survey to a limiting magnitude $Bw \sim 21$ and $R \sim 20$. A total number of 13 DRGs (Distant Red Galaxies) are found to be counterparts to FIRST radio sources in Cetus field with $J-K > 2.3$ and $K < 20$. Deep optical imaging and spectroscopy is required to further investigate the nature of these DRGs.

Taking advantage of the infrared data provided by the FLAMEX survey J and K bands, a total of 57 EROs were found to be counterparts to FIRST radio sources in the Boötes field with $R-K \geq 5$. The optical infrared colour-colour diagram of Pozzetti & Mannucci (2000) was used to separate EROs into passively evolving and dusty star-forming galaxies finding that there is 18/25 (72%) of EROs are early type galaxies with redshifts between 0.6 and 2 and 7/25 (28%) are dusty star-forming galaxies. A total number of 3/7 EROs from this latter group were found to be DRGs with $J-K > 2.3$. Using the NDWFS/FLAMEX deep *Bw R I J K* imaging, the ERO counterparts to FIRST radio sources were photometrically classified into dusty or evolved

galaxies based on simple SED models. This classification cannot provide reliable information about the spectral type due to the degeneracy between age and metallicity, but does provide a rough SED classification at two extremes i.e. “blue” or “red” (Bolzonella et al. 2000).

Spectroscopic follow up of the faint radio population and their surrounding EROs (and DRGs), and deeper optical and infrared imaging is required in order to establish colours for the faint radio population and to explore their morphology in more detail. Deeper optical and infrared imaging will also allow us to select deeper and more complete sample of EROs and to determine the relationship between the radio galaxies and the EROs, allowing for a more detailed study of the faint radio population environment. we plan to follow up the southern Cetus field spectroscopically using the Multi-object spectrograph on the Southern African Large Telescope.

In chapter 4, we investigated broad band properties of a sample of 79 radio emitting X-ray sources, obtained from a correlation of the FIRST 1.4 GHz survey and the publicly available X-ray data of the medium depth XBoötes field. Out of $\sim$ 900 FIRST radio sources that lie in the Boötes field, 92 were found to have an X-ray counterpart and 79 optical counterparts are in common with the radio-X-ray matches. All 79 sources are identified in the full X-ray band (0.5-7 keV), 76 in the hard X-ray band (2-7 keV) and 77 in the soft band (0.5-2 keV).

Optical spectra obtained from the Sloan Digital Sky (SDSS) for 22 sources showed that the majority of the spectroscopically identified sources are broad line AGN (QSO), one source could be a BL Lac object, and 8 sources are spectroscopically identified as galaxies with narrow emission or absorption lines. The redshift distribution of the AGN shows a peak at $z \sim 0.7$, supporting previous studies (Barger et al. 2003) that show that the peak formation of supermassive black holes occurred at relatively recent times ($z < 1$). This leads to the conclusion that medium depth X-ray surveys are well suited for studying and probing this epoch effectively.

The radio and X-ray luminosities were calculated using a combination of photometric and spectroscopic redshifts. The majority (88%) of the sources have high X-ray luminosity in the full band, $L_X > 10^{42}$ erg s^{-1}, with 9 sources with low luminosity, $L_X < 10^{42}$ erg s^{-1}. Results from this work will be used to calculate the X-ray luminosity function and determine its evolution with redshift in a future paper. The X-ray-to-optical flux ratio of the sources shows that the majority (68%) are AGN (log $f_X/f_{opt} = 0 \pm 1$), a significant population (23%) exists with high

X-ray-to-optical flux ratio ($\log f_X/f_{opt} > 1$) corresponding to high redshift or dust obscuration, and 8% have low X-ray-to-optical flux ratio ($\log f_X/f_{opt} \leq -1$) that comprise normal galaxies and low X-ray luminosity sources.

In chapter 5 we briefly investigated the clustering properties of FIRST radio sources identified in the SDSS DR6 survey. The angular two point corelation function has been measured for all FIRST radio sources identified as galaxies, and for various magnitude and flux limited subsamples. The amplitude was found to be higher and the slope is steeper compared to previous results (e.g. Overzier et al. 2003), rather, our measured amplitudes of $A_\omega \approx 0.01$ for the FIRST-SDSS matches are consistent with the results of Magliocchetti & Maddox (2002) for the FIRST-APM matches who measured an amplitude of $A_\omega \approx 0.03$. We also found that the angular correlation scales with the depth of the optical survey SDSS as expected. In contrast the amplitude of the angular correlation function increases as the flux increases. This work is in progress and further in-depth analyses of the data are planned for an upcoming paper.

A forthcoming paper that follows on from this work will present a complete study of FIRST radio sources optically identified in the SDSS DR6 catalogue. Ivezić et al. (2002) have performed this investigation but only for FIRST radio sources identified in the SDSS DR1 data, but with the SDSS DR6 the survey volume has doubled. We will develop sophisticated techniques to discriminate between stars and galaxies. We also plan to discriminate between AGN and star-forming radio galaxies which will allows us to determine the fraction of each population that comprise the faint radio population, taking advantage of the large area covered spectroscopically by SDSS DR6. It will also be important to study the dependence of galaxy clustering as a function of other galaxy properties such as colour. With several galaxy colours it will be possible to probe the nature of the relative clustering bias between different types of galaxies, and with a large volume, there will be high signal-to-noise to perform robust clustering statistics and modelling.

Clustering statistics of the AGN and star-forming radio galaxies will be studied in full detail. With the large volume probed by the SDSS DR7 survey, identification of FIRST radio sources in the SDSS DR7 will yield spectra and redshifts for a large number of FIRST radio sources over the redshift range $0 < z < 0.7$, and this will allow a detailed study of the clustering evolution over this redshift range of all FIRST radio sources identified in the SDSS DR7 as

well as for AGN and star-forming galaxies. Magliocchetti et al. (2004) have studied the clustering statistics of FIRST radio sources identified as AGN in the 2dFGRS survey for only 826 sources. Clustering statistics of other populations e.g., early and late type galaxies or luminous red galaxies will be interesting. It will be also interesting to investigate the clustering measurements of FIRST radio sources unidentified in the SDSS DR7 imaging and spectroscopic data in comparison to the clustering measurement of the optically identified ones as the former set of sources are likely to be at high redshift or comprise a fainter class of optical sources.

In the last part of this thesis we presented a study of the spectral energy distribution of radio sources in a large sample of nearby X-ray selected galaxy clusters at $z < 0.25$. For 139 sources selected at 1.4 GHz and spectroscopically confirmed to be members of the clusters, the VLA was used to measure the fluxes at 4.9, 8.5, 22, and 43 GHz (C, X, K, and Q bands) nearly simultaneously, and determine the distribution of the spectral energy distribution (SED). Sources with extended morphology may be resolved out at high frequencies due to the higher angular resolution of interferometer, making the determination of the spectral shape nontrivial. We downgraded the resolution of our 43 GHz images to match the resolution at 22 GHz, thus enabling reliable comparisons of fluxes at these two frequencies; it was more difficult to match the resolution between the other frequency intervals, and therefore our measurements of the spectral indices involving the two lower frequencies e.g., between 8.5 and 22 GHz, are *lower* limits. The flux measurement of point-like (or barely resolved) sources, or "cores" embedded in extended sources, on the other hand, was more straightforward.

For $\sim$ 70 core/point-like sources that were detected in at least three frequencies, we studied the distribution of the spectral shape via the "two-colour" diagram, and found that the spectral shape cannot be described by simple power-laws for the bulk of the sources. About 60% of sources have $\alpha_{KQ} > \alpha_{CX}$, indicating a flattening of the spectral shape above 8 GHz or so, and only one third of the sources have steep spectra from 4.9 to 43 GHz. The spectral index distribution was determined using survival statistics that take non-detections (upper limits) into account. The compact sources are found to have "flatter" spectral shape than the extended sources.

It was found that the spectral indices do not correlate with properties of host galaxies or clusters, such as the colour and luminosity of the galaxies, the radio luminosity at 1.4 GHz, the

distance of the host galaxy to the cluster centre, and the mass of the host clusters. This result agrees with previous studies, and suggests that the radio emission may be dominated by the small scale physics of the nucleus, rather than by the cluster environment.

In an attempt to estimate the contamination of the SZE signal due to radio point sources in cluster surveys, we made use of the spectral index distributions in several frequency bands to extrapolate the well-measured Radio Luminosity Function (RLF) at 1.4 GHz to the frequencies employed by several on-going radio/millimeter wave experiments. As the extrapolation depends on the Spectral Index Distributions (SIDs) employed, we bracketed the possible range of the predicted RLFs by using SIDs in intermediate frequency bands e.g., $8-20$ GHz, that are known to be biased in opposite ways. The amplitude of the resulting RLFs at $\nu \geq 30$ GHz is in general $3-10$ times lower compared to the 1.4 GHz amplitude. Under the assumption that the RLF follows a pure density evolution with redshift of the form $\phi(z) \propto \phi(z=0)(1+z)^{\gamma}$, such that the abundance of sources at $z = 1$ is 5 times the local value, we found that the fraction of clusters that may be seriously affected by point sources is small; at the cluster mass scales close to the detection limits of the on-going surveys e.g., $2-3\times10^{14}M_{\odot}$, and at the redshift where we expect the experiments to detect most of the clusters i.e., $z \sim 0.6$, less than 8% of the clusters will be contaminated at the 20% level or above, that is, the total fluxes from AGNs are at least 20% of the SZE flux.

There are two aspects that need to be improved for a better forecast within our analysis framework. Currently, the largest uncertainty in our modelling is the redshift evolution of cluster radio galaxies. If not properly accounted for, any unexpected evolution of the radio sources may be misinterpreted as changes in the cluster mass function, and cause errors in the determination of the properties of the dark energy. This could be investigated further through a survey of cluster radio galaxies at intermediate redshift ($0.3 \leq z \leq 1.0$). In addition, in our forecast, it is implicitly assumed that the number of radio galaxies (N_{RG}) a cluster can host is proportional to the cluster mass (M_{200}). If, instead, $N_{RG} \propto M_{200}^{s}$ with $s < 1$, we would overestimate the AGN contribution in high mass clusters. To check this assumption, one needs to determine the halo occupation distribution for radio galaxies. To this end, we have attempted to construct the halo occupation distribution of radio galaxies, using a large sample of radio galaxies in the local Universe (Lin et al. in preparation).

APPENDIX A

Appendix 1

The radio data table

The total number of FIRST radio sources identified in Boötes field is 688, and 119 FIRST radio sources are identified in Cetus field. Table A.1 lists only 206 radio counterparts (with best photometric redshift) that are identified in four bands (Bw, R, I, K) and used for the $K - z$ relation in Boötes field. The columns of Table A.1 are as follows:

1. The NDWFS name, set by the J2000 coordinates of each galaxy.
2. The total 1.4 GHz flux density from the FIRST catalogue.
3. The Bw apparent magnitude from the NDWFS photometry.
4. The R apparent magnitude from the NDWFS photometry.
5. The I apparent magnitude from the NDWFS photometry.
6. The K apparent magnitude from the NDWFS photometry.
7. The derived photometric redshift and the corresponding 68% percentile errors.
8. The confidence of the best fit given by χ^2.

Table A.1: List of the FIRST radio sources optically identified in four bands (Bw, R, I, K) in Boötes field. Column 1 lists the name of the optical counterparts in NDWFS survey and column 2 indicates the 1.4 GHz flux densities. Columns 3-6 list the Bw, R, I, K - band magnitudes (Vega system). The derived photometric redshift is displayed in column 7 (and the corresponding 68% percentile errors). The last column provides the confidence of the best fit given by χ^2.

Object name	$S_{1.4}$ (mJy)	*B*w	*R*	*I*	*K*	Photo_z	χ^2	Class
NDWFS_J142439.6+3349	2.71	25.32	23.41	21.88	17.97	$0.875^{+0.082}_{-0.107}$	0.04	E
NDWFS_J142449.3+3343	2.02	26.36	25.16	24.28	19.27	$1.490^{+0.422}_{-0.166}$	0.14	E
NDWFS_J142525.2+3345	4.66	23.73	22.51	21.34	17.49	$1.300^{+0.072}_{-0.013}$	0.05	Burst
NDWFS_J142532.8+3301	7.33	20.89	20.34	20.07	17.69	$0.455^{+0.079}_{-0.131}$	0.33	Burst
NDWFS_J142536.6+3316	1.46	23.10	20.20	19.27	16.64	$0.455^{+0.048}_{-0.117}$	0.01	Burst
NDWFS_J142543.9+3355	298.44	23.05	22.61	21.46	19.59	$1.030^{+0.017}_{-0.043}$	1.34	Burst
NDWFS_J142544.9+3337	1.45	22.21	19.93	19.18	16.54	$0.300^{+0.065}_{-0.300}$	0.08	E
NDWFS_J142611.0+3339	1.70	24.72	23.35	21.81	18.05	$0.880^{+0.084}_{-0.032}$	0.44	S0
NDWFS_J142616.8+3309	1.09	25.52	23.91	23.06	18.46	$1.780^{+0.075}_{-0.067}$	0.83	Burst
NDWFS_J142624.2+3346	3.44	24.04	23.08	22.39	18.32	$1.370^{+0.292}_{-0.073}$	0.47	S0
NDWFS_J142632.4+3346	1.67	22.53	21.26	19.92	16.65	$0.860^{+0.048}_{-0.065}$	0.60	E
NDWFS_J142633.6+3332	4.97	19.87	19.17	19.06	17.32	$0.300^{+0.164}_{-0.070}$	0.84	E
NDWFS_J142643.3+3351	2.86	25.97	24.27	22.73	18.48	$1.055^{+0.023}_{-0.101}$	0.04	E
NDWFS_J142652.1+3300	1.24	24.48	21.31	19.87	16.51	$0.650^{+0.010}_{-0.015}$	0.10	E
NDWFS_J142658.8+3333	2.34	19.45	17.79	17.01	14.17	$0.510^{+0.053}_{-0.102}$	0.03	Sa
NDWFS_J142701.6+3305	18.38	23.15	19.93	18.88	16.16	$0.495^{+0.105}_{-0.066}$	0.03	Burst
NDWFS_J142703.3+3326	1.70	22.71	22.03	21.29	17.99	$1.280^{+0.067}_{-0.046}$	0.03	Sa
NDWFS_J142707.9+3327	1.07	25.51	21.85	20.17	16.87	$0.860^{+0.032}_{-0.059}$	1.63	Burst
NDWFS_J142708.9+3341	1.24	23.25	20.51	19.34	16.51	$0.665^{+0.010}_{-0.027}$	0.36	Burst
NDWFS_J142734.3+3357	4.54	20.63	18.30	17.54	14.74	$0.210^{+0.099}_{-0.092}$	0.08	E
NDWFS_J142743.4+3313	4.63	22.40	19.58	18.55	15.64	$0.645^{+0.008}_{-0.011}$	0.31	Burst
NDWFS_J142753.5+3340	1.10	20.27	18.11	17.36	14.74	$0.150^{+0.222}_{-0.150}$	0.01	E
NDWFS_J142753.6+3310	1.65	23.47	21.76	20.53	17.08	$0.710^{+0.047}_{-0.029}$	0.13	Sa
NDWFS_J142755.9+3321	16.74	25.61	25.29	24.95	19.99	$1.845^{+0.002}_{-0.050}$	1.30	E
NDWFS_J142813.4+3307	2.14	19.30	16.87	16.14	13.78	$0.345^{+0.026}_{-0.083}$	0.04	Burst
NDWFS_J142822.9+3318	2.24	22.82	19.75	18.75	16.10	$0.545^{+0.027}_{-0.145}$	0.01	Burst
NDWFS_J142847.1+3323	2.35	16.74	15.13	14.47	12.24	$0.055^{+0.121}_{-0.055}$	0.02	S0
NDWFS_J142901.8+3302	2.09	25.54	21.64	20.15	16.76	$0.750^{+0.213}_{-0.096}$	0.06	Burst
NDWFS_J142902.4+3333	4.70	21.04	18.29	17.52	14.92	$0.250^{+0.160}_{-0.097}$	0.02	E
NDWFS_J142906.7+3348	16.23	23.60	23.23	22.73	19.14	$1.715^{+0.179}_{-0.133}$	0.00	Sa
NDWFS_J142910.3+3358	2.24	25.96	24.64	23.60	18.92	$1.255^{+0.076}_{-0.067}$	0.29	E
NDWFS_J142911.7+3331	51.14	23.75	22.13	20.99	18.25	$0.790^{+0.025}_{-0.020}$	0.06	Burst
NDWFS_J142915.2+3303	1.79	27.62	24.81	23.21	17.44	$1.915^{+0.508}_{-0.025}$	2.03	Burst
NDWFS_J142916.1+3355	2.07	24.18	22.48	20.85	17.44	$1.035^{+0.067}_{-0.011}$	0.06	Burst
NDWFS_J142929.8+3302	4.96	23.38	19.68	18.47	15.49	$0.555^{+0.037}_{-0.014}$	0.10	Burst
NDWFS_J142940.7+3305	2.83	24.32	23.24	22.51	18.56	$1.755^{+0.063}_{-0.120}$	0.47	Burst
NDWFS_J142942.6+3356	3.64	19.24	18.58	18.43	16.51	$0.455^{+0.046}_{-0.163}$	1.03	Burst
NDWFS_J142944.5+3311	3.76	22.44	20.72	19.58	16.67	$0.655^{+0.015}_{-0.053}$	0.61	S0

Table A.1: continued...

Object name	$S_{1.4}$ (mJy)	Bw	R	I	K	Photo_z	χ^2	Class
NDWFS_J143002.6+3317	4.56	22.02	19.25	18.37	15.76	$0.395^{+0.064}_{-0.101}$	0.03	Burst
NDWFS_J143004.7+3302	3.18	25.28	23.36	22.02	17.75	$1.350^{+0.028}_{-0.042}$	0.09	Burst
NDWFS_J143008.2+3315	7.28	22.85	19.88	18.83	16.01	$0.620^{+0.012}_{-0.014}$	0.32	Burst
NDWFS_J143023.1+3344	3.28	23.38	20.36	19.21	16.20	$0.515^{+0.008}_{-0.023}$	0.00	E
NDWFS_J143029.7+3335	2.05	21.60	18.90	18.05	15.39	$0.345^{+0.046}_{-0.260}$	0.01	Burst
NDWFS_J143035.8+3342	1.92	24.07	21.35	20.34	17.00	$0.395^{+0.068}_{-0.064}$	0.09	E
NDWFS_J143051.6+3303	1.49	23.47	23.04	22.34	19.54	$1.210^{+0.069}_{-0.074}$	0.01	Irr
NDWFS_J143103.4+3345	3.62	19.29	16.72	15.94	13.39	$0.300^{+0.064}_{-0.226}$	0.04	Burst
NDWFS_J143104.4+3348	1.57	23.27	20.05	18.71	15.67	$0.930^{+0.020}_{-0.020}$	0.35	Burst
NDWFS_J143109.9+3353	27.04	23.88	21.63	20.43	17.48	$0.690^{+0.021}_{-0.010}$	0.31	E
NDWFS_J143115.3+3346	1.04	19.52	17.76	16.99	14.42	$0.055^{+0.104}_{-0.055}$	0.05	Sb
NDWFS_J143138.3+3328	7.19	22.67	21.13	19.86	16.81	$0.745^{+0.019}_{-0.016}$	0.63	E
NDWFS_J143138.4+3322	4.75	24.30	22.88	22.04	18.20	$1.795^{+0.024}_{-0.023}$	0.24	Burst
NDWFS_J143149.1+3309	2.01	21.47	20.86	20.57	19.38	$2.245^{+0.637}_{-0.049}$	0.28	E
NDWFS_J143152.9+3308	1.64	19.95	17.32	16.58	14.13	$0.390^{+0.032}_{-0.060}$	0.09	Burst
NDWFS_J143208.7+3357	5.01	24.20	20.46	19.18	16.00	$0.600^{+0.070}_{-0.087}$	0.08	Burst
NDWFS_J143209.1+3356	1.93	25.53	22.38	20.95	17.28	$0.615^{+0.010}_{-0.021}$	0.13	E
NDWFS_J143216.6+3343	2.81	21.97	19.96	19.04	15.75	$0.510^{+0.030}_{-0.031}$	0.10	Sb
NDWFS_J143220.1+3358	2.09	23.78	22.99	22.05	19.06	$1.050^{+0.073}_{-0.046}$	0.07	E
NDWFS_J143231.9+3312	2.74	21.34	18.40	17.58	14.87	$0.300^{+0.064}_{-0.040}$	0.01	Burst
NDWFS_J143234.9+3328	2.29	19.93	17.80	17.15	14.91	$0.105^{+0.119}_{-0.105}$	0.03	Burst
NDWFS_J143245.4+3301	9.56	22.51	21.78	21.25	18.59	$0.240^{+0.424}_{-0.102}$	0.02	Burst
NDWFS_J143309.3+3336	6.12	22.14	18.94	17.88	15.15	$0.555^{+0.057}_{-0.122}$	0.09	Burst
NDWFS_J143311.0+3358	22.72	21.31	19.00	18.03	15.37	$0.675^{+0.010}_{-0.028}$	0.71	Burst
NDWFS_J143315.7+3328	5.81	23.40	22.62	21.87	18.09	$1.360^{+0.188}_{-0.063}$	0.01	Sd
NDWFS_J143321.0+3345	4.47	23.61	22.89	22.27	18.08	$1.860^{+0.126}_{-0.229}$	0.09	E
NDWFS_J143330.2+3304	1.19	24.68	23.45	22.30	18.74	$1.300^{+0.031}_{-0.038}$	0.20	Burst
NDWFS_J143355.7+3333	1.95	23.54	21.87	21.05	18.01	$0.550^{+0.026}_{-0.052}$	0.11	Sc
NDWFS_J143356.5+3330	1.18	21.32	18.08	17.19	14.56	$0.455^{+0.009}_{-0.021}$	1.37	Burst
NDWFS_J143406.1+3338	1.08	23.49	20.25	19.09	16.15	$0.545^{+0.056}_{-0.052}$	0.12	Burst
NDWFS_J143418.5+3314	1.73	19.68	17.38	16.61	14.07	$0.100^{+0.151}_{-0.100}$	0.03	Burst
NDWFS_J143435.1+3343	5.62	25.21	22.94	21.46	17.73	$1.205^{+0.014}_{-0.017}$	0.05	Burst
NDWFS_J143445.3+3328	30.03	18.90	16.90	16.18	13.59	$0.200^{+0.186}_{-0.135}$	0.02	S0
NDWFS_J143446.5+3324	12.39	19.44	17.41	16.70	14.20	$0.200^{+0.048}_{-0.200}$	0.04	S0
NDWFS_J143506.2+3331	1.36	23.12	19.79	18.67	15.76	$0.545^{+0.066}_{-0.103}$	0.03	Burst
NDWFS_J143508.5+3305	1.46	23.99	22.26	20.97	17.71	$0.735^{+0.046}_{-0.041}$	0.13	E
NDWFS_J143510.2+3354	32.88	23.85	23.13	22.32	19.12	$1.210^{+0.064}_{-0.064}$	0.00	E
NDWFS_J143513.3+3331	2.15	23.94	21.86	20.56	17.79	$0.760^{+0.022}_{-0.013}$	0.43	Burst
NDWFS_J143514.9+3321	3.48	22.35	20.02	18.64	16.28	$0.785^{+0.028}_{-0.009}$	1.01	Burst

Table A.1: continued...

Object name	$S_{1.4}$ (mJy)	Bw	R	I	K	Photo_z	χ^2	Class
NDWFS_J143518.8+3313	1.86	25.28	21.40	20.07	16.51	$0.555^{+0.091}_{-0.095}$	0.04	Burst
NDWFS_J143527.3+3312	1.30	20.13	19.55	19.06	17.41	$0.655^{+0.046}_{-0.057}$	0.07	Burst
NDWFS_J143527.9+3311	39.60	24.89	24.10	22.93	17.45	$1.700^{+0.102}_{-0.105}$	0.74	E
NDWFS_J143528.4+3319	23.27	19.01	18.83	18.73	16.98	$0.455^{+0.074}_{-0.221}$	0.26	Irr
NDWFS_J143540.9+3311	2.65	21.77	20.09	19.18	16.66	$0.690^{+0.018}_{-0.020}$	0.12	Burst
NDWFS_J143541.2+3342	1.46	23.65	21.76	20.33	17.26	$1.185^{+0.015}_{-0.032}$	0.22	Burst
NDWFS_J143608.5+3353	4.46	19.63	17.40	16.69	14.48	$0.100^{+0.110}_{-0.100}$	0.09	E
NDWFS_J143651.3+3339	1.88	20.44	20.10	19.82	18.35	$0.115^{+0.028}_{-0.115}$	0.00	Burst
NDWFS_J143707.2+3351	1.01	21.96	19.86	18.84	16.05	$0.530^{+0.052}_{-0.028}$	0.00	S0
NDWFS_J143825.6+3349	1.84	24.51	22.74	21.34	17.63	$0.985^{+0.018}_{-0.014}$	0.19	E
NDWFS_J143831.6+3356	8.25	24.59	21.64	20.26	16.98	$0.670^{+0.023}_{-0.016}$	0.38	E
NDWFS_J143842.0+3358	58.95	24.74	23.36	23.29	20.24	$2.305^{+0.186}_{-0.119}$	0.13	Burst
NDWFS_J143843.9+3354	1.13	25.81	24.52	23.88	19.52	$2.430^{+0.327}_{-0.800}$	0.03	E
NDWFS_J142445.7+3418	78.26	22.63	21.38	20.25	17.30	$0.745^{+0.077}_{-0.050}$	0.03	S0
NDWFS_J142449.3+3409	4.53	19.94	19.57	19.28	16.70	$0.535^{+0.049}_{-0.154}$	0.78	Burst
NDWFS_J142458.2+3424	1.74	22.82	20.15	19.23	16.33	$0.345^{+0.113}_{-0.049}$	0.06	E
NDWFS_J142516.5+3452	63.21	22.08	21.06	20.53	18.05	$0.205^{+0.380}_{-0.205}$	0.01	Burst
NDWFS_J142524.2+3409	15.29	20.13	19.68	19.38	17.27	$0.300^{+0.275}_{-0.155}$	0.00	E
NDWFS_J142533.5+3458	2.97	22.43	21.30	20.20	17.97	$0.845^{+0.038}_{-0.028}$	0.03	Burst
NDWFS_J142533.5+3403	3.76	22.86	19.98	18.97	16.19	$0.455^{+0.044}_{-0.057}$	0.34	E
NDWFS_J142601.9+3431	3.14	21.26	20.98	20.82	18.23	$1.415^{+0.210}_{-0.120}$	0.39	Burst
NDWFS_J142616.7+3428	1.55	20.30	18.67	18.05	16.00	$0.605^{+0.013}_{-0.019}$	0.08	Burst
NDWFS_J142623.3+3434	1.51	23.94	21.92	20.55	17.93	$0.835^{+0.026}_{-0.025}$	0.02	E
NDWFS_J142639.7+3443	3.97	22.86	19.55	18.52	15.92	$0.590^{+0.018}_{-0.029}$	1.73	Burst
NDWFS_J142702.3+3459	14.10	23.12	21.40	20.49	18.21	$0.680^{+0.023}_{-0.031}$	0.08	Burst
NDWFS_J142729.7+3411	1.17	24.43	22.78	21.36	18.42	$0.880^{+0.230}_{-0.074}$	0.03	Burst
NDWFS_J142731.9+3452	2.33	24.66	21.26	19.91	17.22	$0.725^{+0.077}_{-0.063}$	0.61	Burst
NDWFS_J142750.4+3441	1.62	22.19	20.60	19.64	17.29	$0.710^{+0.033}_{-0.017}$	0.24	Burst
NDWFS_J142758.7+3459	7.01	24.54	22.01	20.82	17.20	$0.550^{+0.047}_{-0.034}$	0.22	S0
NDWFS_J142759.6+3454	1.46	19.76	17.39	16.68	14.64	$0.150^{+0.227}_{-0.150}$	0.05	E
NDWFS_J142809.7+3405	2.00	22.61	19.66	18.81	16.35	$0.505^{+0.050}_{-0.020}$	0.55	Burst
NDWFS_J142811.0+3441	2.09	25.50	21.94	20.42	17.14	$0.840^{+0.083}_{-0.065}$	0.13	Burst
NDWFS_J142817.9+3452	1.60	22.69	21.16	20.29	16.85	$0.645^{+0.021}_{-0.046}$	1.85	Irr
NDWFS_J142825.4+3455	10.83	22.69	20.25	19.41	16.29	$0.300^{+0.025}_{-0.115}$	0.09	E
NDWFS_J142826.1+3405	1.37	23.35	19.70	18.58	15.69	$0.555^{+0.025}_{-0.021}$	0.55	Burst
NDWFS_J142849.7+3432	2.62	19.72	17.63	16.81	14.08	$0.095^{+0.069}_{-0.095}$	0.03	Sa
NDWFS_J142852.1+3452	4.11	21.54	20.84	19.93	17.03	$1.050^{+0.057}_{-0.051}$	0.01	Irr
NDWFS_J142905.6+3449	31.42	23.98	22.64	21.56	17.59	$1.355^{+0.238}_{-0.038}$	0.22	Burst
NDWFS_J142906.3+3433	2.59	21.33	18.51	17.66	15.30	$0.515^{+0.013}_{-0.014}$	0.05	Burst

Table A.1: continued...

Object name	$S_{1.4}$ (mJy)	Bw	R	I	K	Photo_z	χ^2	Class
NDWFS_J142929.7+3441	4.32	22.06	19.04	18.19	15.50	$0.490^{+0.021}_{-0.020}$	0.20	Burst
NDWFS_J142937.5+3441	10.97	24.48	22.38	21.11	18.04	$0.750^{+0.054}_{-0.041}$	0.14	E
NDWFS_J142938.0+3439	2.90	21.78	19.61	18.93	16.33	$0.530^{+0.025}_{-0.035}$	0.09	Burst
NDWFS_J143022.0+3449	1.59	19.63	17.16	16.43	14.17	$0.380^{+0.012}_{-0.016}$	0.37	Burst
NDWFS_J143104.1+3421	1.01	24.18	21.51	20.48	17.62	$0.485^{+0.033}_{-0.145}$	0.01	E
NDWFS_J143113.0+3450	4.09	24.41	21.47	20.20	17.44	$0.750^{+0.020}_{-0.066}$	0.15	Burst
NDWFS_J143114.1+3436	17.23	23.30	20.04	19.01	16.37	$0.555^{+0.052}_{-0.053}$	0.70	Burst
NDWFS_J143121.8+3440	1.40	21.23	19.03	18.36	15.48	$0.250^{+0.069}_{-0.094}$	0.65	Sa
NDWFS_J143125.7+3430	1.68	25.21	23.05	21.51	18.09	$1.125^{+0.074}_{-0.096}$	0.09	Burst
NDWFS_J143126.5+3448	1.11	24.60	21.36	19.94	16.73	$0.725^{+0.216}_{-0.047}$	0.10	E
NDWFS_J143131.1+3427	1.19	19.99	17.56	16.77	14.65	$0.430^{+0.011}_{-0.013}$	1.21	Burst
NDWFS_J143154.4+3436	1.33	25.20	22.74	21.35	18.31	$0.785^{+0.037}_{-0.019}$	0.15	Burst
NDWFS_J143214.3+3426	17.75	22.72	20.05	19.12	16.59	$0.405^{+0.100}_{-0.060}$	0.53	E
NDWFS_J143232.4+3445	5.33	21.86	19.25	18.53	16.04	$0.195^{+0.220}_{-0.061}$	0.00	Burst
NDWFS_J143239.1+3442	4.08	24.33	20.89	19.91	17.07	$0.450^{+0.041}_{-0.012}$	0.69	Burst
NDWFS_J143259.2+3406	1.14	26.77	25.56	23.76	19.00	$1.125^{+0.223}_{-0.079}$	0.41	E
NDWFS_J143318.2+3420	1.25	20.34	17.92	17.14	14.80	$0.350^{+0.027}_{-0.079}$	0.26	Burst
NDWFS_J143319.3+3423	2.58	22.96	19.94	18.96	16.08	$0.445^{+0.107}_{-0.127}$	0.04	Burst
NDWFS_J143322.7+3435	8.08	22.45	19.42	18.40	15.82	$0.610^{+0.020}_{-0.114}$	0.20	Burst
NDWFS_J143332.7+3402	1.24	23.40	20.01	18.80	15.88	$0.555^{+0.070}_{-0.039}$	0.01	E
NDWFS_J143332.8+3403	2.67	24.97	23.26	22.21	18.72	$0.645^{+0.073}_{-0.096}$	0.06	Sb
NDWFS_J143333.1+3421	3.34	24.32	21.00	19.80	16.93	$0.650^{+0.023}_{-0.092}$	0.03	Burst
NDWFS_J143351.7+3455	1.88	21.06	18.04	17.24	14.74	$0.505^{+0.017}_{-0.013}$	1.28	Burst
NDWFS_J143404.5+3420	5.11	25.48	22.36	20.97	17.50	$1.070^{+0.043}_{-0.061}$	0.06	Burst
NDWFS_J143410.3+3423	3.18	22.75	20.13	19.29	16.70	$0.345^{+0.064}_{-0.094}$	0.09	Burst
NDWFS_J143411.2+3445	1.30	21.40	18.72	17.78	15.05	$0.605^{+0.010}_{-0.013}$	0.03	Burst
NDWFS_J143413.8+3455	2.60	23.17	20.42	19.43	16.88	$0.620^{+0.020}_{-0.028}$	0.13	Burst
NDWFS_J143430.5+3427	1.50	24.30	23.81	22.48	18.00	$1.430^{+0.068}_{-0.046}$	1.23	E
NDWFS_J143449.3+3410	1.51	23.55	21.47	20.69	17.27	$0.425^{+0.054}_{-0.106}$	0.88	Sb
NDWFS_J143450.1+3409	3.61	21.46	18.91	18.23	15.78	$0.355^{+0.048}_{-0.228}$	0.06	Burst
NDWFS_J143453.5+3436	24.99	24.13	22.79	21.55	18.26	$0.830^{+0.060}_{-0.081}$	0.00	E
NDWFS_J143529.2+3434	43.27	24.15	20.74	19.87	17.18	$0.450^{+0.023}_{-0.019}$	2.62	Burst
NDWFS_J143539.8+3443	23.22	26.21	22.40	20.67	16.66	$0.780^{+0.040}_{-0.040}$	0.21	E
NDWFS_J143658.0+3440	1.86	23.39	20.31	19.24	15.96	$0.350^{+0.081}_{-0.052}$	0.08	E
NDWFS_J143703.3+3435	3.99	23.12	20.18	19.11	16.66	$0.615^{+0.012}_{-0.032}$	0.01	Burst
NDWFS_J143707.0+3418	1.20	17.56	15.32	14.60	12.50	$0.100^{+0.110}_{-0.031}$	1.10	E
NDWFS_J143715.3+3406	4.48	21.29	19.19	18.29	15.81	$0.650^{+0.010}_{-0.016}$	0.38	Burst
NDWFS_J143805.5+3427	1.84	22.92	22.04	21.38	18.80	$0.665^{+0.060}_{-0.061}$	0.02	Burst
NDWFS_J142438.4+3544	1.72	24.85	21.11	19.70	16.72	$0.680^{+0.038}_{-0.023}$	0.20	Burst

Table A.1: continued...

Object name	$S_{1.4}$ (mJy)	Bw	R	I	K	Photo_z	χ^2	Class
NDWFS_J142440.4+3511	1.06	24.03	23.09	22.27	16.98	$1.850^{+0.110}_{-0.101}$	0.09	E
NDWFS_J142456.3+3528	11.62	21.38	20.54	19.79	17.58	$0.655^{+0.138}_{-0.049}$	0.02	Sc
NDWFS_J142522.2+3522	1.17	25.44	21.80	20.20	16.94	$0.855^{+0.059}_{-0.067}$	0.80	Burst
NDWFS_J142531.7+3533	8.13	23.97	20.24	18.94	16.14	$0.595^{+0.022}_{-0.015}$	0.73	Burst
NDWFS_J142534.5+3535	1.24	24.23	20.63	19.26	16.34	$0.730^{+0.074}_{-0.021}$	0.25	Burst
NDWFS_J142604.9+3545	1.26	23.83	20.35	18.74	15.73	$0.840^{+0.022}_{-0.016}$	2.07	Burst
NDWFS_J142610.9+3542	2.17	23.39	20.80	19.48	16.50	$0.740^{+0.020}_{-0.018}$	0.14	Burst
NDWFS_J142620.3+3537	6.02	19.97	17.49	16.73	14.31	$0.150^{+0.242}_{-0.064}$	0.13	Burst
NDWFS_J142628.3+3510	1.45	22.21	19.41	18.54	16.09	$0.510^{+0.015}_{-0.047}$	0.04	Burst
NDWFS_J142632.1+3508	95.31	24.03	23.00	21.90	18.14	$1.050^{+0.106}_{-0.063}$	0.21	Sc
NDWFS_J142639.3+3510	2.56	25.96	23.36	21.80	18.18	$0.850^{+0.092}_{-0.151}$	0.09	E
NDWFS_J142649.0+3522	1.33	24.01	20.28	19.10	16.21	$0.590^{+0.007}_{-0.022}$	0.42	Burst
NDWFS_J142651.4+3519	3.96	19.55	18.88	18.31	16.93	$0.680^{+0.036}_{-0.036}$	0.29	Burst
NDWFS_J142653.8+3512	1.75	19.10	17.28	16.58	14.39	$0.055^{+0.048}_{-0.055}$	0.16	E
NDWFS_J142711.7+3500	2.30	23.81	20.73	19.44	16.42	$0.695^{+0.017}_{-0.017}$	0.03	Burst
NDWFS_J142714.8+3500	2.14	22.84	20.23	19.08	16.35	$0.675^{+0.013}_{-0.022}$	0.45	Burst
NDWFS_J142716.7+3517	2.88	24.21	22.14	21.05	17.79	$0.555^{+0.055}_{-0.033}$	0.09	Sa
NDWFS_J142752.2+3530	2.28	21.04	20.29	20.05	18.09	$0.300^{+0.211}_{-0.221}$	0.11	E
NDWFS_J142804.5+3521	2.26	22.43	19.22	18.30	15.61	$0.455^{+0.011}_{-0.027}$	0.78	Burst
NDWFS_J142805.2+3535	1.21	23.43	21.81	20.77	17.28	$0.660^{+0.036}_{-0.040}$	0.30	Sb
NDWFS_J142810.3+3538	1.01	19.10	18.52	18.27	16.42	$0.345^{+0.192}_{-0.185}$	0.05	Irr
NDWFS_J142828.9+3513	2.19	21.71	18.68	17.80	15.20	$0.545^{+0.014}_{-0.035}$	0.45	Burst
NDWFS_J142839.7+3542	1.56	25.37	23.18	22.96	18.30	$2.240^{+0.054}_{-0.112}$	1.62	Burst
NDWFS_J142842.5+3543	20.48	23.39	20.91	19.88	17.41	$0.655^{+0.040}_{-0.020}$	0.16	Burst
NDWFS_J142904.2+3538	1.43	19.66	17.10	16.59	14.03	$0.340^{+0.124}_{-0.011}$	0.65	Burst
NDWFS_J142943.6+3541	1.45	23.67	21.96	20.77	18.04	$0.700^{+0.024}_{-0.020}$	0.11	E
NDWFS_J143004.0+3505	1.13	22.29	19.71	18.87	15.72	$0.250^{+0.150}_{-0.060}$	0.20	S0
NDWFS_J143011.5+3500	4.66	19.74	19.34	18.90	17.33	$0.680^{+0.101}_{-0.079}$	0.01	Burst
NDWFS_J143059.8+3522	1.43	24.24	20.32	18.96	15.99	$0.645^{+0.027}_{-0.033}$	0.05	Burst
NDWFS_J143108.3+3525	2.07	24.93	22.71	21.30	17.34	$1.335^{+0.084}_{-0.065}$	0.07	Burst
NDWFS_J143112.4+3543	2.26	23.62	21.85	20.64	17.69	$0.730^{+0.051}_{-0.087}$	0.22	E
NDWFS_J143112.5+3535	9.64	26.64	23.10	21.50	17.01	$1.405^{+0.042}_{-0.361}$	0.02	Burst
NDWFS_J143142.6+3512	1.20	25.67	21.45	20.18	16.51	$0.450^{+0.114}_{-0.057}$	0.26	Burst
NDWFS_J143143.5+3535	4.82	17.37	15.31	14.57	12.58	$0.100^{+0.021}_{-0.100}$	1.24	Burst
NDWFS_J143213.5+3509	16.26	24.48	22.61	21.14	17.98	$0.840^{+0.210}_{-0.035}$	0.18	E
NDWFS_J143224.6+3535	6.99	25.70	23.95	23.47	19.14	$2.160^{+0.145}_{-0.124}$	0.10	Burst
NDWFS_J143227.2+3514	1.08	19.31	17.53	16.87	14.37	$0.390^{+0.069}_{-0.390}$	0.09	S0
NDWFS_J143230.2+3536	2.51	22.92	22.24	21.90	18.14	$2.175^{+0.269}_{-0.132}$	0.08	Sa
NDWFS_J143239.5+3501	13.29	19.44	18.15	17.43	15.26	$0.550^{+0.032}_{-0.026}$	0.53	E

Table A.1: continued...

Object name	$S_{1.4}$ (mJy)	*B*w	*R*	*I*	*K*	Photo_z	χ^2	Class
NDWFS_J143246.7+3533	2.18	25.12	23.41	22.49	18.13	$1.825^{+0.047}_{-0.072}$	0.05	Burst
NDWFS_J143308.0+3531	2.33	22.42	20.85	19.84	17.02	$0.660^{+0.015}_{-0.078}$	0.13	E
NDWFS_J143339.3+3540	3.11	23.71	20.63	19.54	16.86	$0.595^{+0.048}_{-0.069}$	0.02	Burst
NDWFS_J143404.3+3502	1.83	25.36	21.20	19.88	16.71	$0.645^{+0.038}_{-0.032}$	0.30	Burst
NDWFS_J143406.2+3540	1.27	19.20	16.90	16.15	13.90	$0.100^{+0.086}_{-0.035}$	0.22	Burst
NDWFS_J143422.0+3525	7.74	24.43	21.24	19.76	16.56	$0.765^{+0.025}_{-0.035}$	0.06	E
NDWFS_J143434.2+3510	67.51	22.17	19.90	18.90	15.98	$0.520^{+0.023}_{-0.071}$	0.00	E
NDWFS_J143456.0+3529	2.79	24.19	23.06	22.14	18.08	$1.635^{+0.084}_{-0.243}$	0.09	Burst
NDWFS_J143619.4+3501	5.74	23.80	21.62	20.25	17.92	$0.870^{+0.045}_{-0.037}$	0.09	Burst
NDWFS_J143713.6+3505	59.62	19.65	19.33	19.15	17.25	$0.500^{+0.057}_{-0.294}$	0.22	Burst
NDWFS_J143723.7+3507	100.05	22.63	20.97	20.16	17.43	$0.515^{+0.077}_{-0.065}$	0.08	Sa
NDWFS_J143746.1+3506	3.81	23.36	20.41	19.35	16.54	$0.610^{+0.010}_{-0.027}$	0.08	Burst

APPENDIX B

Appendix 2

Matching procedure

The cross correlation between the FIRST and SDSS catalogues was performed using SQL (Structured Query Language) in the SDSS database (Cas Jobs). The query written in the language SQL is given as follow:

```
SELECT
p.objID,
str(p.ra,12,8) as RA,
str(p.dec,12,8) as Dec,
str(p.modelMag_u,9,6) as modelMag_u,
str(p.modelMag_g,9,6) as modelMag_g,
str(p.modelMag_r,9,6) as modelMag_r,
str(p.modelMag_i,9,6) as modelMag_i,
str(p.modelMag_z,9,6) as modelMag_z,
```

```
str(p.modelMagErr_u,9,6) as modelMagErr_u,
str(p.modelMagErr_g,9,6) as modelMagErr_g,
str(p.modelMagErr_r,9,6) as modelMagErr_r,
str(p.modelMagErr_i,9,6) as modelMagErr_i,
str(p.modelMagErr_z,9,6) as modelMagErr_z,

str(p.dered_u,9,6) as dered_u,
str(p.dered_g,9,6) as dered_g,
str(p.dered_r,9,6) as dered_r,
str(p.dered_i,9,6) as dered_i,
str(p.dered_z,9,6) as dered_z,

str(p.petroMag_u,9,6) as petroMag_u,
str(p.petroMag_g,9,6) as petroMag_g,
str(p.petroMag_r,9,6) as petroMag_r,
str(p.petroMag_i,9,6) as petroMag_i,
str(p.petroMag_z,9,6) as petroMag_z,

str(p.petroMagErr_u,9,6) as petroMagErr_u,
str(p.petroMagErr_g,9,6) as petroMagErr_g,
str(p.petroMagErr_r,9,6) as petroMagErr_r,
str(p.petroMagErr_i,9,6) as petroMagErr_i,
str(p.petroMagErr_z,9,6) as petroMagErr_z,

--get photometric redshift
str(z.z,9,7) as Photz,z2.photozcc2,z2.photozd1,z.t,
str(z.zErr,9,7) as Photzerr,
z.quality as photz_quality,

-- Get spectroscopic redshift
```

```
str(ISNULL(s.z,-99),9,7) as SpecZ,
str(ISNULL(s.zerr,-99),9,7) as SpecZerr,
str(ISNULL(s.zConf,-99),6,4) as zConf,
ISNULL(s.zwarning,-99) as zwarning,
ISNULL(s.zstatus, -99) as zstatus,
ISNULL(s.SpecClass,-99) as SpecClass,
s.eclass,
s.eCoeff_2,s.eCoeff_1,
dbo.fPhotoTypeN(p.type) as type,
ISNULL(s.ObjType,-99) as Objtype

FROM #x x, #upload u, PhotoPrimary as p

JOIN Photoz as z on p.ObjID= z.ObjID
LEFT OUTER JOIN Photoz2 as z2 on p.ObjID= z2.ObjID
LEFT OUTER JOIN SpecObj as s on s.bestobjid=p.objid

WHERE u.up_id = x.up_id and x.objID=p.objID
and (p.type = dbo.fphototype(''galaxy'') or p.type = dbo.fphototype(''star''))
and ((flags_u & 0X10000000)!0=0)
and ((flags_u & 0X8100000c00a0)=0)
and (((flags_u & 0X400000000000)=0 ) or (psfmagerr_g<=0.2))
and (((flags_u & 0X100000000000)=0 ) or (flags_u & 0X1000)=0)
ORDER BY x.up_id
```

APPENDIX C

Appendix 3

Here we describe the construction of the spectral index distributions, SID(1.4 – 5, NVSS/GB6) and SID(8 – 20, AT20G), shown in Fig. C.1.

The NRAO VLA Sky Survey (Condon et al. 1998, NVSS) is a 1.4 GHz survey covering the sky north of $\delta = -40°$, with a resolution of 45″. The nominal detection limit is 2.5 mJy. The Green Bank 4.85 GHz (GB6) survey (Gregory et al. 1996) used NRAO's (former) 91m telescope to survey the sky within $0° < \delta < 75°$, with a resolution of 3.5″, and a detection threshold of 18 mJy. We first match the NVSS source catalog to the the spectroscopic sample of SDSS DR6 (with a conservative matching radius of 10″), and limit the combined sample to $z < 0.4$, as we are interested in the radio galaxies in the local Universe. We then cross correlate the NVSS/SDSS sample with GB6 (again using a conservative matching radius of 1′), keeping all unmatched NVSS/SDSS sources. Because of the differences in the angular resolution of the two radio surveys, we further limit ourselves to NVSS sources for which there are no neighboring sources from NVSS within a radius of 4′. This is to ensure that both surveys measure the "total" flux from the sources, and to avoid sources that might be blended in the lower resolution GB6 survey. Finally, to account for the differences in the detection limits, we set a high flux cut (100 mJy) for NVSS sources so that we can be sure to include all sources with $\alpha_{LC} > -1.4$. Of the

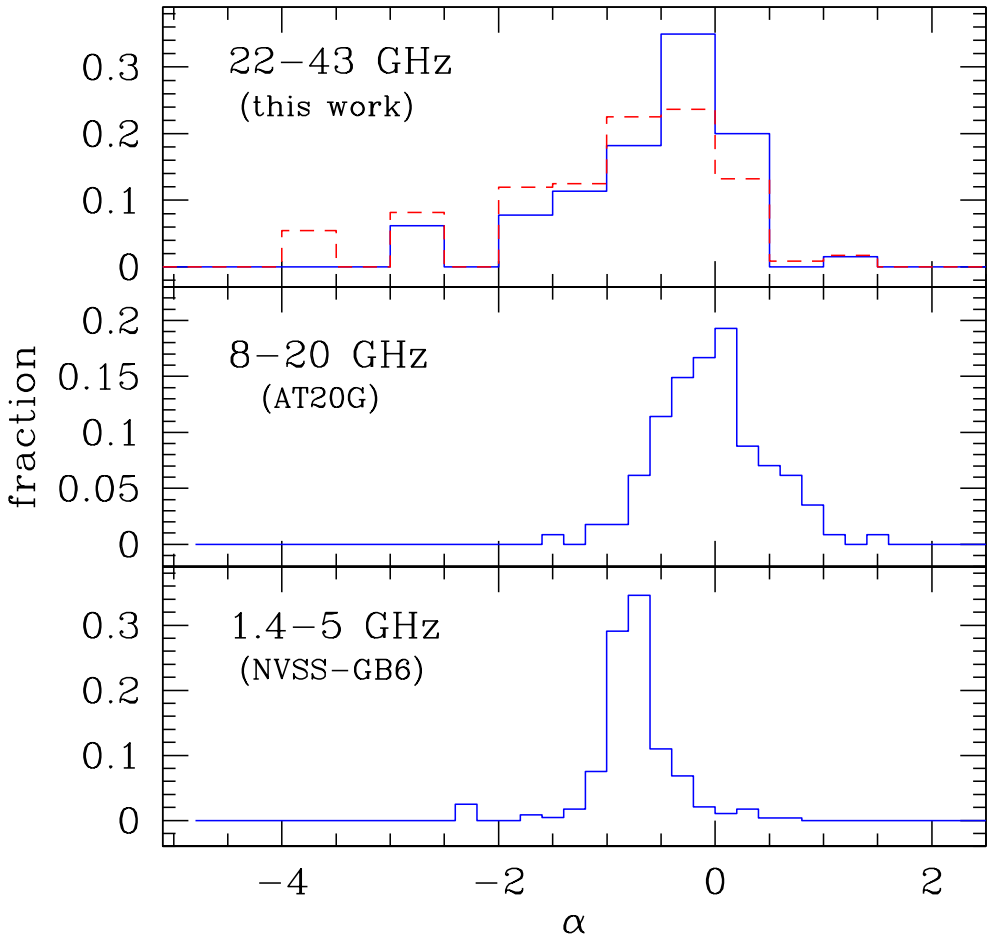

Figure C.1: The spectral index distribution in three frequency bands. *Top*: the SID in 22 – 43 GHz band as determined from our VLA data. *Middle*: the 8 – 20 GHz SID determined from the AT20G survey, using data presented in Sadler et al. (2006). *Bottom*: the 1.4 – 5 GHz SID based on data from the NVSS and GB6 surveys.

resulting 292 NVSS sources, 9 are not detected in GB6, and we assign 18 mJy as the upper limit in the 4.85 GHz flux for these sources. The SID from this sample is shown in the lower panel in Fig. C.1. We note our result is not sensitive to the flux cut applied to the NVSS sources, and on the requirement for the "isolatedness" of the sources. Neither setting the cut to 200 mJy (so that we are complete for sources with $\alpha_{LC} > -1.9$) nor including sources with neighbors closer than $4'$ changes the mean value of the SID beyond one sigma level.

The Australia Telescope Compact Array is conducting a large survey at 20 GHz (AT20G) that will eventually cover the sky south of $\delta = 0^{\circ}$. A bright source catalog based on observations up to 2004 is reported by Sadler et al. (2006). We use the 114 sources stronger than 100 mJy at 20 GHz that are also detected at 8.6 GHz to construct the SID, and show the result in the middle panel of Fig. C.1. Because the sources are selected at 20 GHz, the SID is biased towards positive values. Furthermore, the redshifts for the majority of the sources are not available, and thus the result may not be representative of the restframe 8 – 20 GHz SID. Nevertheless, this sample provides a distribution that is at the opposite extreme compared to that from our VLA observations, and therefore the two SIDs should bracket the true distribution.

Bibliography

Abazajian, K., Adelman-McCarthy, J. K., Agüeros, M. A., et al. 2004, AJ, 128, 502

Abell, G. O. 1958, ApJS, 3, 211

Abell, G. O., Corwin, Jr., H. G., & Olowin, R. P. 1989, ApJS, 70, 1

Abraham, R., Glazebrook, K., & McCarthy, P. 2004, AJ, 127, 2455

Adelman-McCarthy, J. K., Agüeros, M. A., Allam, S. S., et al. 2008, ApJS, 175, 297

Afonso, J., Georgakakis, A., Almeida, C., et al. 2005, ApJ, 624, 135

Akiyama, M., Ohta, K., Yamada, T., et al. 2000, ApJ, 532, 700

Alexander, D. M., Brandt, W. N., Hornschemeier, A. E., et al. 2001, AJ, 122, 2156

AMI Collaboration, Barker, R., Biddulph, P., et al. 2006, MNRAS, 369, L1

Antonucci, R. 1993, ARAA, 31, 473

Arimoto, N. & Yoshii, Y. 1987, AAP, 173, 23

Astier, P., Guy, J., Regnault, N., et al. 2006, AAp, 447, 31

Babbedge, T. S. R., Rowan-Robinson, M., Gonzalez-Solares, E., et al. 2004, MNRAS, 353, 654

Baldwin, J. A., Phillips, M. M., & Terlevich, R. ????

Baldwin, J. E., Boysen, R. C., Hales, S. E. G., et al. 1985, MNRAS, 217, 717

Barger, A. J., Cowie, L. L., Brandt, W. N., et al. 2002, AJ, 124, 1839

Barger, A. J., Cowie, L. L., Capak, P., et al. 2003, AJ, 126, 632

Barger, A. J., Cowie, L. L., Mushotzky, R. F., & Richards, E. A. 2001, AJ, 121, 662

Barger, A. J., Cowie, L. L., & Richards, E. A. 2000, AJ, 119, 2092

Barger, A. J., Cowie, L. L., & Wang, W.-H. 2007, ApJ, 654, 764

Bauer, F. E., Alexander, D. M., Brandt, W. N., et al. 2002a, AJ, 124, 2351

Bauer, F. E., Alexander, D. M., Brandt, W. N., et al. 2002b, AJ, 124, 2351

Baugh, C. M., Gardner, J. P., Frenk, C. S., & Sharples, R. M. 1996, MNRAS, 283, L15

Baum, W. A. 1957, AJ, 62, 6

Baum, W. A. 1962, in IAU Symposium, Vol. 15, Problems of Extra-Galactic Research, ed. G. C. McVittie, 390–+

Becker, R. H., White, R. L., & Helfand, D. J. 1995, ApJ, 450, 559

Bell, E. F. 2003, ApJ, 586, 794

Benitez, N. 1998, MNRAS, arxiv/9811189, 95

Benítez, N. 2000, ApJ, 536, 571

Benn, C. R., Rowan-Robinson, M., McMahon, R. G., Broadhurst, T. J., & Lawrence, A. 1993, MNRAS, 263, 98

Bergstrom, S. & Wiklind, T. 2004, A&A, 414, 95

Berry, M. 1989 (Bristol: Hilger, 1989)

Bertin, E. & Arnouts, S. 1996, AAPS, 117, 393

Best, P. 2004, MNRAS, 351, 70

Best, P. N., Arts, J. N., Röttgering, H. J. A., et al. 2003, MNRAS, 346, 627

Best, P. N., Kauffmann, G., Heckman, T. M., & Ivezić, Ž. 2005, MNRAS, 362, 9

Best, P. N., Longair, M. S., & Roettgering, H. J. A. 1998, MNRAS, 295, 549

Blain, A. W., Smail, I., Ivison, R. J., & Kneib, J.-P. 1999, MNRAS, 302, 632

Blake, C., Ferreira, P. G., & Borrill, J. 2004a, MNRAS, 351, 923

Blake, C., Mauch, T., & Sadler, E. M. 2004b, MNRAS, 347, 787

Blake, C. & Wall, J. 2002a, MNRAS, 329, L37

Blake, C. & Wall, J. 2002b, MNRAS, 337, 993

Bolton, J. G., Stanley, G. J., & Slee, O. B. 1949, NATURE, 164, 101

Bolton, R. C., Cotter, G., Pooley, G. G., et al. 2004, MNRAS, 354, 485

Bolzonella, M., Miralles, J.-M., & Pelló, R. 2000, AAP, 363, 476

Bondi, M., Ciliegi, P., Venturi, T., et al. 2007, AAP, 463, 519

Bondi, M., Ciliegi, P., Zamorani, G., et al. 2003, AAP, 403, 857

Brand, K., Brown, M. J. I., Dey, A., et al. 2006, ApJ, 641, 140

Brand, K., Rawlings, S., Hill, G. J., & Lacy, M. 2003, New Astronomy Review, 47, 325

Brand, K., Rawlings, S., Hill, G. J., & Tufts, J. R. 2005, MNRAS, 357, 1231

Brandt, W. N., Alexander, D. M., Hornschemeier, A. E., et al. 2001, AJ, 122, 2810

Brinkmann, W., Laurent-Muehleisen, S. A., Voges, W., et al. 2000, AAP, 356, 445

Brodwin, M., Brown, M. J. I., Ashby, M. L. N., et al. 2006, ApJ, 651, 791

Brookes, M. H., Best, P. N., Rengelink, R., & Röttgering, H. J. A. 2006, MNRAS, 366, 1265

Brown, M. J. I., Brand, K., Dey, A., et al. 2006, ApJ, 638, 88

Brown, M. J. I., Dey, A., Jannuzi, B. T., et al. 2003, ApJ, 597, 225

Brusa, M., Comastri, A., Mignoli, M., et al. 2003, AAP, 409, 65

Bruzual, G. & Charlot, S. 1993, ApJ, 405, 538

Bruzual, G. & Charlot, S. 2003, MNRAS, 344, 1000

Bruzual A., G. 1983, ApJ, 273, 105

Burles, S., Nollett, K. M., & Turner, M. S. 2001, PRD, 63, 063512

Calzetti, D., Armus, L., Bohlin, R. C., et al. 2000, ApJ, 533, 682

Carlstrom, J. E., Holder, G. P., & Reese, E. D. 2002, ARAA, 40, 643

Carroll, S. M., Press, W. H., & Turner, E. L. 1992, ARAA, 30, 499

Chaboyer, B. 1996, Nuclear Physics B Proceedings Supplements, 51, 10

Chaboyer, B., Demarque, P., Kernan, P. J., & Krauss, L. M. 1998, ApJ, 494, 96

Chaboyer, B. & Krauss, L. M. 2002, ApJL, 567, L45

Chan, B., Cram, L., Sadler, E., et al. 2004, MNRAS, 352, 1245

Ciliegi, P., Elvis, M., Wilkes, B. J., Boyle, B. J., & McMahon, R. G. 1997, MNRAS, 284, 401

Ciliegi, P., Zamorani, G., Bondi, M., et al. 2005, AAP, 441, 879

Ciliegi, P., Zamorani, G., Hasinger, G., et al. 2003, AAP, 398, 901

Cimatti, A., Daddi, E., Cassata, P., et al. 2003, AAP, 412, L1

Cimatti, A., Daddi, E., & di Serego Alighieri, S. 1999, A&A, 352, 45

Cimatti, A., Villani, D., Pozzitti, L., & di Serego Alighieri, S. 2000, MNRAS, 318, 453

Coble, K., Bonamente, M., Carlstrom, J., et al. 2007, AJ, 134, 897

Coleman, G. D., Wu, C.-C., & Weedman, D. W. 1980, ApJ, 43, 393

Colless, M., Dalton, G., Maddox, S., et al. 2001, MNRAS, 328, 1039

Collister, A. A. & Lahav, O. 2004, PASP, 116, 345

Condon, J. J. 1984, ApJ, 287, 461

Condon, J. J. 1989, APJ, 338, 13

Condon, J. J. 1992, ARAA, 30, 575

Condon, J. J., Anderson, M. L., & Helou, G. 1991, ApJ, 376, 95

Condon, J. J., Cotton, W. D., Greisen, E. W., et al. 1998, AJ, 115, 1693

Connolly, A. J., Csabai, I., Szalay, A. S., et al. 1995, AJ, 110, 2655

Connolly, A. J., Scranton, R., Johnston, D., et al. 2002, ApJ, 579, 42

Connolly, A. J., Szalay, A. S., Dickinson, M., Subbarao, M. U., & Brunner, R. J. 1997, APJL, 486, L11+

Cooray, A. R., Grego, L., Holzapfel, W. L., Joy, M., & Carlstrom, J. E. 1998, AJ, 115, 1388

Cowan, J. J., Pfeiffer, B., Kratz, K.-L., et al. 1999, ApJ, 521, 194

Cowie, L. L., Barger, A. J., Bautz, M. W., et al. 2001, ApJl, 551, L9

Cowie, L. L., Songaila, A., & Barger, A. J. 1999, AJ, 118, 603

Cress, C. M., Helfand, D. J., Becker, R. H., Gregg, M. D., & White, R. L. 1996, ApJ, 473, 7

Croton, D. J., Springel, V., White, S. D. M., et al. 2006, MNRAS, 365, 11

Cruz, M. J., Jarvis, M. J., Rawlings, S., & Blundell, K. M. 2007, MNRAS, 375, 1349

Daddi, E., Cimatti, A., Broadhurst, T., et al. 2002, AAP, 384, L1

Danese, L., Franceschini, A., Toffolatti, L., & de Zotti, G. 1987, ApJL, 318, L15

De Breuck, C., van Breugel, W., Stanford, S. A., et al. 2002, AJ, 123, 637

de Ruiter, H. R., Arp, H. C., & Willis, A. G. 1977, AAPS, 28, 211

de Vries, W. H., Morganti, R., Röttgering, H. J. A., et al. 2002, AJ, 123, 1784

de Young, D. S. 2002, The physics of extragalactic radio sources (The physics of extragalactic radio sources, by David S. De Young. Chicago, Ill. : University of Chicago Press, 2002.)

de Zotti, G., Ricci, R., Mesa, D., et al. 2005, AAP, 431, 893

Dunkley, J., Komatsu, E., Nolta, M. R., et al. 2008, ArXiv e-prints/0803.0586

Dunlop, J. S. & Peacock, J. A. 1990, MNRAS, 247, 19

Eales, S., Rawlings, S., Law-Green, D., Cotter, G., & Lacy, M. 1997, MNRAS, 291, 593

Edge, D. O., Shakeshaft, J. R., McAdam, W. B., Baldwin, J. E., & Archer, S. 1959, MEMRAS, 68, 37

Eisenstein, D. J., Annis, J., Gunn, J. E., et al. 2001, AJ, 122, 2267

El Bouchefry, K. & Cress, C. M. 2007, Astronomische Nachrichten, 328, 577

Elston, R., Rieke, G., & Rieke, M. 1989, ApJ, 31, 80

Elston, R., Rieke, M., & Rieke, G. 1988, ApJ, 331, L77

Elston, R. J., Gonzalez, A. H., McKenzie, E., et al. 2006, ApJ, 639, 816

Elvis, M., Wilkes, B. J., McDowell, J. C., et al. 1994, ApJS, 95, 1

Fabbiano, G. 1989, ARAA, 27, 87

Fanaroff, B. L. & Riley, J. M. 1974, MNRAS, 167, 31P

Feigelson, E. D. & Nelson, P. I. 1985, APJ, 293, 192

Fernández-Soto, A., Lanzetta, K. M., Chen, H.-W., Pascarelle, S. M., & Yahata, N. 2001, ApJS, 135, 41

Ferrarese, L., Mould, J. R., Kennicutt, Jr., R. C., et al. 2000, ApJ, 529, 745

Fiore, F., Brusa, M., Cocchia, F., et al. 2003, AAP, 409, 79

Flores, H., Hammer, F., Thuan, T. X., et al. 1999, ApJ, 517, 148

Fomalont, E., Kellermann, K., Cowie, L., et al. 2006, ApJs, 167, 103

Fowler, J. W., Niemack, M. D., Dicker, S. R., et al. 2007, AO, 46, 3444

Franceschini, A., Braito, V., Persic, M., et al. 2003, MNRAS, 343, 1181

Franx, M., Labbé, I., Rudnick, G., et al. 2003, ApJL, 587, L79

Freedman, W., Madore, B. F., Gibson, B. K., et al. 2001, ApJ, 553, 47

Freedman, W. L., Madore, B. F., Mould, J. R., et al. 1994, NATURE, 371, 757

Fukugita, M., Ichikawa, T., Gunn, J. E., et al. 1996, AJ, 111, 1748

Gandhi, P., Crawford, C. S., Fabian, A. C., & Johnstone, R. M. 2004, MNRAS, 348, 529

Georgakakis, A., Afonso, J., Hopkins, A., et al. 2005, ApJ, 620, 584

Georgakakis, A., Hopkins, A. M., Afonso, J., et al. 2004, MNRAS, 354, 127

Georgakakis, A., Mobasher, B., Cram, L., et al. 1999, MNRAS, 306, 708

Georgantopoulos, I., Georgakakis, A., Akylas, A., et al. 2004, MNRAS, 352, 91

Giacconi, R., Zirm, A., Wang, J., et al. 2002, ApJS, 139, 369

Gibson, B. & Brook, C. 2001, MNRAS-astrph/0105384

Gioia, I. M., Maccacaro, T., Schild, R. E., et al. 1990, ApJS, 72, 567

Glazebrook, K., Blake, C., Economou, F., Lilly, S., & Colless, M. 1999, MNRAS, 306, 843

Gonzalez, A. H. & Maccarone, T. J. 2002, ApJ, 581, 155

Gower, J. F. R., Scott, P. F., & Wills, D. 1967, MeMRAS, 71, 49

Gregory, P. C., Scott, W. K., Douglas, K., & Condon, J. J. 1996, ApJS, 103, 427

Griffith, M. R. & Wright, A. E. 1993, AJ, 105, 1666

Grimm, H.-J., Gilfanov, M., & Sunyaev, R. 2003, MNRAS, 339, 793

Gruppioni, C., Mignoli, M., & Zamorani, G. 1999a, MNRAS, 176, 365

Gruppioni, C., Mignoli, M., & Zamorani, G. 1999b, MNRAS, 304, 199

Guiderdoni, B. & Rocca-Volmerange, B. 1987, AAP, 186, 1

Gunn, J. E., Carr, M., Rockosi, C., et al. 1998, AJ, 116, 3040

Gunn, J. E., Siegmund, W. A., Mannery, E. J., et al. 2006, AJ, 131, 2332

Haarsma, D. B., Partridge, R. B., Windhorst, R. A., & Richards, E. A. 2000, ApJ, 544, 641

Hall, P. B., Sawicki, M., Martini, P., et al. 2001, AJ, 121, 1840

Hamilton, A. J. S. & Tegmark, M. 2004, MNRAS, 349, 115

Hamilton, T. T. & Helfand, D. J. 1993, ApJ, 418, 55

Hammer, F., Crampton, D., lilly, S., Le Feve, O., & Kenet, T. 1995, MNARS, 276, 058

Hamuy, M., Phillips, M. M., Suntzeff, N. B., et al. 1996, AJ, 112, 2398

Hansen, B. M. S., Anderson, J., Brewer, J., et al. 2007, ApJ, 671, 380

Hansen, F. K., Cabella, P., Marinucci, D., & Vittorio, N. 2004, ApJL, 607, L67

Hernquist, L. 1989, Nature, 340, 687

Hewett, P. C. 1982, MNRAS, 201, 867

Hill, G. J. & Lilly, S. J. 1991, ApJ, 367, 1

Hill, G. J. & Rawlings, S. 2003, New Astronomy Review, 47, 373

Ho, L. C., Filippenko, A. V., & Sargent, W. L. W. 1997, ApJ, 487, 568

Hogg, D. W. 1999, ArXiv Astrophysics e-prints

Hogg, D. W., Cohen, J. G., Blandford, R., & Pahre, M. A. 1998, ApJ, 504, 622

Hopkins, A., Moabsher, B., Cram, L., & Rowan-Robinson, M. 1998, MNRAS, 296, 839

Hopkins, A. M., Afonso, J., Chan, B., et al. 2003, AJ, 125, 465

Hopkins, A. M., Connolly, A. J., Haarsma, D. B., & Cram, L. E. 2001, AJ, 122, 288

Hopkins, A. M., Connolly, A. J., & Szalay, A. S. 2000, AJ, 120, 2843

Hornschemeier, A. E., Brandt, W. N., Garmire, G. P., et al. 2001, ApJ, 554, 742

Hu, E. & Ridgway, S. 1994, AJ, 107, 1303

Hubble, E. 1929, Proceedings of the National Academy of Science, 15, 168

Huynh, M., Jackson, C., Norris, R., & Prandoni, I. 2005, AJ, 130, 1373

Infante, L. 1994, AAP, 282, 353

Isobe, T., Feigelson, E. D., & Nelson, P. I. 1986, ApJ, 306, 490

Ivezić, Ž., Menou, K., Knapp, G. R., et al. 2002, AJ, 124, 2364

Ivison, R. J., Chapman, S. C., Faber, S. M., et al. 2007, ApJL, 660, L77

Jackson, C. & Londish, D. 2000, Publications of the Astronomycal Society of Australia, 17, 234

Jannuzi, B. T. & Dey, A. 1999, in Astronomical Society of the Pacific Conference Series, Vol. 191, Photometric Redshifts and the Detection of High Redshift Galaxies, ed. R. Weymann, L. Storrie-Lombardi, M. Sawicki, & R. Brunner, 111–+

Jarvis, M. J. & Rawlings, S. 2004, New Astronomy Review, 48, 1173

Jarvis, M. J., Rawlings, S., Eales, S., et al. 2001a, MNRAS, 326, 1585

Jarvis, M. J., Rawlings, S., Lacy, M., et al. 2001b, MNRAS, 326, 1563

Jimenez, R., Padoan, P., Matteucci, F., & Heavens, A. F. 1998, MNRAS, 299, 123

Jones, D. H., Saunders, W., Colless, M., et al. 2004, MNRAS, 355, 747

Kauffmann, G., Heckman, T. M., Tremonti, C., et al. 2003, MNRAS, 346, 1055

Kellermann, K. I., Sramek, R., Schmidt, M., Shaffer, D. B., & Green, R. 1989, AJ, 98, 1195

Kelson, D. D., Illingworth, G. D., Tonry, J. L., et al. 2000, ApJ, 529, 768

Kenter, A., Murray, S. S., Forman, W. R., et al. 2005, ApJS, 161, 9

Kewley, L. J., Groves, B., Kauffmann, G., & Heckman, T. 2006, MNRAS, 372, 961

Kim, A. G., Gabi, S., Goldhaber, G., et al. 1997, ApJL, 476, L63+

Knox, L., Holder, G. P., & Church, S. E. 2004, ApJ, 612, 96

Koo, D. C. 1985, AJ, 90, 418

Lacy, M., Bunker, A. J., & Ridgway, S. E. 2000, AJ, 120, 68

Laing, R. A., Riley, J. M., & Longair, M. S. 1983, MNRAS, 204, 151

Landy, S. D. & Szalay, A. S. 1993, ApJ, 412, 64

Lanzetta, K. M., Yahil, A., & Fernández-Soto, A. 1996, Nature, 381, 759

Large, M. I., Mills, B. Y., Little, A. G., Crawford, D. F., & Sutton, J. M. 1981, MNRAS, 194, 693

Leavitt, H. S. & Pickering, E. C. 1912, Harvard College Observatory Circular, 173, 1

Ledlow, M. J. & Owen, F. N. 1995, AJ, 109, 853

Ledlow, M. J. & Owen, F. N. 1996, AJ, 112, 9

Lehmann, I., Hasinger, G., Schmidt, M., et al. 2001, AAP, 371, 833

Leibundgut, B. 2001, ARAA, 39, 67

Leitherer, C., Schaerer, D., Goldader, J. D., et al. 1999, ApJS, 123, 3

Lilly, S. J. 1988, ApJ, 333, 161

Lilly, S. J., Le Fevre, O., Hammer, F., & Crampton, D. 1996, ApJL, 460, L1+

Lilly, S. J. & Longair, M. S. 1984, MNRAS, 211, 833

Lima, M. & Hu, W. 2005, PRD, 72, 043006

Lin, Y.-T. & Mohr, J. J. 2003, ApJ, 582, 574

Lin, Y.-T. & Mohr, J. J. 2007, ApJS, 170, 71

Ling, E. N., Barrow, J. D., & Frenk, C. S. 1986, MNRAS, 223, 21P

Loh, E. D. & Spillar, E. J. 1986, AJL, 307, L1

Longair, M. S. 1984 (Cambridge: University Press, 1984)

Lupton, R. H., Ivezic, Z., Gunn, J. E., et al. 2002, in Society of Photo-Optical Instrumentation Engineers (SPIE) Conference Series, Vol. 4836, 350–356

Maccacaro, T., Gioia, I. M., Wolter, A., Zamorani, G., & Stocke, J. T. 1988, ApJ, 326, 680

Madau, P. 1995, ApJ, 441, 18

Madau, P., Ferguson, H. C., Dickinson, M. E., et al. 1996, MNRAS, 283, 1388

Madau, P., Pozzetti, L., & Dickinson, M. 1998, ApJ, 498, 106

Maddox, S. J., Efstathiou, G., Sutherland, W. J., & Loveday, J. 1990, MNRAS, 243, 692

Magliocchetti, M. & Maddox, S. J. 2002, MNRAS, 330, 241

Magliocchetti, M., Maddox, S. J., Hawkins, E., et al. 2004, MNRAS, 350, 1485

Magliocchetti, M., Maddox, S. J., Lahav, O., & Wall, J. V. 1998, MNRAS, 300, 257

Magliocchetti, M., Maddox, S. J., Lahav, O., & Wall, J. V. 1999, MNRAS, 306, 943

Magorrian, J., Tremaine, S., Richstone, D., et al. 1998, AJ, 115, 2285

Mainieri, V., Bergeron, J., Hasinger, G., et al. 2002, AAP, 393, 425

Mann, R. G., Oliver, S., Carballo, R., et al. 2002, MNRAS, 332, 549

Mann, R. G., Oliver, S. J., Serjeant, S. B. G., et al. 1997, MNRAS, 289, 482

Mannucci, F., Pozzetti, L., Thompson, D., et al. 2002, MNRAS, 329, L57

Mason, B. S., Myers, S. T., & Readhead, A. C. S. 2002, in The Ninth Marcel Grossmann Meeting, ed. V. G. Gurzadyan, R. T. Jantzen, & R. Ruffini, 2201

Mauch, T., Murphy, T., Buttery, H. J., et al. 2003, MNRAS, 342, 1117

McCarthy, P., Persson, S., & West, S. 1992, ApJ, 386, 52

McCarthy, P. J. 1993, ARAA, 31, 639

McGreer, I. D., Becker, R. H., Helfand, D. J., & White, R. L. 2006, ApJ, 652, 157

McLure, R. J. & Jarvis, M. J. 2004, MNRAS, 353, L45

McLure, R. J., Willott, C. J., Jarvis, M. J., et al. 2004, MNRAS, 351, 347

McMahon, R. G., White, R. L., Helfand, D. J., & Becker, R. H. 2002, ApJS, 143, 1

Merloni, A., Heinz, S., & di Matteo, T. 2003, MNRAS, 345, 1057

Mignoli, M., Pozzetti, L., Comastri, A., et al. 2004, AAP, 418, 827

Miller, G. E. & Scalo, J. M. 1979, ApJS, 41, 513

Miller, N. A. & Owen, F. N. 2001, ApJS, 134, 355

Mobasher, B., Idzi, R., Benítez, N., et al. 2004, ApJL, 600, L167

Moran, E. C., Lehnert, M. D., & Helfand, D. J. 1999, ApJ, 526, 649

Moretti, A., Campana, S., Lazzati, D., & Tagliaferri, G. 2003, ApJ, 588, 696

Morrison, G. E. & Owen, F. N. 2003, AJ, 125, 506

Murray, S. S., Kenter, A., Forman, W. R., et al. 2005, ApJS, 161, 1

Nandra, K. & Pounds, K. A. 1994, MNRAS, 268, 405

Negrello, M., Magliocchetti, M., & De Zotti, G. 2006, MNRAS, 368, 935

Nevalainen, J. & Roos, M. 1998, AAP, 339, 7

Newman, P. R., Long, D. C., Snedden, S. A., et al. 2004, in Proceedings of the SPIE conference, Vol. 5492, 533–544

Newsam, A., McHardy, I., Jones, L., & Mason, K. 1997, MNRAS, 292, 378

Norman, C., Hasinger, G., Giacconi, R., et al. 2002, ApJ, 571, 218

Obrić, M., Ivezić, Ž., Best, P. N., et al. 2006, MNRAS, 370, 1677

Oort, M. J. A. 1987, AAPS, 71, 221

Oswalt, T. D., Smith, J. A., Wood, M. A., & Hintzen, P. 1996, Nature, 382, 692

Overzier, R. A., Röttgering, H. J. A., Rengelink, R. B., & Wilman, R. J. 2003, AAP, 405, 53

Owen, F. N. & Ledlow, M. J. 1997, ApJS, 108, 41

Owen, F. N., Ledlow, M. J., & Keel, W. C. 1995, AJ, 109, 14

Padovani, P., Allen, M. G., Rosati, P., & Walton, N. A. 2004, AAp, 424, 545

Papovich, C., Moustakas, L. A., Dickinson, M., et al. 2006, ApJ, 640, 92

Peacock, J. A. & Dodds, S. J. 1994, MNRAS, 267, 1020

Peacock, J. A. & Nicholson, D. 1991, MNRAS, 253, 307

Peebles, P. J. E. 1980, The large-scale structure of the universe (Research supported by the National Science Foundation. Princeton, N.J., Princeton University Press, 1980. 435 p.)

Peebles, P. J. E. 1993 (Princeton Series in Physics, Princeton, NJ: Princeton University Press, |c1993)

Pettini, M., Shapley, A. E., Steidel, C. C., et al. 2001, ApJ, 554, 981

Pier, J. R., Munn, J. A., Hindsley, R. B., et al. 2003, AJ, 125, 1559

Pierce, M. J., Welch, D. L., McClure, R. D., et al. 1994, Nature, 371, 385

Pierpaoli, E. & Perna, R. 2004, MNRAS, 354, 1005

Pozzetti, L. & Mannucci, F. 2000, MNRAS, 317, L17

Prandoni, I., Gregorini, L., Parma, P., et al. 2001, AAP, 369, 787

Prandoni, I., Parma, P., Wieringa, M., et al. 2006, A&A, 457, 517

Prestage, R. M. & Peacock, J. A. 1983, MNRAS, 204, 355

Ranalli, P., Comastri, A., & Setti, G. 2003, AAP, 399, 39

Rawlings, S., Eales, S., & Lacy, M. 2001, MNRAS, 322, 523

Rees, N. 1990, MNRAS, 244, 233

Reid, N. 1998, Proceedings of the National Academy of Science, 95, 8

Reiprich, T. H. 2006, AAP, 453, L39

Reiprich, T. H. & Böhringer, H. 2002, ApJ, 567, 716

Rengelink, R. 1998, PhD thesis, Rijksuniversiteit Leiden, (1998)

Richards, E. 2000, ApJ, 533, 611

Richer, H. B., Brewer, J., Fahlman, G. G., et al. 2004, AJ, 127, 2904

Roche, N., Almaini, O., Dunlop, J., Ivison, R., & Willott, C. 2002, MNRAS, 337, 1282

Rosati, P., Tozzi, P., Giacconi, R., et al. 2002, ApJ, 566, 667

Rovilos, E., Georgakakis, A., Georgantopoulos, I., et al. 2007, AAP, 466, 119

Rowan-Robinson, M. 2003, MNRAS, 345, 819

Rowan-Robinson, M., Mann, R. G., Oliver, S. J., et al. 1997, MNRAS, 289, 490

Ruhl, J., Ade, P. A. R., Carlstrom, J. E., et al. 2004, in Holland and Stafford Withington Proceedings of the SPIE, Vol. 5498, 11–29

Rutledge, R. E., Brunner, R. J., Prince, T. A., & Lonsdale, C. 2000, ApJS, 131, 335

Sadler, E., McIntyre, V., jackson, C., & Cannon, R. 1999, Publications of the Astronomical Society of Australia, 16, 247

Sadler, E. M., Jackson, C. A., Cannon, R. D., et al. 2002, MNRAS, 329, 227

Sadler, E. M., Ricci, R., Ekers, R. D., et al. 2006, MNRAS, 371, 898

Sadler, E. M., Ricci, R., Ekers, R. D., et al. 2008, MNRAS

Sakai, S., Mould, J. R., Hughes, S. M. G., et al. 2000, ApJ, 529, 698

Sánchez-Sutil, J. R., Muñoz-Arjonilla, A. J., Martí, J., et al. 2006, AAP, 452, 739

Sandage, A., Saha, A., Tammann, G. A., et al. 1996, ApJL, 460, L15+

Sanders, D. B. & Mirabel, I. F. 1996, ARAA, 34, 749

Sarkar, S. 1999, in Dark matter in Astrophysics and Particle Physics, ed. H. V. Klapdor-Kleingrothaus & L. Baudis, 108–+

Sawicki, M. J., Lin, H., & Yee, H. K. C. 1997, AJ, 113, 1

Schatz, H., Toenjes, R., Pfeiffer, B., et al. 2002, ApJ, 579, 626

Schmidt, B. P., Kirshner, R. P., Eastman, R. G., et al. 1994, ApJ, 432, 42

Scranton, R., Johnston, D., Dodelson, S., et al. 2002, ApJ, 579, 48

Sehgal, N., Trac, H., Huffenberger, K., & Bode, P. 2007, ApJ, 664, 149

Seymour, N., McHardy, I. M., & Gunn, K. F. 2004, MNRAS, 352, 131

Simpson, C., Almaini, O., Cirasuolo, M., et al. 2006, MNRAS, 373, L21

Slipher, V. M. 1917, Proceedings of the American Philosophical Society, 56, 403

Smail, I., Owen, F., Morrison, G., et al. 2002, MNRAS, 581, 844

Spergel, D. N., Bean, R., Doré, O., et al. 2007, ApJS, 170, 377

Spergel, D. N., Verde, L., Peiris, H. V., et al. 2003, ApJS, 148, 175

Spinrad, H., Dey, A., Stern, D., et al. 1997, ApJ, 484, 581

Stern, D., Moran, E. C., Coil, A. L., et al. 2002a, ApJ, 568, 71

Stern, D., Tozzi, P., Stanford, S. A., et al. 2002b, AJ, 123, 2223

Stocke, J. T., Morris, S. L., Gioia, I. M., et al. 1991, ApJS, 76, 813

Stockton, A., McGrath, E., & Canalizo, G. 2006, ApJ, 650, 706

Stoughton, C., Lupton, R. H., Bernardi, M., et al. 2002, AJ, 123, 485

Strateva, I., Ivezić, Ž., Knapp, G. R., et al. 2001, AJ, 122, 1861

Sullivan, M., Hopkins, A. M., Afonso, J., et al. 2004, ApJS, 155, 1

Sunyaev, R. A. & Zeldovich, Y. B. 1970, ApSS, 7, 3

Sutherland, W. & Saunders, W. 1992, MNRAS, 259, 413

Szokoly, G. P., Bergeron, J., Hasinger, G., et al. 2004, ApJS, 155, 271

Takagi, T., Mortier, A. M. J., Shimasaku, K., et al. 2007, MNRAS, 381, 1154

Tanvir, N. R., Shanks, T., Ferguson, H. C., & Robinson, D. R. T. 1995, Nature, 377, 27

Teplitz, H. I., Malkan, M. A., Steidel, C. C., et al. 2000, ApJ, 542, 18

Toffolatti, L., Argueso Gomez, F., de Zotti, G., et al. 1998, MNRAS, 297, 117

Tozzi, P., Mainieri, V., Rosati, P., et al. 2009, ArXiv e-prints

Tozzi, P., Rosati, P., Nonino, M., et al. 2001, ApJ, 562, 42

Tresse, L. & Maddox, S. J. 1998, ApJ, 495, 691

Treyer, M. A., Ellis, R. S., Milliard, B., Donas, J., & Bridges, T. J. 1998, MNRAS, 300, 303

Urry, C. & Padovani, P. 1995, PASP, 107, 803

Visser, A. E., Riley, J. M., Roettgering, H. J. A., & Waldram, E. M. 1995, AAPS, 110, 419

Voges, W., Aschenbach, B., Boller, T., et al. 1999, AAP, 349, 389

Waddington, I., Windhorst, R. A., Dunlop, J. S., Koo, D. C., & Peacock, J. A. 2000, MNRAS, 317, 801

Waddington, I., Windhorst, R. A., Dunlop, J. S., Koo, D. C., & Peacock, J. A. 2001, VizieR Online Data Catalog

Wang, J. X., Malhotra, S., Rhoads, J. E., et al. 2004, AJ, 127, 213

White, M. & Majumdar, S. 2004, ApJ, 602, 565

White, R. L., Becker, R. H., Helfand, D. J., & Gregg, M. D. 1997, ApJ, 475, 479

Willott, C., Rawlings, S., & Blundell, K. 2001, MNRAS, 324, 1

Willott, C. J., Rawlings, S., Jarvis, M. J., & Blundell, K. M. 2003, MNRAS, 339, 173

Wilman, R. J., Miller, L., Jarvis, M. J., et al. 2008, MNRAS, 388, 1335

Wilman, R. J., Röttgering, H. J. A., Overzier, R. A., & Jarvis, M. J. 2003, MNRAS, 339, 695

Windhorst, R. A., Miley, G. K., Owen, F. N., Kron, R. G., & Koo, D. C. 1985, ApJ, 289, 494

Windhorst, R. A., van Heerde, G. M., & Katgert, P. 1984, AAPS, 58, 1

Wold, M., Armus, L., Neugebauer, G., jarrett, T., & Lehnert, M. 2003, AJ, 126, 1776

Wolstencroft, R. D., Savage, A., Clowes, R. G., et al. 1986, MNRAS, 223, 279

Worsley, M. A., Fabian, A. C., Barcons, X., et al. 2004, MNRAS, 352, L28

Worthey, G. 1994, ApJS, 95, 107

Wrobel, J. M., Taylor, G. B., Rector, T. A., Myers, S. T., & Fassnacht, C. D. 2005, AJ, 130, 923

Yan, L. & Thompson, D. 2003, ApJ, 586, 765

York, D. G., Adelman, J., Anderson, Jr., J. E., et al. 2000, AJ, 120, 1579

Zheng, W., Mikles, V. J., Mainieri, V., et al. 2004, ApJS, 155, 73

Zheng, W., Overzier, R. A., Bouwens, R. J., et al. 2006, ApJ, 640, 574